**Microstructure and Creep Behavior of Mg-Al Alloys
Containing Alkaline and Rare Earth Additions**

By

Nicholas David Saddock

A dissertation submitted in partial fulfillment
of the requirements for the degree of
Doctor of Philosophy
(Materials Science and Engineering)
in The University of Michigan
2008

Doctoral Committee:

Professor J. Wayne Jones, Co-Chair
Professor Tresa M. Pollock, Co-Chair
Professor Jyotirmoy Mazumder
John E. Allison, Ford Motor Company

Dedication

To my Wife, who supported, cared, loved and motivated through the good and the difficult times

To my Father, who instilled in me a natural curiosity in the world and always aided me with my curiosity on how things work

To my Mother who taught me how to laugh, love, and live

To my Grandfathers who inspired me towards engineering and taught me, through practice, to always reach for a higher level

Without your support, love, direction, and achievements I would never have taken the steps to actively participate in the world, but would have remained as an outsider watching it pass.

Acknowledgements

To all the lab mates, of both the Jones and Pollock groups (and many visitors), who have challenged, befriended, aided and taught me along the way, best of luck in your careers and lives.

To my colleagues from WPI, who developed my interest in materials science and guided me to the best suited graduate program and advisors: Dr. Diran Apelian, Dr. Anacleto de Figueredo, Dr. Yancy Riddle and Dr. Mahklouf Mahklouf.

To the many employees of the University of Michigan and members of the Ann Arbor community, you all support this fine academic institute and make this town a great place to grow, live, and work. My time here has opened my eyes to countless activities, views, beliefs and people in areas I was previously blind.

Table of Contents

List of Tables

List of Figures

Abstract

Microstructure and Creep Behavior of Mg-Al Alloys
Containing Alkaline and Rare Earth Additions

By

Nicholas David Saddock

Co-Chairs: J. Wayne Jones and Tresa M. Pollock

In the past few decades governmental regulation and consumer demands have lead the automotive companies towards vehicle lightweighting. Powertrain components offer significant potential for vehicle weight reductions. Recently, magnesium alloys have shown promise for use in powertrain applications where creep has been a limiting factor. These systems are Mg-Al based, with alkaline earth or rare earth additions. The solidification, microstructure, and creep behavior of a series of Mg- 4 Al- 4 X:(Ca, Ce, La, and Sr) alloys and a commercially developed AXJ530 (Mg – 5 Al – 3 Ca – 0.15 Sr) alloy (by wt%) have been investigated.

The order of decreasing freezing range of the five alloys was: AX44, AXJ530, AJ44, ALa44 and ACe44. All alloys exhibited a solid solution primary α-Mg phase surrounded by an interdendritic region of Mg and intermetallic(s). The primary phase was composed of grains approximately an order of magnitude larger than the cellular

structure. All alloys were permanent mold cast directly to creep specimens and AXJ530 specimens were provided in die-cast form. The tensile creep behavior was investigated at 175 °C for stresses ranging from 40 to 100 MPa. The order of decreasing creep resistance was: die-cast AXJ530 and permanent mold cast AXJ530, AX44, AJ44, ALa44 and ACe44.

Grain size, solute concentration, and matrix precipitates were the most significant microstructural features that influenced the creep resistance. Decreases in grain size or increases in solute concentration, both Al and the ternary addition, lowered the minimum creep rate. In the Mg-Al-Ca alloys, finely distributed Al_2Ca precipitates in the matrix also improved the creep resistance by a factor of ten over the same alloy with coarse precipitates. The morphology of the eutectic region was distinct between alloys but did not contribute to difference in creep behavior.

Creep strain distribution for the Mg-Al-Ca alloys developed heterogeneously on the scale of the α-Mg grains. As additional bulk strain accumulated, strain localized along grain boundaries between grains with significantly different Schmid factors. At these locations cavities and cracks formed that led to the eventual creep failure. Grain size influenced the plastic strain distribution during creep.

Chapter 1

Introduction

1.1   Background and Objectives

The continued push for transportation system lightweighting has been a governing force in materials design and applications.   Rising energy costs, stringent emission requirements, and increased customer demand have been major factors in the implementation of lighter material systems. Within the automotive industry, the largest impact of vehicle lightweighting will be realized in structural and powertrain components, each having unique design criteria.   This investigation is focused on magnesium alloys that are promising for automotive powertrain applications.

Within the last decade, one approach to decreasing powertrain mass has focused on the substitution of low cost, creep resistant magnesium alloys for steel and aluminum components [1, 2]. This has stimulated the development of several candidate magnesium alloys that contain aluminum, alkaline earth and/or rare earth additions.   Though many investigations have examined the microstructure and creep behavior, there remains a limited understanding of the influence of these additions on the solidification behavior, castability, microstructure, and creep deformation mechanisms.

Some of the magnesium alloys developed were based on the binary magnesium-aluminum system, with Al additions between 5 and 9 wt%. Aluminum additions improve the strength, corrosion behavior, creep resistance, and castability of magnesium at a reasonably low and stable price, compared to other alloying alternatives. Magnesium-aluminum alloys have been increasingly used in automotive applications for steering wheels, seat brackets, and instrument panels.   Unfortunately, the creep behavior of these alloys is marginal at temperatures beyond 150 °C and 50 MPa [3], whereas powertrain components typically operate between 150-200 °C and at stresses up to 100 MPa. The poor creep resistance has been attributed to the formation of the thermally unstable β-$Mg_{17}Al_{12}$ phase [2, 4-8] and the development of more creep resistant magnesium alloys

1

has focused on the identification of alloying elements that hinder the formation of this phase.

Some of the earliest creep resistant magnesium alloys contained rare earth (RE) additions [9], which are typically added in the form of a naturally occurring ore termed mischmetal. Mischmetal is comprised of lanthanum, cerium, praseodymium and neodymium which account for approximately 50%, 25%, 15% and 10% weight percent of the ore, respectively. Rare earth additions of a few weight percent (2-5 wt%) provide a dramatic increase in the creep behavior compared to the binary Mg-Al alloys, although recent data has suggested that microstructural instabilities limit use at temperatures above 150 °C [10, 11]. An understanding of the different mischmetal constituents and their effect on microstructure and creep has yet to be developed. Rare-earth containing magnesium alloys are of interest to the automotive industry [12-14], but due to their relatively-high costs, many alloy investigations have shifted to less expensive alloying additions of Ca and Sr.

Within the last decade a group of creep resistant magnesium alloys with aluminum additions between 4 and 8 wt%, and ternary additions of either calcium and/or strontium, between 1 and 3 wt%, have been developed for powertrain applications. These alloys have excellent creep resistance in the die-cast state, in some cases up to 175 °C with stresses of 100 MPa. BMW AG has begun commercial use of a composite aluminum-magnesium engine block using the magnesium alloy AJ62 (Mg-6 Al-2 Sr wt%) [15]. The USCAR MPCC project has selected several components (oil pans, valve covers, timing chain covers and engine blocks) for feasibility studies of the recently developed creep resistant alloys (primarily containing Al, Ca, and Sr additions) in the development of a magnesium intensive powertrain [16, 17].

Despite the favorable properties of these recently developed creep resistant alloys, little is known about the influence of alloy composition on solidification, microstructure development, and creep deformation mechanisms. The objective of this research is to investigate the role of composition on solidification behavior, permanent mold castability, microstructural development and mechanisms of creep in a series of ternary magnesium alloys. The nominal alloy compositions selected for this research are the four ternary systems of Mg – 4 Al – 4 X:(Ca, Ce, La, Sr) and the commercial AXJ530 alloy.

The specific objectives of this research are:

1) To investigate the influence of the ternary additions of Ca, Ce, La and Sr on the freezing range of the alloys.

2) To develop a permanent mold casting technique and to characterize as-cast microstructure as a function of composition.

3) To investigate the tensile creep behavior at 175 °C for stresses between 40 and 100 MPa.

4) To develop an understanding of the influence of microstructure on the creep behavior of these alloys.

5) To study the creep strain distribution on the length scale of the microstructure and identify approaches for improvement of the creep resistance of this class of alloys.

1.2   Approach

Master alloy ingots were procured from the Norsk Hydro Company with compositions of Mg – 4 Al – 4 X:(Ca, Ce, La, Sr). The AXJ530 alloy was provided by the General Motors Company.

The solidification behavior of each alloy was examined by inductively melting ~100 g samples of each alloy and recording the solidification cooling curve, with a calibrated, special limits of error type K thermocouple to determine liquidus and the temperature at which solidification terminated.

A permanent mold casting cell was constructed in Ann Arbor, MI at the Ford Motor Company ELM casting facility. The master alloy ingots were permanent mold cast for microstructural characterization and creep studies. Tensile creep testing of these alloys was completed across the stress range of 40 to 100 MPa at 175 °C.

Microstructural investigations of the as-permanent-mold-cast samples were completed using optical and scanning electron microscopy. The primary alpha grain interiors were examined for precipitates using a Phillips CM12 TEM. Investigations of the grain structure for each alloy were completed using a Phillips XL30 FEG equipped with an electron back-scatter detector used for OIM analysis. Solidification induced segregation was measured by wavelength dispersion analysis (WDS) using an EPMA and the data was analyzed using a standard technique [18-20]. Estimates of the strengthening

effects of solutes were calculated from an equation for solid solution strengthening in Mg-Al binary solutions [21].

The creep strain distribution at the length scale of the grain structure was quantified using a digital image correlation-based strain mapping technique [22, 23]. Creep tests were periodically interrupted and the strain distribution, on the length scale of the microstructure, was measured via analysis of surface marker displacements. The distribution of creep strain and the onset of creep damage was observed and its relation to creep strain accumulation and creep life was examined.

This dissertation contains seven chapters. A brief background, objective and approach of the research are provided in Chapter 1. A review of the literature relevant to the creep behavior, microstructure, processing and deformation for magnesium alloys is covered in Chapter 2. Experimental procedures and analysis techniques used throughout the study are presented in Chapter 3. Chapter 4 describes the results and their significance from the solidification analyses, permanent mold casting, and characterization of microstructure. In Chapter 5 the tensile creep behavior and the influence of microstructure on creep behavior are presented. Chapter 6 presents the results of the strain distribution and damage accumulation studies for the permanent-mold-cast alloys. Chapter 7 summarizes major conclusions and their significance and provides recommendations for future studies.

Chapter 2

Background and Literature Review

This chapter surveys the literature most pertinent to the objectives of this thesis. The background and review is divided into three main sections. Section 1 provides a brief overview of the uses of magnesium and its alloys, an introduction to elemental magnesium, some physical metallurgy, a short explanation on magnesium naming conventions, and a discussion of casting processing routes (i.e. sand-cast, permanent-mold-cast (gravity-cast). Section 2 reviews the composition, microstructure and creep of magnesium and its alloys with three subsections that focus on: commonly used magnesium alloys, die-cast creep resistant alloys and heat-treatable creep resistant alloys. Section 3 concludes with a summary of the literature and key observations pertaining to the objectives of this research.

2.1 Magnesium and its Alloys

2.1.1 Applications

Currently magnesium is gaining use in numerous applications from electronic (i.e. cell phones, electronic cases), consumer goods (i.e. hand held appliances and tools), automotive (i.e. powertrain, body panels), and aerospace (i.e. helicopter transmission casings). This chapter discusses the composition, microstructure, and creep of a few common alloys, including die-casting alloys, and heat treatable alloys.

The components that are currently being investigated for use in magnesium powertrains fall into two categories: (a) operating up to 150 °C and (b) above 150 °C. The first set of these powertrain components are subjected to a less severe environment, typically having no contact with engine coolant and maximum operating temperatures no greater than 150 °C [3]. They consist of the intake manifold, transfer case, automatic transmission housings, and various accessory mounts and brackets (i.e. air conditioner,

power steering pump, emissions air pump). Currently available creep resistant magnesium alloys meet or exceed the design requirements of many of these components (e.g. the transfer case) and have been in service for some time. The second set of components consists of the cylinder block, cylinder heads, oil pan, and engine front cover. These components are subjected to the harshest environment of the powertrain components, experiencing stresses and temperatures from the combustion chamber, corrosion issues from the coolants, contact with circulating oil, and the need for a multitude of gaskets and fasteners. They typically operate in the temperature range of 175-200 °C at stresses between 50-100 MPa [3]. The highest commercial payoff for creep resistant magnesium alloys is at these higher temperatures and stresses.

2.1.2   Elemental Magnesium and its Physical Metallurgy

Magnesium was first isolated by British chemist Sir Humphrey Davy in 1808 using wet magnesium sulphate in a voltaic electrolytic cell with a mercury cathode [3]. Pure magnesium exhibits a high reactivity with oxygen and water, in part, due to the two valence electrons and electrode potential of -2.375 (potential Volts) [24]. Magnesium, if left unprotected, develops a hydroxide film [4], which in contrast to aluminum, is not protective against further oxidation. This reactivity varies with alloying additions, can be controlled with careful engineering design (coatings, fixtures, and fastening), and is not a key consideration in this investigation. The reactivity of magnesium limited its early uses mainly to powder and ribbon applications for pyrotechnical purposes. It was not until World War I and II and the advent of the aviation and missile industries, that the use of magnesium and its alloys began to grow.

Magnesium crystallizes to a hexagonal close packed structure, Figure 2.1, with lattice parameters of a = 0.3209 nm and c = 0.5211 nm (c/a = 1.624, compared to that of an ideal HCP structure 1.633) [3]. Five other metallic elements exhibit an HCP structure at room temperature (zinc, titanium (below 882 °C), zirconium (below 863 °C), beryllium, and cadmium), with respective c/a ratios of 1.856, 1.588, 1.590, 1.586, 1.886 [25]. The a and c lattice parameters expand with increased temperature, and in the case of magnesium the change in lattice spacing from room temperature to 597 °C for the a and c lattice parameter is reported to be 0.00573 nm and 0.00962 nm, respectively and c/a

(at 597 °C) = 1.62458 [3]. Alloying additions of aluminum decrease the a and c lattice parameters, while increasing the c/a ratio, Figure 2.2. This is the expected trend since the reported atomic bond length of aluminum ($\approx$ 286 pm) is less than that of magnesium ($\approx$ 320 pm) [26]. Lattice parameters of several other binary magnesium alloys have been reported. Two values for the binary magnesium-calcium system are reported. For a Mg-Ca alloy measured at the solubility limit (Mg- 0.73 at% Ca) the lattice parameters increased from 'pure' magnesium to a = 0.32125 nm and c = 0.52656 nm (c/a = 1.6391) [27].   A binary Mg-0.61 at% Ca alloy quenched below the eutectic was also reported to have lattice parameters of a = 0.32098 nm and c = 0.52113 nm (c/a = 1.62356) [28]. This follows the expected trend with calcium ($\approx$ 394 pm) having a larger atomic bond length than magnesium ($\approx$ 320 pm) [26]. Magnesium lattice parameters with binary additions of strontium, cerium and lanthanum (all of which have interest in automotive creep resistant magnesium alloys) have not been reported [29-31]. This is due to the extremely low (< 0.5 wt%) solubility of these additions in the magnesium matrix. Lattice parameters with binary additions of these elements would be expected to increase, due to the increase in atomic bond length for these elements, Table 2.1.

Table 2.1 Atomic bond length (in pm) of alloying elements in creep resistant magnesium [26]

Mg	Al	Ca	Sr	Ce	La
320	286	394	430	365	374
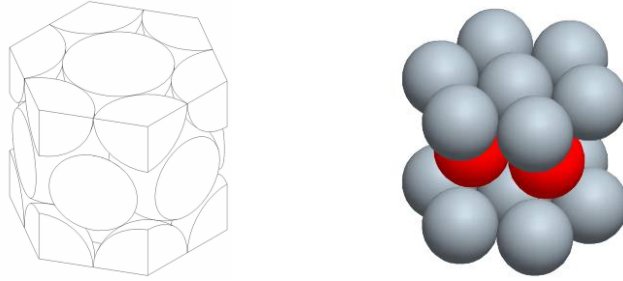
Figure 2.1 Unit cell of hexagonal close packed (HCP) crystal structure. Model is drawn to the dimensions for magnesium (atomic radius = 0.160 nm, a = 0.32092 nm, and c = 0.52105 nm).
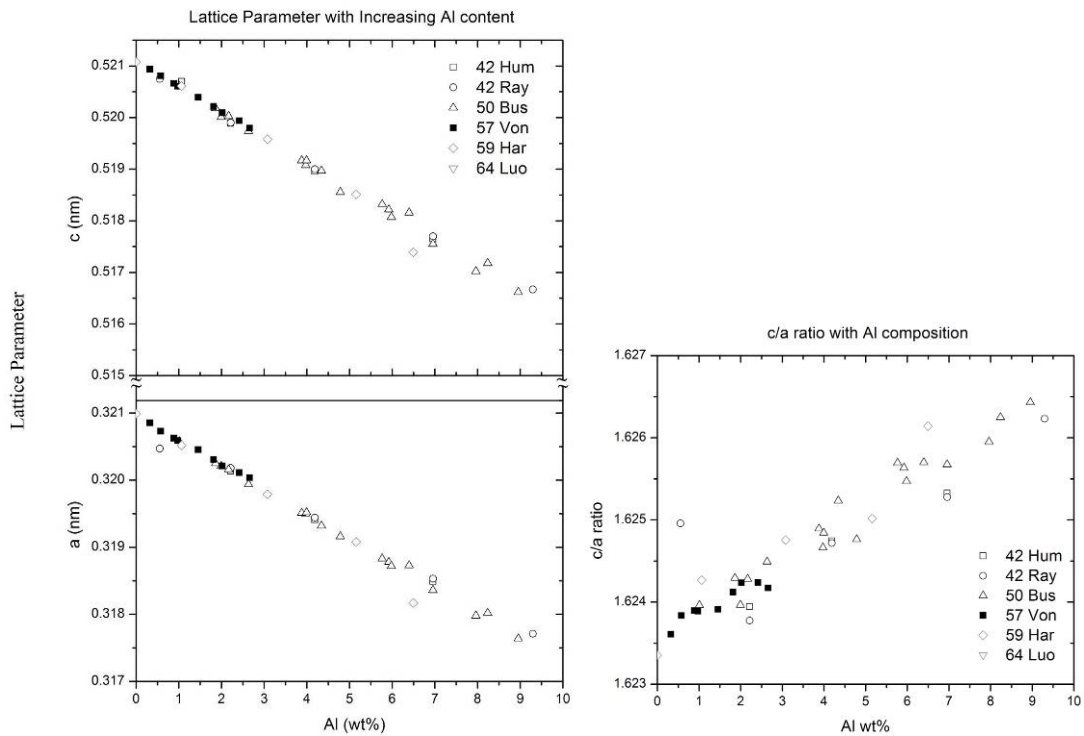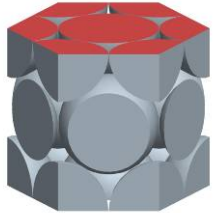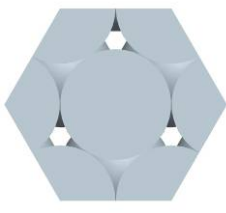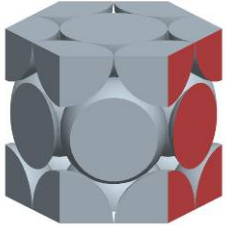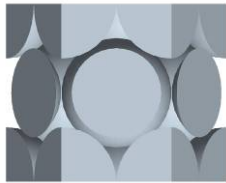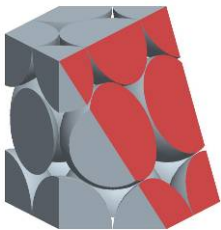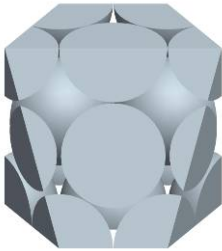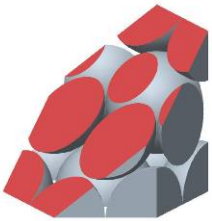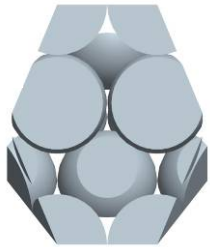
Figure 2.2 (a) Change in a and c lattice parameter for alpha magnesium with increasing composition of aluminum and (b) Change in c/a ratio with increasing composition of aluminum [32].

2.1.3   Slip Systems in Magnesium

Numerous studies have focused on identification of the active slip systems in magnesium alloys [33-49]. The observed slip systems in magnesium are basal {0001} [36, 38-45], prismatic {10$\bar{1}$0}[33-38], first order pyramidal {10$\bar{1}$1} [41], and second order pyramidal {11$\bar{2}$2} [46-49]. A summary of slip planes and directions with cited investigations is reported in Table 2.2. While active slip systems in magnesium and its alloys are still under investigation it is generally agreed that basal slip is favored, with activation of other slip systems depending on stress level, temperature, and alloy composition.

A study that investigated the room temperature critical resolved shear stress in pure magnesium (approximately 99.99 wt%) determined τ_{crss} to be approximately 0.45 MPa (+/- 0.0074 MPa) for basal slip and 0.50 MPa for slip on the first order pyramidal plane [41]. This indicates that slip would first occur on the basal plane but be closely followed by slip on the first order pyramidal plane.

Table 2.2 Crystallographic Slip Planes, Slip Directions and References for Magnesium and solid solution alloys.

Crystallographic Plane	Normal to Slip Plane	Slip Plane	Slip Direction	Reference
Basal		{0001}	<1120>	[36, 38-45]
Prism		{10$\bar{1}$0}	<1120>	[33-38]
Pyramidal I		{10$\bar{1}$1}	<1120>	[41]
Pyramidal II		{11$\bar{2}$2}	<1123>	[46-49]

2.1.4   Overview of Cast Microstructures

A schematic illustration of the major characteristics of cast magnesium alloy microstructures is shown in Figure 2.3. The α-Mg grain size varies with cooling rate during casting, where coarser grains are associated with slower cooling rates. Within the grains there is dendritic structure, porosity and eutectic phases. The influence of cooling rate on cell size, grain size, and eutectic structure are discussed in more detail in the following sections. The influence of composition on grain size and eutectic morphology is also presented and the influence of processing on porosity formation is addressed.
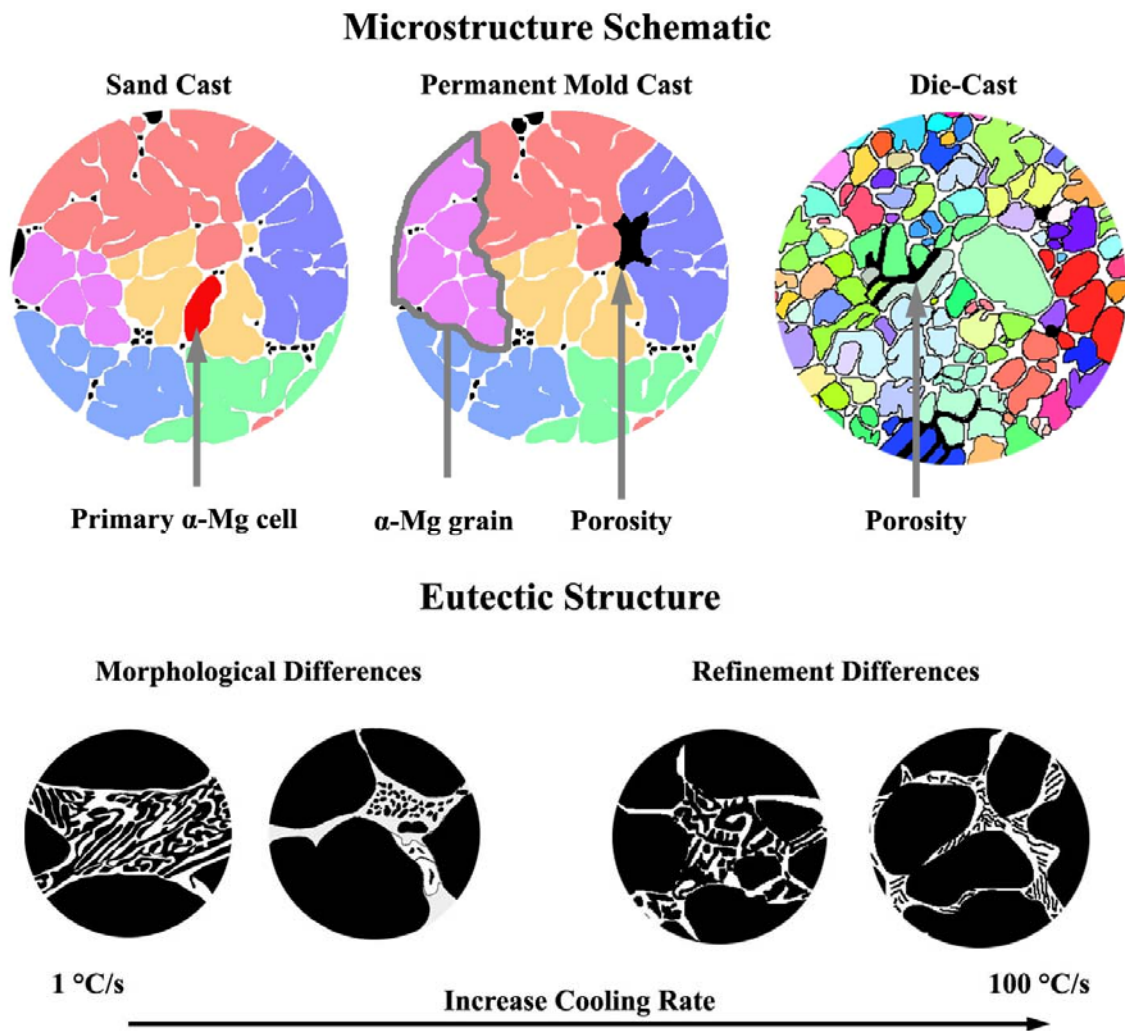
Figure 2.3 Schematic representation of magnesium alloy microstructure and influence of cooling rate, composition, and processing. Note that adjacent cells of the same orientation (indicated by color) are defined as a grain.

Cooling rate during solidification influences the microstructure of cast Mg alloys. Sand casting has a slower cooling rate (~ 1 °C/s) than permanent mold casting (~10 °C/s) or die-casting (~100 °C/s) resulting in a modest increase in the average cell size of the α-Mg and a large increase in grain size. Sand cast and permanent mold cast microstructures have grain sizes on the order of hundreds of micrometers (100-300 μm), while die-cast microstructure have grain sizes on the order of tens of micrometers (10-20 μm). Later it will be shown that die cast microstructures have clusters of cellular alpha magnesium that form larger individual grains (30-60 μm). The cooling rate also has a pronounced influence on the scale of the eutectic phases. In the case of Mg-Al-Ca system, alloys that were solidified at 1 °C/s to 100°C/s exhibited the same intermetallic phase with the C36 crystal structure [50, 51], along with a markedly refined morphology. Compositional changes have little effect on the cellular morphology.

Sand cast microstructures have very low levels of porosity and with proper design of chills, vents, and risers it can essentially be eliminated. Porosity in permanent mold cast alloys is primarily shrinkage porosity and in this study it has been measured at <<1% volume fraction in the gage region. Die cast alloys have significant entrapped gas and shrinkage porosity (5-10% volume fraction) [52]. Entrapped gas limits the ability to heat-treat the alloys because of blister formation at the solution temperatures.

2.1.5   Magnesium Alloy Designation

The naming convention of magnesium alloys is based on an alpha-numeric designation system, Table 2.3. For example the Mg alloy AZ91 has a nominal composition of Mg – 9 Al – 1 Zn (by wt%). A brief description is provided here and a detailed explanation of this standardized system can be reviewed elsewhere [53]. Table 2.4 contains two commercial alloys that are discussed in this study but do not use the standard naming convention.

Table 2.3 Alloy designation alphabetical symbols and corresponding elemental addition(s).

Designation	A	E	H	J	K	M	Q	S	T	W	X	Z
Element	Al	Rare Earths	Th	Sr	Zr	Mn	Ag	Si	Sn	Y	Ca	Zn

Table 2.4 Dead Sea Magnesium creep resistant alloys and compositions (wt%).

Alloy	Mg	Al	Ca	Mn	Sr	Zn	Sn
MRI230D	Bal	6.45	2.25	0.27	0.25	<0.01	0.84
MRI153M	Bal	7.95	0.98	0.20	0.27	<0.01	<0.01

2.1.6 Processing Routes

Magnesium alloys may be cast or wrought. For this thesis only cast processing will be considered. The casting techniques that are currently in use, in order of their respective cooling rates from slowest to fastest include: sand casting (~1 °C/s), squeeze casting (~10 °C/s), permanent mold casting (~10 °C/s), thixocasting (~50 °C/s), and high pressure die-casting (~100 °C/s) [54, 55]. Powertrain components are primarily fabricated via sand-casting and die-casting. The greatest differences in manufacturing between sand casting and die-casting is the associated costs and cast component complexities. Prominent metallurgical differences between sand-casting and die-casting are grain size, segregation, porosity, and intermetallic formation.

Sand casting, although more expensive in terms of large batch (millions of castings) manufacturing costs compared to die-casting, has the advantage of being able to produce more geometrically complex components. Die-casting is constrained by tooling limits (two die halves that must mate and a limited number of accessory die-slides) whereas sand castings can be produced with more complicated inserts and cavities through use of complicated core structures.

Sand-casting allow a quiescent fill and slower solidification rate, while die-castings fill turbulently with a more rapid solidification rate. Die-casting, due to the inherently turbulent mold filling, provides little time for the gas occupying the mold prior to metal injecting to escape during each shot. Inevitably a significant fraction (5-10% volume fraction) becomes entrapped and remains in the component after solidification.

Heat-treating a die-cast component causes blisters (surface ruptures) where entrapped gas expands and damages the component [56]. Thus, one advantage of sand-casting over die-casting is the ability to heat-treat the sand cast components. Through heat treatment, precipitates are formed in the α-Mg grains. These precipitates, in combination with other strengthening mechanisms, provide a creep resistant microstructure. Many of the creep resistant alloys used in aerospace applications are sand cast and then heat treated to develop optimal creep strengths. Die-casting has not been favored for these components since they have only been required in limited volume.

Recently, Suzuki et al. [57], have successfully developed lower temperature short-time aging treatments (200 °C, 1 h) for the automotive die-cast alloy, AXJ530. These heat-treatments provide some additional creep resistance through precipitation. The studies were completed on die-cast tensile specimens and volume fraction porosity was not reported. Final die-cast powertrain components have large (> 5% volume fraction) amounts of porosity. These findings provide a foundation for experimentation with different processing methods (e.g. vacuum die-casting to further reduce porosity [56]) and low temperature short time aging studies on die-cast components.

Varying microstructural refinement between sand casting and die-casting leads to differences in the mechanical behavior. A refined cell size and much finer grain size of the primary alpha magnesium is present for die-casting, due to high cooling rates. Refinement of the intermetallic phases within the eutectic region has also been observed. This decrease in grain size, following the Hall-Petch relationship [58, 59] Equation 2.1, would be expected to increase the yield strength of the material. Depending on the operative creep mechanism, a decrease in grain size would also be expected to decrease the creep resistance of an alloy. This is discussed further in the following section on creep mechanisms, section 2.1.7

$$\sigma_y = \sigma_0 + kd^{\frac{1}{2}} \qquad\qquad \text{Equation 2.1}$$

Understanding the interrelationship between processing routes, chemistry, microstructure, and mechanical behavior is important for optimizing properties of magnesium alloys. This investigation will utilize permanent mold cast samples to study the influence of composition on microstructure and creep behavior. Permanent mold

casting was selected for its attractive costs, intermediate cooling rate and availability when compared to sand-casting and die-casting.

2.1.7 Creep mechanisms

The phenomenon of creep in metallic systems has been extensively studied over the years and detailed descriptions of the fundamental phenomena are reviewed elsewhere [60-66]. In general, creep strain is accumulated through either dislocation motion (i.e. glide, glide-climb) or diffusional flow [60]. While a unified model accounting for the creep behavior and operative mechanisms across all stress, temperatures, and alloys has yet to be defined, classes of models exist that broadly describe the creep behavior of crystalline materials. These mechanisms and models, briefly discussed below, lie in two main categories: diffusional creep and power-law creep.

When creep strain accumulates via diffusional it is either referred to as Nabarro-Herring creep (diffusional flow through grains) or Coble creep (diffusional flow along grain boundaries). Other mechanisms of creep deformation are Harper-Dorn creep (mechanisms remain under debate [67]), power-law creep (dislocation and diffusion), and power-law breakdown (which involves dislocation climb under higher vacancy concentration than thermal equilibrium, associated with larger stress exponents (> 7 in pure metals) [68]). Grain boundary sliding (GBS) is an accommodating mechanism in creep, operating with diffusion creep [64] or intragranular slip [69], and up to 80% (or more) of the accumulated strain has been attributed to this mechanism [69]. Two sub-categories of GBS termed Rachinger or Liftshitz have been identified, both resulting in grain boundary offsets. In Rachinger GBS, strain accumulation is rate controlled through a displacement of adjacent grains that maintain their original shape but exhibit relative displacements, typical of superplastic behavior. Rachinger GBS is identified by an overall increase in the number of grains within gauge, along the stress axis. Liftshitz GBS occurs as an accommodating process for stress-directed vacancy diffusion (i.e. Nabarro-Herring/Coble Creep), and is marked by grain elongation along the tensile axis [69].

Ashby [70] developed plots that predict the deformation mechanism from predictive models for deformation and material properties. From these plots deformation mechanisms are inferred for a given system, grain size, loading, and homologous temperature. Frost and Ashby [60] published a compilation of these deformation maps and the magnesium map is shown in Figure 2.4 Though these creep mechanisms have been widely accepted in the field, debate continues over the validity of certain mechanisms [71-74] and existing models [68]. These debates are founded in the inability of models to accurately predict creep behavior across many different materials and microstructures.
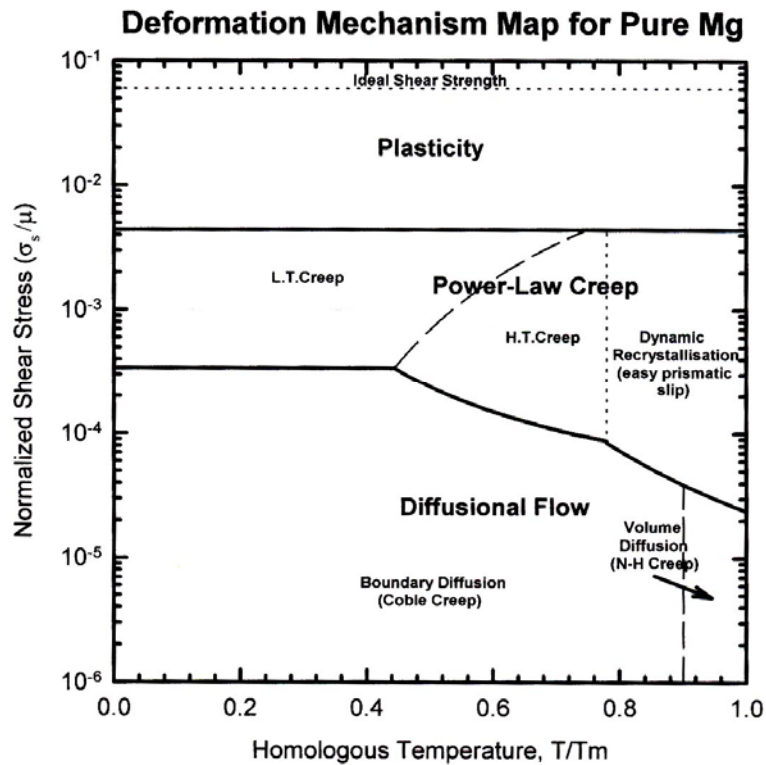
Figure 2.4 Mg deformation mechanism map [60].

Diffusion creep is generally represented with use of the Nabarro-Herring [75, 76], Equation 2.2 or Coble [77], Equation 2.3 models, where D_{xx} is the diffusion coefficient (sd – self diffusion, gb – grain boundary diffusion), σ is the applied stress, b is the Burgers vector, k is Boltzmann's constant, T is temperature, d is grain size, and α is a material constant. Another diffusional based creep model that accounts for deformation

16

through grain boundary sliding accommodation is that developed by Raj and Asby [78], Equation 2.4, where τ_a is the applied shear stress, Ω is the atomic volume, and d is the grain size.

In the diffusional models, grain size (d) has a significant influence on creep rate. Depending on the operative creep mechanisms (e.g. dislocation climb, diffusion, grain boundary sliding), the grain size may play a substantial role in the creep behavior of a material. Sand cast alloys, having a larger grain size than die-cast alloys, should thus theoretically exhibit an improved creep behavior [79, 80] for diffusion-driven creep mechanisms, while trading off room temperature yield strength, as predicted by the Hall-Petch equation. Therefore, a compromise on grain size would be necessary to powertrain components to assume sufficient room temperature mechanical strength and adequate creep resistance if diffusional creep mechanisms are expected to contribute significantly to the overall creep deformation.

$$\dot{\varepsilon} = \frac{D_{sd}\sigma b^3}{kTd^2} \qquad\qquad \text{Equation 2.2}$$

$$\dot{\varepsilon} = \frac{\alpha_3 D_{gb}\sigma b^4}{kTd^3} \qquad\qquad \text{Equation 2.3}$$

$$\dot{\varepsilon} = 42\frac{\tau_a\Omega}{kT}\frac{1}{d^2}D_{eff} \qquad\qquad \text{Equation 2.4}$$

Numerous models for power-law creep have been proposed with the predominate theme that of a combination of diffusion and dislocation motion through either solute drag or dislocation glide-climb controls creep. In its most general form power-law creep is represented with Equation 2.5 where C is a constant, σ – applied stress and n – the stress exponent.

$$\dot{\varepsilon} = C\sigma^n \qquad\qquad \text{Equation 2.5}$$

The power-law models have numerous forms based on material, temperature, stress, and presumed mechanisms [63, 64, 68, 69, 81] and, in general terms, may be modeled by the Arrhenius equation of the form of Equation 2.6. Here A is a material constant, σ is the applied stress, n is the stress exponent, Q_c is the creep activation energy, R is the ideal gas constant, and T is the absolute temperature. More complex power-law models account for the macroscopic variables of stress and temperature and incorporate microstructural variables and physical properties (i.e. lattice parameter, atomic volume, bond energies, moduli, diffusion) [60].

$$\dot{\varepsilon} = A\sigma^n \exp\left(-\frac{Q_c}{RT}\right)$$
Equation 2.6

The stress exponent, n, and creep activation energy, Q_c, are often used to assess the dominant creep mechanism. In the case of pure metals and Class M alloys (solid solution alloys behaving similar to pure metals) [82], n is between 4-7 and has been traditionally referred to as dislocation climb controlled creep or 5-power-law creep [64]. In power-law creep of multiphase materials n has a much larger range and has been reported to be as high as 30-40 for precipitation strengthened alloys [63]. Solid solution alloys, designated as class I [63] or class A alloys, have a stress exponents near 3 [83]. Stress exponents of ~1-2 have been attributed to diffusional creep and GBS [69].

The creep activation energy, Q_c, is nearly the same as the activation energy for self diffusion, Q_{sd}, in pure metals above a critical temperature (generally > 0.5 T_m), indicates that diffusion-controlled creep is dominant [63]. In multiphase materials this is not the case and Q_c is often much higher than Q_d [63]. Investigations of activation energies and stress exponents in magnesium alloys have also reported Q_c higher than Q_d [38, 69, 84-86].

2.2 Microstructure and Creep

2.2.1 Pure Magnesium

Shi and Northwood [87] examined the creep behavior of pure polycrystalline magnesium. Tests were conducted under constant load for stresses between 20 and 50 MPa and for temperature between 150 and 200 °C. From power law creep, a stress exponent was calculated to be n=5.86 and a creep activation energy of Q_c=106 kJ/mol. These values were in the range generally reported of creep controlled by dislocation climb. The authors report that the data collected supports dislocation network models for recovery creep in single phase materials and class II alloys (solid solution alloys)[63].

Milička [88] investigated the primary and steady-state creep behavior of fine grained (grain size not reported) magnesium at stresses of 9.8-19.6 MPa and temperatures between 197 – 497 °C. Stress exponents were not reported but creep activation energies (Q_c) dependent on applied stresses were reported. Values ranged between 167.5 – 220 kJ/mol for the loads between 19.6 to 9.8 MPa, respectively. These values are greater than that reported for self diffusion of magnesium 125 kJ/mol [63]. This investigation concluded that the elongation in the primary stages of creep in polycrystalline magnesium above $0.5T_m$ is described by a power-law behavior.

A companion study by Milička et al. [89] investigated the high temperature (127 – 527 °C) creep mechanisms in polycrystalline Mg for stresses between 10 – 100 MPa. The investigation reported two distinct regions (dependent on applied load) of creep behavior that was separated by a narrow transition (of ~9 MPa) between the two. In the high stress region ($\sigma \approx 40$ to 100 MPa), the creep activation energy (Q_c) was found to be close to that for lattice self diffusion, 134 kJ/mol. In the lower stress region, Q_c was reported to decrease (216.9 kJ/mol to 153.7 kJ/mol) with increasing stress (10 to 40 MPa), respectively. The stress exponent for the high stress region varied from 7.5 to 10 and was constant (across the stresses investigated) for a given temperature. In the low stress region ($\sigma \approx 10 - 31$ MPa), stress exponents varied between 7.5 – 20 and was dependent on both load and temperature. The authors concluded, though no TEM investigation were completed, that the rate controlling process in the low stress region was 'nonbasal slip of screw dislocations in pyramidal slip systems limited by a nucleation

of kink motion'. The rate controlling mechanism in the high stress region was 'the velocity of dislocation being controlled by nonconservative motion of jogs on screw segments'

2.2.2 Mg-Al Alloys

Magnesium-aluminum alloys form the base for many of the commercial alloy systems (AM50, AM60, AZ31, and AZ91). Figure 2.5 shows the Mg-Al binary diagram [32]. Aluminum is one of the most soluble elements in magnesium at a maximum of 12.7 atomic % at 437 °C. At appropriate levels of binary addition, Al provides a good balance of strength, ductility, castability, and corrosion resistance [90]. Alloying magnesium with aluminum is also relatively affordable. The Mg-Al system has poor elevated temperature properties which have been attributed to the eutectic morphology [5, 6] and formation of the β-$Mg_{17}Al_{12}$ phase [2, 4, 7, 8].

Manganese (in minor additions of about 0.25 wt%) is a common ternary addition to the Mg-Al alloys and improves the corrosion resistance by tying up elemental impurities of Fe, Ni, and Cu that are detrimental to corrosion properties through the formation of intermetallic phases (e.g. Al_3,(Fe,Mn)) [53]. No effect on bulk mechanical properties from the manganese additions are reported [53].
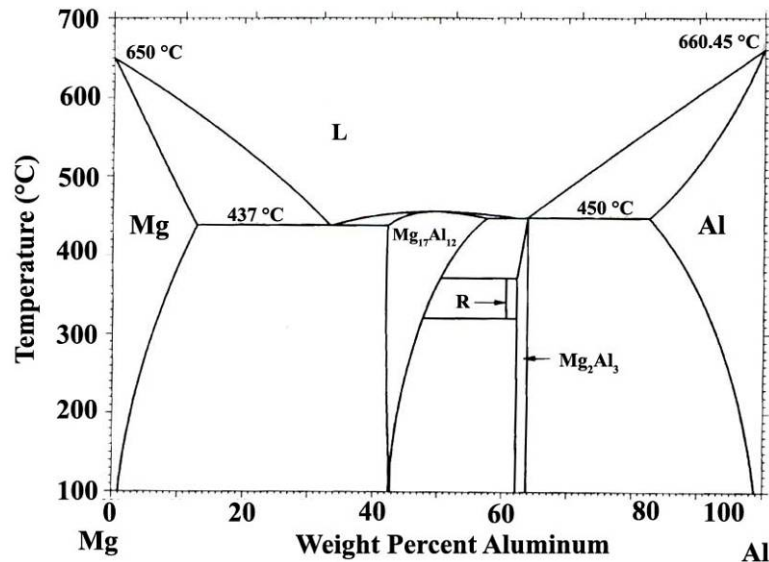
Figure 2.5 The magnesium-aluminum binary phase diagram [45].

The casting [90, 91], solidification behavior [5, 92-94] and mechanical properties [21, 95-100] of Mg-Al alloys have been studied by numerous researchers. The addition of aluminum for die-casting has been reported to increase fluidity, surface finish, and to decrease the tendency for die soldering [90, 91]. Binary aluminum additions also increase the yield strength, but contribute to a decrease in ductility as Al content increases (specifically over 9 wt% [90, 101]). This has been attributed to the formation of the brittle intermetallic phase $Mg_{17}Al_{12}$. Micrographs of AM60 and AM50 are shown in Figure 2.6.
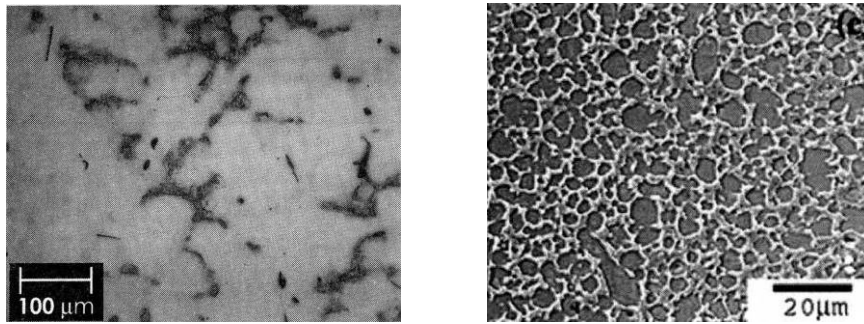
Figure 2.6 Magnesium-Aluminum alloys of AM60 and AM50, respectively. The AM60 on the left is an optical micrograph of a permanent-mold-cast alloy [48]. The AM50 on the right is a BSE-SEM image of a high-pressure-die-cast alloy [53].

The creep behavior of Mg-Al alloys has been investigated to understand the phenomenological behavior of commercial alloys [95, 102, 103] and to develop an understanding of the microstructural influence and creep mechanisms [99, 104-106]. Mg-Al alloys have relatively poor creep resistance compared to the other commercial magnesium alloys. Regardless, AM50 and AM60 have sufficient creep resistance at stresses below 50 MPa and temperatures below 150 °C [3]. Researchers [2, 7] attribute the reduction in creep properties at higher temperatures to softening of the $Mg_{17}Al_{12}$ phase, though Dargusch [86] has pointed out that the research of Fukuchi and Watanabe [107] demonstrates that near stoichiometric $Mg_{17}Al_{12}$ remains brittle above 200 °C and does not exhibit appreciable plasticity or a decrease in yield stress for temperatures in excess of 260 °C. Dargusch [86] also indicates that the elevated temperature properties are poor, not due to softening of the intermetallic phases, but rather some other undetermined mechanisms [104, 106]. In a related investigation [104] it was experimentally determined that by increasing the aluminum content in magnesium,

(simultaneously increasing the volume fraction of the β-$Mg_{17}Al_{12}$ phase) the creep resistance increased (marked by a decrease in creep rate and creep strain), indicating that it is not a softening of the eutectic that governs the creep behavior as has been suggested [2, 4, 7, 8], but other materials properties. The authors discuss that aluminum in solution is a likely creep strengthening mechanism, along with continuous precipitation of the β phase which are assumed to act as effective obstacles to dislocations. It is noted by Dargusch et al. [104] that these obstacles have thin plate morphology, parallel to the basal plane and therefore do not present significant cross sections to dislocations that would be mobile on that plane. It is also of note that Dargusch, et al. observed displacement of surface line markers in AZ91 after creep at 150 °C for low stresses (20 - 40 MPa) and strains up to 20% [99] and they attribute this to grain boundary sliding.

The degree of solute strengthening at various temperatures has been the focus of many investigations in magnesium [21, 36, 47, 108]. These investigators aimed at understanding the influence of alloy additions and concentration on the lattice parameters of Mg. The changes in lattice parameters were then used to account for strengthening (or softening) mechanisms. An addition of a solute atom expands (or contracts) the unit cell unevenly resulting in a change in the c/a ratio. This c/a ratio will have influence on the τ_{crss} of each slip system. The ultimate goal was to tailor solute concentrations to control the c/a ratio and influence the τ_{crss} on various slip systems in the HCP Mg lattice.

Examining the τ_{crss} and c/a ratio of other HCP metals provides additional insight. For HCP metals there is an order of magnitude difference in the τ_{crss} for the same slip systems. In the case of Mg, Cd, and Zn, the τ_{crss} (at room temperature) on the $\{0001\}$ (basal) is 0.43 MPa [41], 0.57 MPa [109] and 0.18 MPa [110], respectively. Yet for Ti and Be the τ_{crss} on the $\{0001\}$ is approximately 110 MPa and 39 MPa, respectively. This difference is used to explain why other slip systems (i.e. prismatic slip on $\{10\bar{1}0\}$ planes in the $<11\bar{2}0>$ directions) are favored in different HCP metals. A complete understanding for this difference has yet to be reported but it has been noted [25] that there are variations between the lattice parameters and thus the c/a ratios of these metals, Table 2.5. Mg, Cd, and Zn all have near or larger than ideal basal plane separation (using a hard packed sphere model) (and they all have lower τ_{crss} on the basal plane). Ti, Zr, and

Be, have smaller basal plane separation (and higher τ_{crss} on the basal plane) supporting slip dominant on other crystallographic planes and directions other than basal.

Table 2.5 Reported c/a ratios of hcp metals [25].

Metal	Ideal	Cd	Zn	Mg	Zr	Ti	Be
c/a	1.633	1.886	1.856	1.624	1.590	1.588	1.586

Returning to the discussion on Mg solute strengthening, Agnew et al. [47] have attempted to significantly influence the lattice parameters of α-Mg by alloying with various elements, the goal being to activate different slip systems to increase the deformability for sheet metal forming. The effect of dilute solute (Al, Li, Cd, Zn, Pb, In) on single crystal magnesium alloys has been investigated [37, 45, 108] and it is agreed that the solute increases the τ_{crss} on the basal plane by a factor of $(c-c_o)^n$, (c is the concentration of solute atoms, c_o is the minimum concentration for solute strengthening (≈0.1 at. %) and n is 1/2~2/3). Others [21] have studied the effect of concentrated Mg-Al alloys taking into consideration many of the commercial complexities not considered in the single crystal studies. For example, in commercial alloys with concentrations of 6-10 wt% Al, there is a trade off of basal strengthening and prismatic softening, and increases in Al act as a grain refiner in Mg alloys (Hall-Petch effect) paralleling increases in solid solution strengthening. Equation 2.7 has been proposed to account for the material strength, the Hall-Petch flow strength and the solid solution strengthening (where σ_o = 11 MPa, $k = 0.3$ MPa m$^{-1/2}$, $B_n = 21.2$ MPa (at.)$^{-1/2}$ or 39.5 MPa (at.)$^{-2/3}$, and m = 5.6 or 5 when n = 1/2 or 2/3, respectively). The results closely follow those reported for the single crystal dilute alloys that had been oriented for basal slip. It was concluded that solute strengthening on the basal plane is the dominant effect for solid solution strengthening in these polycrystalline alloys.

$$\sigma_p = \sigma_o + kd^{-1/2} + mB_n c^n \qquad\qquad \text{Equation 2.7}$$

2.2.3   Mg-Al-Zn Alloys

The Mg-Al-Zn alloy system, with the most common alloy AZ91D, is most often used in room temperature applications as seat frames and instrument panels (although it is rapidly being replaced by AM60 due to inferior energy absorbing capability). It is not generally utilized as a creep resistant alloy. The creep rupture life is less than 250 h for stresses greater than 60 MPa and/or temperatures above 150 °C [111], and is thus not considered for use in automotive powertrain applications.   An understanding of the microstructure and creep behavior provides insight into the creep strengthening mechanisms for magnesium alloys.

The microstructure of this alloy has been analyzed for die-cast and permanent mold cast conditions (samples from the center of ingots). In the permanent mold cast condition Regev et al. [112], observed a magnesium solid solution matrix containing approximately 5 wt% Al in solution (from EDS). A second phase, decorating the grain boundaries was reported as β-$Mg_{17}Al_{12}$. The reported size of the α-Mg grains was about 300 μm. The die-cast alloys exhibit the same general microstructure as the permanent mold cast ingots, except for two major differences. The grain size of the die-cast alloy was approximately 15 μm and the volume fraction of the β-phase was higher [111]. Reports on the amount of solute in solution were not provided.

In the die-cast condition, AZ91 was reported to have a minimum creep rate an order of magnitude higher than in the coarse grain ingot [111]. This is opposite to trends reported in the Mg-Al-Ca alloy system for coarse versus fine grained microstructures [84, 113]. No explanation for the difference in the minimum creep rates of die-cast versus ingot cast AZ91 was provided [111].   The stress exponent for the course grained magnesium is reported as n=11 and independent of temperature (tests were conducted between 120-180 °C) and stress (between 40-115 MPa). The stress exponent measured for the die-cast AZ91 was reported as n=6.9 at 150 °C and n=5.4 at 180 °C, for stress between 30-100 MPa. In die-cast AZ91 dislocations were observed on planes other than the basal plane. Regev et al. [111], attribute this as a likely source of the significant elongation observed in these alloys. In the case of coarse grained AZ91 it has been proposed that creep deformation is governed by dislocation motion on the basal plane, cross slip on non-basal planes, and intergranular cavitation [112].   Along with this

difference in creep, elongation between 9 and 15 %, for the coarse grained AZ91 [112], and between 7 and 15 % for the fine grained die-cast AZ91 was reported [111]. These elongations are more than that reported in the creep of pure magnesium (~ 3% [87]) and may be attributed to slip on many systems allowing for the increase in ductility [111].

More recent investigations have focused towards precipitation hardening of AZ91 [114, 115]. Peak hardness was achieved through precipitation of β – $Mg_{17}Al_{12}$ asymmetric-lozenge-shaped plates lying parallel to the basal plane [114]. It is noted that the aging response is not as large as in many aluminum alloys because the precipitates are not efficient obstacles for dislocations and the values of N_v (number of precipitates per unit volume) are (at least) an order of magnitude less than in high-strength precipitate strengthened aluminum alloys.

2.2.4   Mg-Al-Ca Alloys

Mg-Al-Ca alloys currently demonstrate the most promise for a combination of improved creep resistance, die-castability, and reasonable cost for automotive powertrain applications. Alloys based on the Mg-Al-Ca system have seen service in various powertrain components including oil pans, valve covers, and front engine covers [17]. This class of alloy continues to show promise as research on processing and creep strengthening mechanisms continues.

Investigations on calcium containing magnesium alloys [116, 117] reported that calcium additions greatly improved the creep resistance of magnesium alloys with Ca additions. Poor die casting characteristics (e.g. hot tearing/cracking, die sticking) were reported, especially for Ca additions over 0.5 wt%. The poor die-castability limited commercialization of these alloys. Later research [8, 84, 117-122] on the Mg-Al-Ca system demonstrated improved creep resistance, with much of the research focused on alloying to improve the castability. Lou and Shinoda [117] found that elevated levels of zinc (~8%) restored die-castability in Mg- 8Zn - 5Al - (0.2-1.2)Ca, while maintaining some improvement to the creep resistance. There is no report of the mechanisms for this improved castability [123]. Sohn et al. [8, 124, 125], reported incremental improvements in creep of AM50 through Ca additions between 0.25 and 0.88 wt%, especially at the elevated temperatures (150-200 °C), while still retaining the ability to die-cast the alloys.

The study of Horie et al. [121], was in strong agreement with the previous creep strengthening results of Sohn et al. [8, 124, 125]. Lou and Shinoda [95], and Pekguleryuz, M. and J. Renaud [8, 117, 122] on the role of Ca additions.

Powell, Lou, and co-workers [84, 118-120] die-cast a series of alloys containing elevated levels of Ca (1.8-3.1 wt%) with a nominal Al content of 5 wt%. Surprisingly at these high Ca levels these alloys were not subject to the previously reported hot cracking/die soldering and retained the improved creep properties from the Ca additions. The studies identified an optimum composition of Mg - 5 Al - 3 Ca - 0.15 Sr for castability and creep resistance (AXJ530). Terada et al. [126], successfully cast a Mg-5 Al-1.72 Ca alloy with results similar to those of Powell, Lou, and co-workers [84, 118-120].

The investigations on Mg-Al-Ca discussed above all observed a microstructure containing a primary α-magnesium solid solution phase surrounded by intermetallic compounds at the interdendritic regions. Figure 2.7 shows a die-cast and permanent-mold-cast microstructure of Mg-Al-Ca alloy (AXJ530). Initial studies on Mg-Al-Ca alloys [116, 117] did not describe the formation of the intermetallic compounds, but did determine that alloying with Ca fully suppressed the formation of the intermetallic β phase, $Mg_{17}Al_{12}$. Pekguleryuz and Renaud [122], Sohn et al [8]., and Lou et al. [84], all reported an Al_2Ca (or $(Mg,Al)_2Ca$ compound, with increasingly (with respect to the listed order of publications) sophisticated levels of experimentation (standard-less EDS, X-Ray diffraction, and TEM diffraction, respectively) to develop this conclusion. It was proposed that this higher temperature phase Al_2Ca fully suppressed the formation of the low temperature $Mg_{17}Al_{12}$ phase resulting in "metallurgical stability of the grain boundaries at elevated temperature" [122] as being the key component to alloy strengthening at 150 °C. Sohn et al [8], noted that the volume fraction of the Al_2Ca phase increased with increasing concentration of Ca. They also attributed the improved creep resistance to the increase in Al_2Ca. Lou et al. [84], reported the compound as hexagonal $(Mg,Al)_2Ca$ with an improved thermal stability compared to $Mg_{17}Al_{12}$ and a coherent interface with the α-Mg matrix. They argued that the calcium containing phase was effective at pinning the grain boundaries, therefore improving the overall creep resistance.
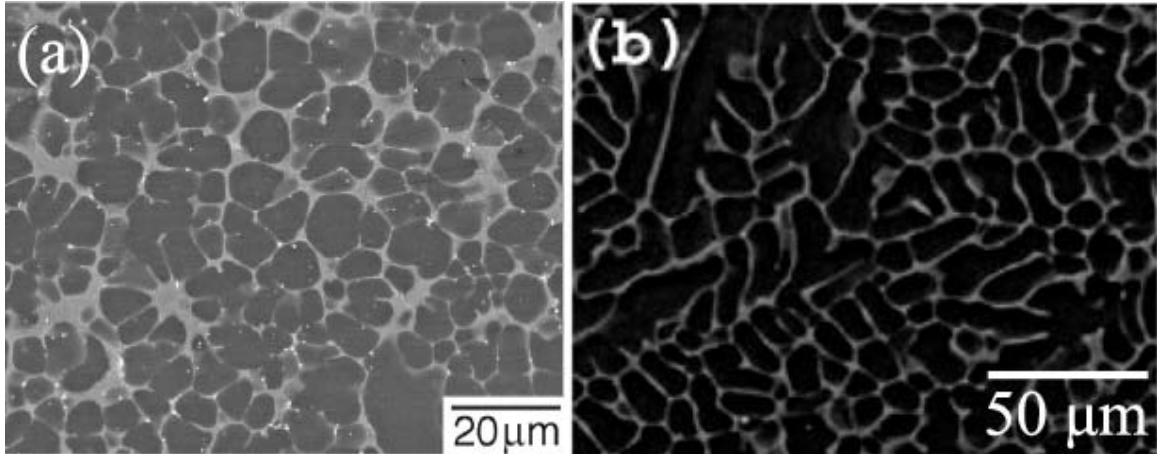
Figure 2.7 Microstructures of Mg-Al-Ca alloy (AXJ530) (A) BSE-SEM Die-cast [20] and (B) BSE-SEM Permanent-mold-cast [83]. Note, the difference in coarseness between the two processing conditions. Both exhibit an α-Mg primary phase, surrounded by eutectic, C36 an α-Mg primary phase, surrounded by eutectic, C36 and Mg.

More recently, investigations by Suzuki, et al. [50, 51, 127] have been conducted on the Mg-Al-Ca system, including electron diffraction analysis for phase identification [50], phase stability [127], and determination of solidification paths [51]. It was found that, contrary to the published literature, the major eutectic phase formed was a dihexagonal C36 $(Mg,Al)_2Ca$ phase that was stoichiometrically close to $Mg_2Al_4Ca_3$. The C36 phase was found to be thermally stable at 773 K (500 °C), but decomposed to C14 (Mg_2Ca) and C15 (Al_2Ca) at 673 K (400 °C) and below. At the operative temperature of powertrain components, the decomposition of C36 is reported as sluggish. Spherodization of C36 and C15 occurred at higher temperatures (200 °C) with sufficiently long aging times (1000+ hrs) [127].

The solidification path and liquidus projection for the Mg-rich corner of the ternary Mg-Al-Ca system was experimentally determined [51], Figure 2.8. The phases that may form are C14, C36, and A12 ($\beta - Mg_{17}Al_{12}$) with a saddle point at Mg-14.5Al-7.5Ca at a temperature of 807 K (534 °C). The solidification path of most Mg-Al-Ca commercial alloys intersect the eutectic valley near this saddle point. The saddle point is of importance, since small variations in Al and/or Ca may push the alloy onto a solidification path towards the A12 phase ($\beta - Mg_{17}Al_{12}$), which is thought to be detrimental to the creep resistance of these alloys.
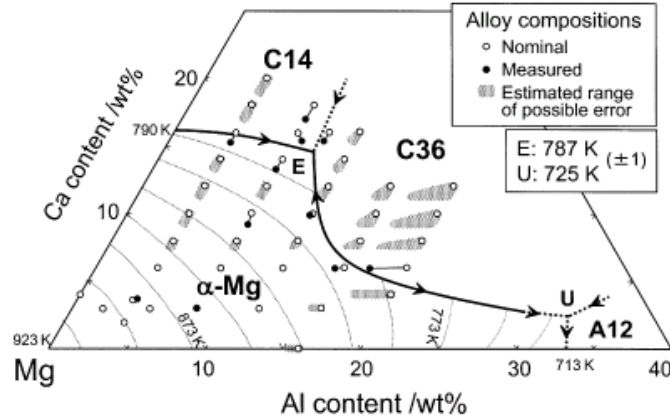
Figure 2.8 Liquidus projection of the Mg rich corner for the Mg-Al-Ca system [86].

The creep characteristics of calcium-containing magnesium alloys have been extensively studied [57, 84, 85, 113, 118, 120, 121, 125, 126, 128-138]. Many of these investigations inferred operative creep mechanisms by calculating the stress exponent from experimental results (assuming the validity of a power law creep expression). Some of these studies considered both the creep constitutive response along with microstructural observations [57, 132, 136], but detailed reports of operative creep mechanisms have yet to be completed.

Terada et al. [126] studied die-cast Mg - 5% Al – 0.29% Mn – 1.72% Ca alloy and its creep properties. The stress exponent in the temperature range of 150 – 225 °C was reported to be n = 10. The calculated activation energy for creep in this alloy at these temperatures was Q_c = 142 kJ/mol, which is close to the activation energy for self diffusion in magnesium. Using classic power law creep models, they concluded that these values indicate that the dominant creep mechanism was controlled by dislocation climb in the α-Mg grains [126]. A significant improvement (3x) in creep properties of AM530 was reported for these calcium additions. The creep mechanism affected by addition of calcium was not reported.

Lou, Powell, and co-workers [84, 118, 120] studied the effects of calcium and micro-alloying additions of strontium (<0.20 wt%) on die-cast magnesium-aluminum alloys. In these study it was inferred from the stress exponent (n=1.5) at 175 °C and low stresses (<70 MPa) that grain boundary sliding dominated the creep deformation. At high stresses (>70 MPa, n=8.5) creep was driven by dislocation controlled climb and glide. This study also discussed the significance of the formation of the intermetallic

28

(Mg,Al)$_2$Ca and proposed this compound as having a positive effect on the creep resistance of these alloys. The study found that within the matrix of Mg-Ca-Al-Sr alloys studied, the alloy with a chemistry of 5 wt% aluminum, 3 wt% calcium, 0.15 wt% strontium, had the highest resistance to creep. The role of the Sr addition on the creep behavior is not well understood.

Horie, et al. [121], studied the creep behavior of die cast and permanent mold cast Mg - 2Zn - 0.8Ca − 2 RE (rare earth mischmetal) − 0.5Zr, between 120 − 180 °C at stresses between 40 - 100 MPa. The die-casting samples were reported to have decreased thermal stability, yet still maintained a 10-fold improvement over the permanent mold cast samples in creep resistance. A stress exponent for the die-cast alloys was calculated at greater than seven. Fine precipitates within the α-Mg grains were reported and it was concluded they play a very important role in improving the tensile properties and creep deformation of Mg-Zn-Ca-RE-Zr alloys.

Sohn et al. [8, 124, 125], studied the bolt load retention (compressive creep), of die-cast AM50 with Ca additions between 0.25 and 0.88 wt%. They reported a stress exponent of 6-9 for stresses ranging from 40 to 70 MPa at 150 °C and concluded that for the alloying range studied, calcium had no significant effect on the stress exponent. The improvement in creep behavior through the Ca additions was attributed to the microstructural change at the grain boundaries.

Suzuki, et al. [57], studied the effect of precipitation strengthening on die-cast AXJ530 and found an improvement in the creep rate on the order of 2-5x of that observed in an as-cast sample (without precipitates). Figure 2.9 shows the density, spacing, and morphology of the precipitates as a function of time for 300 °C heat treatments. The improvement in creep behavior at 175 °C for 80 and 100 MPa for AXJ530 processed to the optimum hardness condition is shown in Figure 2.10. The C15 - Al$_2$Ca precipitates are disc-shaped, contained within the α-Mg grains, and are oriented parallel to the basal plane. Improvements in the volume fraction of precipitates and optimization of alloying and heat treatment could possibly further improve creep strengthening.
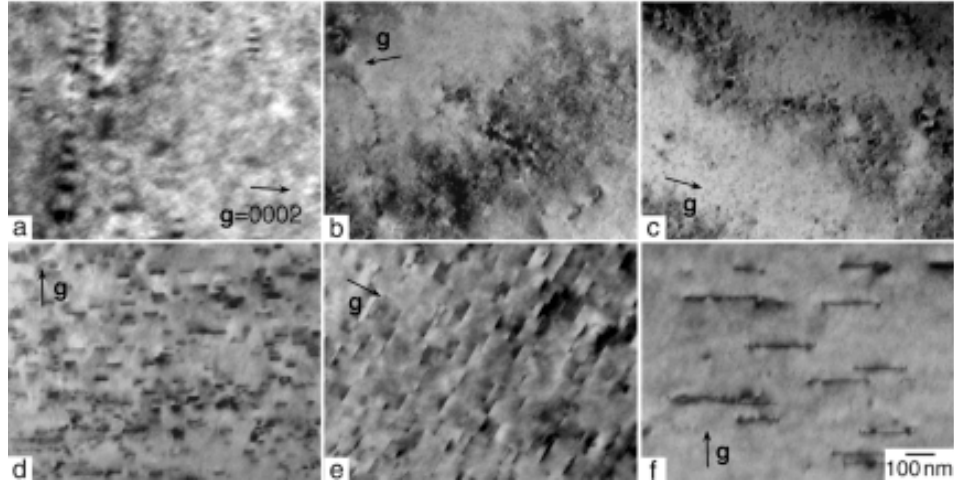
Figure 2.9 TEM BFI for precipitation of Al2Ca (dark contrast phase) within α-Mg grains for die-cast AXJ530 as a function of time (a) 0 s (b) 30 s (c) 100 s (d) 600 s (e) 3.6 ks (f) 36 ks[20] Note optimal hardness is achieved at 3.6 ks (1 hr).
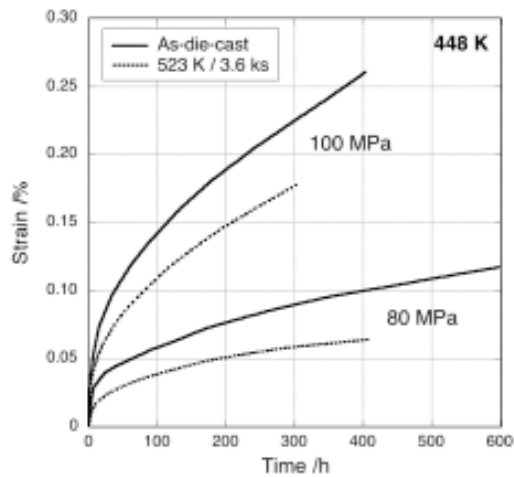
Figure 2.10 Creep behavior of die-cast AXJ530 at 175 °C at 80 and 100 MPa in as-die-cast and optimum precipitate conditions [20].

In a companion study by Suzuki et al. [139], the effect of strontium additions on the microstructure and strength of Mg-5Al-3Ca was studied by substituting the Ca for Sr at the levels of 0.25, 0.5, 0.75, 1, 2, and 3 wt%. With as little as 0.25 wt% Sr, the $Mg_{17}Sr_2$ intermetallic was observed in the interdendritic regions of the microstructure, which had not been reported in AXJ530 (0.15 Sr wt%). This indicates, as would be predicted by the binary phase diagram, that limited strontium is soluble in α-Mg but remains available in the liquid, during solidification, to form intermetallic phases. The strontium additions did have an influence on the α-Mg, contributing to an increase in the

lattice parameters (c and a) with up to ~0.5 wt% additions, and then a decrease in lattice parameters for Sr additions between 0.5 and 1.5 wt%. Larger additions had little to no further influence on the lattice parameters. This gradual decrease in lattice parameters was marked by an increase in both hardness and elastic modulus in the range of 0 - 1.5 wt % Sr and the hardness/elastic modulus remained constant for Sr additions from 1 wt% up to about 3 wt % (Mg-5Al-3Sr).

Suzuki et al. [139] also demonstrated how strontium affects the microstructure and strength through partitioning of the ternary elements (Sr/Al) during solidification. For solidification of Mg - 5 Al - 3 Ca alloy, a tie line can be constructed between the α-Mg and liquid phase (Figure 2.8), where the intersection of this line with the Mg-Al boundary corresponds to the maximum Al content in α-Mg. The same construction can be completed considering the Mg - 5 Al - 3 Sr alloy (Figure 2.12) where the maximum Al content in the α-Mg is increased. Therefore the partitioning influence of alloying additions affects the solidification path. Strontium additions greater than 1% improved the solid-solution strengthening of the α-Mg phase by increasing the Al in the α-Mg. This suggests that tailoring alloy compositions and processing (solidification path) could lead to improvements in hardness and creep behavior.

2.2.5   Mg-Al-Sr Alloys

The Mg-Al-Sr ternary system is currently the only magnesium system used in the commercial production of engine blocks. A microstructure of the Mg-Al-Sr alloy, AJ62x is shown in Figure 2.11. The BMW Company produces a composite aluminum-magnesium crankcase (engine block) with a Mg - 6Al - 2Sr (wt%) alloy [15], AJ62x. The AJ62x is die-cast around a pre-cast aluminum insert (the insert makes up the engine cylinders, all coolant passages, and the crank seats of the block) where the Mg alloy comprises the surrounding structural block. In development of this program the target alloy was Mg - 5Al - 2Sr, AJ52x, but it was found that the addition of one percent aluminum offered improvements in die-castability while maintaining sufficient elevated temperature properties. It has also been reported that strontium additions may contribute to a decrease in surface tension of the alloy. Which was believed to increase intergranular capillary feeding during solidification [140]. The same report outlined

improvements in grain refinement in sand cast AZ91 through minor additions (0.02%) of Sr.
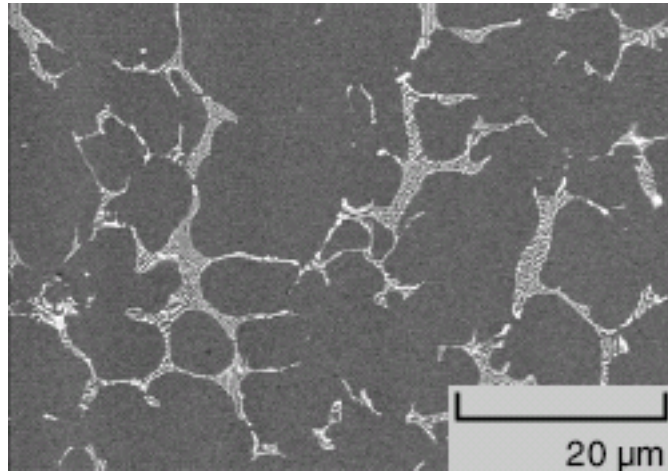
Figure 2.11 SEM micrograph of die-cast AJ62x [108]. The dark contrast phase is α-Mg solid solution. The eutectic contains Mg and the major phase $Mg_{17}Sr_2$. The bright contrast, low volume fraction phase is Al_4Sr.

Research on Sr-containing alloys has focused on solidification paths [141-143], castability [140, 144, 145], and elevated temperature properties [146, 147]. Shown in Figure 2.12 is a calculated/experiment ternary liquidus projection for the Mg-Al-Sr system. Based on alloy compositions of the commercial Mg-Al-Sr alloys, the solidification path will follow through the α-Mg phase field to the eutectic valley for $Mg_{17}Sr_2$ + Mg and then follow this valley to the valley between the Al_4Sr and Mg. Both of these phases have Al solubility and have previously been incorrectly identified as Al_6MgSr_{10} [142] and $Al_3Mg_{13}Sr$ [147]. This path is in excellent agreement with microstructural observations, Figure 2.11.
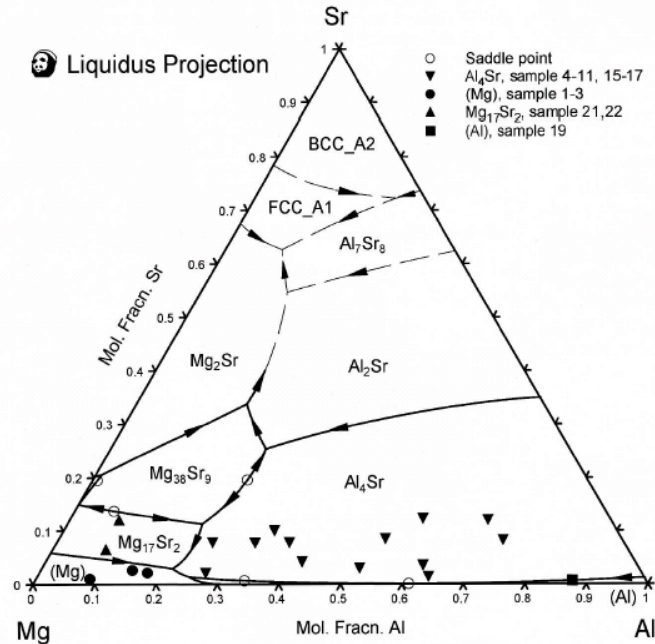
Figure 2.12 Calculated liquidus projection of the Mg-rich corner of the Mg-Al-Sr system with plotted experimental compositions [104].

Although a detailed understanding of the mechanisms for improved creep resistance is lacking, it is reported to be due to a combination of solute strengthening of the primary phase and the intermetallic melt temperature and morphology. The creep resistance of the AJ62x alloy system is reported to be comparable (or even improved) over the rare earth system, AE42 alloy [144, 147].

2.2.6 Mg-Al-RE Alloys

Rare earth (RE) containing magnesium alloys were the earliest developed creep resistant alloys [9]. By the mid-1900's, these magnesium alloys were receiving significant attention [116, 148-150]. Rare-earth alloys are of interest to the automotive industry [12-14], but their high cost and susceptibility to hot tearing during die-casting, has increased interest in lower cost alloying additions (i.e. Ca, Sr, Si).

The rare earth containing alloys use mischmetal as an alloy constituent rather than a 'pure' elemental addition for cost savings. Mischmetal is a naturally occurring ore largely containing lanthanum (>50%), cerium (20-35%), praseodymium (4-10%) and neodymium (10-20%) [151], and other rare earth impurities. The Al and rare earth additions provide significant improvements in creep behavior [149, 150]. Further

investigations [152] of mischmetal-containing alloy systems have shown that ternary additions of zirconium [150] and manganese further improved the creep behavior. Creep strengthening mechanisms of these alloys were believed to be precipitation of intermetallic phases along the grain boundaries, though detailed investigations of the microstructure were not possible due to equipment limitations of the time. Later studies utilizing modern microscopy techniques (TEM) [153] identified precipitates within the alpha magnesium of permanent mold Mg-1.3RE after aging.

Recently interest in the AE series has increased [11-14, 151]. These studies have seen successful adoption of ACM522 (Mg- 5Al- 2Ca - 2RE) and AE44 for automotive applications such as oil pans [13] and die-cast structural engine cradle [14], respectively. Commercial implications for these systems motivate a more detailed understanding of the creep resistance and phase formation / stability in Mg-Al-RE containing alloys.

Although detailed investigations on solidification paths and phase formation/stability (with detailed TEM diffraction analysis) for the AE series of alloys have yet to be completed, XRD analysis has been conducted [10, 11]. The thermodynamic modeling for the rare earth alloying additions is lacking with many of the mischmetal elemental constituents (i.e. La, Pr, Nd) not being modeled in thermodynamic databases [154]. The compounds reported include $Mg_{12}RE$ [155, 156], $Al_{11}RE_3$ [11, 157], Al_4RE [11, 86], and Al_2RE [11] with significant dependence of the intermetallic compounds that form on cooling rate and on thermal exposure cycles.

Sieracki et al. [158] reported a decrease in the creep behavior of AE42 above test temperatures of 175 °C. Powell et al. [10, 11] later attributed this decrease in creep resistance at elevated temperatures to a decrease in the volume fraction of eutectic $Al_{11}RE_3$, marked by a simultaneous increase in Al_2RE and the formation of $Mg_{17}Al_{12}$. The resultant microstructure is shown in Figure 2.13, where the changes in eutectic morphology can clearly be seen.
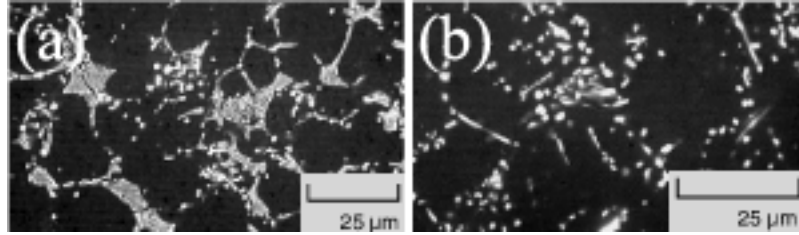
Figure 2.13 BSE SEM images of (a) AE42 as-die-cast and (b) AE42 after creep testing at 175 °C [115].

Moreno et al. [156, 159], investigated the creep, microstructure, and stability of two rare-earth magnesium alloys, AE42 and MEZ. The composition of AE42 was Mg - 3.7Al - 2.69 RE - 0.21 Mn and MEZ was Mg - 1.92RE - 0.33Zn - 0.26Mn. In their study the AE42 alloy exhibited superior yield and tensile strengths due, in part, to solid solution strengthening from Al of the primary α-Mg. Creep tests in the regime of 150 and 175 °C, 75 and 80 MPa respectively, showed that this solid solution strengthening did not translate to improved higher temperature long-time creep resistance. Creep stress exponents varied between n = 3 to 7, indicative of power law creep with dislocation glide or climb. It was also determined through TEM analysis that microstructural instability in the near-grain boundary areas occurred during creep and it was speculated that this had a significant effect on creep behavior.

2.2.7   Mg-Al-Si Alloys

Volkswagen was the first automotive company to use a creep resistant magnesium alloy in an elevated temperature application with the VW Beetle's engine block being cast from AS41, during the 1970's. An example of a die-cast Mg-Al-Si alloy (AS21) can be seen in Figure 2.14. The ternary system exhibits moderate creep properties at elevated temperatures up to about 150 °C. These alloys (AS21, AS41) do not have sufficient creep resistance for modern powertrain applications, yet remain attractive for lower temperature applications due to their moderate creep strength, castability, and cost. An investigation on their microstructure and creep behavior provides insight on creep strengthening mechanisms.
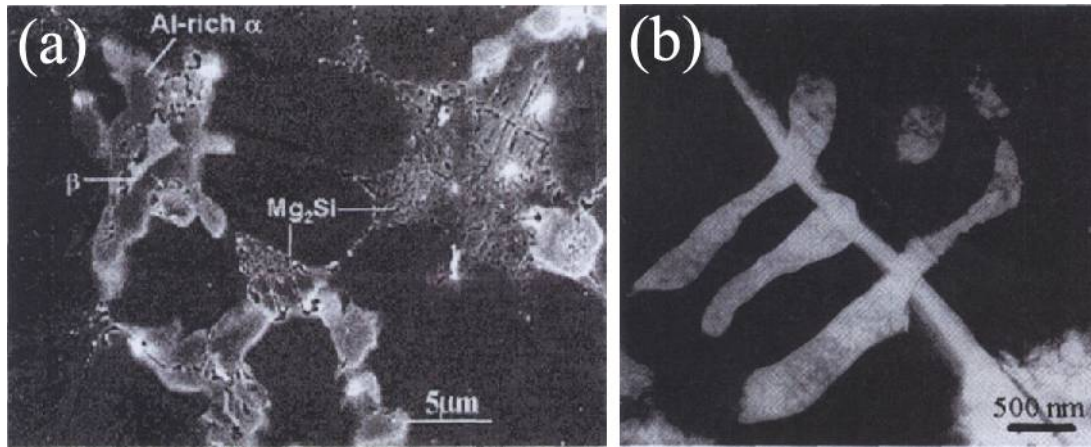
Figure 2.14 (A) SEM image of the microstructure for a high-pressure die-cast AS21 alloy depicting the different phases. (B) TEM micrograph of Mg2Si particle with branched arms into neighboring α-Mg grains [129].

To achieve moderate creep resistance in these alloys, they must be die-cast to obtain a fine dispersion of the Mg_2Si particles along the grain boundaries [1]. In permanent mold or sand cast conditions these alloys have very poor mechanical properties. Recent investigations have found that calcium additions [160] can improve sand castability by modifying the morphology of the Mg_2Si and Mg dendrites. Creep resistance remains low due to the low volume fraction of the Mg_2Si precipitates in the sand cast condition.

Brofin et al [161], studied the solidification features of die cast magnesium-aluminum-silicon alloys. EDS analysis showed that the majority of the precipitates were the intermetallic compound Mg_2Si. These particles have Chinese script morphology. The investigation also reported the existence of the $Mg_{17}Al_{12}$ phase, which has previously been discussed as being detrimental to the creep behavior of magnesium alloys. The results are in strong agreement with another study on the AS alloys [162].

Dargusch et al. [162] investigated the role of silicon content on microstructure and creep in Mg-Al-Si alloys. They observed that as Si concentration increased above the eutectic (>1.14 wt%) some of the Mg_2Si particles appear with a block morphology amongst the Chinese script-type morphology observed at lower Si contents (<1.14 wt%). It was also reported that Si additions up to 2.64 wt% continue to significantly decrease the creep rate in these die cast alloys. Dargusch et al. [162] hypothesize that due to the branched arms of the Chinese script Mg_2Si, a more creep resistant microstructure was

36

formed through connecting neighboring grains. Another important strengthening consideration from the study was the solute aluminum within the α-Mg dendrites and its segregation behavior during solidification. The aluminum content from the dendrite core to edge varied from 4 to 11 wt%, or a difference of 7 wt%. This segregation behavior may contribute to the strengthening of the α-Mg dendrites. In this alloy fine β precipitates were observed in the high aluminum regions within the α-Mg and are believed to have formed after casting, during the cooling process.

2.3 Heat-treatable Magnesium Alloys

2.3.1 Mg-Th and Mg-Th-RE Alloys

The magnesium-thorium and magnesium-thorium-rare earth alloy systems were first investigated in the 1940s [163, 164]. Initial investigations focused on the hot-formability of these alloys (0-10 wt% thorium) [163]. Leontis [164] investigated the creep behavior of these alloys with rare earth additions. Though this alloy system had good creep resistance, it saw limited use due to the radioactivity of thorium. The mechanisms for improvement in creep resistance were not thoroughly investigated, but were hypothesized as an effect of fine grain size, and undissolved compounds [148, 163-165]. Use of experimental techniques (i.e. TEM investigations) was limited due to the era of these studies and thus no reports of precipitation strengthening were presented.

2.3.2 Mg-Y-Nd-HRE (Heavy Rare Earths) Alloys

The most widely used creep resistant aerospace alloy system is the Magnesium-Yttrium-Rare Earths (WE alloys) system. The major rare earth element in these alloy systems neodymium with heavy rare earth impurities. These alloys exhibit dramatically improved creep properties, when compared to the current automotive alloy systems, capable of withstanding stresses of 100-200 MPa at temperatures above 200 °C. The alloys are processed through sand casting and in some cases extruded. The improvements in creep are gained from precipitation through solution treatment, quenching, and ageing. Microstructures for this group of alloys are shown in Figure 2.15.
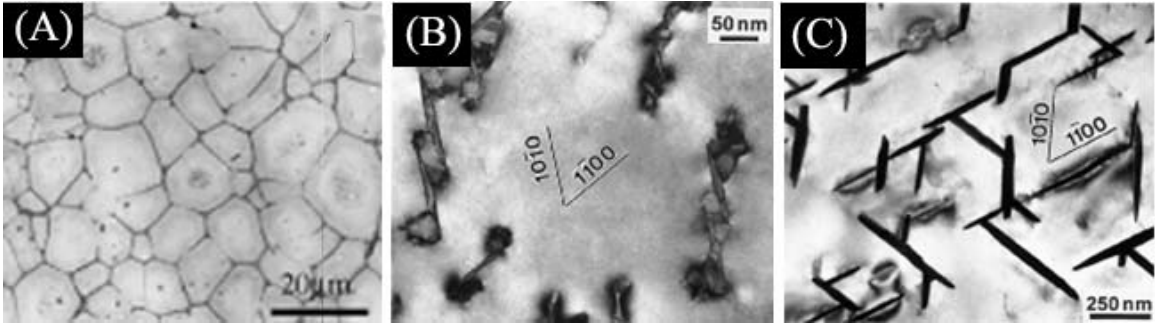
Figure 2.15 Microstructure of Mg-Y-Nd alloys for an (A) SEM image of Mg - 2.5Y - 2.5Nd - 0.4Zr [133] (B) TEM image of Mg - 5Y - 2Nd - 1.5HRE - 0.4Zr aged at 250 °C for 48 h showing metastable β' precipitates [134] and (C) TEM image showing same alloy from (B) aged at 250 °C for 2400 h. Note precipitates observed within the α-Mg grains [166].

2.3.3   Mg-Ag-RE(Nd) Alloys

Following the development of Mg-RE-Zr alloys, investigations were continued to improve the age hardenability of this alloy system though Nd and Ag additions [3]. The hardenability was successfully increased by Ag and Nd additions that lead to the development of the aerospace alloy QE22, with creep resistance up to 250 °C. The increase in hardenability and improvements in creep were attributed to the formation of a $Mg_{12}Nd_2Ag$ phase through an unknown precipitation sequence [167]. An example of a Mg-Ag-RE(Nd) alloy micrograph is shown in Figure 2.16. Note both the precipitates in the α-Mg and eutectic intermetallic phases along the grain boundary.
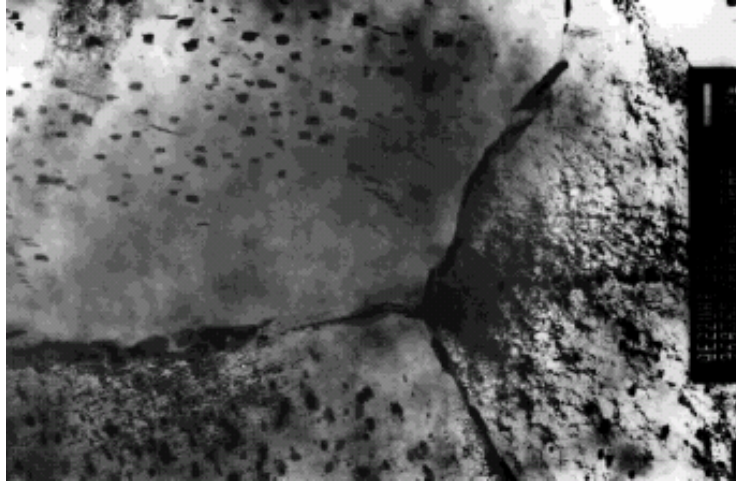
Figure 2.16 A TEM image of QE22 in T4 (solution) heat treatment condition. Maker bar is equal to 1 micrometer. Note the intermetallics along the grain boundaries and precipitates within the α-Mg grains [136].

Investigations on alumina fiber reinforcement of this alloy system have reported additional improvements to the creep properties [168-171], with incremental creep improvements at moderate temperatures of 200 °C.

2.3.4   Mg-Sc Alloy

To further improve the creep resistance and mechanical properties of aerospace alloys, scandium additions to Mg alloys have been investigated [172-174]. These alloys are precipitation hardened by Mn_2Sc plate-like precipitates parallel to the basal plane [174]. The Mg - 6Sc - 1Mn as-cast alloy has improved creep properties when compared to the WE43 alloy in both the as-cast and T6 heat treatment condition. Figure 2.17a shows the general microstructure of Mg - 6Sc - 1 Mn and Figure 2.17b shows a TEM micrograph of an α-Mg grain interior with Mg_2Sc precipitates. Figure 2.18 compares the creep behavior of WE43-T6 to several scandium containing Mg alloys.
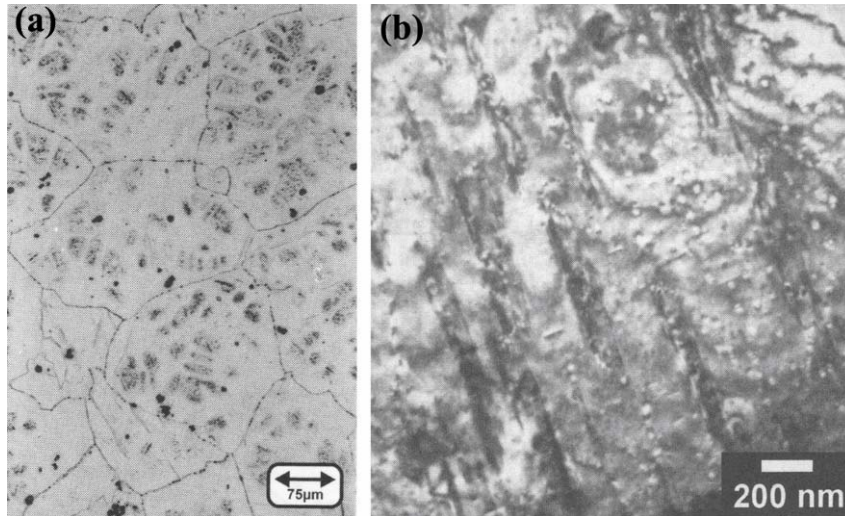
Figure 2.17 (a) Micrograph of an as-cast Mg – 6Sc – 1Mn Alloy [140] and (b) Micrograph of an annealed (350 °C 30 min) Mg – 3.71Y – 2.12Nd – 1.28 Sc 1.18 Mn (wt%)[142]. Note basal oriented Mn2Sc precipitates.
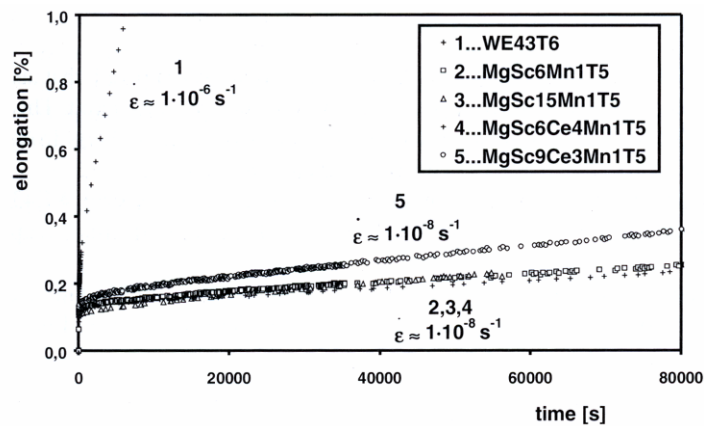
Figure 2.18 Creep behavior of scandium containing Mg alloys compared to WE43-T6 [140].

2.3.5 AMC-SC1 Alloy

The alloy system designated as AMC-SC1, was developed by the Australian Magnesium Corporation (AMC), for sand cast (SC) automotive powertrain applications [55]. The alloy composition is Mg – 1.7 Nd – 1 RE – 0.55 Zn – 0.7 Zr [175] and was selected by the USCAR-MPCC project to be used to cast the experimental engine blocks [17]. Detailed reports of microstructure, alloying constituents, and mechanisms for creep improvement for this alloy are not yet available in the literature. The alloy is strengthened through solution treatment and precipitation strengthening, using a T6 heat treatment. It is also reported, seen in Figure 2.19, that the microstructure contains α-Mg grains

'locked' by magnesium-rare earth phases at the grain boundaries and triple points. Clusters of rod shaped intermetallics phases within the α-Mg grains, with a stoichiometry close to $Mg_{12}(La_{0.43}Ce_{0.57})$, have been reported [176].
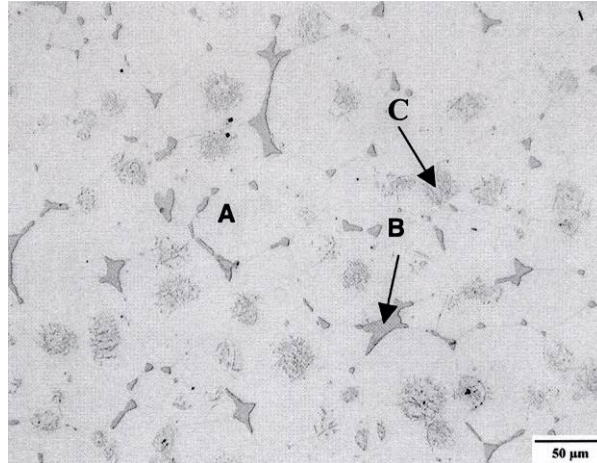
Figure 2.19 Optical micrograph of AMC-SC1 in the T6 heat-treatment condition with (A) marked out solid solution α-Mg grains, (B) magnesium-rare earth intermetallic phases at the grain boundaries and triple points, and (C) clusters of rod-shaped intermetallics within the α-Mg grains with stoichiometry close to $Mg_{12}(La_{0.43}Ce_{0.57})$ [176].

Dunlop, et al [177] examined the effect grain size had on the creep resistance of AMC-SC1, through Zr additions. Interestingly, it was found that the creep rate increased with decreasing grain size (as expected), up to a threshold (between 235 and 110 μm), shown in Figure 2.20. With further grain refinement, to an average grain size of 46 μm, the creep rate decreased a ½ order of magnitude. The reported creep rates are sufficiently low that the results must be viewed with skepticism. An alloy creeping at $\dot{\varepsilon} \approx 5.5 \times 10^{-10}$ (the fastest creep rate reported in the investigation) would accumulate less than 2% strain over the course of a year. Regardless of the low creep rates, die-cast alloys have been reported to have a grain size typically of 10-20 μm raising the question of the effect the grain size has on creep behavior in these magnesium alloys.
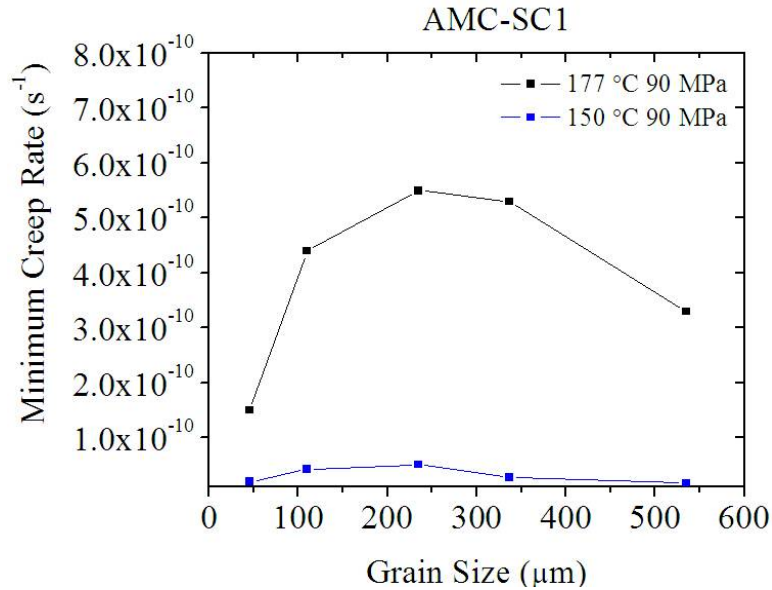
Figure 2.20 Steady state creep rate as a function of grain size for AMC-SC1, data from [14].

2.4   Aging

The heat treatable sand case alloys (i.e QE, WE, ZK, and HZ), primarily used in aerospace applications offer improved creep resistance, in comparison to the automotive Mg alloys, at the expense of increased cost and density. Much of the strengthening of these alloys is attributed to their ability to be precipitation hardened, which is evident from the change in hardness observed in Figure 2.21. As previously discussed AXJ530 alloy has been reported to be age-hardenable [57], but this increase is only 7-10 Hv as opposed to the 22 Hv seen in WE54 [166] and the 36 Hv in AZ91. The alloys in Figure 2.21 exhibit an increase in creep strength for the increases in hardness. This improvement in hardness and creep strength is most evident in WE54.
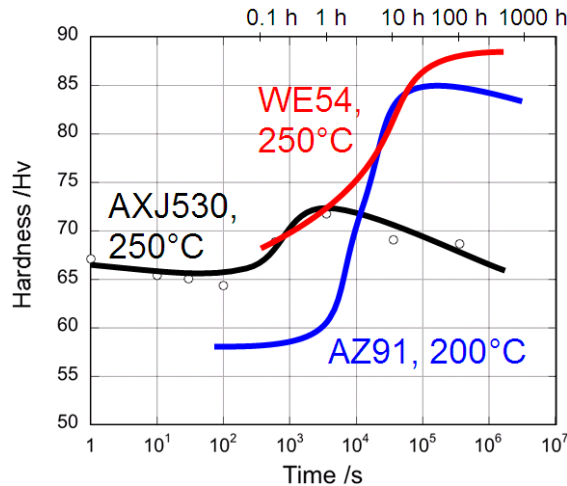
Figure 2.21 Hardness as a function of time for 3 Mg alloy systems (AXJ530 [40], AZ91 [146], and WE54 [93, 160]). Figure courtesy of A. Suzuki.

An interesting observation in comparing the age hardenability of the die-cast AXJ530 and sand cast WE54 is the habit plane and morphology of the precipitates formed in each alloy. WE43 gains its full strength after a solution and aging treatment of 48 h at 250 °C. The precipitation sequence in WE54 is described in detail elsewhere [166]. The morphologies and habit planes of each of the precipitates in each alloy are unique. In WE54 precipitation first occurs as β' irregularly faceted globules with the relationship of $(100)_{\beta'}//\{11\overline{2}0\}_\alpha$ and $(001)_{\beta'}//\{0001\}_\alpha$. With additional aging a shear assisted transformation of the globules to a metastable plate morphology occurs. This β_1 phase has a habit plane parallel to the $\{1\overline{1}00\}_\alpha$ and orientation relationship of $(\overline{1}12)_{\beta'}//\{1\overline{1}00\}_\alpha$ and $[110]_{\beta'}//[0001]_\alpha$. It is a combination of the globules and metastable β_1 plates, both with a large cross-sections to the basal plane, that provide WE43 with much of its creep resistance [166]. In AXJ530, C15 – Al_2Ca precipitates form parallel to the basal plane with the following relationship: $\{111\}_{C15}//(0001)_\alpha$ $[01\overline{1}]_{C15}//[0\overline{1}10]_\alpha$. The decreased age hardenability of AXJ530 compared to the WE54 is attributed to the limited basal cross-section the C15 precipitates have compared to the β_1 precipitates in WE54 [178].

2.5   Summary of Creep Characteristics of Mg Alloys

The creep behavior of magnesium and its alloys has been the focus of numerous investigations that are discussed above and summarized in Table 2.6. These studies were conducted at stresses of 10 to 120 MPa for temperatures between 25 and 527 °C. In general, the phenomenological creep behavior of magnesium and its alloys has been described as having two definable regions of creep, a high stress and low stress region (in some studies these regions were also temperature dependent). The transition stress between these regions was alloy dependent. The reported stress exponents in the low stress regions were 1.5 - 2 and for the high stress region between 4 and 20. It has therefore generally been agreed throughout the literature on creep resistant magnesium alloys that the rate creep behavior of the alloys is described by power law creep. This indicates that the creep deformation rate is controlled by dislocation motion through climb and/or glide, diffusion controlled dislocation motion, or dislocation motion controlled by a solute atmosphere. At very high temperatures (outside of the interest range for automotive applications) creep would be diffusion controlled and grain boundary sliding (or diffusion accommodated GBS) would become more significant.

Reported creep mechanisms in magnesium alloys have often been inferred from calculating the stress exponent and creep activation energy, determining the stress/temperature regime that the alloy is operative in (from deformation maps), and developing conclusions from the theories in the literature that use similar alloys and reported stress exponent.   Unfortunately few investigations fully describe the microstructure, details of creep strain accumulation (macro or micro) or creep damage accumulation behavior.   These investigations are crucial to understanding the creep deformation behavior. For example, the generally accepted range of the stress exponent for an alloy operating in the power-law creep regime is wide (n = 2 – 42) [83] . Stress exponents have been measured from 1.5 to as high as 20 in Mg alloys with their behavior still predicted by power-law creep [9, 84, 112]. Note that many investigations that report low stress exponents completed relatively short time creep tests where primary creep could still be operating.

Table 2.6 Calculated creep parameters and proposed mechanisms for select magnesium alloys.

Alloy	Stress (MPa)	Temperature (°C)	Qc (kJ/mol)	Grain Size (µm)	Stress Exponent (n)	Notes	Proposed Mechanism	Ref.
Mg 99.99%	20-50	150-200	106	100	5.86	Machined Ingot	Dislocation Networks	[87]
Mg 99.99%	9.8-98	127-527	92-134**	-	7.5-10*,**	Powder Metallurgy	Dislocations non-basal and cross slip	[89]
AZ91	60-120	25	-	-	4.6	Die-cast	Dislocation Climb	[179]
AZ91	30-100	150-180	-	15	6.9 @ (150 °C) 5.4 @ (180 °C)	Die-cast	Dislocation motion on basal as well as other planes	[111]
AZ91	40-115	120-180	220-94*	300	11	Machined Ingot	Dislocation motion, cross slip, caviation	[112]
AZ91	20-40	125-175	30-45	<10	2	Die-cast	GBS-observed marker displacement	[86]
AZ91	50-80	125-175	94	<10	5	Die-cast	-	[86]
AM60B	20-60	150	-	-	4	Die-cast	Diffusion controlled Dislocation climb/glide mechanism	[95]
AM60B	>60	150	-	-	10	Die-cast	Break-down powerlaw	[95]
AM50	50-95	150	121	9.2	4-6	Die-cast	High-temperature climb of dislocations	[100]
AM50	20-50	225	121	9.2	4-6	Die-cast	High-temperature climb of dislocations	[100]

Table 2.6 Calculated creep parameters and proposed mechanisms for select magnesium alloys.

AM50	95-120	150	162	9.2	8-13	Die-cast	High-temperature climb of dislocations	[100]
AM50	50-120	225	162	9.2	8-13	Die-cast	High-temperature climb of dislocations	[100]
AM50	50-120	150-225	126	10	6	Die-cast	Dislocation climb	[126]
AM50+ 1.72Ca	80-120	150-225	142	10	10	Die-cast	Dislocation climb	[126]
AM50+ 1.72Ca	120-150	150-225	142	10	20	Die-cast	Dislocation climb	[126]
AC53	42-70	150-200	120	10	1.5	Die-cast	GBS	[84]
AC53	42-70	100-150	40	10	1.5	Die-cast	GBS	[84]
AC53	70-97	150-200	120	10	8.5	Die-cast	Dislocation climb	[84]
AC53	70-97	100-150	40	10	8.5	Die-cast	Dislocation Climb	[84]
AS21	20-70	125-175	30-45	<10	2	Die-cast	GBS-observed Marker Displacement	[86]
AS21	70-80	125-175	94	<10	5	Die-cast	-	[86]
AE42	20-80	125-175	30-45	<10	2	Die-cast	GBS-observed Marker Displacement	[86]
AE42	50-100	125-175	-	10-20	3-7	Die-cast	Dislocation Glide/Climb	[159]

* Reported as temperature dependent
** Reported as stress dependent

Grain boundary sliding has been reported in magnesium alloys [9, 69, 86, 180]. There is nearly uniform acceptance of GBS as a significant and rate controlling creep mechanism for multiphase Mg alloys. The first, and most convincing study on GBS utilized a binary solid solution strengthened Mg - 0.78 Al (wt%) single phase alloy with microstructural observation both pre/post crept and quantification of marker line offsets at the grain boundaries [181]. Dargusch et al. [86] observed a region of localized damage, presumably at a grain boundary, in a multiphase AZ91 sample that had been crept to 20% strain. They hypothesized that this damage was a result of grain boundary sliding and stated that they made no further attempts to quantify GBS in the study. An alloy review paper [9], appropriately, discussed the supporting literature of GBS in Mg alloys. This created additional support for GBS as a rate-limiting mechanism, particularly in the low (< 2) stress exponent regime. Thus many of the reports [180, 182, 183] in the literature base GBS mechanisms on phenomenological creep behavior, not microstructural evidence. Importantly, most investigations do not report grain size or equate cell size with grain size, therefore quantification of GBS in dendritic Mg alloys is difficult. This investigation implements a digital image correlation technique to measure microstructural-scaled creep strain. Quantification of GBS in Mg alloys (at stresses and temperatures representative of powertrain components) is accomplished by measuring microstructural strain distribution measurements.

Alloying is also an important characteristic for creep strengthening. Mg-Al alloys have poor creep resistance in comparison to other Mg based alloy systems (i.e. at 80 MPa and 150 °C AM50: $\acute{\varepsilon} \sim 10^{-2}$ [100] compare AX53: $\acute{\varepsilon} \sim 10^{-4}$ s^{-1} [84]). The inclusion of Zn in an Mg-Al alloy (AZ91) does not appreciably increase the creep strength. The poor creep resistance of these alloys has been attributed to the formation of the $\beta - Mg_{17}Al_{12}$ phase during solidification. This phase has poor thermal stability [2, 4, 7, 8] and unfavorable creep strengthening morphology [5, 6]. Sufficient addition of Si [161, 162] or RE [149, 150] to the Mg-Al binary suppress the formation of the β and form different eutectic intermetallics. The resultant microstructure (i.e. β suppressed) has improved thermal stability of the intermetallics and creep strengthening morphologies. Additional creep strength is gained through alloying Ca [116, 117] and/or Sr [146, 147] to the Mg-Al binary. This also changes the solidification path, forming eutectic intermetallics other

than β. The understanding of the microstructural features that improve the creep strength of the Mg-Al-Ca/Sr alloys over the Mg-Al-RE or Mg-Al-Si is incomplete. It is interesting to note that many of the investigations (Table 2.6) report the creep rate controlling mechanism as dislocation motion in the primary α-Mg grains and yet attribute an improvement in creep strength to the formation of eutectic intermetallics.

2.6   Summary

The creep resistant magnesium alloys for automotive applications are based mainly on the Mg-Al system with ternary and higher order elemental additions. The higher order additions are typically lower cost elements that enhance castability and/or mechanical properties (i.e. sufficient fatigue resistance, tensile strength, ductility, corrosion). For the lower stress/temperature applications, alloys within the Mg-Al-Si ternary system (i.e. AS21, AS41) have sufficient creep resistance. However, the stresses and temperatures (100 MPa, 150-200 °C) of powertrain components require more robust alloy systems with higher creep resistance. Currently alloy systems containing Mg-Al-Sr have been cast around an aluminum crankcase, creating an aluminum core and magnesium structure, for industrial products. Other alloy systems containing Mg-Al-RE, Mg-Al-Ca and higher order systems have been developed (MRI-330D, AXJ530, Mg-Al-Ca-Zn, etc). There is a lack of understanding of the microstructure and creep deformation and strengthening mechanisms for these alloys systems.

The microstructure and creep resistance of the automotive Mg alloys have all been investigated with varying degrees of microstructural analysis. These investigations have not agreed on the microstructural features that provide the difference in creep strength observed between alloys. Microstructural features influencing creep have been listed as: intermetallics pinning the grain boundaries, softening (at temperature) of eutectic, dislocation climb-glide, solid solution strengthening, and precipitation strengthening. Some have suggested that solid solution strengthening contributes significantly to the creep behavior, yet provide limited supporting data and do not describe the mechanism by which solid solution strengthening is accomplished (i.e. strain field interactions, stacking fault energies, diffusion). There has also been a lack of

48

studies that systematically change solute content in α-Mg and quantify the resulting creep strength. Others have argued it is the intermetallic phases formed, and their behavior during creep (i.e. morphology, stability, melting temperature, strength), yet the conclusions are often speculative with little or no data linking the properties of the intermetallics to creep strength in support of the conclusions. Various investigations suggest grain boundary sliding as a key deformation mechanism. Little data links the influence of the eutectic region and specifically the intermetallic phases located within these regions to the creep strength and mechanism of GBS. Neither do these studies distinguish the grain structure from the cell structure. This aspect of structure (α-Mg cells are not individual grains) will be clarified in this thesis along with particular attention to the eutectic structure. Precipitation strengthening of the primary α-Mg phase for the automotive creep resistant Mg alloys has received little study, probably largely due to the lack of heat-treat-ability for die-cast components. Precipitation strengthening of the α-Mg primary phase will be presented for the Mg-Al-Ca alloys.

This thesis investigates the influence of composition (i.e. the ternary addition of Ca, Ce, La and Sr on Mg - 4 Al - 4 X along with the GM alloy AXJ530) on the microstructure (i.e. intermetallic morphology, solid solution strengthening differences, and grain/cell structure) and creep behavior. The alloys were permanent mold cast and die-cast AXJ530 samples were provided by the GM for additional investigations. The varied composition resulted in different microstructures. Experimental investigations of each alloys microstructure and creep behavior linked the microstructure features to creep strength for each alloy.

The composition affected the solidification path of each alloy which resulted in the formation of different intermetallics and changes in segregation behavior. The size of the grains was different for each alloy, but little change at the scale of the cells. Alloy composition influenced the ability to precipitation strengthen certain alloys. Precipitates formed (as a result of the processing route) in the Mg-Al-Ca alloys were observed in the primary α-Mg grains. These precipitates influenced the creep behavior, in the best case, by decreasing the minimum creep rate approximately an order of magnitude.

Creep strain developed heterogeneously on the length scale of the grain structure during primary creep stain accumulation (approximate the strain at the $\acute{\epsilon}_{min}$). There was a

greater tendency for localized shearing across grains in large grain material. As creep strain continued to accumulate, after the grains have strain hardened, localized damage initiated along the grain boundaries, predominately at high angle grain boundaries. This damage was of the form of cracks and cavities and was generally located at near grain boundaries that experienced elevated strain (up to 40%) and evidence of significant plasticity (slip offsets). The creep rate accelerated as additional damage formed and coalesced up to failure. Extremely limited evidence (1 case) of damage indicative of grain boundary sliding was observed, where shear was measured between two grains.

Chapter 3

Experimental Procedure

This chapter discusses the experimental procedures, techniques, and analyses used in this research. This chapter is divided into six sections: experimental materials, solidification studies, permanent mold casting techniques, microstructural characterization, mechanical testing, and micro-composition analysis.

3.1   Experimental Materials

A series of master alloy ingots were supplied by the Norsk Hydro Company. The nominal compositions are listed in Table 3.1. Compositional analyses (mass spectroscopy, flame atomic absorption spectrometry, and ICP-AES) of the as received ingots are in Table 3.2. AXJ530 ingot was provided by the General Motors Corporation.

Table 3.1 Nominal Composition (wt%) of magnesium alloys utilized in this study.

Alloy	Mg	Al	Ca	Sr	Ce	La
AX44	Bal.	4	4	-	-	-
AJ44	Bal.	4	-	4	-	-
ACe44	Bal.	4	-	-	4	-
ALa44	Bal.	4	-	-	-	4
AXJ530	Bal.	5	3	0.2	-	-

Table 3.2 Measured composition (in wt% from mass spectroscopy, flame atomic absorption spectrometry and ICP-AES) of magnesium alloys utilized in this study.

Alloy	Al	Ternary Addition	Mn	Si	Fe	Cu	Ni	Mg
AX44	3.62	3.71	0.015	0.0030	0.0232	0.0014	0.0003	Bal.
AJ44	3.94	4.27	0.012	0.0029	0.0187	0.0006	0.0001	Bal.
ACe44	3.99	3.96	0.014	0.0032	0.0200	0.0005	0.0001	Bal.
ALa44	3.95	4.04	0.013	0.0029	0.0236	0.0006	0.0001	Bal.
AXJ530	4.83	2.90	0.300	-	0.0010	0.0020	0.0006	Bal.

3.2   Solidification Cooling Curve Preparation and Collection

Analyses of solidification cooling curves were preformed with 100 g samples cut from the master alloy ingots. These samples were melted with a controlled induction melting system, Figure 3.1a. Traditional DTA or DSC analysis was not performed due to the reactive and corrosive nature of liquid magnesium. The melting chamber, detailed schematically in Figure 3.1b, consisted of a 10 kW induction coil, environmental chamber, uncoated mild steel crucible and type K thermocouple for temperature measurement. The chamber was backfilled with a protective cover gas of 1% sulfur hexafluoride with a balance of argon to limit melt oxidation.
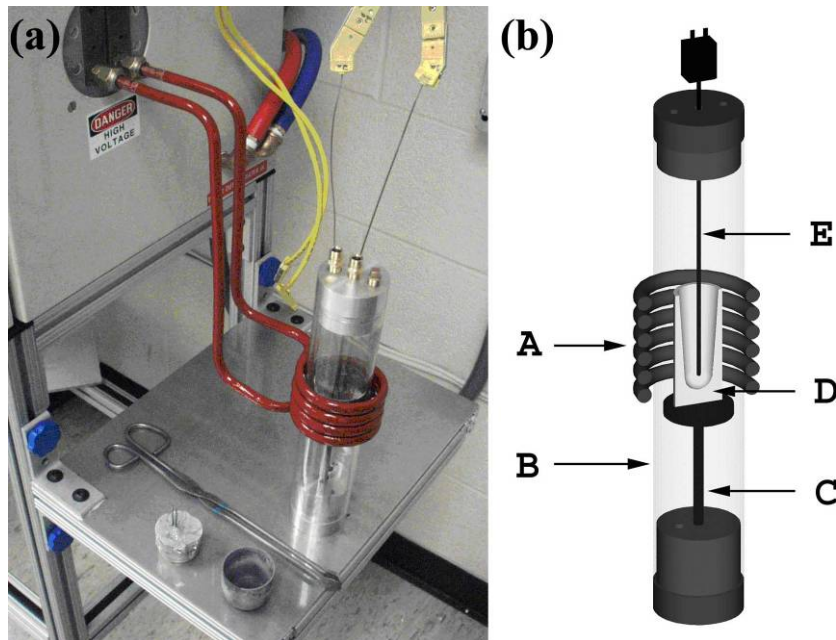
Figure 3.1 (a) 10 kW induction melting system used for alloying and thermal analysis (b) Schematic of melting apparatus: A) cross section of induction coil, B) quartz environmental chamber, C) crucible stand, D) cross section of crucible, E) thermocouple.

A single type K thermocouple, 0.040" in diameter (for rapid response to temperature changes), was inserted in the center of a melt. Data was recorded every 500 ms on a DATAQ DI-1000TC device connected to a PC with WinDaq data acquisition software. Calibration of the temperature measurements was completed using reference temperatures of distilled H_2O as an ice bath and boiling water along with freezing

temperatures of pure tin (232 °C), lead (328 °C), magnesium (650 °C) and aluminum (660 °C) [24].

Liquidus temperatures and the temperature at which solidification terminates were determined by differentiating the temperature-time cooling curve, and measuring the deviation from linearity during cooling through the range from all liquid to all solid. An example of a temperature-time cooling curve and the first derivative is shown in Figure 3.2. Negligible undercooling was observed for the alloys investigated. After thermal analysis the sample was re-melted and cast into a steel crucible for microstructure characterization, Figure 3.3. The crucible was coated with a light boron nitride refractory coating.
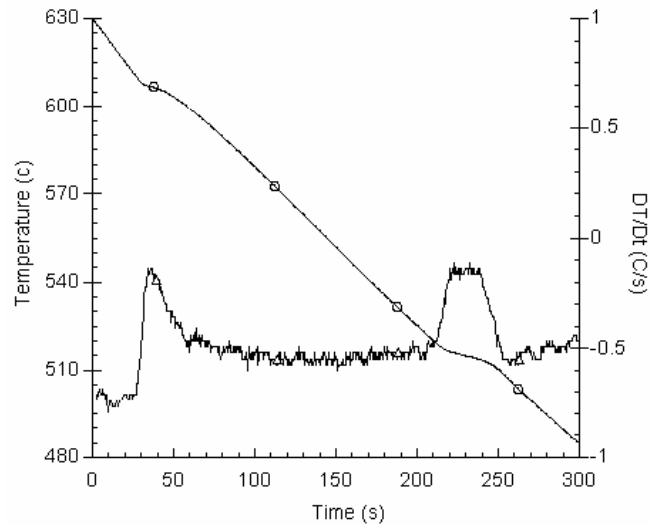
Figure 3.2 Example of a temperature-time cooling curve and first derivative (example alloy AX44).

Figure 3.3 Button specimen cast after solidification analysis for microstructural investigations.

53

3.3   Permanent Mold Casting

The permanent mold used for specimen casting was designed according to ASTM B108-02 with minor modifications for desired specimen geometry. The mold was CNC machined from 1018 steel and machining prints are included in Appendix A. An image of the machined mold is shown in Figure 3.4. The mold is two mirror halves, with the left half in the figure standing on edge, viewed looking down the pour spout and sample vents. The mold half on the right, lying on its back shows the geometric details of the face of the mold. Knockout pins for part ejection, electric resistance heaters for preheating the mold, and thermocouples for monitoring mold temperature were incorporated in the mold. Each mold half contained six type K thermocouples, mounted from the exterior side of each tool, within 1.6 mm (1/16'') of the mating tool surfaces. The red dots in the figure denote the locations of the thermocouples.
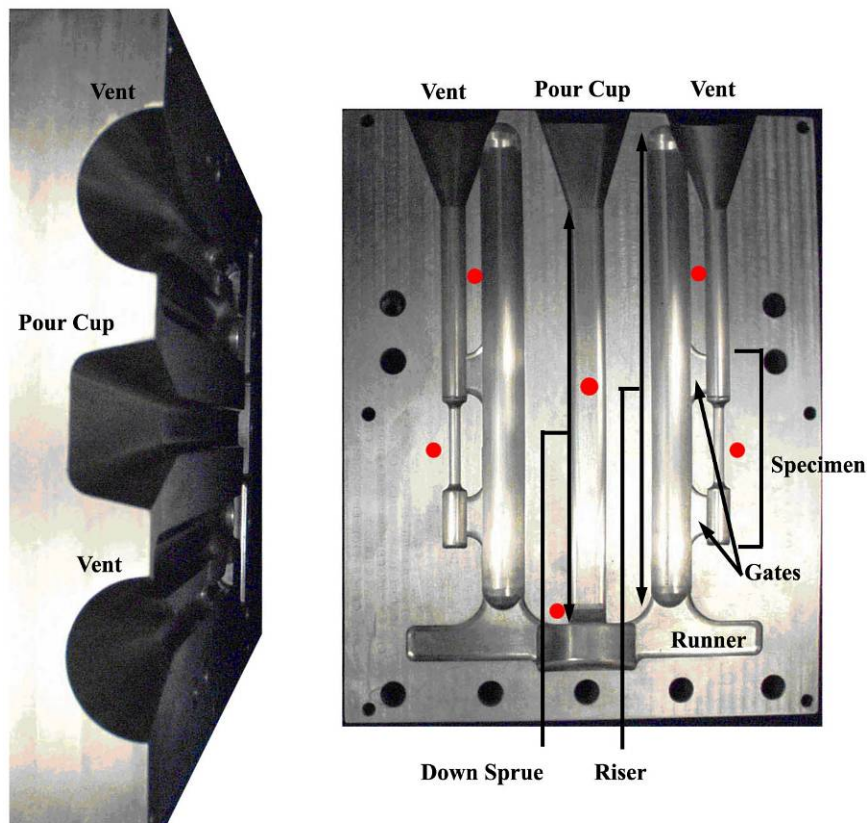
Figure 3.4 Permanent mold (adopted from ASTM B108-02) used for casting tensile creep specimens. The red dots denote locations of thermocouples that are approximately 1.6 mm from surface.

3.3.1   Validation Modeling of Permanent Mold

The geometry of the permanent mold designed for casting specimens was meshed using ProCast®, a FEM solidification code to analyze liquid flow during mold filling, specifically in the gage region of the sample. Filling was analyzed to ensure that the two liquid fronts (from the top gate and specimen) would not meet in the gage, and that the thermal profile across the gage was reasonably uniform during solidification. Due to the nature of a two gate system on each side (top and bottom) of the gage, the potential of forming a knit line (the point where two liquid or semi-solids meet in a die cavity) within the gage was a primary concern. A secondary consideration in mold design was that the heat-transfer of the mold and solidifying metal would not be uniform across the constrained gage. Lack of uniformity could potentially lead to hot tearing due to the constrained geometry and thermal gradient.

The fluid flow during the mold filling sequence is shown in Figure 3.5, at three progressive times during mold filling. Molten metal first fills the lower grip section of the specimen and then flows quiescently up the gage. As the riser fills more rapidly the molten metal reaches the upper gate prior to the gage being completely filled. Due to the narrow cross section of the gates, the flow of metal is adequately slowed while the gage is fully filled and the two liquid/semi-solid fronts meet somewhere in the grips. The simulation was executed for mold filling pressures of 3 and 4 MPa, with little variation between each pressure. These mold filling pressures were calculated as the head pressure exerted by liquid magnesium prior to and just after filling the gage, respectively. No knit lines were observed in the gage section of any castings produced.

After the mold was completely filled, the potential for hot tearing of the tensile sample was addressed. The same mold model that was run for fluid flow during mold filling was used to calculated heat flow during solidification and cooling. A snapshot of the cast component temperature during the cooling sequence is shown in Figure 3.6. The gage section temperature is fairly uniform, and both grip sections are only about 30 °C warmer than the gage section. This is a strong indication that the castings cool with sufficient uniformity to avoid hot tearing in the gage section. No hot tearing was observed in the gage sections of the castings produced for this study, supporting this prediction. However, near the pour cup and down sprue of the mold, where there is a

large degree of geometric constraint from the wide pour cup and narrow down sprue, a 200 °C thermal gradient was calculated and the formation of internal cracks at this location were observed with x-radiography.
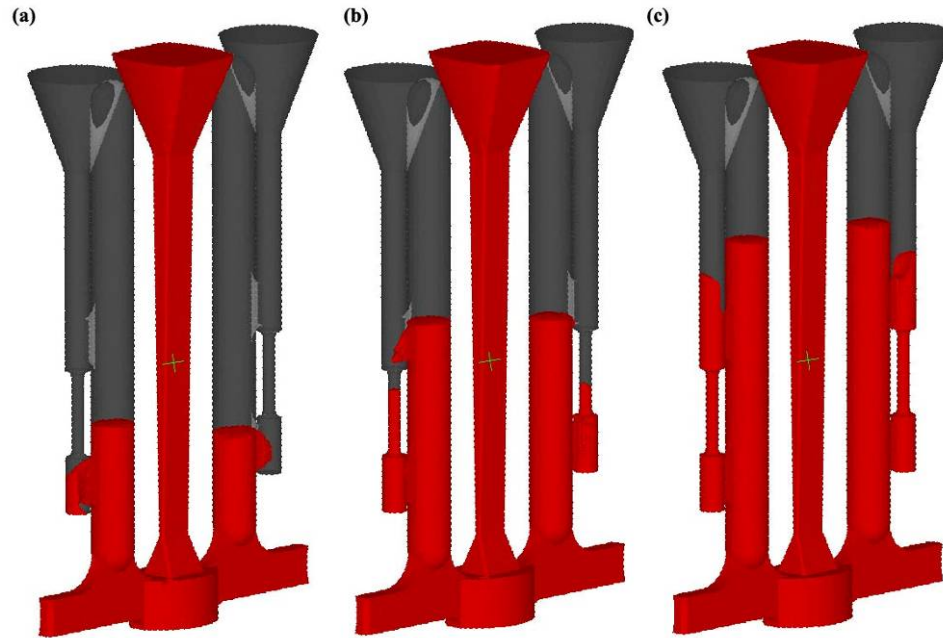
Figure 3.5 Fluid flow of AM60 from the ProCast® mold model during part filling. (a) ~10 s (b) ~15 s (c) ~20 s.
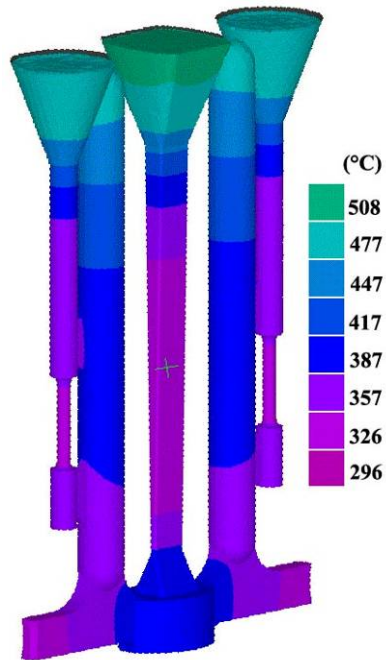
Figure 3.6 Calculated temperature distribution during cooling of ProCast® mold model.

3.3.2   Casting Parameters

Permanent mold casting of the each alloy was completed at the Ford - ELM casting facility in Ann Arbor, MI. The casting cell, Figure 3.7, consisted of a 30 kW resistance Striko-Dynarad melt furnace, furnace controller, and cover gas lid with cover gas mixing control. The melt pot was an uncoated hemispherical crucible of 1008 series mild steel, 23 cm in diameter.

Figure 3.7 Permanent mold casting cell, ELM casting laboratories, Ann Arbor, MI.

Prior to casting, approximately fifty-pound charges of master alloy were melted, yielding twenty to thirty castings per charge. After melting, the liquid was held for approximately one hour before casting began. The isothermal hold temperature was 685 °C for the AX44, AJ44, and AXJ530 and 750 °C for the ACe44 and ALa44. The melts was de-drossed before and periodically during the casting sequence as the surface of the melt oxidized.

The melt handling tools (i.e melt skimmer, ladle) were spray coated with a boron nitride refractory coating. These tools were pre-heated prior to handling the melt. The melt was protected with a cover gas lid, designed with an access door actuated through a foot operated pneumatic cylinder. The cover gas used for melt protection was a mixture of 0.5% SF_6, in 25% CO_2, and dry air (by volume).

The mold was spray coated with a boron nitride coating and subsequently baked at 300 °C prior to casting. This coating was periodically reapplied to the mold, as

necessary, during an alloy casting sequence. The mold was pre-heated to an initial average temperature of 200 °C before casting. Mold temperatures were recorded during mold pre-heat and the alloy casting cycle, using a National Instruments® data acquisition board with Labview® software. Temperatures were measured every 500 ms at each location and averaged across each tool half. Average mold temperature increased with each casting, due to the superheat of the melt. The influence of the mold temperature on microstructure and mechanical properties is discussed in detail in subsequent chapters.

A single casting consisted of the following sequence: ladling the superheated liquid metal from the crucible (10-15 seconds), pouring the metal in to the pre-heated mold (30-45 seconds), a dwell (105-120 seconds) to allow for complete solidification, and part ejection (20-40 seconds). This cycle was repeated until the melt crucible was empty of usable liquid metal, yielding approximately 20 castings. A solidified casting after ejection from the mold is shown in Figure 3.8.

Optimum casting parameters (i.e. type of mold coating, mold pre-heat, melt super heat, pour time, dwell time, part ejection) were determined prior to casting the alloys by completing a parametric casting sequence for the alloy AM60. Minor adjustments were made to the determined casting parameters for each alloy due to the difference in casting behavior from the AM60 used in the parametric study. The most significant adjustment was an increase in melt hold temperature from 685 to 750 °C for the rare earth containing alloys. This increase led to a more complete mold fill for the rare earth alloys compared to the incomplete mold fills at 685 °C.
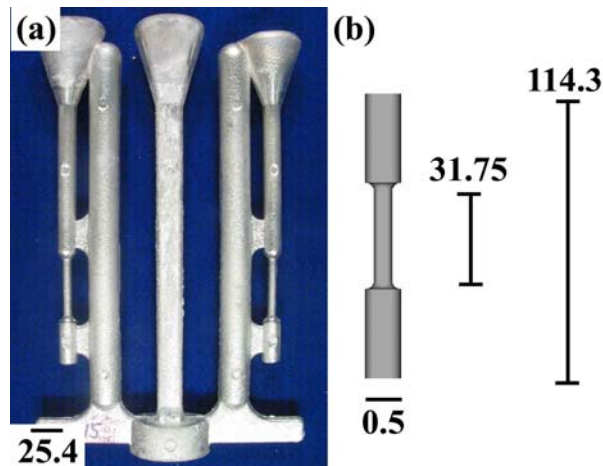
Figure 3.8 (a) Permanent mold casting (AXJ530) (b) Cylindrical creep sample geometry after removal from permanent mold casting (measurements in mm).

3.3.3   Soundness of Castings

Variations in casting conditions (e.g. mold temperature) important to microstructure development were monitored. Bulk composition was measured using inductively coupled plasma (ICP) to assess compositional uniformity between castings. Radiography of select castings was completed to examine bulk porosity, inclusions, and internal cracks and voids. Selected gage sections were metallographically prepared to examine the extent of porosity, the presence of inclusions and their variation between casting cycles. Bulk density was also determined for select samples across a casting campaign to investigate changes that may have occurred from processing.

Temperature variation in each mold half for each cycle was investigated during a casting sequence that consisted of twenty to thirty pours over one to two hours. The average temperature for each mold was determined by averaging the six thermocouples in each mold at each time interval. The average temperature within an individual casting cycle was determined by averaging the previously determined average mold temperature over each cycle. Cycles were determined by a combination of the time, mold temperature and an indicator flag (in the raw data file) that was marked at the beginning of each pour. Comparisons were then be made between mold temperatures, casting cycle and specimen microstructures.

Bulk compositions of selected cast specimens were measured at General Motors Technology Center – Warren, MI, using an inductively coupled plasma (ICP) technique. Samples (30 g) from the gage were dissolved into a hydrochloric acid solution. This solution was ignited in a plasma flame and the light emissions were recorded using a spectrometer. The unit was calibrated prior to and after use with a solution made from pre-made standards, with known volumes (+/- 0.1 ml) of the elements under investigation. Trace elements were investigated using 500 mg samples dissolved into solution and measured using the same technique.

Radiography was completed at X-R-I Testing® located in Troy, MI. The x-ray source used was a Phillips 320 kV tungsten target (anode) operated at 120 kV and 10 mA. A phosphor image capture plate, 43.8 x 35.5 cm (17x14 in), with a target to film distance (TFD) of 1.5 m (60 in.) was used to collect radiography images. The phosphor

image plate was digitized and analyzed using AGFA Rad view software with the assistance of an XRI testing - ASNT NDT Level III radiography technician.

The samples that had been x-rayed were sectioned and metallographically prepared for microstructure analysis. The resolution for defect detection (e.g. porosity or inclusions) with x-rays is dependent on alloy and defect density and cross section thickness. Because the alloys investigated have non-standard compositions and creating standards (having a varying thickness with controlled defect size) is costly and time consuming, it was assumed that defects less than 500 μm would not be visible in the radiography results. Therefore the microstructure (cell size/area fraction) and defects (porosity and inclusions) were investigated laterally across six regions of the gage of the specimen at five different locations (from top to bottom) to ensure consistence with the radiography results (i.e. consistent microstructure and low levels of porosity and inclusions).

Density was measured using the Archimedes method (in air and ultra pure ethanol). Triplicate measurements were made for each sample and averaged. The system was calibrated before and after each run using a standard of lead-silica glass. The resolution of the scales was +/- 0.0001 g and the accuracy of the technique was +/- 0.001 g/cm^3.

3.4   Microstructural Characterization

3.4.1   Scanning Electron and Optical Microscopy

Samples removed from the gage were mounted in cold mount epoxy resin. Metallographic preparation consisted of grinding the sample using silicon carbide paper from 120 grit to 1200 grit, and polishing with 3 μm and 1 μm diamond paste on neoprene polishing pads. The final polish was completed by hand on a neoprene pad with 0.05 μm colloidal silica or 0.05 μm diamond paste. For some investigations vibratory polishing was completed with a 0.05 μm alumina – ethanol slurry [92, 93]. When necessary, samples were dip-etched in a solution of 5 ml nitric acid, 50 ml acetic acid, 60 ml ethanol, and 20 ml de-ionized water.

The microstructural examination of metallographically prepared samples was conducted using a Nikon optical microscope and a Phillips XL30 FEG SEM. For the latter a typical working distance of 10 mm with an accelerating voltage of 20 kV, spot size of 5, and aperture set at 2 were utilized for the majority of the microstructural investigations. The volume fraction of the α-Mg phase was determined by the standard point count method using a fine grid with 552 markers. Eutectic volume fraction was calculated by difference. Alpha cell size measurements were completed by a line intercept method using ten randomly placed lines per micrograph and calculating the average cell size. At least 500 measurements were completed for each sample.

3.4.2   Transmission Electron Microscopy

Samples from the gage sections were prepared for TEM examination using standard techniques. Sections of approximately 1 mm in thickness were ground to a thickness of 0.120 mm by grinding on 1200 grit SiC paper. Samples were then punched to obtain 3mm diameter discs. A final thinning and polishing was completed on a twin-jet polisher using a solution of 8 vol. % perchloric acid in methanol. Electro-polishing was completed at approximately -30 °C, at a voltage between 10 and 20 V with a resulting current between 10 – 30 mA. A Phillips CM12 120 kV microscope equipped with a Gatan double tilt holder was used for phase identification and microstructure characterization.

3.4.3   Grain Size and Orientation

Orientation image mapping (OIM), or EBSD, was conducted on each alloy to determine grain size and specifically, to locate grain boundaries relevant to strain mapping experiments. A Phillips XL30 FEG equipped with an EDAX EBSD detector and OIM TSL analysis software for data acquisition and pattern analysis was used.

Individual grains were identified from OIM scans and the line intercept method was used to measure grain size. Due to time intensive nature of gathering OIM data, fewer grains (20-50) were analyzed per alloy for calculation of an average grain size. Additionally, grains in an etched Mg-4Al-4Ca alloy were imaged using polarized light on an optical microscope which revealed different colors for individual grains.

Sample preparation for OIM analysis involved electro-polishing the samples prior to indexing. The electro-polishing process was required to remove residual stresses introduced during solidification and subsequent machining of the samples. The electrolyte used was an 8% perchloric acid, 35 % butyl cellosolve and 57% methanol solution. The solution was cooled in an ethanol-LN bath to -40 °C. The sample was the cathode and a platinum anode was used with a DC power supply operated at 30 V and 1 A. Electro-polishing was conducted for approximately 10 minutes after the temperature stabilized. After polishing, samples were stored in a vacuum dessicator, to minimize surface degradation. Care was taken to prepare samples as close as possible to the time at which OIM analysis was conducted.

Samples were oriented 70° from the electron gun as recommended by EDAX for their EBSD detector. An accelerating voltage of 20 kV was used. The gain and bias on the EBSD detector was set independently for each set of experiments to optimize Kikuchi patterns, confidence index, and frame rate. Generally, a frame rate of 4 fps or higher was used. In some alloys/samples, depending on the quality of the surface finish, the accelerating voltage was increased, spot size decreased, and aperture fully opened to achieve indexable Kikucki patterns, confidence indexes and frame rates. The region scanned and the step size also varied depending on the alloy and processing. Die-cast alloy microstructures were investigated using EBSD and required a finer step size, ~0.5 μm, (ultimately dictating a smaller scan area of 100 x 100 μm) to complete scans in reasonable times. The permanent mold alloys were scanned with step size of ~5 μm on areas as large as 1000 x 2000 μm.

3.5   Thermal Exposure

Samples from each alloy were thermally aged for 500 hrs at 175 °C, the highest creep temperature in this study, to investigate microstructural stability. The samples were sectioned from the gage and sealed in a quartz tube that was twice evacuated and back-filled with ultra pure argon. A thermocouple, attached to a data acquisition system, was placed adjacent to the sample for the duration of the test to ensure constant temperature. The temperature was recorded every 300 seconds over the 500 hrs. The samples were

water quenched after aging by breaking the quartz tube in water immediately after its removal from the furnace.

3.6 Mechanical Testing

Permanent mold creep samples were sectioned from the castings and machined with grooves for extensometry and threads for grips. The gage section was left in the as-cast condition except in cases where parallel flats were machined onto the gage region. Drawings for the cylindrical samples and samples with parallel flats are located in Appendix A. The flats, required for strain mapping studies, were machined using a vertical mill. Shallow machining passes were used to minimize the formation of residual stresses.

3.6.1 Tensile Testing

Tensile testing was performed to determine yield strength, ultimate tensile strength and ductility of the cast specimens. Two specimens from each alloy were tested at room temperature and the results did not deviate significantly between the two tests, the average of these tests is reported. Tensile properties, at a strain rate of 10^{-4} s^{-1}, for each alloy are shown in Figure 3.9a. The averaged stress-strain curves for each alloy: AX44, ACe44, ALa44, AJ44, and AXJ530 are shown in Figure 3.9 b, c, d, e, and f, respectively. All alloys exhibited tensile ductilities between 0.75 and 2.5 % strain and very limited to no observable necking. Ultimate tensile strengths varied between 100 and 135 MPa. Yield strength was determined by taking the 0.2% offset for each stress-strain curve. The tabulated values from the tensile testing are shown in Table 3.3.

Table 3.3 Tensile properties at room temperature of permanent mold cast alloys.

Alloy	YS (MPa)	UTS (MPa)	% Ductility
AX44	85	127	2.30
AXJ530	90	135	2.25
AJ44	90	100	0.75
ALa44	65	107	2.00
ACe44	60	107	2.50

The AXJ530 exhibited the highest yield strength and ultimate tensile strength. The AJ44, had a similar yield strength but exhibited a much lower ductility and ultimate tensile strength. The two rare earth alloys had the lowest ultimate tensile strength and had similar yield strengths, ductilities, and ultimate tensile strengths.

AXJ530 has a slightly higher yield strength and ultimate tensile strength than AX44. Differences in grain size may contribute to small differences in yield strength. AXJ530 had a measured average grain size of 148 μm where AX44 had a larger grain size of 257 μm (presented in detail in Chapter 5). It is also possible that compositional differences and differences in solute distribution between, AXJ530 and AX44 could contribute to the differences in yield strength and this is discussed in section 4.5.
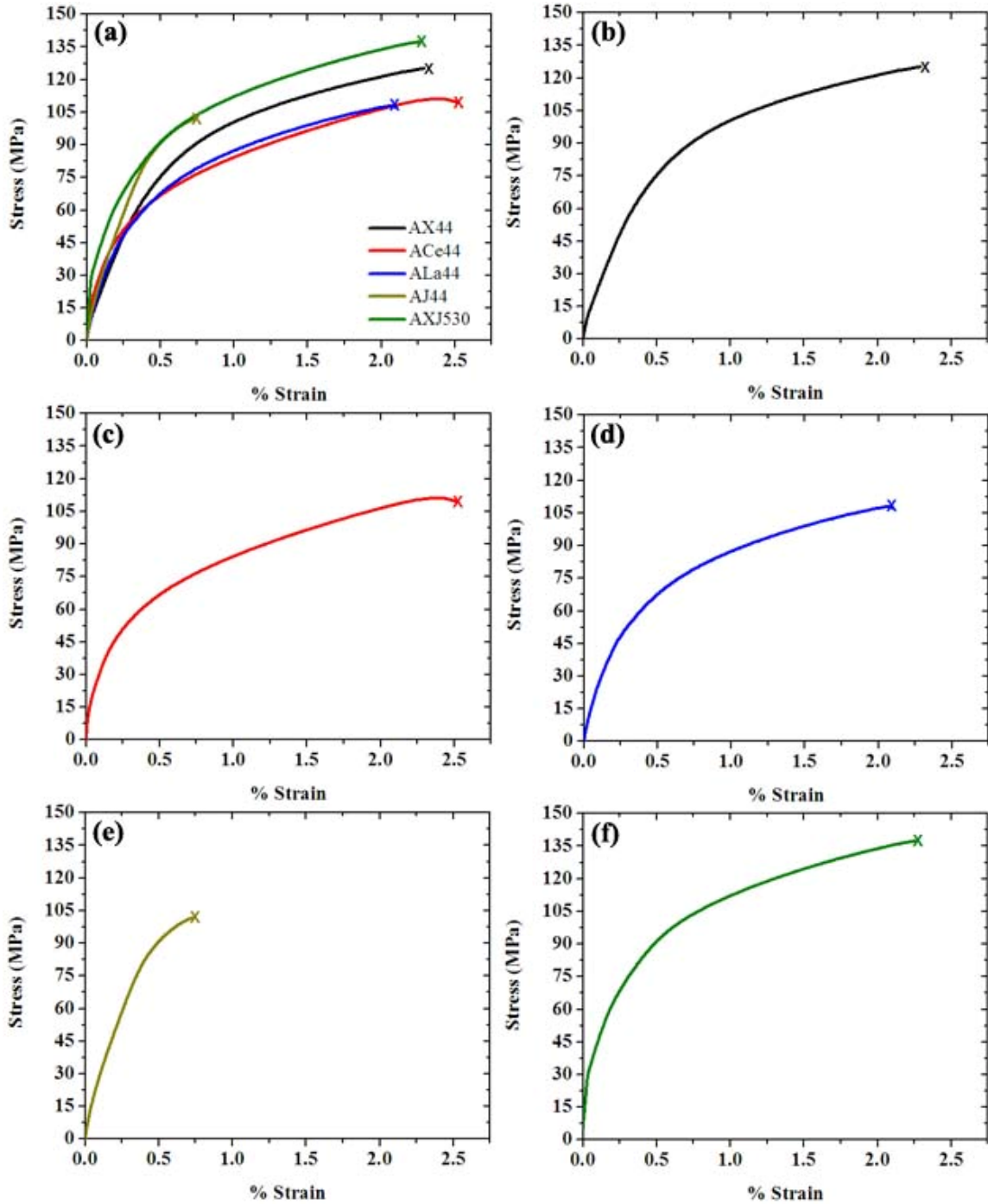
Figure 3.9 Room temperature tensile behavior of permanent mold cast alloys for (a) all alloys (b) AX44 (c) ACe44 (d) ALa44 (e) AJ44 and (f) AXJ530. Results are average of two tensile tests at a strain rate of 10-4 s-1.

3.6.2   Creep Testing

3.6.2.1   Equipment and Calibration

Creep tests were conducted with four Arc-weld constant load creep frames. A schematic of the creep load train is shown in Figure 3.10. The creep frames utilized a 20:1 lever ratio in loading the samples. The tests were conducted according to ASTM standard E319-00. The weights used for application of the load were calibrated to +/- 0.0005 kg (0.001 lbs) prior to the start of this investigation. The lever ratio of the creep frames was adjusted as close (+/- .5 mm (1/64")) to 20:1 as possible using a machinists rule. A counter balance weight at the forward section of the lever arm was used to adjust for variation in load arising from the extensometry, grips, and test sample. For consistency, specific extensometers and grips were then exclusively used with a corresponding creep frame.
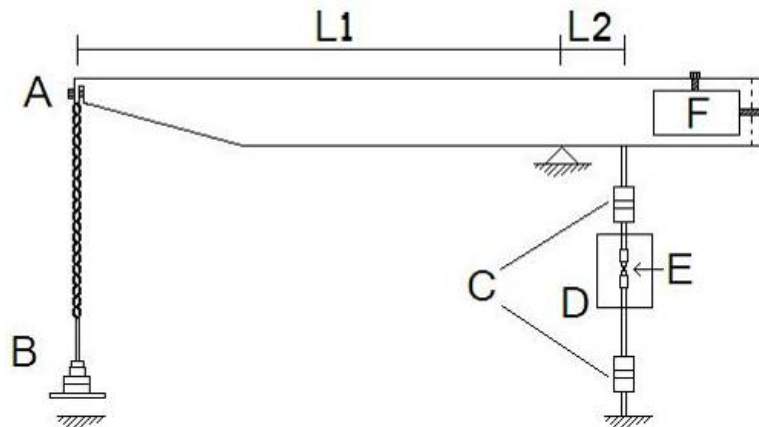
Figure 3.10 Load train and relating components. A) Set screw for minor adjustments of lever ratio B) Load tray with weights C) Universal joints for minor misalignments in specimen and grips D) Clam-shell style tube furnace E) Creep specimen and F) Counter balance. Note lever ratio of creep frame is fixed and computed from L1/L2 (20:1).

Each creep frame was calibrated prior to use with a calibrated load cell. The weights were incrementally added to the load tray of the creep frame and the load cell was positioned in place of the creep specimen. The load was incrementally stepped (0-72.6 kg (0-160 lbs)) across the entire operable range of the load cell (0-1451.5 kg (0-3200 lbs)) in five pound increments over a time period of approximately thirty minutes. The output voltage was measured during loading and unloading to ensure consistent in the

results. A typical calibration curve is shown in Figure 3.11 and the calculated lever ratios for each creep frame are given in Table 3.4.
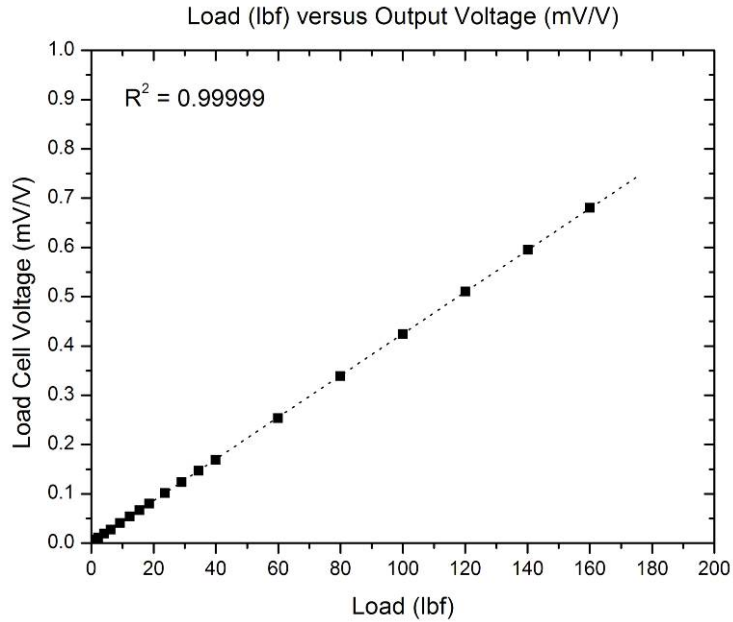
Figure 3.11 Example (Frame 1) of a load cell calibration curve measured against applied load.

Table 3.4 Calculated lever ratios for creep frames from load cell calibration.

Creep Frame	Calculated Lever Ratio
1	20.08
2	20.10
3	20.26
4	20.05

Super linear variable capacitance (SLVC) transducers were used to measure creep displacements. The signal from the SLVC was converted to voltage (0-10 V) through a signal conditioner prior to data acquisition and subsequent strain calculations. Each SLVC was always connected to the same signal conditioner to ensure consistency between tests. The SLVCs were calibrated on an annual schedule using a Mitutoyo® dial indicator fixtured in a jig with a dial gage. The dial was incremented 0.127 mm (0.005 in) through the entire range of the SLVC 6.35 mm (0.25 in) and the resulting voltage was recorded for each step. The SLVCs have a linear displacement to voltage output. The correlation coefficient (R^2) for all the SLVCs was calculated as 0.999995 or better and an example of a calibration curve is shown in Figure 3.12. The SLVCs maintained the same calibration over the three year of creep testing. The SLVCs are capable of accurately

measuring displacements corresponding to 0.001 V or 0.00254 mm (0.0001 in). For the gage length 31.75 mm (1.25 in.) of the specimens used in this study a strain resolution of 0.0008 or 0.08% was thus possible. It should also be noted that since the SLVCs were only linear over 6.35 mm (0.25") they were only capable of measuring creep strains up to 20% in these samples. The maximum strain accumulated in any sample was less than 14%.

<figure>
SLVC Calibration Curve

$R^2=1$

Position (in.) vs Voltage (V)
</figure>
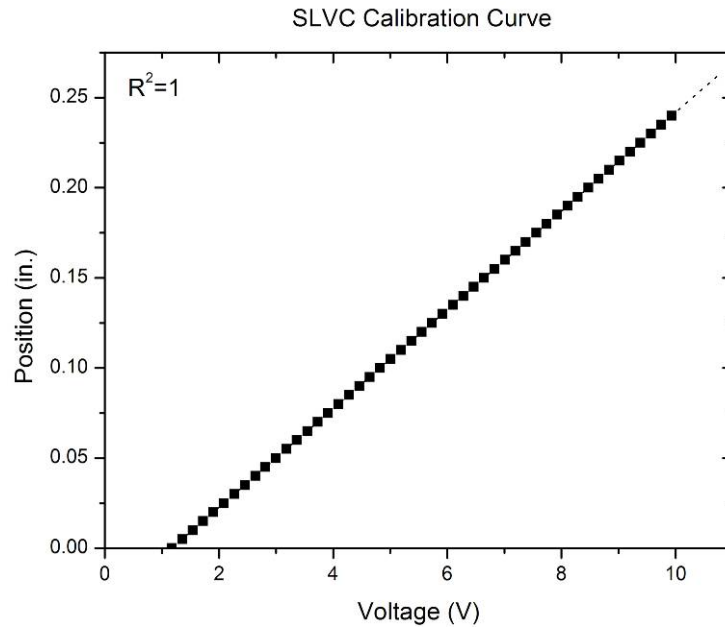
Figure 3.12 SLVC (Channel 7 L1-12-166) calibration curve showing linear output voltage against indexed position.

3.6.2.2   Creep Testing Parameters

Creep testing was conducted between temperatures of 100 °C and 175 °C and stresses of 40 to 100 MPa. Creep strain was measured via extensometry with two attached SLVCs. The extensometry attached to the machined grooves on the specimen shoulders directly above and beneath the sample gage. An example of a loaded creep specimen, prior to installing in the furnace and creep frame is shown in Figure 3.13.

In reporting creep strain a single SLVC channel was used when the two channels did not deviate. If there was minor deviation the channels were averaged post testing through a data analysis algorithm. In the very few cases where there was significant difference between each channel, SLVCs were spot calibrated and if both performed according to their calibration, the creep test was considered invalid and a new test was

performed for a complementary sample. The latter rarely occurred and resulted from improper seating of the knife edges or mechanical problems with the extensometer shaft sticking during creep.
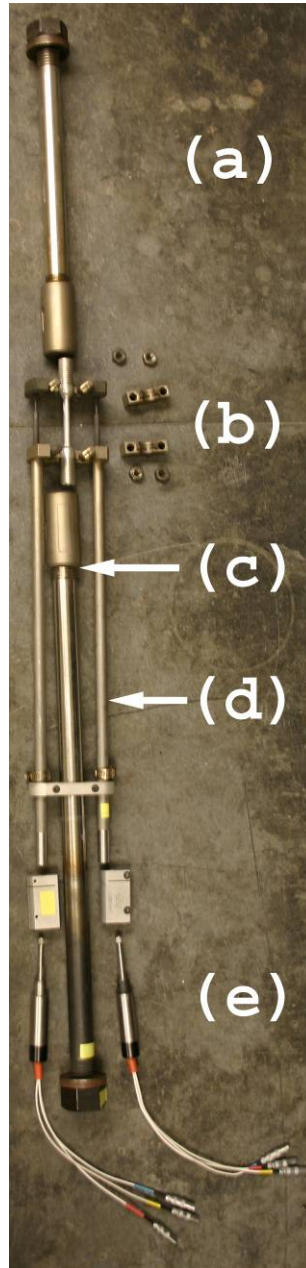
Figure 3.13 Assembled creep extensometry showing (a) upper grip (b) specimen (c) lower grip (d) extensometry (e) SLVC.

The data acquisition system for creep data collection used a National Instruments data acquisition system with in house written Labview software®. Time, temperature and each SLVCs displacement voltage were displayed on screen and updated every 500

ms. These values were recorded to file every 4 seconds. In data analysis, the data is first read into the program (time, voltage SLVC A, voltage SLVC B, and temperature). The user specifies values: time to load specimen at start of test, number of point to average across (using a central moving average), number of points to use in calculating a creep rate (using a simple linear regression). The time required to load the specimen at the start of the test is used to determine loading strain segment of the data recorded. The loading strain, or strain accumulated during the loading of the sample was removed from further analysis and written to a file for future reference. Thus the strains reported in this study are creep strains.

Creep rates were calculated using a simple linear regression moving-fit routine. Instead of averaging across the creep strain, a strain rate was calculated by making a linear least square fit through the user-specified number of points (typically 200). The strain rate routine used the already averaged creep strain data since it represented the creep behavior and provided a smoothed data output for strain rate. This point is important since in fitting a line through X number of already averaged data points provided the operator with the ability to over analyze the data through data smoothing, ultimately resulting in significant shifts of the creep strain rate curve. To combat this possible error the operator had to first choose appropriate averaging and linear fit windows and then check to ensure that the analysis was representative of the raw data (not shifted from over-averaging and linear fitting). Generally, in cases where the data set was very small or large (<20 hours or >1000 hrs, respectively) each set of raw creep data was processed in two steps of the routine twice. The first step averaged and smoothed the creep strain curve. The raw data was then processed again on the second step to smooth the creep rate. This was completed by selecting first a large (120-300 pts) averaging window and smaller creep rate liner fit window (<100 pts). The second iteration would be used to do less averaging of the raw data (window <30 pts) but a large window for the liner fit (200-400 pts). Data in question was always checked against the raw data to ensure that the curves represented the data without shifting and only smoothing.

3.6.3 Measurement of Local Creep Strain Accumulation by Strain Mapping

A strain mapping technique developed by Biery et al. [22, 23] was used to measure creep strain distributions at the microstructural length scale. The technique uses a periodic array of markers, produced by vapor deposition, Figure 3.14, which are imaged by scanning electron microscopy at selected intervals during creep to allow the determination of the 2D displacement field resulting from creep. Differentiation of the displacement field yields development of the 2D strain field, which can be compared spatially with microstructural features (e.g. grain size and cell size).
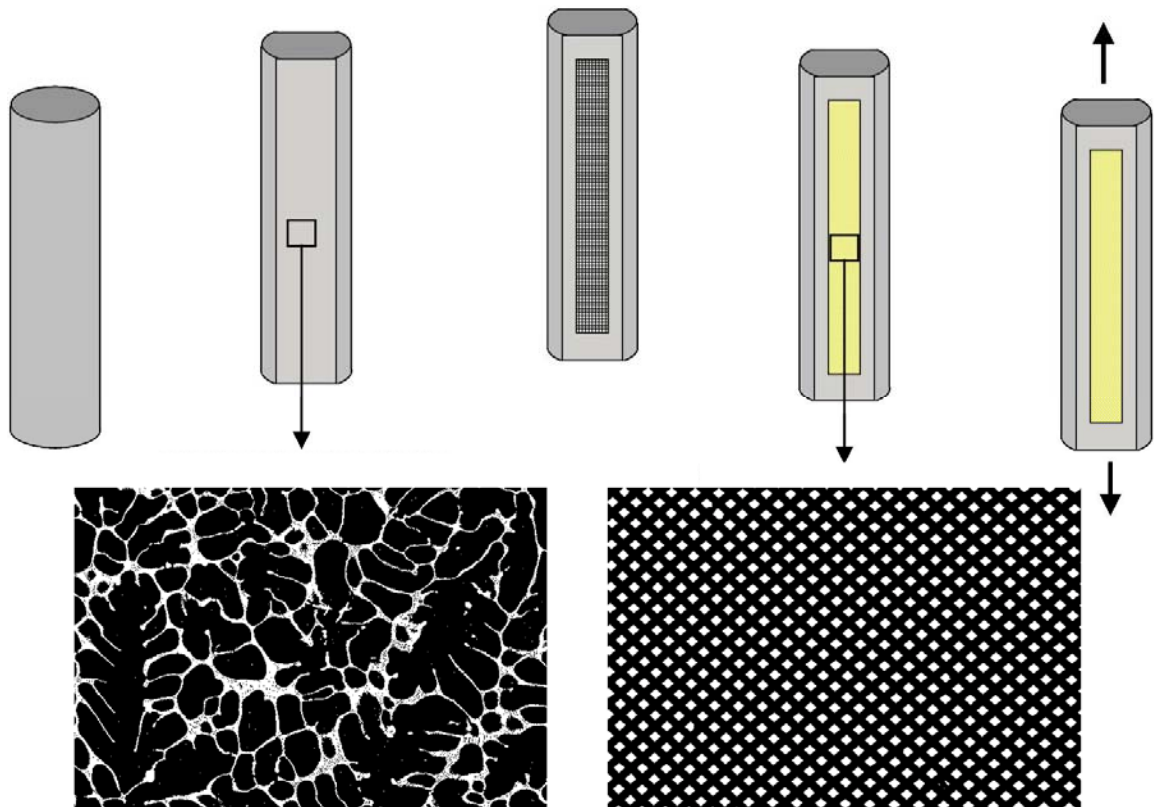
Figure 3.14 Schematic representation of the series of steps in calculating a strain distribution on the microstructural scale for a sample. The gray cylindrical tube represents the gage of the same and the steps progress from left to right.

A creep sample with machined flats is metallographically prepared to reveal microstructure and the region of interest is masked using a fine nickel mesh. Markers are created with the vapor deposition of gold through the nickel mesh. The mesh is removed

after deposition, producing a periodic array of markers on the surface of the specimen. A schematic detailing deposited markers and their respective spacing is shown in Figure 3.15.
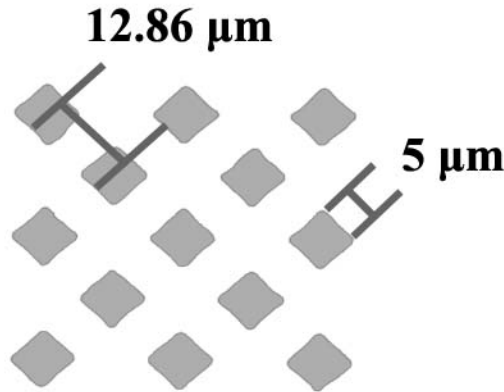
Figure 3.15 Schematic of the deposited markers with size and spacing information.

The nickel mesh, in this study has 2000 lines per inch (5 μm squares with 12.86 μm between markers, center to center measured tangentially). Two methods were used for preparing the mask from the nickel grid. Both methods yielded similar results, but the latter was more consistent. The first method was to cut, with a razor, a section from the bulk sheet that was slightly smaller than the area of the gage. This section was then secured with adhesive electrical tape at each end and rolled flat using a cotton swab and ethanol. The ethanol aided in adhering the grid to the sample surface prior to taping. This technique was that it led to cotton fibers and debris being trapped in some of the holes of the mesh and often resulted in torn edges of the grid and folded regions where the grid was constrained by the tape. These limitations produced some regions with markers that were of insufficient quality to use in subsequent analyses.

An improved method used femtosecond laser to remove a section of grid from the bulk grid. A larger section of the grid was mechanically removed from the bulk and carefully taped to a glass slide. The section of interest was cut by making ten passes at a velocity of 2 cm/s and a power of 220 mW. The grids sectioned in this manner could then be adhered to the sample without using tape. Ethanol was used to float them on the surface of the gage and a neoprene tube was used to roll them flat. Once the sample was positioned, the edges were gently held down to prevent bowing while the ethanol evaporated. This technique allowed the grids to be positioned accurately with no folds,

limited dirt and debris in the grid area and greatly improved the quality of the vapor deposited markers.

After the gold markers had been vapor deposited on the sample the same regions imaged prior to deposition were again imaged to record the non-deformed state of the markers. Care was taken to return to the same regions where the microstructure was previously imaged. This provided a microstructure image and an image of the grids before creep deformation. It was quite difficult to consistently return to the same region on a microstructural level. However, features such as porosity, scratches and uniquely shaped microstructural features aided this process.

Once the sample was imaged, it was loaded into a creep frame, thermally stabilized and crept. At periodic strains (i.e. change of creep stage - primary to secondary, 1% creep strain, minimum creep rate, or specific amount of accumulated strain) the sample was removed from the creep frame and the same regions previously imaged for microstructure and non-deformed girds were again re-imaged. These image pairs of non-deformed and deformed markers were used to calculate displacements and strain distributions. The technique was repeated for the same samples for increasingly higher levels of strain.

The algorithms used to calculate the relative marker displacements and strain distribution consisted of the following steps. First the two images, non-deformed and deformed, are loaded into the program. These two images are used to determine the average shape of the markers. Once the markers have been defined, the program assigns a single pixel point to each marker and stores this data as an array for each image. The algorithm then has the user select a reference marker (the same marker in each image). This marker is used as the starting point to index through the array of pixels that represent each marker. At each pixel the algorithm determines the amount of displacement the pixel has experienced relative to the same marker in the non-deformed image. Once the displacements for each matched marker are determined, strain is calculated and then 2D Von Mises strain using Equation 3.1. Note that out of plane strain ($\varepsilon_{zz}, \varepsilon_{zy}, \varepsilon_{zx}$) are assumed equal to zero. The calculations provide a strain distribution across the region of interest. This strain distribution is then overlaid on the microstructure and microstructural features, if any, can be identified that are influencing the creep strain behavior.

$$\varepsilon_{eff} = \sqrt{\frac{2}{9}\left(\varepsilon_{xx}^{2} + \varepsilon_{yy}^{2} + \left(\varepsilon_{xx} - \varepsilon_{yy}\right)^{2} + 6\varepsilon_{xy}^{2}\right)}$$ Equation 3.1

This technique was developed and implemented at Carnegie-Mellon and was applied to γ-titanium aluminides [22, 23], where it was shown to be capable of accurately measuring strains on the scale of the microstructure (tens of micrometers). This experimental technique was later used to study polycrystalline B2 RuAl [184], where it was reported that bulk strain measurements, from extensometry, agreed well with averaged strain mapping measurements made at the surface of the sample. This is one indicator that the strain mapping technique is not just measuring surface strains, but rather making fairly accurate measurements of strain that would be fairly representative in the bulk.

3.7   Measurement of Elemental Segregation by Scheil Analysis

To quantify the segregation behavior, degree of solution strengthening, and the solidification characteristics of the alloying additions, the element distributions on the microstructural level were quantified in as-cast material. Micro-segregation was analyzed with an electron micro-probe analyzer (EPMA) combined with a Scheil type analysis [18-20, 185]. The micro-segregation analysis, coupled with analysis of solid solution strengthening was used to assess the influence of the alloying additions on the magnesium solidification and creep behavior.

Sample preparation for the EPMA was the same as that for microstructural analysis. Colloidal graphite was lightly applied to the metallographic side of the epoxy mount. The most consistent compositional data was collected when the surface was un-etched, polished only with a diamond paste (0.05 μm), and had a high mirror like luster when inserted into the EPMA. A moderate to heavy pressure was used to achieve this finish in polishing.

A representative region of the microstructure was selected and an array of points was overlaid on top of the microstructure, a schematic of the microstructure and scan points may be seen in Figure 3.16. The EPMA gathered compositional data at each of the points in the array. In this study the array was large enough to include a region of 450 x 450 μm, representative of at least one grain (to fully represent the solidification

sequence). The array was standardized between samples to be a square of 30 x 30 points, with 15 μm between each point. At least two complete arrays were collected from each sample. The first array was taken near the edge of the sample and the second array was taken near the center of the gage of the sample.   These arrays were compared to ensure that there was no measurable difference in composition between different regions in the same sample. In all cases it was found that the scans contained the same representative data, and were therefore combined into one data set to provide a more detailed data set for analysis.
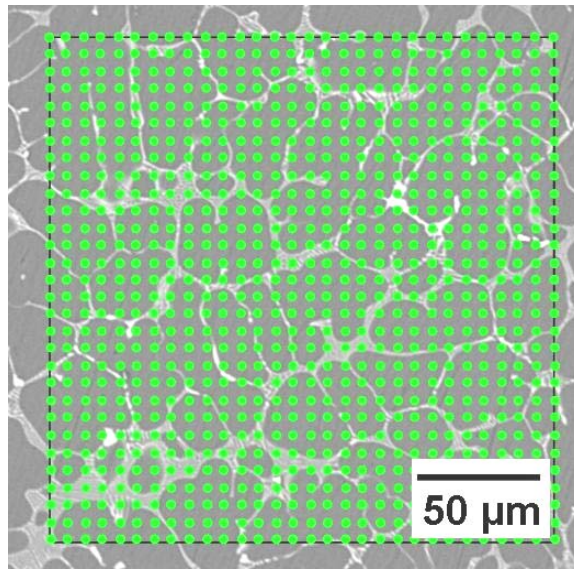
Figure 3.16 Example of the array of points, overlaid on microstructure, prior to compositional analysis. Note this array is not the same dimensions (30 by 30 with a step size of 15 μm) as those used in actual studies.

The compositional data was filtered to remove any points that were out of the compositional window of 99-101 total weight percent. Points that were outside of this window are most likely due to oxides or films that formed on the surface of the sample from preparation and handling, porosity (where beam interaction was uniquely reflected to the detectors), topography on the surface of the sample, or occasional inclusions.

The compositional dataset was then sorted from highest to lowest composition with respect to the major element in the primary phase (i.e. with respect to magnesium). The ordering represents the solidification sequence, in the sense that magnesium was the primary phase that first began to freeze during solidification. The first magnesium to

freeze would contain the least solute in solution according to the binary or higher order phase diagrams. In this study, the ternary additions were left associated to their respective magnesium composition. For example, if a single point had 98.5 wt % Mg, 1.4 wt% Al and 0.1 wt% Ca, the column containing magnesium was sorted, the Al and Ca (1.4 and 0.1 wt%, respectively) remained linked to the magnesium composition.

Next the total number of points was determined and an apparent fraction solid was calculated. Therefore if 800 points remained after filtering non-representative points from the data set, the first point was then assigned an apparent fraction solid of 1/800 or .125 % f_s. Each subsequent point was indexed (i.e. 2/800, 3/800...), representing incremental steps during solidification. An example of several data points, prior to sorting and sorted, with calculated volume fractions, is shown in Table 3.5.

Table 3.5 Example of raw data, as collected from EPMA, and an analyzed data set (wt%).

| Data Point | Raw Data | | | | | Analyzed Data | | | | |
	Mg	Al	Ca	Total		Apparent Fraction Solid		Mg	Al	Ca	Total
1	92.4	5.1	1.7	99.3		1/899	0.0011	96.9	2.3	0.1	99.4
2	94.0	3.9	0.7	98.8		2/899	0.0022	96.8	2.1	0.1	99.1
3	96.9	2.3	0.1	99.4		3/899	0.0033	96.6	2.1	0.1	99.0
4	96.8	2.1	0.1	99.1		4/899	0.0044	96.5	2.3	0.1	99.0
.	.	.	.	.		.	.	.	.	.	.
.	.	.	.	.		.	.	.	.	.	.
.	.	.	.	.		.	.	.	.	.	.
896	96.0	2.6	0.2	98.9		896/899	0.9967	96.0	2.6	0.2	98.9
897	70.6	15.5	13.6	99.9		897/899	0.9978	94.0	3.9	0.7	98.8
898	96.6	2.1	0.1	99.0		898/899	0.9989	92.4	5.1	1.7	99.3
899	96.5	2.3	0.1	99.0		899/899	1.0000	70.6	15.5	13.6	99.9

This set of data was then plotted, Figure 3.17, and could representatively be compared among the different alloy systems studied. Along with qualitative comparisons, the solidification behavior of each alloy could be modeled using the Scheil equation [186] Equation 3.2a/b or the modified Scheil equation [187], Equation 3.3. C_s is the composition of the solid, the C_L is the composition of the liquid, C_o is the bulk composition, f_s is the fraction solid, and k is the distribution or partition coefficient. The α term in the modified Scheil equations is the Fourier number and is defined in Equation 3.4. The terms in the Fourier number are D, diffusivity of the solute, t for time, and L for

length scale of the back diffusion. The Scheil equation assumes that there is negligible diffusivity in the solid or back diffusion, that the liquid remains homogenous and that the solid-liquid interface is in equilibrium. The modified Scheil equation accounts for back diffusion of solute through the incorporation of the Fourier term. Through curve fitting, partition coefficients are calculated using the compositional variation of each elemental addition. These partition coefficients can be compared for each element in each alloy system and are valuable for determining the effect of segregation on the solidification behavior. The change in solute distribution after thermal ageing and creep of the specimens was assessed using this EPMA segregation technique.
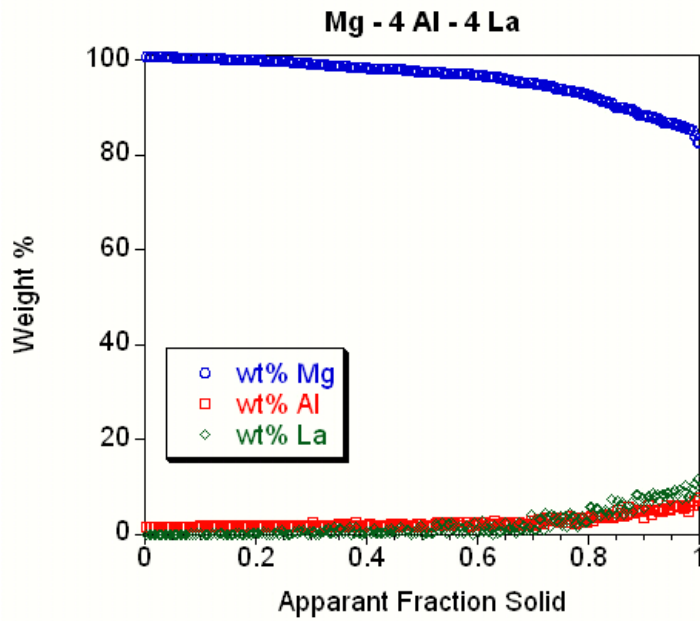
Figure 3.17 Analyzed compositional data plotted prior to Scheil curve fitting.

$$C_s = kC_o(1 - f_s)^{k-1}$$
Equation 3.2a

$$C_l = C_o(1 - f_s)^{k-1}$$
Equation 3.2b

$$C_s = kC_o(1 - (1 - 2\alpha k)f_s)^{\frac{k-1}{1-2\alpha k}}$$
Equation 3.3

$$\alpha = \frac{Dt}{L^2}$$
Equation 3.4

The compositions were measured using a Cameca SX100 electron micro-probe analyzer (EPMA). The accelerating voltage and beam current were operated at 20 kV and 15 nA, respectively. The crystal spectrometers used to gather the X-ray spectra are listed in Table 3.6. Element, spectrometer crystal, characteristic x-ray line and standard used for calibration are listed in Table 3.7. Beam alignment was completed using Benitoite and spectrometer alignment with Androdite. The electron interaction volume of the beam with the sample is reported to be 1-3 μm [188]. Calibration of the instrument was verified against known elements, alloys, and minerals. Step size and count time was dependent on microstructural features that were investigated.

Table 3.6 Crystal Spectrometers abbreviations and chemical names.

Crystal Abbreviation	Crystal Chemical Name
TAP	Thallium acid phthalate
PET	Pentaerythritol
LIF	Lithium Fluoride

Table 3.7 Element, spectrometer crystal, xray radiation line and material used for calibration in EPMA investigations.

Element	Crystal	Line	Calibration Standard
Mg	TAP	Kα	Mg-4Al Homogonized
Al	TAP	Kα	Al 100%
Ca	PET	Kα	Wollastonite
Ce	LIF	Lα	Phosphate Monzite
La	LIF	Lα	Phosphate Monzite
Sr	PET	Kα	Celestite

The EPMA compositions were used to quantify the degree of solid solution strengthening of these alloys. Two representative concentrations were determined: the average concentration of Al in solution of the α-Mg phase and the maximum concentration of Al measured at the near grain boundary region. The average concentration was determined by averaging the Al wt% of the EPMA measurements across the apparent fraction solid α-Mg. The maximum concentration of Al was determined by averaging twenty data points at the near grain boundary region to

minimize the effect of scatter in the EPMA data. Equation 2.7 was used only considering the term mB_nc^n (for solid solution strengthening of Al in the Mg matrix).   As previously described the term c represents the concentration (in atomic percent) of aluminum in solution.   The ternary additions were not included as solid solution strengtheners due to their limited solubility in the α-Mg

Chapter 4

Solidification, Permanent Mold Casting, and Microstructure

This chapter describes the solidification analysis, permanent mold casting, and microstructure of the series of five magnesium alloys (Mg-4Al-4X: (Ca, Ce, La, and Sr) and AXJ530). The chapter is divided into the following five main sections: solidification analysis, permanent mold casting results, microstructure, segregation analysis and summary.

4.1   Solidification Analysis

The cooling curve for each alloy and its first derivative (dT/dt) is shown in Figure 4.1. The black arrows denote the approximate start and end of solidification as determined from the temperatures at transitions from linearity in the first derivative. The results are tabulated in Table 4.1. The calcium containing alloys have the largest freezing range, followed by the strontium, and then the rare earth containing alloys, for the cooling rates in this study (~0.5-1 °C/s). These reported temperatures are accurate to +/- 2 °C, accounting for the errors from calibration, data collection, and analysis.

Several other solidification events were detected between the liquidus and solidus temperatures. Though these events were not characterized in this study, they are representative of different reactions (i.e. phase transformations) occurring during solidification. An example of one of these events is shown in Figure 4.1f, where the solidification path of the Mg-Al-Ca alloy is known to follow the reactions of L $\rightarrow$ α-Mg + L $\rightarrow$ α-Mg + C36 + L $\rightarrow$ α-Mg + C36 + C14 + L [51].

The liquidus and solidus temperatures and freezing ranges provide important insight on process design for permanent mold casting of these alloys. The liquidus temperatures of the alloys are similar (629 to 606 °C), but the freezing ranges vary significantly (24 to 100 °C) among the experimental alloys. Alloys with a narrow freezing range were difficult to cast and this is further discussed in subsequent sections.

Table 4.1 Liquidus, solidus and freezing ranges measured from solidification analysis.

Alloy	Liquidus (°C)	Solidus (°C)	Freezing Range (°C)
AX44	609	509	100
ACe44	629	605	24
ALa44	629	604	25
AJ44	615	550	65
AXJ530	606	509	97
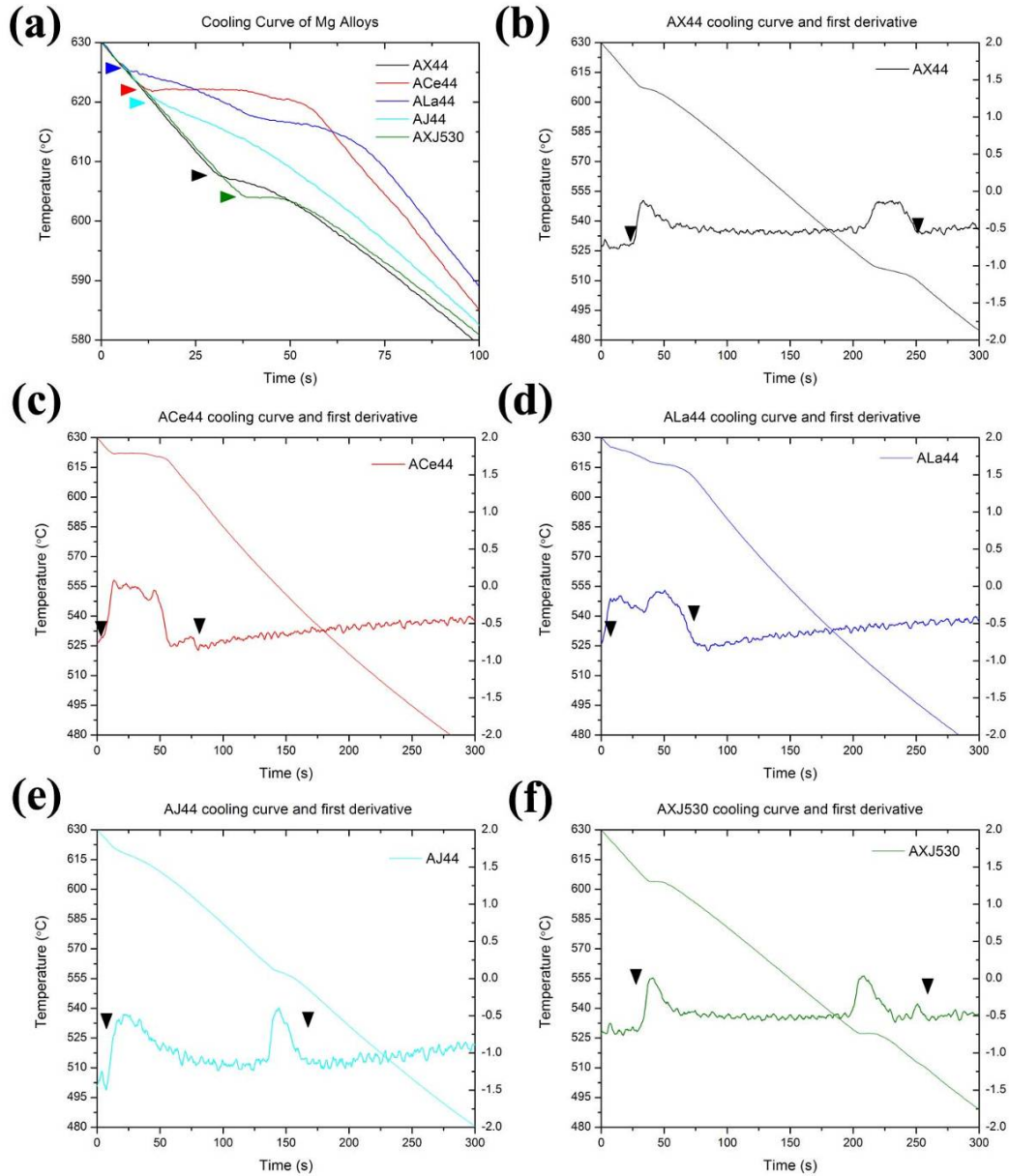
Figure 4.1 Cooling curves and first derivatives for (a) combined alloys highlighting onset of solidification (b) AX44 (c) ACe44 (d) ALa44 (e) AJ44 and (f) AXJ530. Arrows indicate the approximate start and end of the recorded solidification events.

4.2   Permanent Mold Castings

Representative permanent mold castings produced in this study are shown in Figure 4.2.   All alloys were successfully permanent mold cast using the parameters described in section 3.3. Visual examination shows that the AX44 (a) and AXJ530 (e) each have an excellent surface finish, while the AJ44 (d) has a good surface finish, with minor surface oxidation.   However the ACe44 (b) and ALa44 (c) alloys exhibited significant surface oxidation. During ladling the ACe44 and ALa44 melts each rapidly blackened on the liquid surface before being poured into the mold.
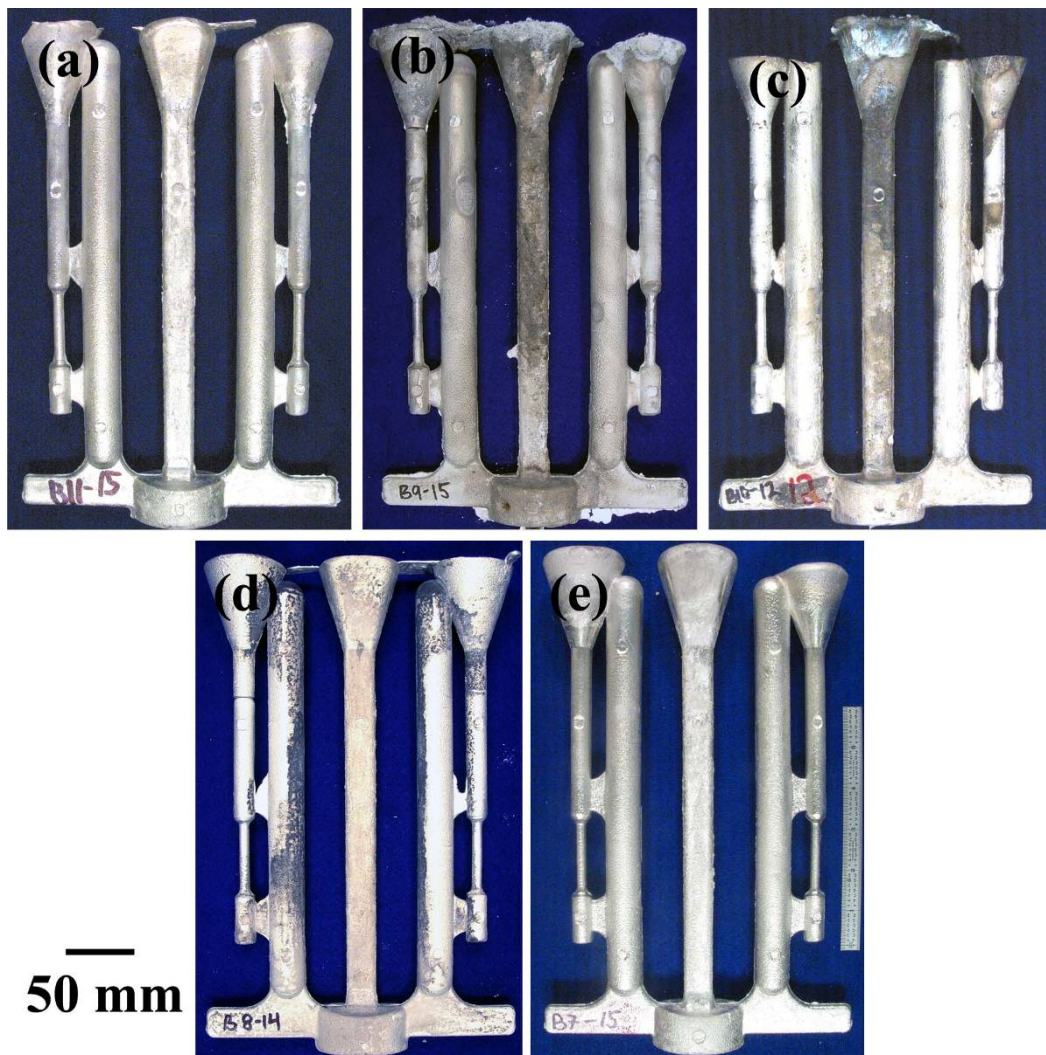
Figure 4.2 As-cast macro images of the permanent mold cast alloys. (a) AX44 casting 15 (b) ACe44 casting 15 (c) ALa44 casting 12 (d) AJ44 casting 14 and (e) AXJ530 casting 15. Note the differences in surface finish and in mold filling (partially frozen gates) between each cast alloy.

Although all alloys were cast with a method to achieve near-complete mold filling, some pours resulted in incompletely filled castings. This was more often the case for the ACe44 and ALa44 alloys. This is clearly seen in Figure 4.2 by comparing the casting gates at the tensile specimen. In the AX44 and AXJ530 alloys the gates were completely filled. In the AJ44 castings the gates were partially frozen off but still had complete lower gates and good material flow where the gate did not freeze off. In the ACe44 and ALa44 the gates are much less complete, though not as clear from the images. In these cases the alloy had the appearance of being semi-solid when it reached the gate. These cases always resulted in an incomplete fill of the mold and an unusable casting. These results are consistent with the thermal analysis results. ACe44 and ALa44 had narrow freezing ranges of 24 °C and 25 °C, respectively, and partial solidification during melt handling and pouring led to incomplete fills, freeze-offs and rougher surfaces.

4.2.1 Thermal measurements during Casting

During each alloy casting run the mold temperature increased by a similar degree for each pour as shown in Figure 4.3. Mold temperature increased at the onset of pouring and continued to increase until the mold was nearly full. At this time the temperature decreased somewhat during solidification and ejection. Since castings were poured in consecutive fashion, with approximately 60-120 seconds between pours, the mold halves did not have sufficient time to return to their initial start temperature of ~200 °C. This resulted in an increase in average mold temperature as the number of castings increased. A typical ΔT of 15-25 °C was recorded between the two mold halves, but this had no influence on the microstructure or defects within any of the alloys studied. The average mold temperature difference was caused by the method that the cover and ejector mold halves were attached to the hydraulic press.
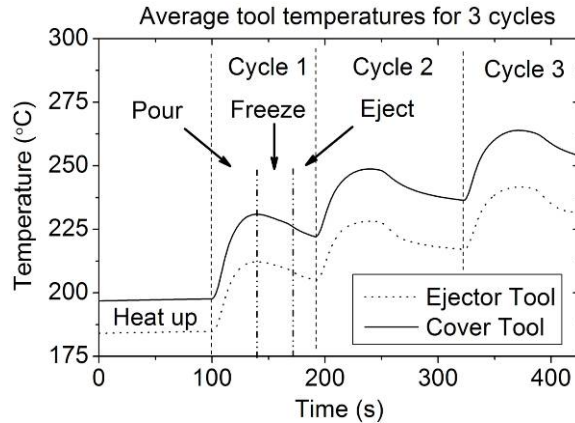
Figure 4.3 The average of the six thermocouples for each mold half against time during a casting campaign. Note the increase in mold temperature resulting from pouring the superheated metal into the mold.

Figure 4.4 shows the average temperature rise in each mold half during each casting run, which was calculated by averaging the temperature in each mold half across the entire cycle. This provided an individual temperature of the mold for reference in examining each casting. An increase in mold temperature over the entire casting campaign was observed with no steady-state or plateau temperature being reached. From the figure it appears that the rate of increase slows as the temperature nears 400 °C and it could be inferred that a steady state mold temperature would be reached between 400 °C and 500 °C. There is a notable down turn in temperature at cycles 8 and 9. This was caused by the time required to recoat the mold with boron nitride, which allowed the mold to cool prior to the subsequent cycle. A similar perturbation occurred for the same reasons between castings 18 and 19.
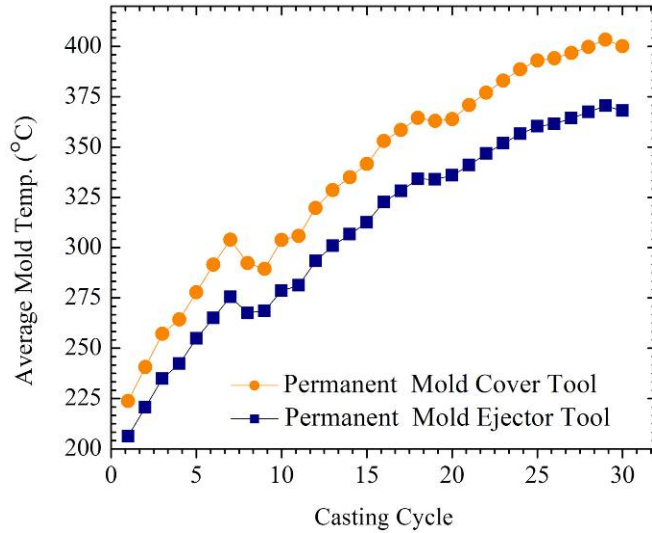
Figure 4.4 Average mold temperature as a function of casting cycle for a typical casting campaign. Shown here is the mold history for AXJ530. Note the large mold temperature difference of nearly 200 °C during the casting campaign.

4.2.2   Radiography

Radiographs of two castings of the AXJ530 campaign are shown in Figure 4.5. Porosity, inclusions, internal cracks and/or voids are not observed in the gage sections, which is typical of all castings that were radiographed. Inclusions that were observed in the casting were always located at the bottom of the down sprue, as shown in Figure 4.5. Porosity was mainly observed in the risers and occasionally in the specimen grips. Porosity, though not desirable, is common in permanent mold casting and, given the locations it occurred, is of no consequence to this study. In some castings cracking between the pour cup and down sprue was observed (Figure 4.5a). This is consistent with the high temperature gradient predicted for this location by the ProCast modeling. Internal cracking was most often seen between sections that rapidly changed from a large to narrow cross section (e.g. vents to risers, pour cup to down sprue).   No notable differences in the radiography results were observed as it related to cycle number (i.e. mold temperature).
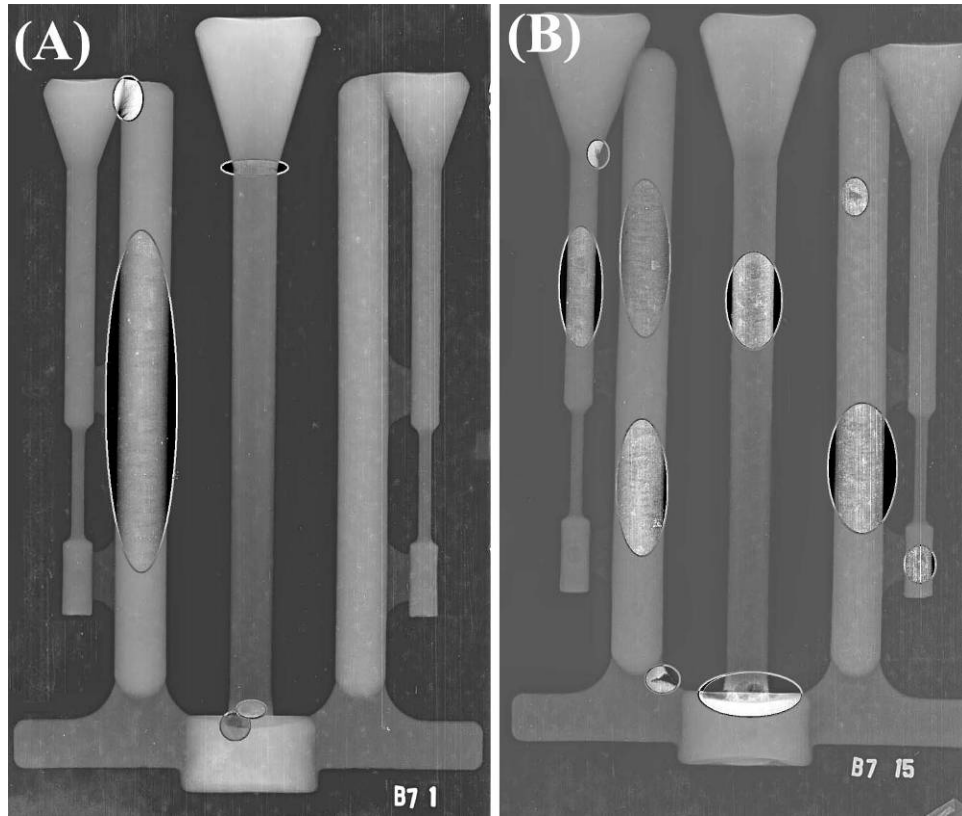
Figure 4.5 Radiography results for two casting from the AXJ530 campaign (A) casting 1 (B) casting 15. Highlighted regions were determined by analyzing the entire casting and then focusing on regions with notable characteristics.

4.2.3   Bulk Composition

Compositions for a number of different casting were determined by ICP to check for uniformity in composition during a casting run and are reported in Table 4.2. Composition was also measured at several locations across the gage of a selected sample to ensure that no macro-segregation occurred. There was no notable difference in composition between alloys that were cast early in a casting campaign or near the end.

Table 4.2 Composition (wt%) measured between cycles for each casting campaign.

Alloy	Cycle	Al	X	Sr	Mn	Fe	Cu	Ni	Mg
AX44	1	3.8	3.5	-	0.01	0.01	<0.003	<0.003	bal.
AX44	17	3.9	3.5	-	0.01	0.01	<0.003	<0.003	bal.
ACe44	16	3.9	4.2	-	0.02	0.02	<0.003	<0.003	bal.
ALa44	1	3.7	4.1	-	0.02	0.02	<0.003	<0.003	bal.
ALa44	17	3.6	4.2	-	0.02	0.02	<0.003	<0.003	bal.
AJ44	2	3.8	4.2	-	0.02	0.01	<0.003	<0.003	bal.
AJ44	17	3.7	4.3	-	0.02	0.01	<0.003	<0.003	bal.
AXJ530	1	5.3	2.6	0.17	0.29	0.004	0.004	0.003	bal.
AXJ530	15	5.1	2.5	0.16	0.31	0.004	0.004	0.003	bal.
AXJ530	22	5.3	2.6	0.17	0.30	0.004	0.004	0.003	bal.

4.2.4 Density Determination – Archimedes Method

The Archimedes method was used to measure density across a series of melt pours of a casting campaign in an effort to investigate variations in porosity arising from the processing technique. The results of the measured density of the gages of six samples from the casting campaign of AXJ530 are reported in Table 4.3. There is very little variation in the measurements for each cast gage section. The apparent density varies insignificantly indicating that there is little difference in porosity between the gage sections of the castings as it relates to when that sample was casting in a campaign. Therefore, mold temperature had no effect on the formation of porosity in this process.

Table 4.3 Apparent density determined using the Archimedes method for a series of casting cycles of AXJ530.

Pour	Mass (g) in 2-Propanol				Mass (g) in air				Apparent ρ
	1	2	3	$\bar{x}$	1	2	3	$\bar{x}$	
1	0.856	0.856	0.856	0.86	1.522	1.523	1.522	1.52	1.788
8	0.931	0.931	0.931	0.93	1.657	1.657	1.657	1.66	1.787
9	0.977	0.976	0.977	0.98	1.737	1.737	1.737	1.74	1.789
15	0.962	0.962	0.961	0.96	1.709	1.709	1.709	1.71	1.789
22	0.999	0.999	0.999	1.00	1.777	1.777	1.777	1.78	1.789
29	0.993	0.993	0.994	0.99	1.765	1.765	1.766	1.77	1.789
						Average Apparent Density			**1.789**

4.3   Microstructures of crucible cooled samples

The microstructures of the 30 g samples that had been thermally analyzed and then cast into a steel crucible are shown in Figure 4.6. In all alloys the microstructure consisted of an α-Mg solid solution primary phase, surrounded by a eutectic region of intermetallics and α-Mg. Qualitatively the volume fraction of primary α-Mg is greater in the AX44, AJ44, and AXJ530 compared to ACe44 and ALa44. There is also a slight difference in dendritic cell size. It is of interest that the ACe44 and ALa44 each exhibit a different eutectic morphology. The ACe44 has a very blocky intermetallic phase (bright contrast) with a small volume fraction of a needle/plate shaped phase. The ALa44 exhibits limited blocky phase and is almost exclusively a needle/plate shaped phase in the eutectic.
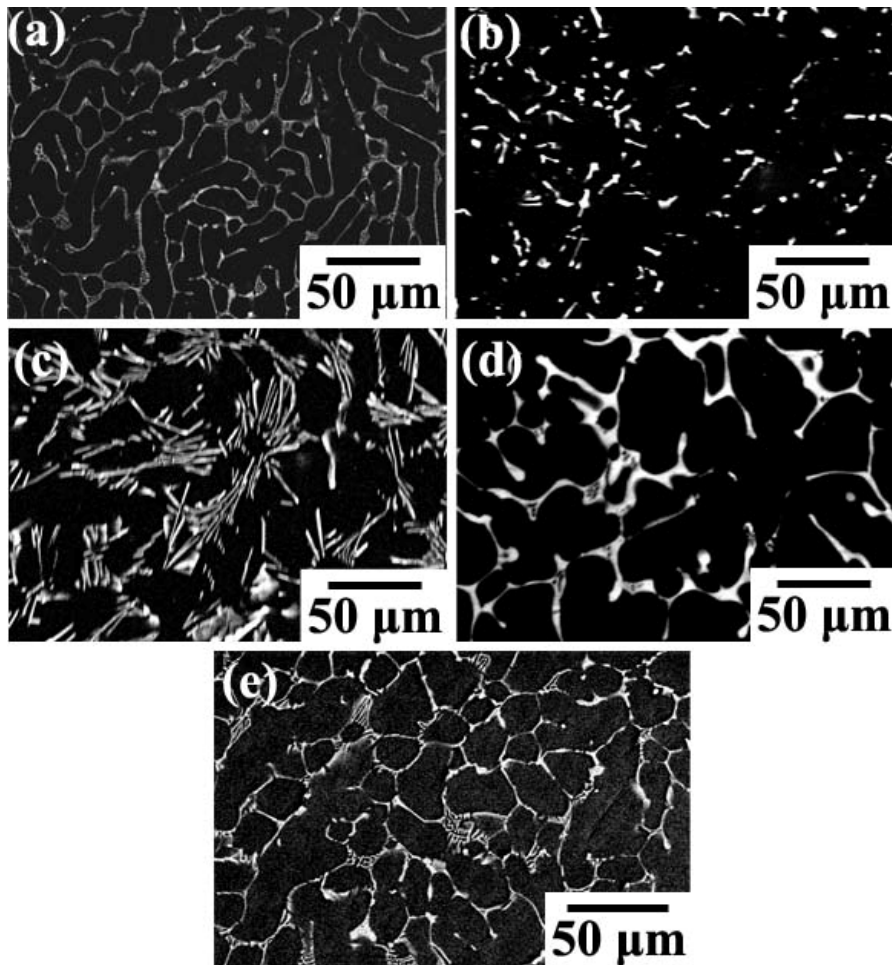
Figure 4.6 Microstructures of (a) AX44 (b) ACe44 (c) ALa44 (d) AJ44 and (e) AXJ530 from thermal analysis.

4.4 Permanent Mold Cast Microstructures

All permanent mold cast alloys, shown in Figure 4.7, exhibit an alpha magnesium primary phase, of dark contrast, surrounded by a eutectic region of magnesium and intermetallic(s), bright contrast. Note that there is difference in eutectic morphology of the rare earth containing alloys, specifically the ACe44. The alloys were examined in an as-cast, post crept, and aged (500 h at 175 °C) conditions. The microstructures reported are all from samples having the similar mold temperature during permanent mold casting of approximately 300 °C. An example of the complex interdendritic eutectic morphology (for AXJ530) is shown in Figure 4.8.

The cell size and area fraction of the primary α-Mg phase is reported in Table 4.4 and Table 4.5, respectively, for each alloy. Grain sizes were measured in the Sr and Ca containing alloys using both polarized light optical microscopy and EBSD. Results of the grain size measurements are shown in Table 4.6.
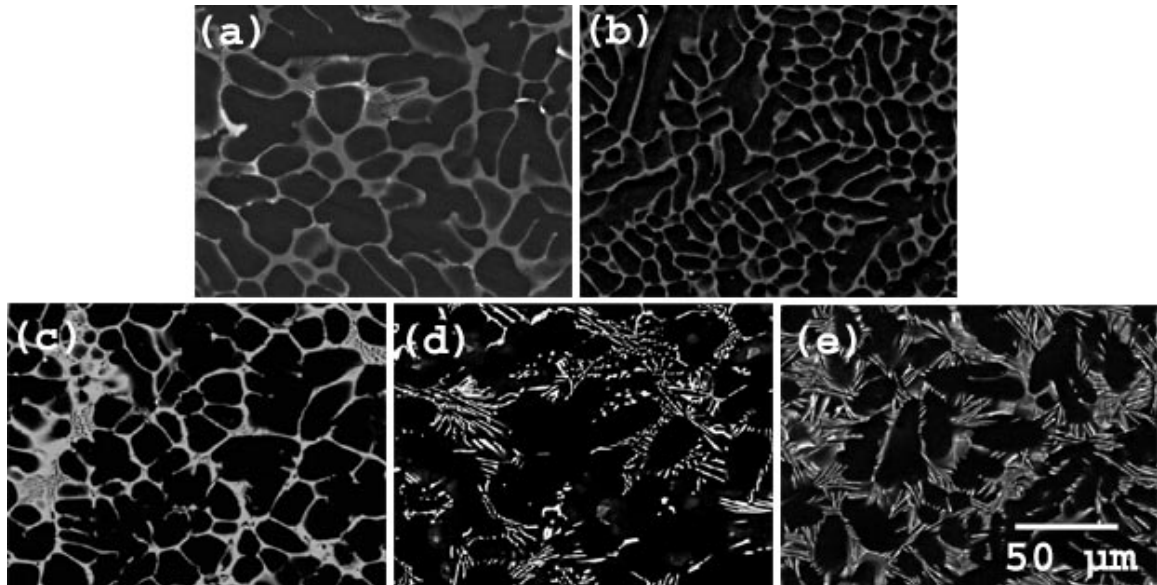
Figure 4.7 As-cast microstructure of permanent mold cast alloys. (a) AXJ530 (b) AX44 (c) AJ44 (d) ACe44 and (e) ALa44.
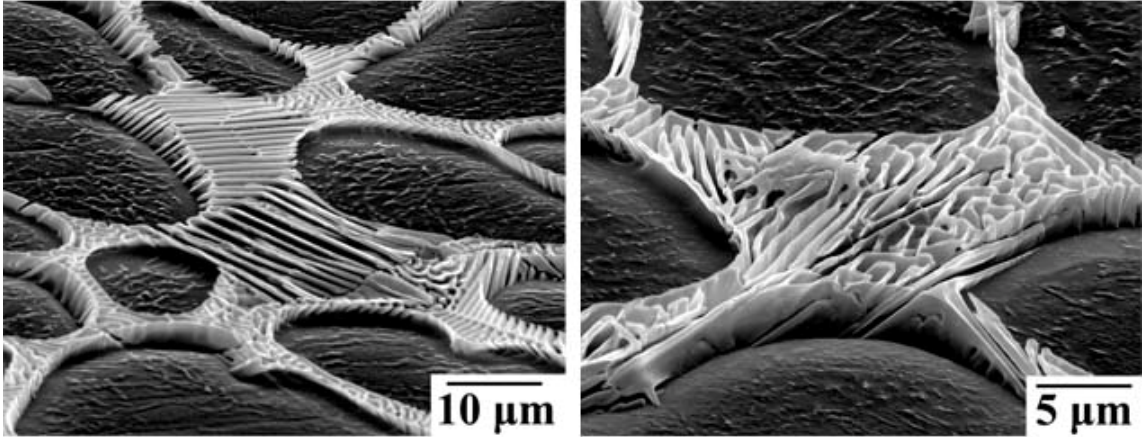
Figure 4.8 Detail of eutectic structure of permanent mold cast AXJ530 in deep etched condition.

Table 4.4 Area fraction (%) and standard deviations of α-Mg for permanent mold cast alloys in as-cast, aged, and crept conditions.   Area fraction of eutectic region represents balance.

Alloy	As-Cast	σ	Aged	σ	Crept	σ
AX44	79	1.2	84	1.3	83	2
ALa44	61	1.9	-	-	57	3.1
ACe44	63	3.3	-	-	62	1.3
AJ44	83	2.5	79	3	85	1.7
AXJ530	83	3.9	84	3.6	82	1.3

Table 4.5 Average cell size (μm) of α-Mg for permanent mold and standard deviations cast alloys in as-cast, aged, and crept conditions with first standard deviation (σ).

Alloy	As-Cast	σ	Aged	σ	Crept	σ
AX44	16	9	16	8	13	8
ACe44	22	16	-	-	20	14
ALa44	19	11	-	-	22	12
AJ44	21	14	19	10	21	13
AXJ530	17	10	17	10	20	12

Table 4.6 Average grain size (μm) measurements and standard deviations for selected permanent mold cast alloys in as-cast condition.

Alloy	Grain Size (μm)	σ
AX44	257	135
AJ44	127	47
AXJ530	148	38
DC - AXJ530	19	6

4.4.1   Microstructure Variation with Cooling Rate

The microstructure of the AXJ530 alloy was investigated at different cooling rates as shown in Figure 4.9. For the AXJ530, across the range of the cooling rates investigated (0.5-100 °C/s), the intermetallics that form have been identified [51, 138] with the major eutectic compound being the C36 phase along with a small amount of C14 (<< 1 volume %). The volume fraction of the primary phase is ~83 %. Thus the major influence of the cooling rate on AXJ530 is on the refinement of the grain and cell size and eutectic structure. The variation in microstructure was also investigated for different mold temperatures for the permanent mold cast alloys.
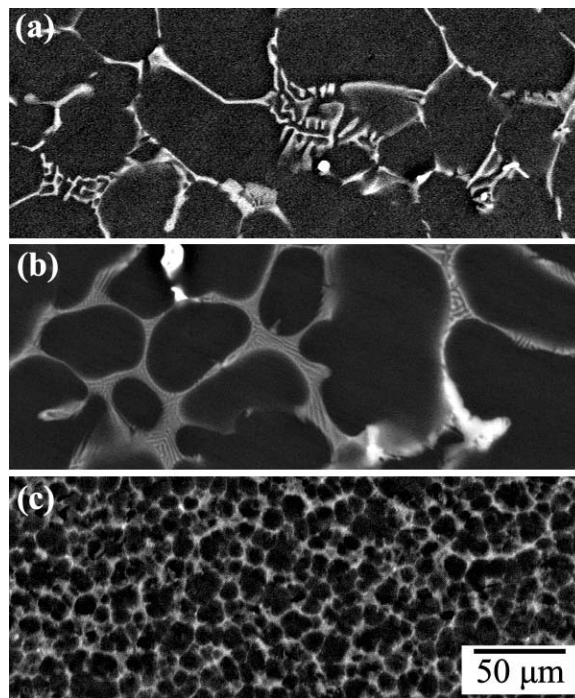
Figure 4.9 Microstructure comparison for AXJ530 solidified with a cooling rate at (a) low cooling rate (0.5 ºC/s) (b) permanent mold cast (~10 ºC/s) (c) die cast (~100 ºC/s).

The microstructure of three samples ($T_{mold} \approx$ 220, 320 and 360 °C) from the AXJ530 permanent mold casting run were investigated for variation in cell size, eutectic morphology, inclusions and micro-porosity as they relate to mold temperature. Figure 4.10 shows the microstructure for three gage regions at different cycles (i.e. mold temperatures) in a casting campaign. Little variation is observed between the samples with the only notable difference being a slightly finer cell size for the earlier casting (i.e.

when the mold was cooler). Eutectic and primary α-Mg morphologies appear the same. The cell sizes measured for castings from different mold temperatures are plotted in the histograms of Figure 4.11. Area fraction of primary α-Mg was also measured for the same samples and no detectable difference was observed.
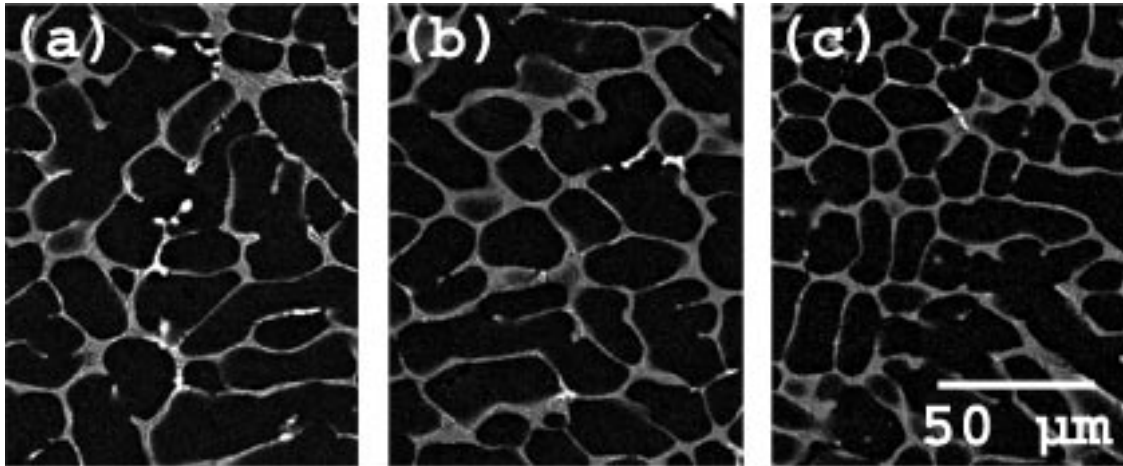
Figure 4.10 Microstructure of the gage for permanent mold casting campaign of the AXJ530 alloy at mold temperatures of (a) 220 °C (b) 320 °C and (c) 360 °C.
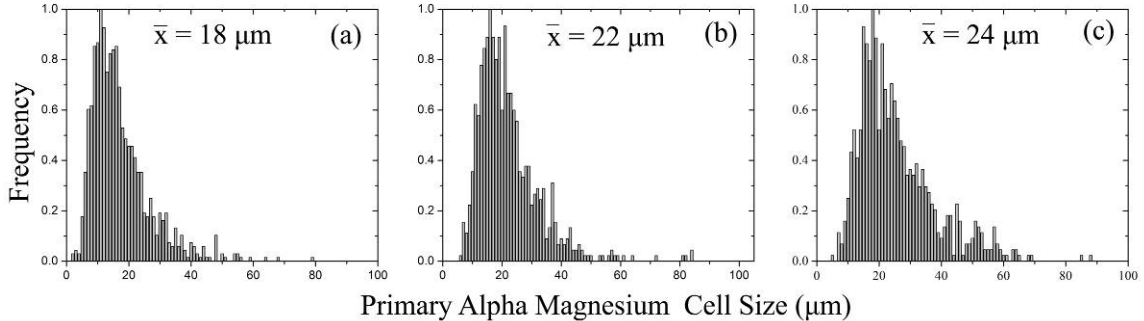
Figure 4.11 Measured primary alpha magnesium cell size distribution across three gage regions of (a) Casting 1 (b) Casting 15 and (c) Casting 29. Note the slight shift in cell size distribution for the castings from 1 to 29 with a mold temperature of 202 °C to 400°C, respectively.

Samples of the five permanent mold cast alloys at the same mold temperature were used to examine cell size distributions, which were constructed from data gathered through the linear intercept measurements of cell size for over 800 cells. As shown in Figure 4.12, all alloys exhibited a log-normal distribution and the average cell sizes are reported in Table 4.5.
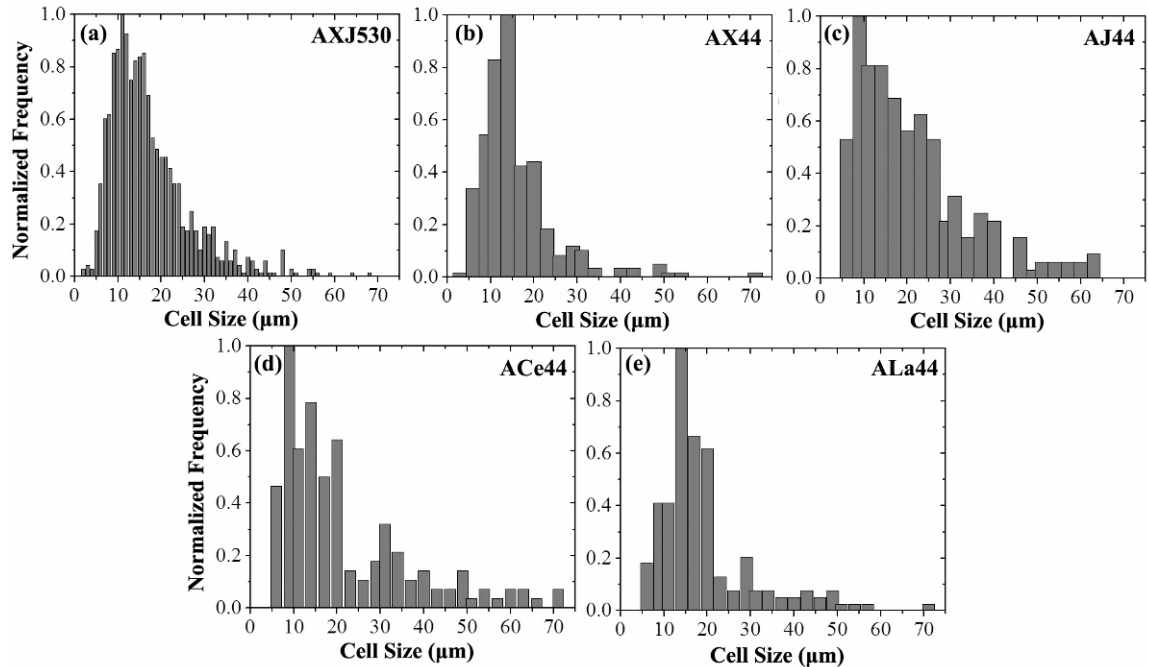
Figure 4.12 Cell size distribution in as-permanent-mold-cast alloys for (a) AXJ530 (b) AX44 (c) AJ44 (d) ACe44 and (e) ALa44.

The microstructure of permanent mold cast AXJ530 was investigated for micro-porosity and inclusions. No inclusions were observed in the gage region of the samples. Porosity, though not frequent enough to statistically quantify, was <<1% in volume fraction. A micrograph showing a typical micro-shrinkage pore is shown in Figure 4.13.
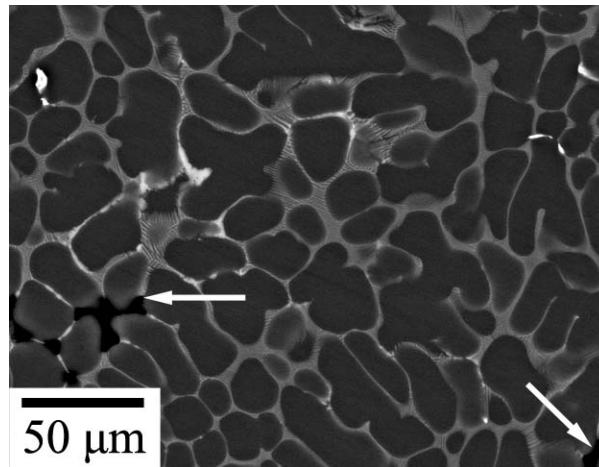
Figure 4.13 Example of observed porosity (indicated by arrows) in a permanent cast alloy. Note morphology that is typical of shrinkage porosity. Alloy is AXJ530 from gage of casting 1.

4.4.2 As-Cast Microstructure

Higher magnification views of the as-permanent-mold-cast alloy microstructures, with the details of the eutectic region are shown in Figure 4.14. The most notable differences between the alloys are the morphology and intermetallic phases within of the eutectic region. These intermetallic phases are as follows: (a) AXJ530 and (b) AX44 a C36 ~ $Mg_2Al_4Ca_3$ phase with a small (< 1%) volume fraction of C14 Mg_2Ca [50, 51], for (c) AJ44 a hP38 – $Mg_{17}Al_2$ with a small (< 1%) volume fraction Al_4Sr – Dl_3 [141-143] and for (d) ACe44 and (e) ALa44 a $Al_{11}RE_3$ phase that decomposes to Al_2Re above 150 °C [10, 11], Table 4.7. Furthermore, the intermetallic morphology of the rare earths are lamellar, whereas a semi-continuous 3D network of the interdendritic intermetallic phases are observed in the Mg-Al-Ca and Mg-Al-Sr.
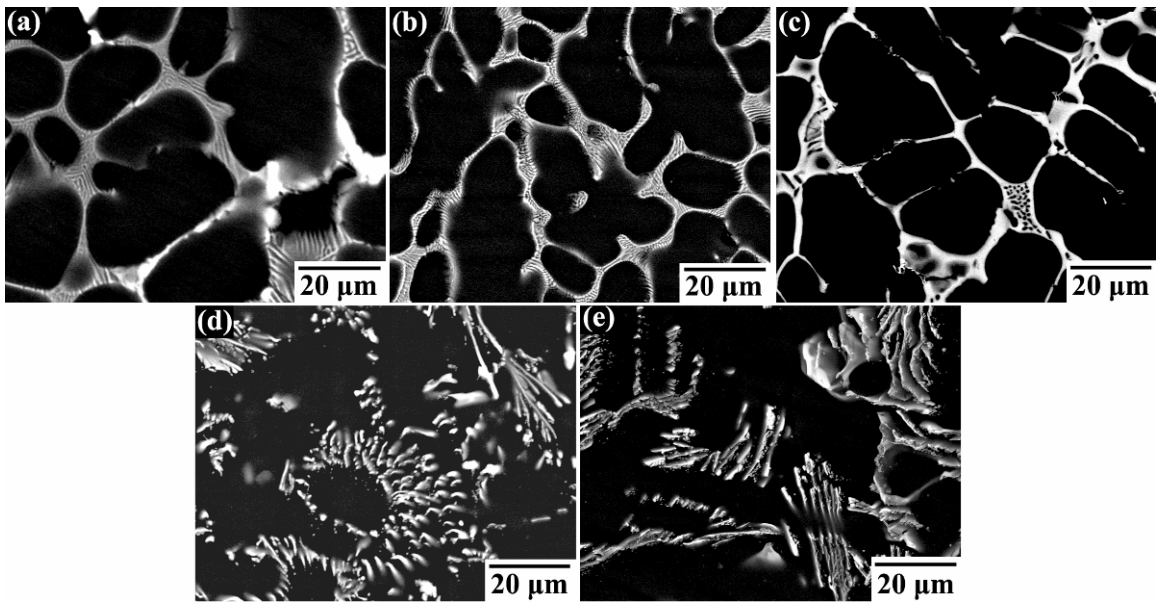
Figure 4.14 As cast permanent mold alloys detailing eutectic for (a) AXJ530 (b) AX44 (c) AJ44 (d) ACe44 and (e) ALa44.

Table 4.7 Intermetallic phases of permanent mold cast alloys.

Alloy	Phase	Reference
AX44	$Mg_2Al_4Ca_3$ - C36	[50, 51]
AXJ530	$Mg_2Al_4Ca_3$ - C36	[50, 51]
AJ44	$Mg_{17}Sr_2$ / Al_4Sr	[141-143]
ACe44	$Al_{11}RE_3$ / Al_2RE	[10, 11]
ALa44	$Al_{11}RE_3$ / Al_2RE	[10, 11]

4.4.3 Microstructures of Crept Samples

The microstructure was examined after creep, for structural and morphological differences. Due to the difference in creep life between each alloy the microstructures have been tested to different test times and strains, shown in Table 4.8. The resultant microstructures after creep are shown in Figure 4.15. The cell size and distribution was quantified for the crept microstructures and is shown in Figure 4.16. There are no notable differences of cell size, distribution, or morphology of the samples after creep indicating that neither the thermal exposure nor stress influenced the microstructure for the conditions studied.

Table 4.8 Creep testing conditions for reported alloys. All tests conducted at 175 °C.

Alloy	Length of Test (h)	Stress (MPa)	% Creep Strain
AXJ530	500	70	0.2%
AX44	690	70	1.0%
AJ44	76	70	3.5% (Failure)
ACe44	6	60	4.8% (Failure)
ALa44	12	60	1.3%
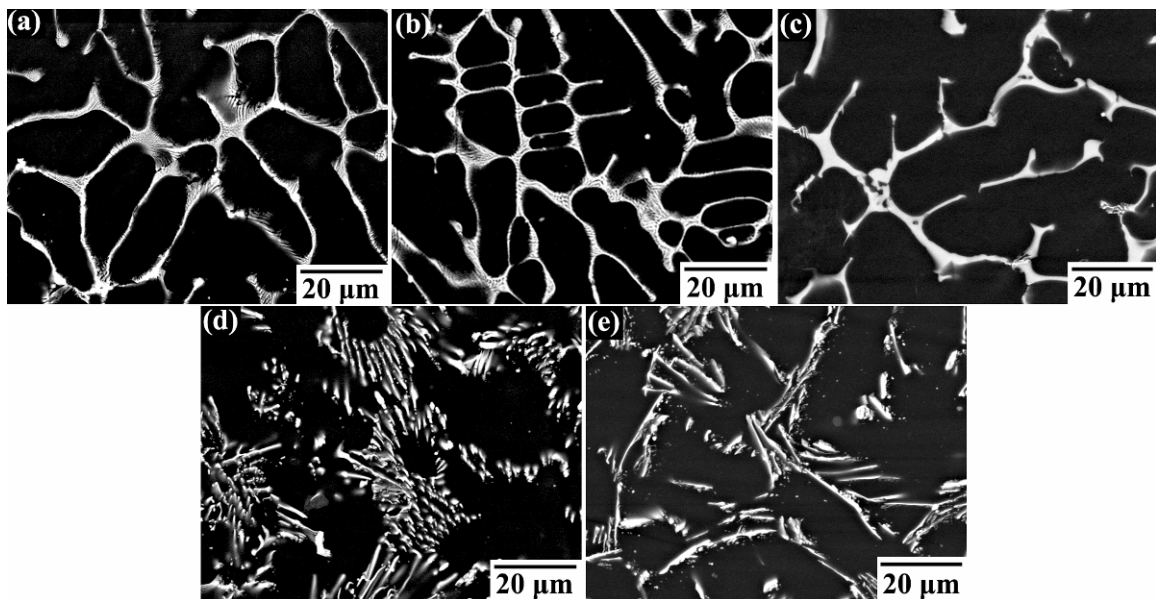
Figure 4.15 Micrographs of crept permanent mold cast samples (a) AXJ530 (b) AX44 (c) AJ44 (d) ACe44 and (e) ALa44.
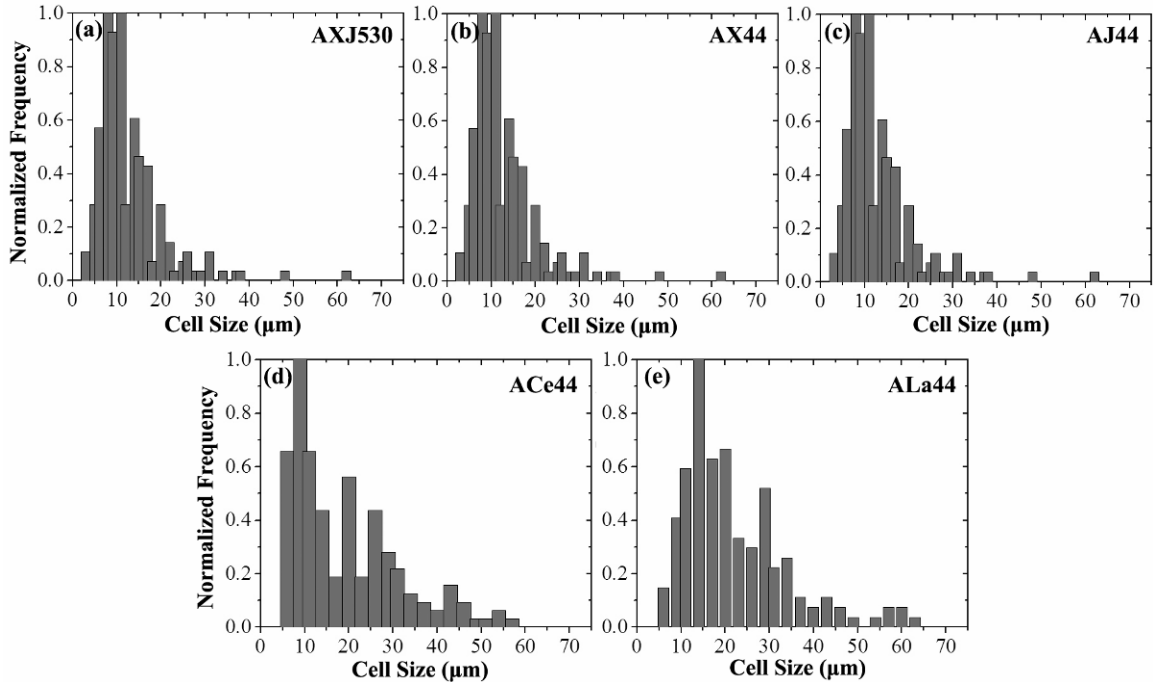
Figure 4.16 Cell size distributions for crept alloys (a) AXJ530 (b) AX44 (c) AJ44 (d) ACe44 and (e) ALa44.

4.4.4   Precipitation Processes in the α-Mg Grain Interior

The grain interior of as-permanent-mold-cast alloys was investigated by TEM for the existence of precipitates. Precipitates were found in the primary α-Mg phase of the Mg-Al-Ca alloys system (AXJ530 and AX44). The precipitates, shown in Figure 4.17 for the AXJ530 and in Figure 4.18 for AX44, are oriented along the basal plane, are plate like in morphology, and are identified as C15 - Al_2Ca. Isothermal ternary phase diagrams for the Mg-Al-Ca alloy at 500 °C and 400 °C are shown in Figure 4.19 [189], which indicates that as the cast specimen cools phase equilibrium between α-Mg and C15 occurs between 500 °C and 400 °C.   Thus it is concluded that the precipitation processes occurred after solidification during cooling. It also indicates that aging would be possible to control the precipitation sequence; this has been demonstrated in studies on die-cast AXJ530 specimens [178].

The morphology of the precipitates depended on the temperature of the permanent mold during casting. The samples cast into a cooler (~200 °C) mold exhibited a fine morphology (100-200 nm in diameter and several atomic planes thick) where the samples cast into a hotter mold (~400 °C) exhibited substantially coarser precipitates (1000 nm (1

µm) in diameter and several atomic planes thick). The precipitates had a strengthening effect on the creep behavior of these alloys and this is discussed in detail in chapter 5.
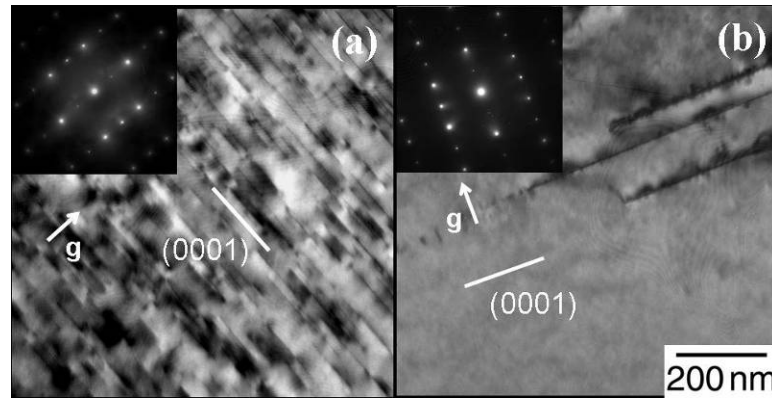
Figure 4.17 TEM bright field images of α-Mg grain interior of permanent mold cast AXJ530, (a) $T_{mold} \approx 250$ °C and (b) $T_{mold} \approx 350$ °C.
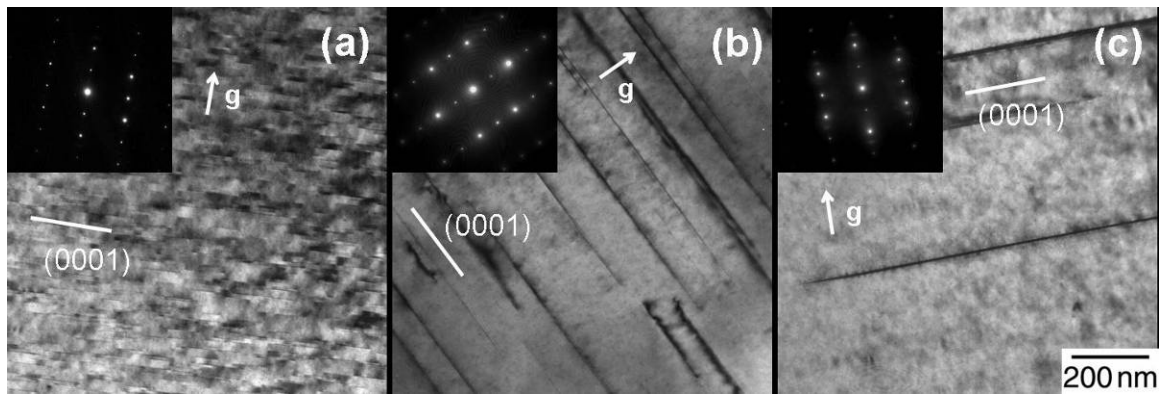
Figure 4.18 TEM bright field images of the α-Mg grain interior for AX44 (a) $T_{mold} \approx 240$ °C (b) T_{mold} 300 °C and (c) $T_{mold} \approx 350$ °C.
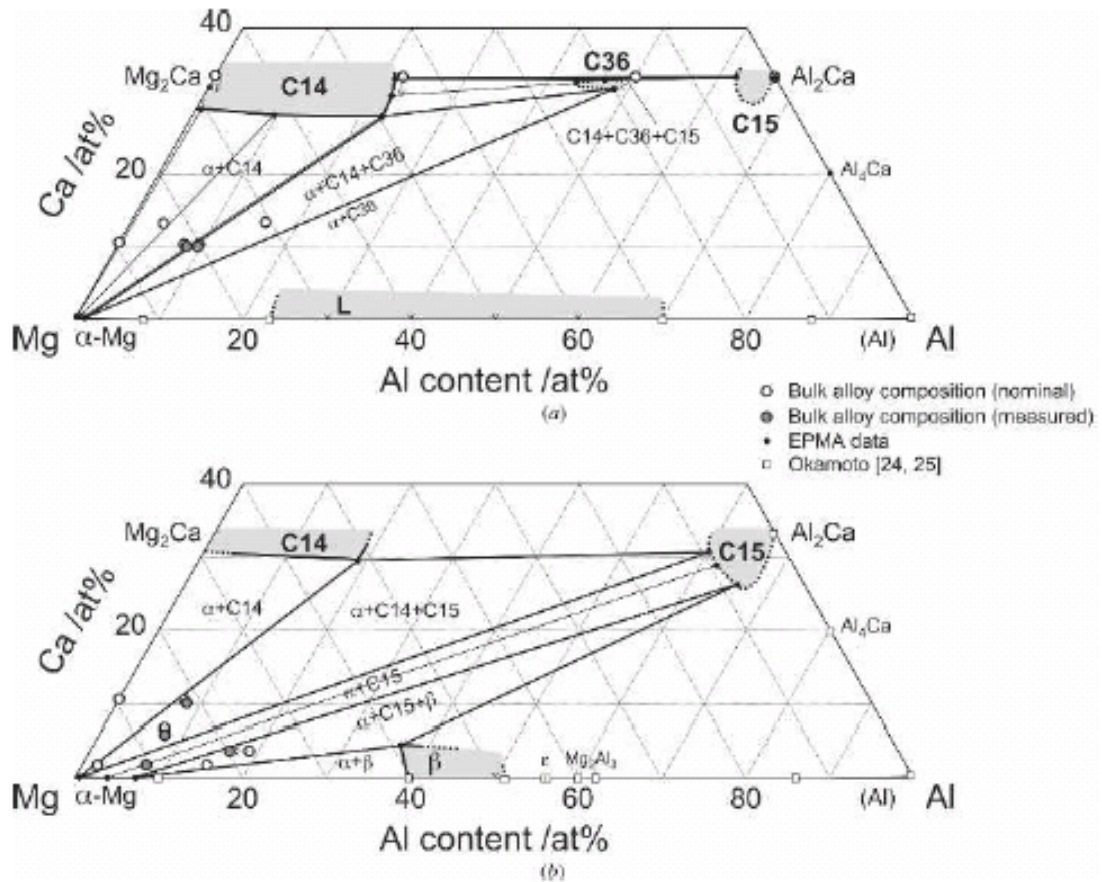
Figure 4.19 Isothermal ternary phase diagrams section of Mg-Al-Ca at (a) 500 °C and (b) 400 °C [189].

Another interesting feature of the precipitates is their distribution within the α-Mg cellular structure. From the TEM investigations precipitates were imaged within several different α-Mg cells. The density and morphology of these precipitates were qualitatively observed to be uniform across regions of the same sample up to the eutectic-primary interface and this agrees with other published work on C15 – Al$_2$Ca in die-cast AXJ530 [178]. This was further confirmed in examination of the AX44 precipitates where they could be observed with the SEM. Figure 4.20 shows the precipitates, bright contrast, with uniform density across several cells. A trace and an arrow indicating a precipitate have been on the figure for clarity. Within the micrograph are bright contrast square markers, used for 2D strain calculations and regions of localized creep damage are also visible.
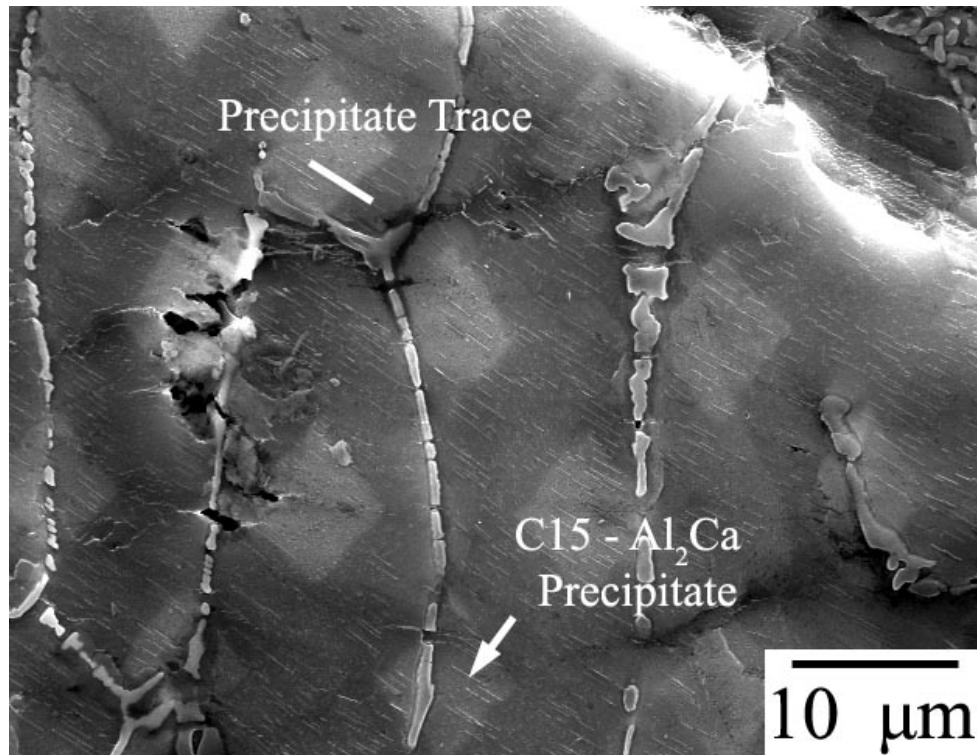
Figure 4.20 As-cast microstructure AX44 containing coarse precipitates uniformly distributed within several cells

No precipitates within the α-Mg grains were observed in AJ44, ACe44 and ALa44 alloys. TEM BFI micrographs of the grain interior of AJ44 and ACe44 are shown in Figure 4.21 and Figure 4.22, respectively. Note that dislocations are present on both the basal and non-basal planes in AJ44, Figure 4.21, and the lack of precipitates in each micrograph. Shown in Figure 4.23, reproduced from [11], is a TEM DFI of die-cast AXJ530 that has been aged to form C15 Al_2Ca basal precipitates. This figure clearly shows that the dislocations are interacting with the precipitates on the basal plane and that dislocations are mobile on multiple slip systems.
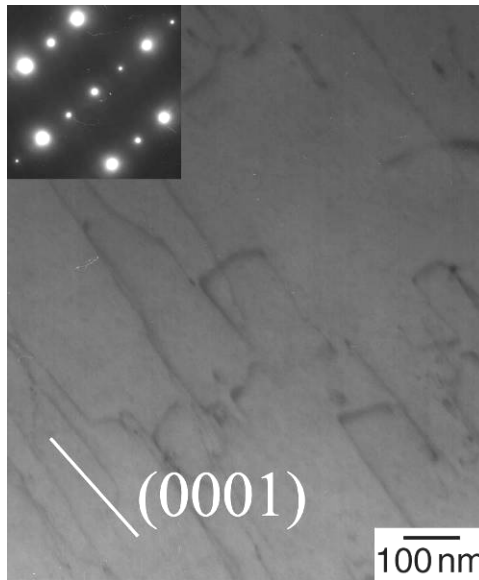
Figure 4.21 TEM BFI of α-Mg grain interior for AJ44 post crept (70 MPa, 175 °C, ε = 3.6 % (failure)). Note basal plane trace and observable dislocations both on and off the basal plane.
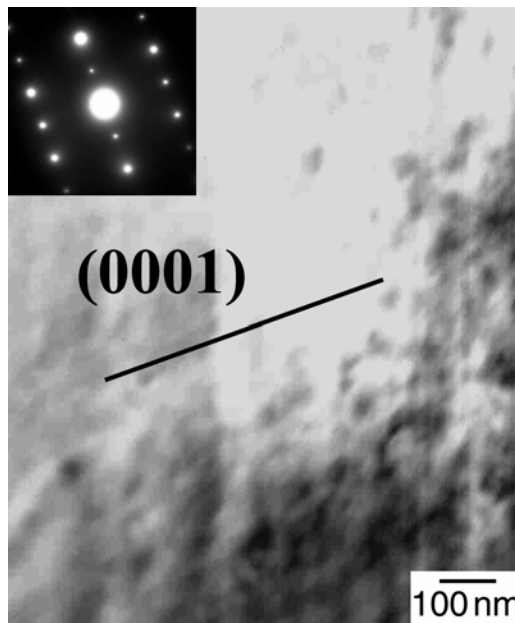
Figure 4.22 TEM BFI of the α-Mg grain interior for ACe44 post crept (60 MPa, 175 °C, ε = 2.1 % (failure)).
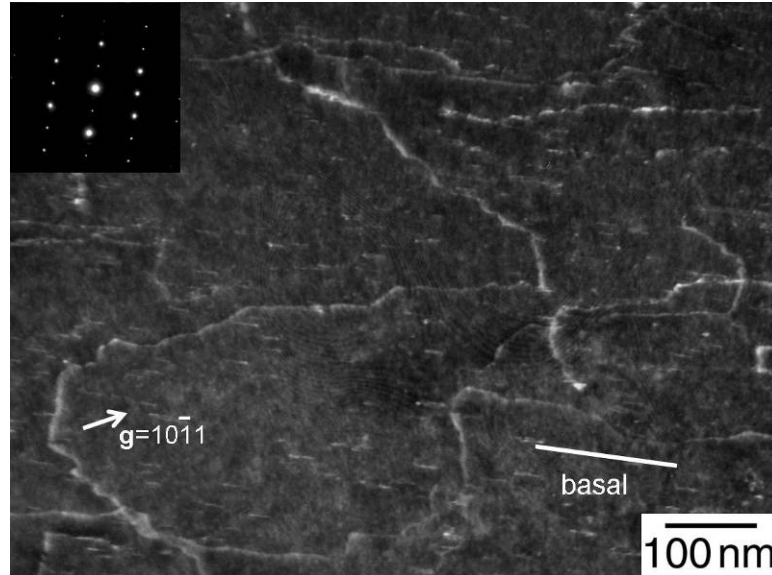
Figure 4.23 TEM DFI of die-cast AXJ530 showing dislocations interaction with basal precipitates and slip on systems other than basal, from [11].

4.4.5   Grain Structure

Grain size was quantified using orientation image microscopy (OIM) maps in the as-permanent-mold-cast alloys. The resultant OIM maps are shown for AX44 in Figure 4.24, AJ44 in Figure 4.25 and AXJ530 in Figure 4.26. The measured grain size for each alloy is reported above in Table 4.6. This analysis reveals that the grain size for these alloys is at least an order of magnitude larger than the cellular structure. Grains are composed of many cells separated by semi-continuous interdendritic regions. These figures suggest that the differing roles of cell boundaries and grain boundaries must be carefully assessed to develop an understanding of the influence of casting conditions and microstructure on the mechanical behavior of cast Mg alloys.
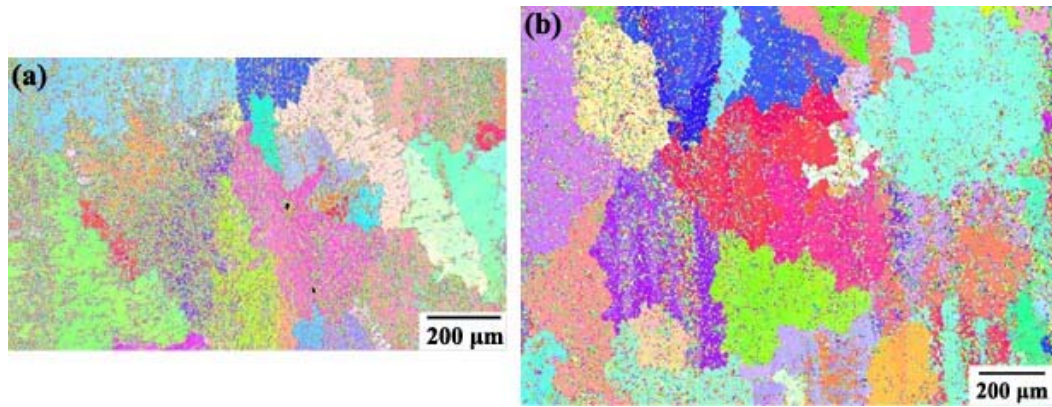
Figure 4.24 Orientation Image Map (EBSD) of AX44 for two regions of the gage (a) and (b).
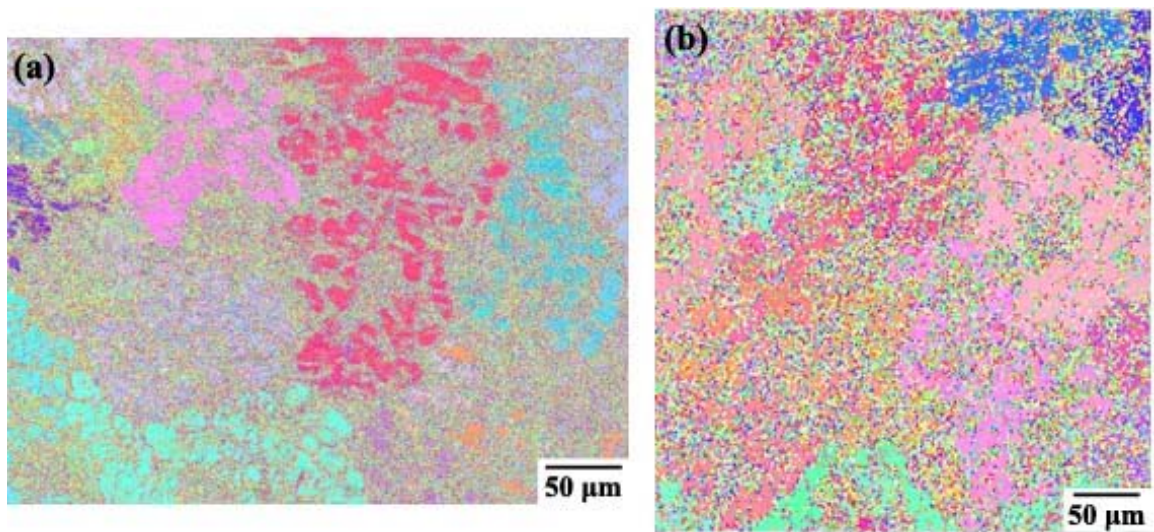
Figure 4.25 Orientation Image Map of AJ44 for two regions of the specimen gage.

Figure 4.26 Orientation Image Map of AXJ530 for a region of the specimen gage.

The as-die-cast AXJ530 grain size was analyzed from OIM maps and is shown in Figure 4.27. The difference between cell size and grain size in the die cast AXJ530 is also apparent, but to a lesser degree, as in the permanent mold alloys. Grains are composed of several cells and are typically two to three times larger than the cell size. The larger grains are regularly dispersed throughout the microstructure with approximately 50 μm between the centers of large grains. As will be discussed in chapter

6, the fact that grain size is not equivalent to cell size has significant implications for creep.
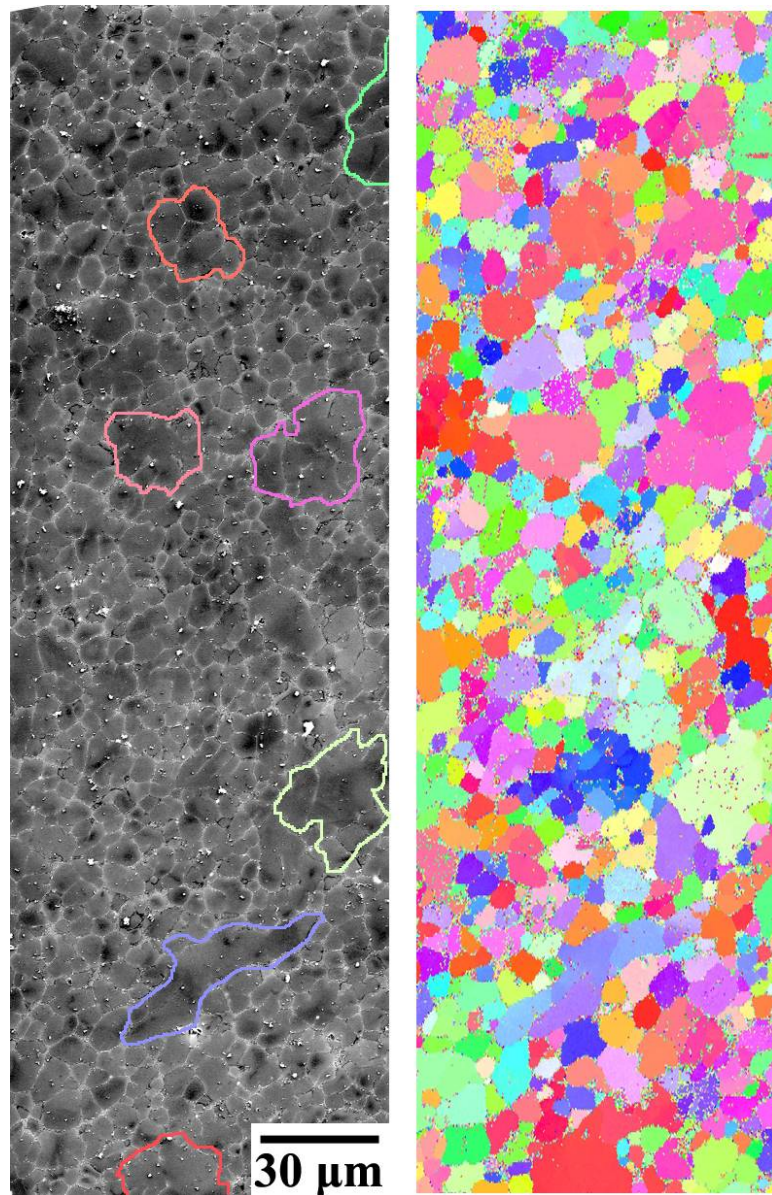
Figure 4.27 Microstructure and EBSD Image (of the same region) of die-cast AXJ530. Note a few grains have been highlighted in the corresponding color to the EBSD map.

Many investigations on the creep behavior of Mg alloys have either reported cell size as grain size or have not measured grain size [8, 84, 104, 126, 136, 148, 156, 157, 159, 162, 190, 191]. Others have not report microstructure or do not specify the cell or grain size in their investigations [11, 13, 15, 102, 103, 111, 117, 129, 134, 144, 147, 150, 152, 179, 192-196]. The important point is that many of the investigations conclude that

the creep behavior is influenced by the primary magnesium grains. Therefore, the absence of a clear understanding of the grain size and grain-level microstructure limits analysis of mechanisms responsible for creep.

Quantifying the grain structure in Mg alloys is critical since it may strongly influence creep behavior. Grain boundaries and/or cell boundaries may inhibit dislocation glide. Diffusion controlled creep, as modeled in Equation 2.2 through Equation 2.4, if operative, is affected by the inverse of the grain size to the second or third power, depending on the operative diffusion creep mechanisms (inter/intra-granular). An inhomogeneous grain size distribution may also influence strain accumulation and creep damage accumulation during creep.

Grain size is dependent on alloy composition and processing [197-200]. The following average grain sizes were determined from grain measurements: AX44 (257 μm), AXJ530 (148 μm), AJ44 (127 μm), and the die-cast AXJ530 (19 μm). Only a limited number of grain size measurements were made in the permanent mold cast alloys, due in part to outside constraints on the use of the orientation image mapping equipment, the necessity for fine step sizes, the large length scale of the grains, and difficulties in sample preparation. In the permanent mold cast alloys, 25 grains were measured in AXJ530, 18 grains in AX44, and 14 grains in AJ44. For the as-die-cast AXJ530, 240 grains were measured.

Comparing the grain size of as-permanent mold cast AX44 to AXJ530, a decrease from an average grain size of 257 μm to 148 μm was measured. The strontium-containing alloy AJ44 had the smallest AGS of the alloys quantified at 127 μm. An understanding of the reasons for the variation in grain size between AX44 and AXJ530 is incomplete. Strontium is a grain refiner in sand cast AZ91 (Mg – 9 Al – 1 Zn) [140] with additions of 0.01 to 0.02 wt% being optimal. Previous studies have focused on the reduction of porosity, not grain refinement, and examined strontium addition between 0 and 0.068 wt%. The AXJ530 alloy investigated in this study contained 0.15 wt% Sr, and grain refinement from strontium seems a very reasonable explanation for the observed difference in grain size.

Also, studies by Fox [201] and Cáceres and Rovera [21] indicate that a decrease in grain size occurs for an increase in aluminum in Mg-Al binary alloys. However, these

studies did not specify a technique for distinguishing between the grain size and cell size (e.g. use of EBSD, etching, and polarized light). The decrease is reportedly greatest (from AGS of ~220 μm to ~110 μm) at low Al (2 to 4 wt%, respectively) concentration [201] and fairly linear (from AGS of 321 μm to 95 μm, respectively) for increased Al concentration (1 to 8 wt% Al) [21]. This is consistent with the finer grain size in AXJ530 compared to the AX44. Swiostek et al. [202] reports an opposite effect on wrought AZ alloys (AZ31, AZ61 and AZ80) where grain size is clearly shown (in the figures provided) to increase with increases in Al content.

Another investigation that suggests that grain refinement might occur due to differences in composition between AXJ530 and AX44 was conducted by Cao et al. [200], who found that in Mg-Al alloys, increases in manganese from 0 to 0.5 wt% led to a refined microstructure. Commercial AZ31 and high purity Mg - 3 Al were studied with a reduction in grain average grain size from 650 μm to 220 μm for the commercial alloy and from about 180 μm to 120 μm in the high purity alloy. The manganese content of the AX44 was 0.015 wt% and of the AXJ530 was 0.30 wt %, again consistent with a decrease in grain size in the AXJ530 alloy. The manganese content for the AJ44 was about 0.012 wt%.

Several other investigations [197-199] have studied on grain refinement of Mg-Al based alloys. These investigations focused on superheating the melt with short hold times [199], native grain refinement [197] (the influence of impurities) and a review of grain refinement techniques (i.e. particle inoculation) in Mg alloys [198]. Since these parameters for grain refinement (i.e. purity levels, superheat and hold times, particle inoculation) were not utilized in this study, they are not considered as potentials pathways for grain refinement observed between the alloys. The influence of grain size on creep behavior is discussed in a later section of this chapter.

4.5   Elemental Segregation

Automotive powertrain magnesium components are typically used in the as-cast state, so quantification of the distribution of solute, particularly in the α-Mg, is important. In this study, the elemental segregation of aluminum and each ternary addition was investigated for the experimental five alloy systems. Understanding the influence of

alloying on the segregation behavior may ultimately permit, alloy compositions to be tailored to increase or decrease solute content in the α-Mg. The solute can act as a solution strengthener or aid in precipitating phases in the Mg matrix. Precipitation within the Mg matrix has been shown to have strengthening effects in Mg-Al-Ca alloys [113, 135] and deleterious (to creep) strengthening effect in Mg-Al alloys [104]. Also, the segregation behavior influences to the composition of the liquid during solidification. If sufficient solute is in solution it will be less available to contribute to solidification during the eutectic reaction. Thus the micro-segregation behavior of the alloying constituents, quantified through partition coefficients, has been characterized for all alloys.

Solute distributions were analyzed through techniques previously summarized, Section 3.7, and described in detail here [18-20, 185]. The segregation analysis technique relied on fitting the Scheil Equation 4.1, or Modified Scheil Equation 4.2 (incorporating a Fourier term for back diffusion - Equation 4.3) to segregation data acquired by WDS analysis. Here Cs is the composition of the solid, k the partition coefficient, C_o the initial composition, f_s the fraction solid, and α the Fourier number.

$$C_s = kC_o(1 - f_s)^{k-1} \qquad\qquad \text{Equation 4.1}$$

$$C_s = kC_o(1 - (1 - 2\alpha k)f_s)^{\frac{k-1}{1-2\alpha k}} \qquad\qquad \text{Equation 4.2}$$

$$\alpha = \frac{Dt}{L^2} \qquad\qquad \text{Equation 4.3}$$

Curve fitting was completed using both the Scheil and modified Scheil equations for comparison. Figure 4.28 shows the composition profile of Al in AXJ530 with Scheil and modified Scheil equations fit to the measured data. Several iterations were completed when using the modified Scheil equation, due to uncertainty with the Fourier term (Equation 4.3). Equation 4.4 [203] was used to calculate the diffusivity of Al in Mg at three temperatures (973, 873, and 673 K) and averaged to provide an approximate diffusivity (~6.0x10^{-8} cm^2/second) during solidification. The length scale (200 μm) and time (100 second) for diffusion to occur (based on microstructure and solidification time) were considered, giving a Fourier number of ~0.00015. Iterations were completed with Fourier values up to four orders of magnitude larger than the above calculated to account for uncertainty in the diffusivity of Al and Mg in the Mg matrix (especially in a ternary

solid solution). There was little difference in the calculated composition solid for this range of Fourier numbers, thus back diffusion is not expected to contribute significantly to the final segregation profile. The initial composition of these alloys, C_o, (Al 4-5 wt%, ternary additions 3-4 wt%) and the partition coefficient, k (estimated from the binary phase diagrams) have significantly more influence than the Fourier term in determining the composition of the solid for the composition windows and partition coefficient in this study.

$$D_{AlMg} = 12e^{\left\{ \frac{(143.6\pm10.9\ \text{kJ/mole})}{RT} \right\}} \frac{cm^2}{s} \qquad \text{Equation 4.4}$$
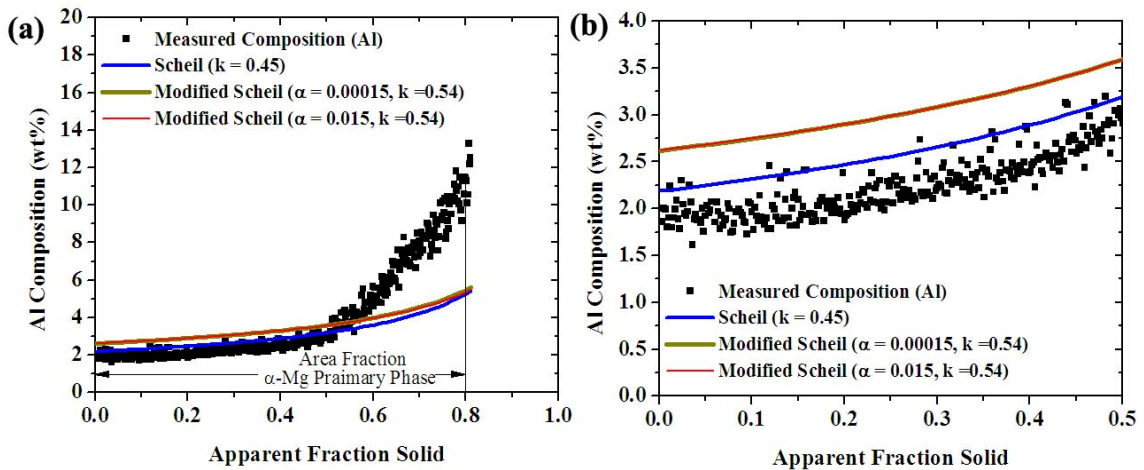
Figure 4.28 Composition profile of Al in AXJ530 with Scheil and Modified Scheil curve fit. (b) is detail of (a).

The partition coefficient (the ratio of the composition of the solid to the composition of the liquid) indicates the degree of segregation of solute. A value less than unity indicates that the element is partitioning preferentially to the eutectic region whereas a value greater than unity indicates that the element is partitioning to the dendrite core. The farther from unity the partition coefficient is, the more strongly it partitions to either the dendrite core or eutectic region. Physical parameters that contribute to the partition coefficient are difference in atomic radii (the tendency for an element to be in solution) and chemical potential of the elements in the liquid. Partition coefficients, k, were first estimated by determining the ratio of the composition of the solid over the

initial composition. The average partition coefficients were calculated by curve fitting the Scheil equation through the compositional range of 0 to 50% fraction solid. For compositional ranges greater than 50%, there was poor agreement of the Scheil and modified Scheil equation with the data. The poor fitting is apparently due to a varying partition coefficient at this later stage of solidification (due to a change in curvature in the phase field boundaries).

The binary phase diagrams for Mg with each alloying constituent are shown in Figure 4.29. Note the extremely limited (<< 1 wt%) solubility of all alloying elements, except Al, in the primary magnesium phase. This is an indication that the ternary additions of Ca, Ce, La, and Sr will have a limited contribution of solid solution strengthening in the primary α-Mg phase in the ternary and higher order systems. Aluminum may have an influence on solid solution strengthening, and the partitioning of aluminum with each ternary addition will be further examined with Scheil analyses. Secondly, the eutectic will be rich in the ternary additions due to their limited solubility in Mg and this will lead to the formation of intermetallics within the eutectic, rather than precipitates in the primary α-Mg phase.
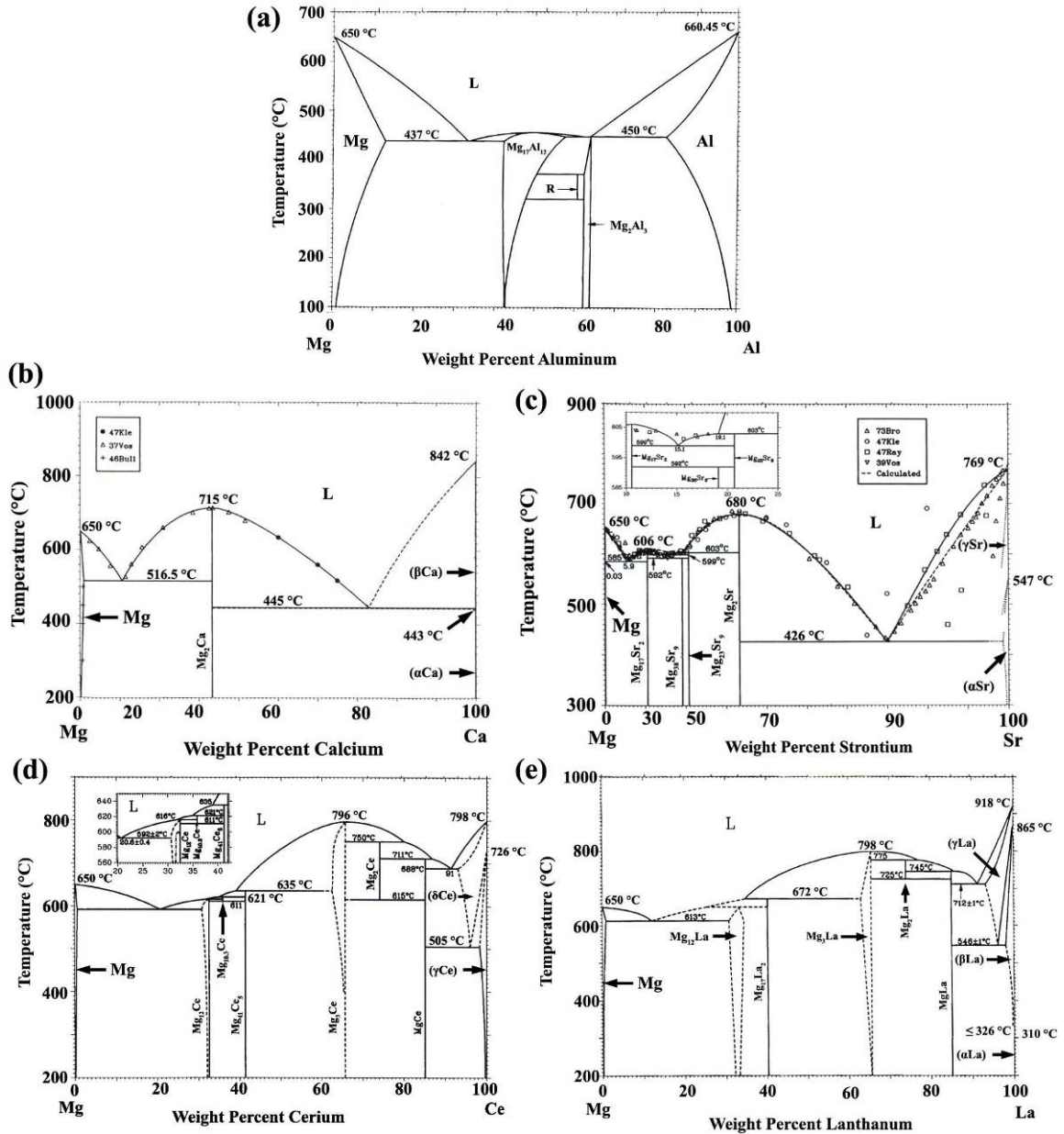
Figure 4.29 Binary phase diagrams of the alloying constituents for (a) Mg-Al [32] (b) Mg-Ca [204] (c) Mg-Sr [29] (d) Mg-Ce [30] and (e) Mg-La [31].

An example of an experimental WDS composition profile (AXJ530), prior to Scheil analysis is shown in Figure 4.30. The profile represents the composition of the solid as a function of apparent solid fraction, for each major alloying element. The sum (total) composition of the alloying constituents is included at the top of the plot and is maintained in a band of 99-101 wt%. The elemental compositional profiles are shown individually for Mg (Figure 4.31), Al (Figure 4.32 and Figure 4.33), and the ternary

109

addition (Ca, Ce, La, and Sr) (Figure 4.34 and Figure 4.35) of the five alloy systems (AXJ530, AX44, AJ44, ACe44, and ALa44) investigated.

Each alloy has the respective area fraction alpha to eutectic region marked by (labeled) a vertical line, designating the approximate boundary from the matrix of primary α-Mg to the eutectic region. In the case of the Ca and Sr containing alloys, a wider cross-hatched region is indicated, representing the overlap (and uncertainty) in the area fraction measurements. Though this line would represent the boundary from primary to eutectic, the spot size of the beam has a cross section of several micrometers and an approximate interaction volume of 3 μm^3. Therefore near the cell boundaries overlap in sampling volumes between the primary magnesium and eutectic region occurs. It is argued that sufficiently large data sets, on a representative scale of the microstructure, were collected to statistically represent the composition profiles of these alloys and negate concerns of interaction volume from different microstructural regions.
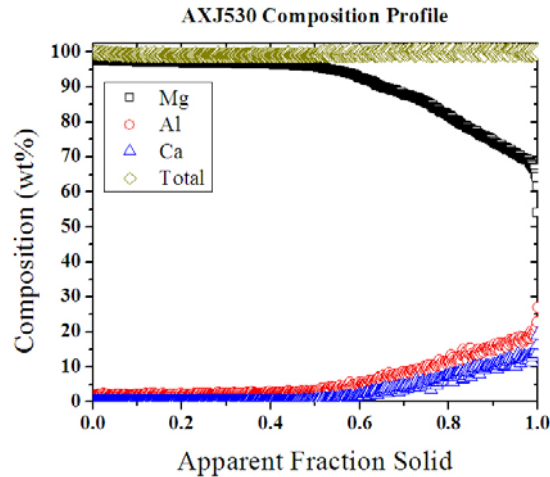
Figure 4.30 Composition profile of AXJ530 for Mg, Al, and Ca. Total weight percent is included.
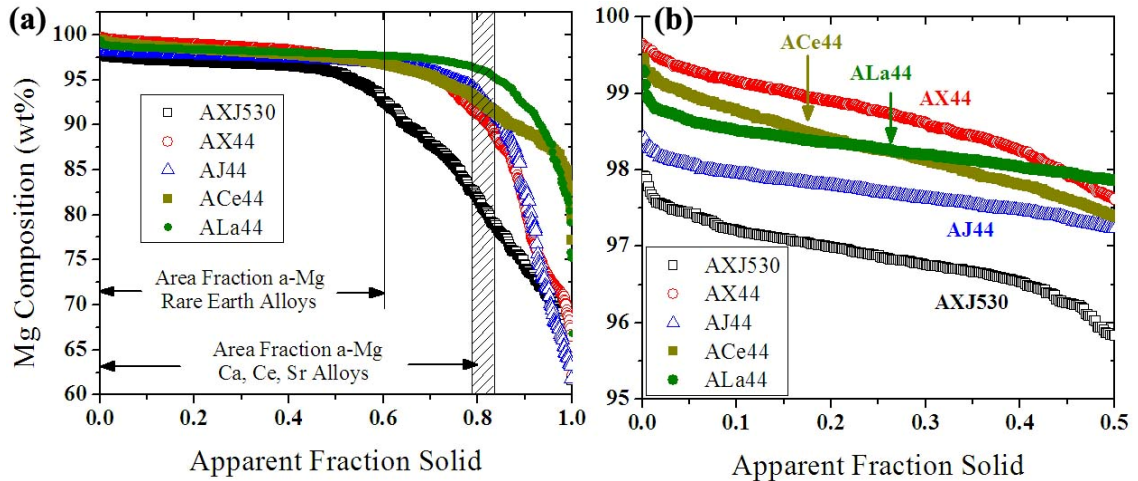
Figure 4.31 (a) Mg composition profile (wt %) for the five permanent mold alloys (b) Detail of fraction solid 0 to 50%.
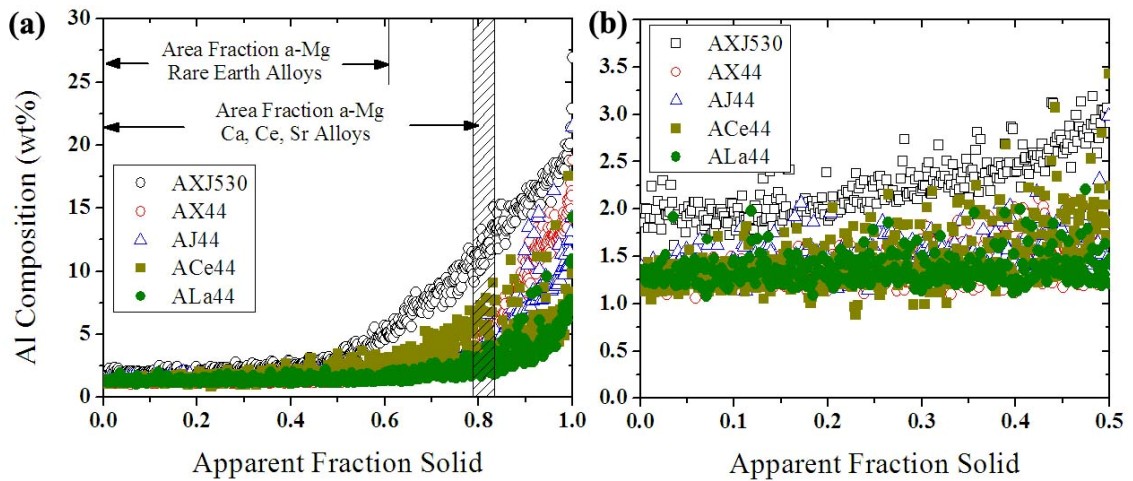
Figure 4.32 (a) Al compositional profile (wt%) for the five permanent mold cast alloys (b) Detail of fraction solid 0 to 50%.
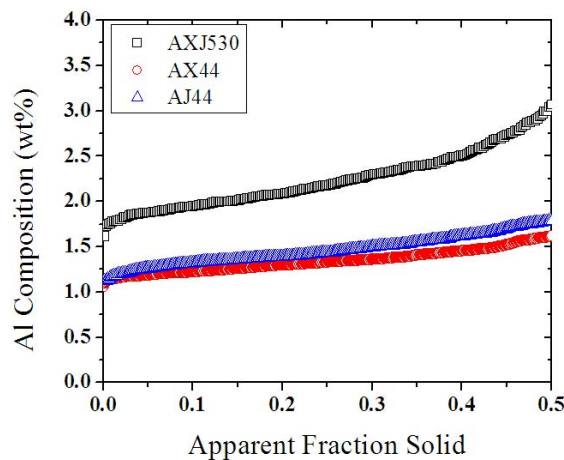
Figure 4.33 Detail of Al concentration, sorted in ascending order, for AXJ530, AX44 and AJ44.
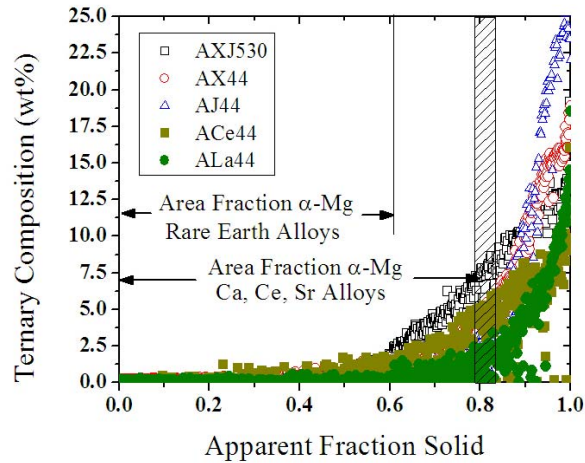
Figure 4.34 Ternary addition composition profile (wt%) for the five permanent mold cast alloys. Details of the lower fraction solid region (0 to 50%) are shown in Figure 4.35.
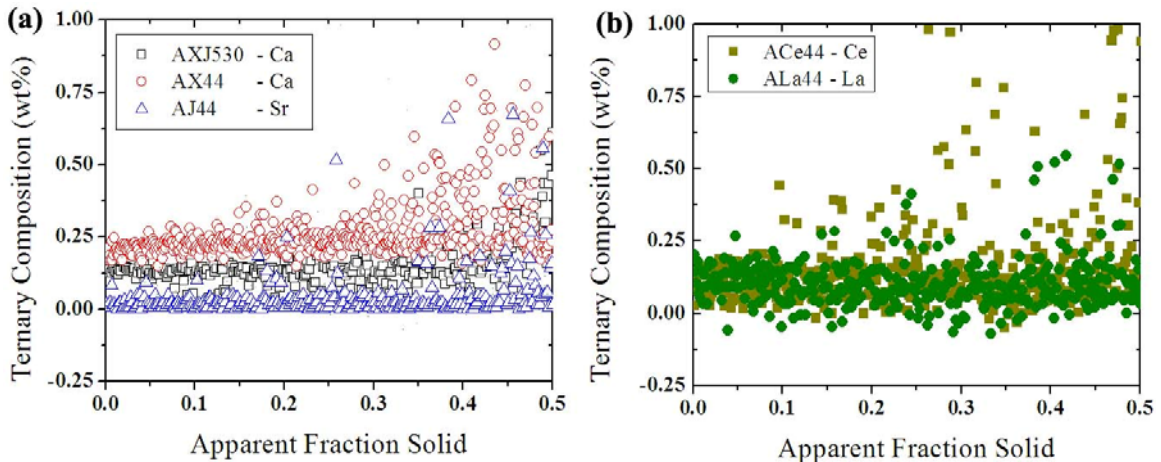
Figure 4.35 Detail of fraction solid 0 to 50% for ternary alloy addition (a) AXJ530, AX44 and AJ44 (b) ACe44 and ALa44.

The most notable observation of the compositional profile curves is that there is a difference in concentration of each element at an equivalent fraction solid among the alloys. This difference is attributed to changes in solidification path, and the solubility, of alloying elements in the α-Mg for each alloy. In Figure 4.31b, at a low apparent fraction solid ($f_s < 0.01$), there is variation in the concentration of Mg from the lowest, ~98 wt% in AXJ530, to a high of ~99.3 wt% in AX44. Thus AX44 has the lowest amount of ternary solute (Al and Ca) within the α-Mg. This segregation difference among alloys is more pronounced in the near-eutectic regions where AXJ530 again has the lowest Mg concentration at ~80 wt% and ALa44 has the greatest at ~97 wt%. Aluminum segregation content also differs (accounting for a difference in Mg

112

concentration), Figure 4.32, where AXJ530 also has the greatest aluminum content both at the grain center and near edge regions (Figure 4.32b with Al content of ~2.0 wt% and 12 wt%, respectively). Figure 4.33 shows the aluminum concentration, sorted in ascending order for AXJ530, AX44 and AJ44. It is interesting to note, and will be discussed in further detail in chapter 5, that the aluminum content of AXJ530 is the greatest, followed by AJ44 (which is slightly greater) than AX44. This indicates that though Al content (and ternary addition) is different between the alloys and solute is one significant creep strengthening mechanism in these alloys. If the solute content was the only mechanism for creep strengthening, then the two rare earth alloys would have an equivalent or greater creep strength than AJ44 and AX44 based on concentration (of solute) alone, indicating that characteristics of the solute (e.g. diffusivity) must also be considered. The other four alloys have very similar Al concentrations at the grain centers (low apparent fraction solids) at ~1.25 wt%. There are differences in Al composition between the alloys at the near grain boundary regions where ACe44 and AX44 have ~1.5 wt%, AJ44 has ~1.4 wt% and ALa44 has ~1.75 wt%. The ternary additions all have low solubilities, Figure 4.34 and Figure 4.35, with minimal increases in ternary composition across the grains. The ternary compositions across the grains for each alloy are: ~0.22 wt% Ca in the AX44, ~0.12 wt% Ce, La and Ca in the three alloys of ACe44, ALa44, and AXJ530, respectively, and ~0.02 wt% Sr for AJ44. Partition coefficients were calculated for each element in each alloy from the profiles and a fit is shown in Figure 4.36. The difference in segregation behavior is quantified with the estimated and calculated average partition coefficients that are tabulated in Table 4.9 and Table 4.10.
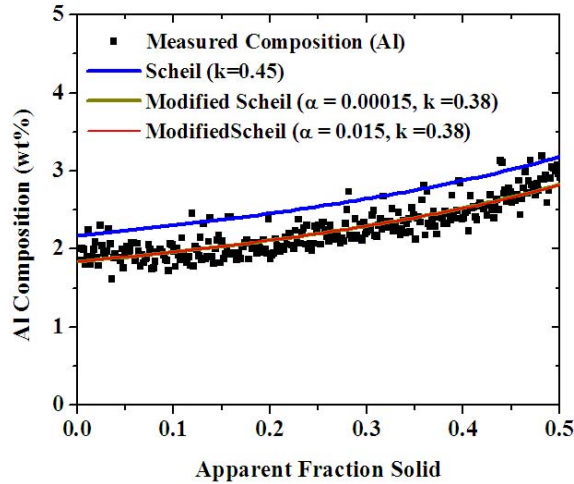
Figure 4.36 Composition Profile Al for AXJ530 with Scheil and modified Scheil fits.

Table 4.9 Estimated partition coefficients, k, from the measured compositions at fs ≈ 0.01 (k = Co/Cs).

	Mg	Al	Ternary Addition	Ternary Element
AX44	1.08	0.32	0.05	Ca
AJ44	1.07	0.35	0.01	Sr
ACe44	1.08	0.32	0.02	Ce
ALa44	1.08	0.34	0.03	La
AXJ530	1.06	0.41	0.05	Ca

Table 4.10 Calculated partition coefficients (k) for fraction solid 0 to 50% using Scheil equation and a modified Scheil equation (Fourier number of 0.00015).

	Scheil			Modified Scheil (α=0.0002)		
Alloy	Mg	Al	Ternary Addition	Mg	Al	Ternary Addition
AX44	1.06	0.30	0.05 (Ca)	1.05	0.32	0.05 (Ca)
ACe44	1.02	0.31	0.03 (Ce)	1.02	0.30	0.03 (Ce)
ALa44	1.01	0.35	0.03 (La)	1.02	0.36	0.03 (La)
AJ44	1.02	0.41	0.02 (Sr)	1.02	0.41	0.02 (Sr)
AXJ530	1.03	0.45	0.06 (Ca)	1.03	0.38	0.06 (Ca)

Prior to a discussion on the differences between partition coefficients for the elements and alloys, a comparison is made between the calculated Scheil partition coefficients and to those calculated from the equilibrium binary phase diagrams. Values from the binary phase diagrams were calculated by determining the composition of the solid and liquid at two temperatures, taking the ratio of C_S to C_L at these temperatures

and tabulating the high, low and average values. The ratio varied at different temperatures due to a slight difference in curvature of the two phase boundaries. These values are listed in Table 4.11. Over all there is good agreement between the values determined from Scheil analysis and those calculated from the binary phase diagrams.

Table 4.11 Partition coefficients calculated from magnesium binary phase diagrams.

Alloy	k_{high}	k_{low}	$k_{average}$
Al	0.31	0.25	0.28
Ca	0.10	0.06	0.08
Ce	0.03	0.02	0.02
La	0.11	0.09	0.10
Sr	0.10	0.07	0.09

Interestingly, there are significant differences in the partitioning in the Mg-Al-Ca alloys AX44 and AXJ530. In the case of the AX44, the Al has a k = 0.30 and the Ca has a k = 0.05, in the case of the AXJ530, which has 1 wt% less calcium and 1 wt% more Al than AX44, the Al has a k = 0.45 and the Ca has a k = 0.06. This indicates that the alloy composition is influencing the solidification behavior and thus partitioning of the ternary additions. Secondly, AXJ530 has 0.15 wt% Sr, which may be influencing the partitioning of Ca (and/or Al) in the primary phase. The phenomena of Sr influencing the partitioning of the ternary elements in these alloys has previously been suggested [139] with limited experimental evidence. The data obtained here clearly demonstrate a higher degree of solubility of Al in the α-Mg phase in AXJ530.

Other interesting characteristics are that the Ce and La containing alloys have similar partition coefficients for both the Al (k = 0.31 and 0.35, respectively) and the Ce or La (k = 0.03, in both cases). The partition coefficient for the ternary addition is less than that in the Ca containing alloys but similar to that in AJ44. This indicates that the Ce, La, and Sr all heavily segregate to the eutectic region. Considering only atomic radii, this would be the expected trend, Table 2.1.

4.6   Summary

The solidification behavior of five alloys (AX44, AJ44, ACe44, ALa44 and AXJ530) has been investigated via analysis of freezing ranges, segregation during

solidification and microstructure analysis. The five alloy systems were permanent mold cast into bulk castings that were quantified using radiography, bulk composition (ICP), density variation and microstructure.

Composition significantly influenced the solidification behavior with AXJ530, AX44, and AJ44 having the largest freezing ranges and ACe44 and ALa44 alloys exhibiting significantly narrower freezing ranges. The microstructure of all alloys consisted of a dendritic, globular primary α-Mg phase and a eutectic region of α-Mg and intermetallic phases. The morphology and continuity of the intermetallic phases varied with alloy composition.

The five alloy compositions were permanent mold cast directly to tensile creep specimens in a pre-heated permanent mold. The bulk castings were then investigated for quality (i.e. acceptable level of casting defects) and consistency via radiography, compositional analysis of specimens, and bulk density investigations (via Archimedes' method). Radiography and metallography indicated that the gage sections were uniformly free of casting defects. Bulk composition was measured within castings and little variation (0.1 wt%) of the concentration of major alloying element (Al, Ca, Ce, La, Sr) observed. There were no measurable changes observed in trace impurities (Fe, Cu, Ni) due to the casting process.

During each casting campaign, typically consisting of 20 castings, mold temperature rose monotonically from approximately 200 °C at the beginning of the run to 400 °C at the end and this affected the cooling rates of the castings. This variation in temperature had only a small influence on primary α-Mg cell size. The cooler mold (200 °C) produced a casting with an average cell size of 18 μm where the elevated temperature mold (400 °C) produced a casting with an average cell size of 24 μm. Mold temperature did influence microstructure in the Ca-containing AX44 and AXJ530 alloys. In both alloys precipitation of the C15- Al_2Ca phase occurred in the primary α-Mg regions, with the precipitates oriented parallel to the basal plane. The precipitates were larger in size with increased in mold temperatures and, as will be seen in Chapter 5, this variation in microstructure had a measurable influence on creep resistance. Precipitation was not observed in ACe44, ALa44 and AJ44 or, as will be shown, was there any dependence of creep behavior on mold temperature for these alloys.

In the calcium-containing AXJ530 and AX44 the eutectic intermetallic phases were predominately C36, with a small (<1 %) volume fraction of C14. In the strontium-containing AJ44 alloy the major eutectic phase was $Mg_{17}Sr_2$ with a minor (<<1%) volume fraction of Al_4Sr. TEM analysis was not conducted for the rare earth-containing ALa44 and ACe44 alloys. However, x-ray diffraction has been conducted on AE42 with mischmetal used for rare-earth additions, where it was reported [10, 11] that the eutectic phases were primarily $Al_{11}Ce_3$ / $Al_{11}La_3$ [157] with minor amounts of Al_4Ce / Al_4La and Al_2Ce / Al_2La phases. Above 150 °C, poor thermal stability of the eutectic phases in AE42 has been observed [10, 11], which may explain the poor creep resistance in the permanent mold cast condition for tests at 175 °C, reported in Chapter 5. The area fraction of the eutectic region is also larger in the rare earth alloys. The area fraction of the primary phase for the alloy systems AX44, AJ44, and AXJ530 was close, lying between 79 - 83 %. The rare earth containing alloys had a smaller area fraction of 61-63 %. The cell size and distribution of the alloys was the same. The average cell size was between 16 – 22 μm and all alloys had a similar log normal distribution.

Grain size, in adddition to dendritic cell size, has been examined in this study by optical microscopy (using polarized light and etched microstructures) and orientation imaging microscopy (OIM). In both the permanent mold and die-cast condition, grain size and cell size are not equivalent and grains are comprised of multiple α-Mg cells. Grain size was dependent on composition. AX44 had the largest measured grain size of 257 μm, while AJ44 and AXJ530 had finer grains sizes of 127 and 148 μm, respectively. The average grain size of the die-cast AXJ530 was 19 μm. Grain size was not investigated in the rare earth containing alloys. It is also important to note that the microstructure of die-cast AXJ530 was similar (same area fraction primary phase, same type and morphology of eutectic intermetallics phases, and presence of C15 – Al_2Ca precipitates in the matrix) to that of permanent mold cast AXJ530, with only refinement due to the significantly higher cooling rate of the die casting process. These similarities and differences in microstructure will be exploited in the investigation of creep behavior and microstructure in Chapter 5.

Scheil analyses revealed differences in the segregation of Al within the α-Mg grains for each alloy. AXJ530 had the greatest average concentration of Al (~4.1 wt%),

followed (in descending order) by AX44 and AJ44 (1.8 wt%), ACe (1.6 wt%) and ALa44 (1.4 wt%). The ternary additions of Ca, Ce, La and Sr segregated significantly to the eutectic regions for all alloys, with concentrations of these elements in the primary Mg ranging from 0 to 0.25 wt%.

In Chapter 5 the results of creep studies conducted on the permanent mold cast alloys and on die cast AXJ530 are presented. Differences in creep resistance will then be described in terms of compositional and microstructural differences among the alloys that have been elucidated in Chapter 4. The latter will focus on differences in grain size, influence of solute, the presence or absence of precipitation in the matrix, and microstructure of eutectic regions.

Chapter 5

Creep Behavior

This chapter examines the constitutive creep response of the permanent mold cast alloys and relates microstructural features (i.e. grain size, solute concentration, precipitate strengthening) to differences in creep strength. In Section 5.1 the tensile creep behavior of the as-permanent-mold-cast specimens is described for stresses ranging between 40-90 MPa at 175 °C, and a comparison of the behavior between die-cast and permanent mold cast AXJ530 is also presented.

Section 5.2 describes the influence of microstructural features on creep strength. The influence of grain size is considered for die-cast and permanent mold cast AXJ530. Next the influence of composition on solidification path is analyzed considering the variation in solute concentration in the α-Mg phase for each alloy (as reported in Chapter 4). The creep resistance of precipitation (C15 - Al$_2$Ca) strengthened α-Mg is also quantified.

5.1   Comparison of Creep Behavior

Creep testing was conducted on the permanent mold cast and die-cast alloys at stresses ranging from 40 to 100 MPa at 175 °C. The alloys can be ranked in order of decreasing creep resistance at 175 °C as: die-cast AXJ530, permanent mold cast AXJ530, AX44, AJ44, ALa44 and ACe44 (with the latter five alloys all permanent mold cast). A comparison of the creep behavior of the calcium and strontium containing alloys is shown in Figure 5.1 and Figure 5.2. The ACe44 and ALa44 were significantly less creep resistant and their creep behavior is presented later. The creep curves of the permanent mold cast alloys exhibited three distinct stages. During the first stage, primary creep, there was a rapid decrease in creep rate. This was followed by a minimum creep rate

119

with an extended steady-state, and finally an acceleration of the creep rate, leading to failure.
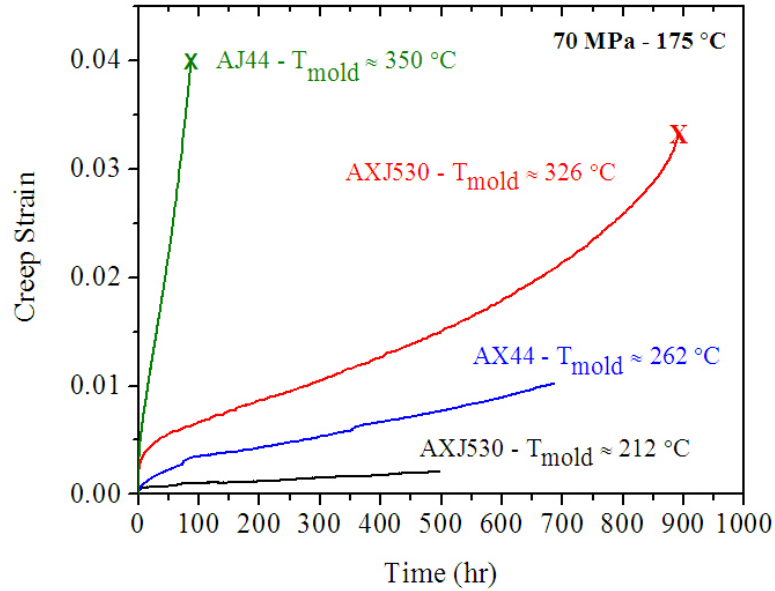
Figure 5.1 Creep strain comparison of Ca and Sr containing permanent mold cast alloys at 70 MPa and 175 °C. The rare earths, presented later, have much lower creep resistance at these test conditions.
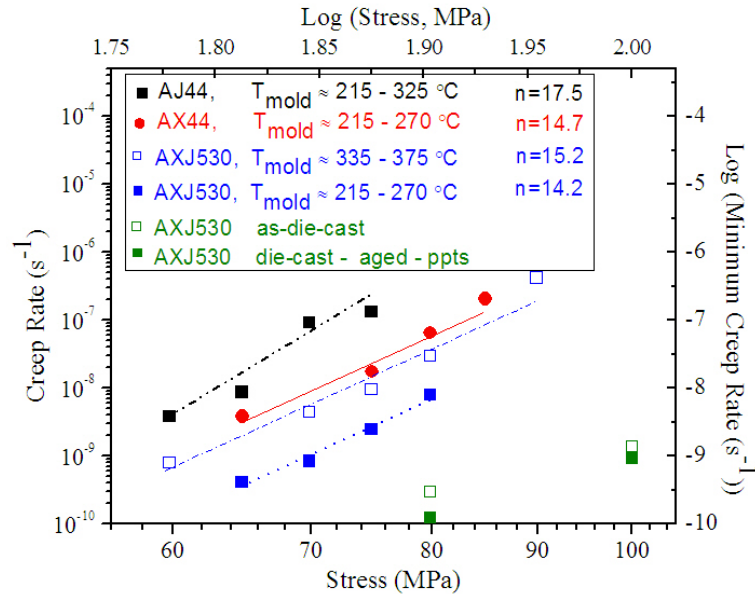
Figure 5.2 Dependence of minimum creep rate on stress at 175 °C for permanent mold cast alloys AX44, AJ44 and AXJ530 and die-cast AXJ530.

Primary creep strain and the duration of primary creep decreased with decreasing creep resistance (from alloy composition) and with applied stress. For the Mg-Al-Ca

alloys the primary creep transient varied from 20 to 50 hours in duration with primary creep strains ranging from 0.5 to 1.0%. The AJ44 alloy reached the end of primary creep between 10 and 15 hours at ~0.5% strain. The Mg-Al-RE alloys exhibited very short primary creep transients less than 5 hours in duration with primary creep strains ranging from 0.5 to 1.0%.

The ductility at failure (for the permanent mold cast samples) ranged between 1.3 and 16% and varied with alloy composition and applied stress. No macroscopic necking was observed in any alloy of the stresses investigated. For the most creep resistant permanent mold cast alloy, AXJ530, failure occurred between 2.5% strain (at 75 MPa) and up to ~5.3% strain (at 90 MPa). AX44 exhibited greater ductility to failure and was between ~5% (at 80 MPa) and 16% (at 85 MPa). The ability of AX44, at higher stresses, to accumulate additional strain prior to the formation of localized creep damage is discussed in Chapter 6. For the AJ44 alloy, failure occurred at 3% strain (at 65 MPa) and 3.8% strain (at 75 MPa). The rare earth alloys behaved similarly (to each other) with failure occurring at 1.3% (at 50 MPa) and at 4% (at 60 MPa).

The stress exponents were determined for the Mg-Al-Ca and Mg-Al-Sr alloys. For the permanent mold cast AXJ530, AX44, and AJ44 the stress exponents were similar and ranged from 14.2 to 17.5. These values, though high for power law creep in single phase alloys, are reasonable considering the multiphase microstructure of these alloys and are near those reported for other Mg alloys [100, 112, 126]. Although only two stress levels were investigated for the die-cast AXJ530, the stress exponent appears lower n ≈ 6.8 and is close to that reported for die-cast AX53 (n=8.5) [84]. Fewer stress levels were examined for the rare earth alloys and the stress dependence was not determined.

The creep testing parameters (i.e. alloy, casting mold temperature, applied stress, test time, accumulated creep strain and minimum creep rate) for the permanent mold cast specimens tested are tabulated in Table 5.1. Due to difficulties in permanent mold casting of the rare earth alloys (ALa44 and ACe44) and poor as-permanent-mold-cast creep resistance, only limited creep testing was completed for these alloys for comparison to the calcium- and strontium-containing alloys. The remainder of this section compares the creep behavior of each permanent mold cast alloy and die-cast AXJ530.

Table 5.1 Summary of creep parameters and test results of as-permanent-mold-cast alloys. All tests conducted at 175 °C.

Alloy	Mold Temperature (°C)	Stress (MPa)	Time (h)	% Creep Strain	Mininum Creep Rate (s^{-1})	Rupture
AXJ530	348	90	22.3	5.3	4.0×10^{-7}	Yes
	380	80	231.5	4.6	3.0×10^{-8}	Yes
	356	75	445.5	2.6	9.0×10^{-9}	Yes
	246	75	667.5	0.9	2.8×10^{-9}	Interrupted
	246	75	496.0	0.6	2.5×10^{-9}	Interrupted
	352	70	891.0	3.4	4.2×10^{-9}	Yes
	334	70	659.8	5.1	7.5×10^{-9}	Yes
	215	70	497.0	0.2	6.2×10^{-10}	Interrupted
	253	65	692.3	0.3	5.0×10^{-10}	Interrupted
	376	60	558.1	0.2	4.2×10^{-10}	Stepped
AX44	266	85	146.7	15.2	2.0×10^{-7}	Yes
	348	80	99.2	13.8	2.5×10^{-7}	Yes
	315	80	72.5	6.8	1.8×10^{-7}	Yes
	246	80	136.7	4.7	6.4×10^{-8}	Yes
	290	75	425.4	3.2	1.7×10^{-8}	Interrupted
	266	70	666.7	1.0	2.0×10^{-9}	Interrupted
	231	65	1005.3	2.0	3.1×10^{-9}	Interrupted
AJ44	293	80	72.3	4.3	1.2×10^{-7}	Yes
	266	75	77.3	4.7	1.2×10^{-7}	Yes
	343	70	86.2	4.0	9.2×10^{-8}	Yes
	278	70	77.4	3.6	8.9×10^{-8}	Yes
	337	65	421.6	2.9	8.0×10^{-9}	Interrupted
	253	65	399.3	3.5	1.5×10^{-8}	Interrupted
	291	60	618.5	1.2	3.1×10^{-9}	Interrupted
ACe44	327	60	3.5	2.1	9.1×10^{-7}	Yes
	253	60	5.6	4.0	1.5×10^{-6}	Yes
	266	50	3.9	1.2	4.7×10^{-7}	Yes
	231	40	574.3	2.1	4.2×10^{-9}	Yes
ALa44	253	60	12.1	1.0	1.1×10^{-7}	Yes
	253	60	29.7	3.8	1.5×10^{-7}	Yes

The creep behavior of die-cast AXJ530, the most creep resistant alloy test, is shown in Figure 5.3. The minimum creep rates observed at 80 and 100 MPa were 2.5 x 10^{-10} s^{-1} and 9.23 x 10^{-10} s^{-1}, respectively, and an order of magnitude lower than observed in the next most creep resistant alloy, permanent mold cast AXJ530 (i.e. 3.6 x 10^{-9} s^{-1} at 80 MPa and 175 °C). Although only two stresses were investigated, the stress exponent was approximately 6.8 which is similar to that reported for die-cast AX53 (n =8.5) [84].
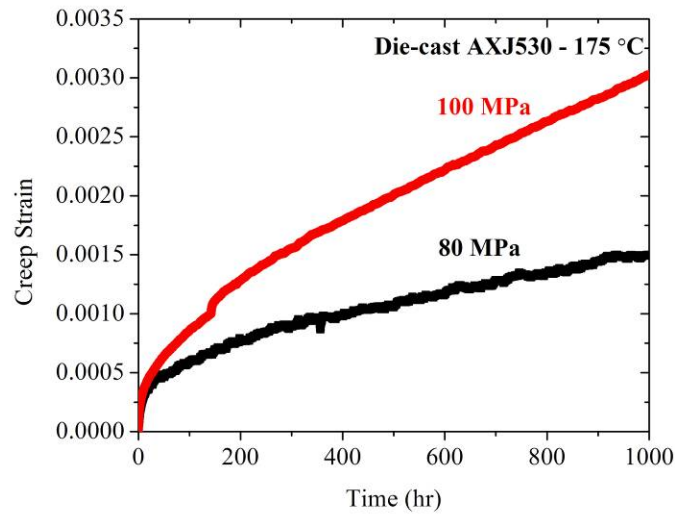
Figure 5.3 Creep behavior of die-cast AXJ530 at 175 °C.

The permanent mold cast AXJ530 was the next most creep resistant alloy studied and creep curves are shown in Figure 5.4. The minimum creep rates for the highest (90 MPa) and lowest (60 MPa) stresses investigated are 4.0 x 10^{-7} s^{-1} and 4.2 x 10^{-10} s^{-1}, respectively.
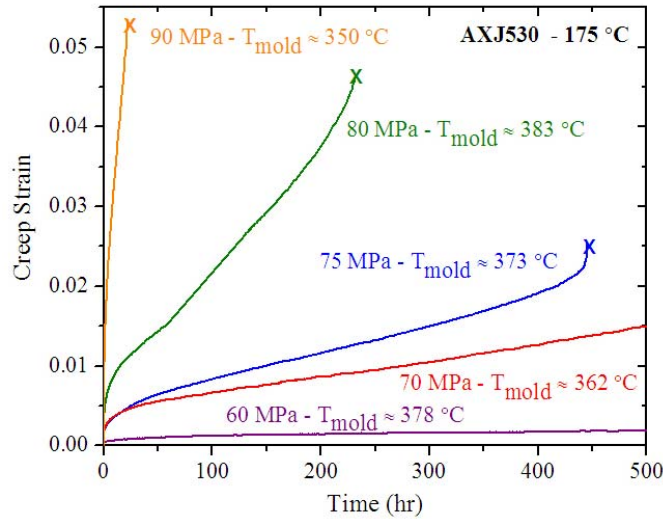
Figure 5.4 Creep strain behavior of permanent mold cast AXJ530 at 175 °C for stress between 60 and 90 MPa.

In permanent mold cast AXJ530 creep rate was sensitive to the mold temperature, the variation of which is described in Section 4.2.1. This effect is shown in Figure 5.5, where casting samples (having different cooling rates from changes in permanent mold temperature) were crept at the same temperature and stress. For the range of permanent mold temperature investigated (200 – 400 °C) the creep rate varied by about an order of magnitude. This difference, further discussed in Section 5.2, is attributed to the change in size and spacing of precipitates (C15 – Al$_2$Ca) in the α-Mg matrix (Figure 4.17).
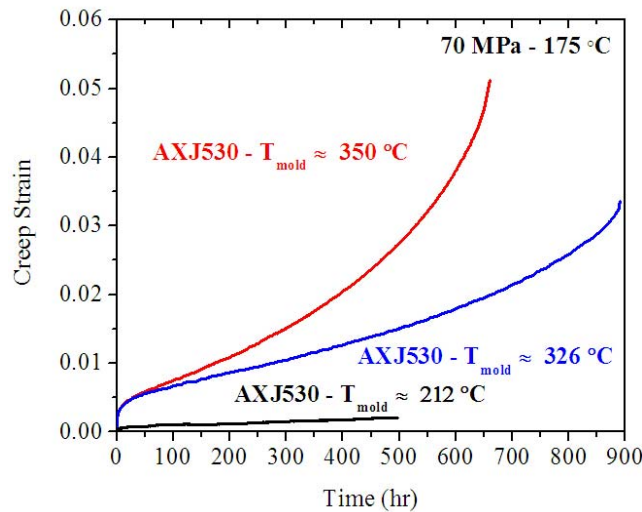
Figure 5.5 Dependence of mold temperature influence on creep strain behavior of AXJ530 at 70 MPa and 175 °C.

The creep behavior of AX44, ranking second in creep resistance among the as-permanent-mold-cast alloys in this investigation, is shown in Figure 5.6. The minimum creep rate ranged between 3.1×10^{-9} s^{-1} and 2.5×10^{-7} s^{-1} for applied stresses from 65 to 80 MPa. The creep behavior of AX44 is most similar to that of permanent mold cast AXJ530, with approximately a factor of five to ten times lower minimum creep rate than that observed for similar microstructures (i.e. precipitate morphology) at comparable stresses (i.e. 2.0×10^{-9} s^{-1} (AX44) compared to 6.2×10^{-10} s^{-1} (AXJ530) at 70 MPa and 175 °C).
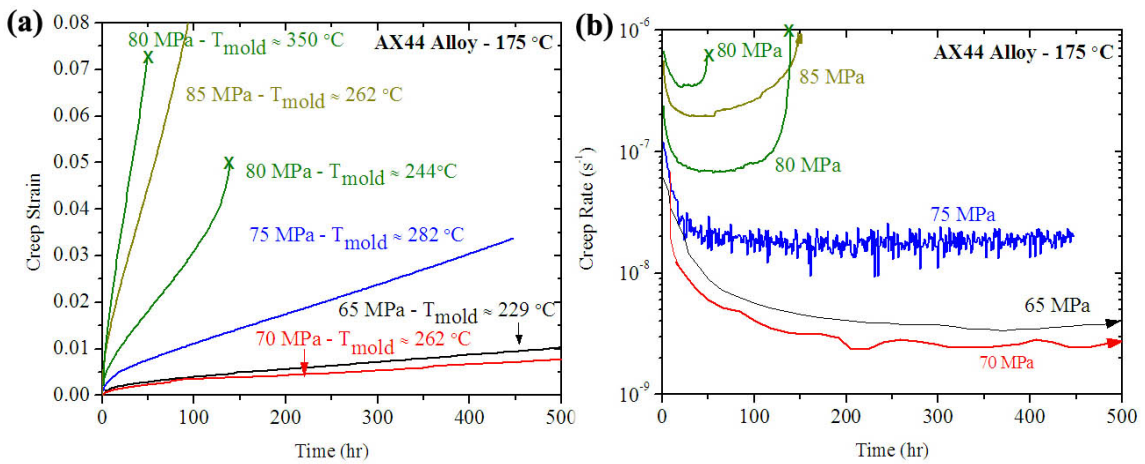
Figure 5.6 Creep behavior of permanent mold cast AX44 at 175 °C for stress between 65 and 85 MPa (a) creep strain and (b) creep rate.

The AX44 minimum creep rate was sensitive to mold temperature, similar to that observed for AXJ530. The change in creep resistance with mold temperature is shown in Figure 5.7 and again is attributed to the change in precipitate size and spacing (Figure 4.18). Samples cast with higher mold temperatures had a coarser precipitate distribution and a poorer creep resistance than samples cast with lower mold temperatures.
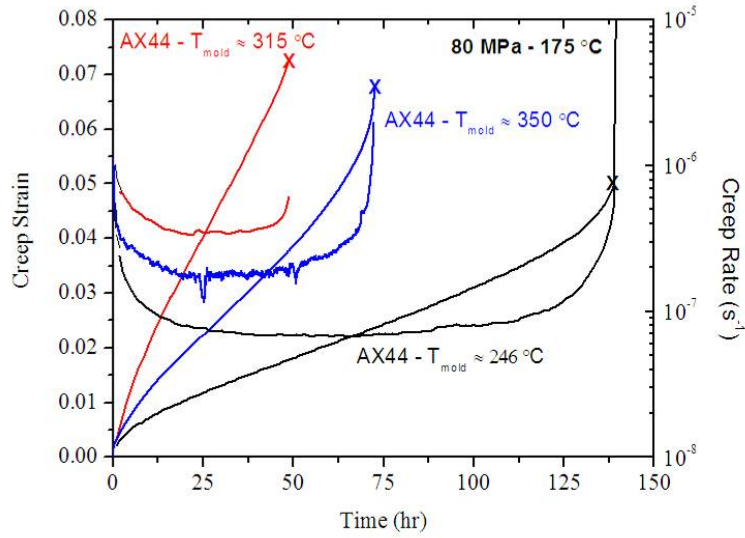
Figure 5.7 Creep behavior of permanent mold cast AX44 at 80 MPa and 175 °C. Average mold temperature listed next to each curve.

The AJ44 had an intermediate creep resistance, among the five alloys investigated. The creep behavior of the AJ44 alloy is shown in Figure 5.8. The minimum creep rate of the AJ44 alloy ranged between 3.1×10^{-9} s^{-1} and 1.2×10^{-7} s^{-1} for stresses from 60 to 80 MPa. For the stresses investigated, an increase of about 1.5 to 2 orders of magnitude (minimum creep rate) above AXJ530 was observed. There was an increase in minimum creep rate of about ½ to 1 order of magnitude between AJ44 and AX44. The creep behavior of AJ44, unlike that observed for the Mg-Al-Ca alloys, did not depend on mold temperature, and no precipitates were observed in the α-Mg matrix of this alloy.
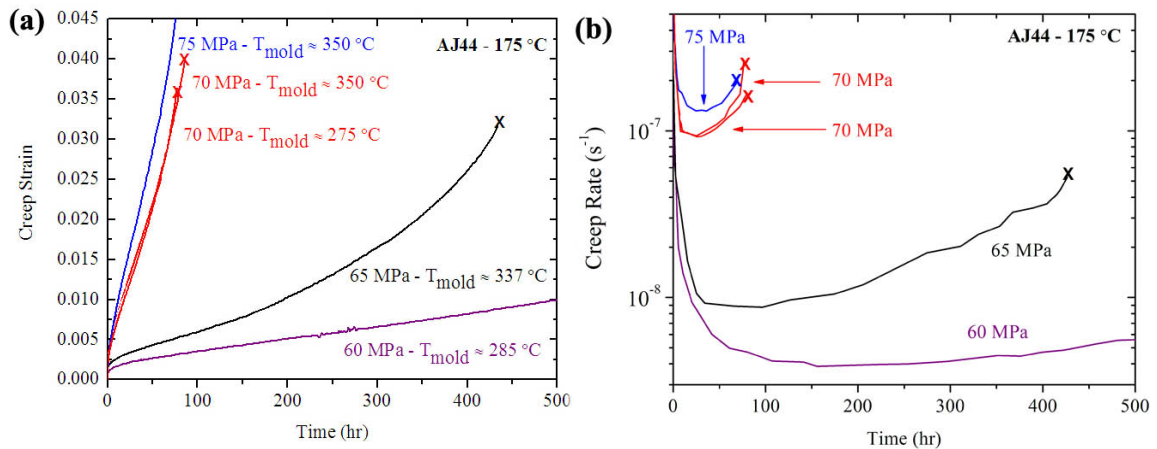
Figure 5.8 Creep behavior of permanent mold cast AJ44 at 175 °C for stress between 60 and 75 MPa (a) creep strain and (b) creep rate.

126

The creep behavior of the rare earth containing alloys is shown in Figure 5.9. ACe44 and ALa44 had similar creep behavior, with the ALa44 being slightly more creep resistant at the stresses and temperature investigated. Both alloys in the as-permanent-mold-cast condition had creep resistances 3 to 4 orders of magnitude lower than that observed for permanent mold cast AXJ530. The minimum creep rate at 60 MPa for ACe44 and ALa44 was 9.1×10^{-7} s^{-1} and 1.5×10^{-7} s^{-1}, respectively, where AXJ530 had a minimum creep rate (at 60 MPa) of 4.2×10^{-10} s^{-1}. There was no effect of mold temperature on creep behavior and the presence of precipitates within the α-Mg matrix was not observed during TEM investigations.
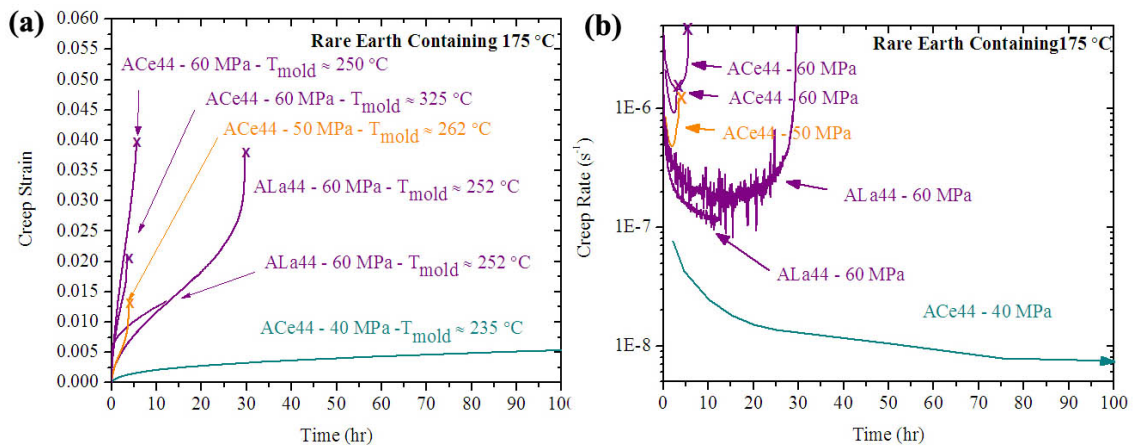
Figure 5.9 Creep behavior of permanent mold cast rare earth containing alloys (ACe44 and ALa44) at 175 °C for stress between 40 and 60 MPa (a) creep strain and (b) creep rate.

Table 5.2 Comparisons of alloys, cast condition, and approximate minimum creep rate at 80 MPa, 175 °C.

Casting Process	Alloy	$\dot{\varepsilon}_{minimum}$ (s^{-1})	approximate time to $\dot{\varepsilon}_{min}$ (h)
Die-cast	AXJ530	10^{-10}	200
Permanent-mold	AXJ530	10^{-9}	70
Permanent-mold	AX44	10^{-8}	50
Permanent-mold	AJ44	10^{-7}	20
Permanent-mold	ALa44*	10^{-5}	-
Permanent-mold	ACe44*	10^{-5}	-

* minimum creep rate at 80 MPa extrapolated from log σ - log $\dot{\varepsilon}_{min}$ data at lower stresses

Table 5.2 summarizes creep behavior of the alloys (and casting process) at 80 MPa and 175 °C. The minimum creep rates for ALa44 and ACe44 have been extrapolated from log σ vs. log ε data. Among these alloys the microstructure varied due to casting process (i.e. die-cast and permanent mold cast), composition (i.e. ternary additions (Ca, Ce, La, and Sr)), and due to cooling rate differences during solidification (i.e. mold temperature varied between 200-400 °C). In the following section the influence on creep behavior of these microstructural variations, especially grain size, solute concentration, and matrix precipitation, are examined.

5.2   Influence of Microstructure and Composition on Creep

Many investigations of creep in Mg alloys attribute differences in creep behavior to variations in microstructure. Some [13, 84, 130, 162] report that the intermetallic phase precipitated along grain boundaries pins the grains retarding GBS, while others [8, 129] do not specify the mechanism for the improvements in creep behavior, but do correlate the improvement in creep resistance to the suppression of an intermetallic (e.g. $Mg_{17}Al_{12}$) and formation of a different phase (e.g. Al_2Ca). Many report [11, 84, 100, 126, 129, 136, 144, 159, 191, 194, 196, 205] that the thermal stability of the intermetallic has a strong influence on creep behavior. Terada et al. [206] concluded that the eutectic intermetallic phase covers the grain boundaries and improves creep strength by sustaining the stress-independent component of the internal stress and (suggested) that the presence of the continuous intermetallic phase reduced the mobile dislocation density and/or glide velocity of dislocations, though dislocation densities were not investigated. Precipitation within the matrix has also been attributed to creep strengthening in Mg alloys [102, 104, 195, 207]. This section examines the influence of microstructure on creep strength in light of new information on grain size variation and provides a detailed characterization of the potential affects of solute segregation and precipitation on creep behavior of as-cast Mg alloys.

A schematic overview of the microstructure is illustrated in Figure 5.10, where the features that may influence creep behavior are depicted. At the center of the figure is an illustration of a microstructure where the size of α-Mg grains (d) and cells (λ) have

been differentiated. The scale of the grains and cells are refined in the die-cast condition, but the grain and eutectic structure remains similar. In the top left corner, the composition profile (from the center to edge of a grain) for two alloys is plotted comparing Mg and ternary addition. It is evident that the solute concentration varies between alloys. Moving clockwise around the figure, the C15-Al_2Ca precipitates within the α-Mg of the Mg-Al-Ca alloys are illustrated for two different samples that had cooled at different rates, resulting in a coarse and fine precipitate distribution. Finally at the bottom of the figure are schematic representations of the different eutectic morphologies resulting from alloy composition. In this section the influence of these microstructural features on creep behavior is described, with specific focus on (1) microstructural scale (i.e. grain and cell size) (2) solute concentration in the matrix (3) precipitates in the matrix and (4) the morphology of the eutectic region. Based on the experimental observations, approaches for improvement of creep behavior are proposed.

(2) Solute Concentration

(3) Precipitation Strengthening

Mg-Al-Ca

(C15 - Al$_2$Ca)

α- Mg

λ

(1a) Cell Size

d

(1b) Grain Size

(4) Eutectic Morphology

Mg-Al-Ca

Mg-Al-Sr

Mg-Al -RE
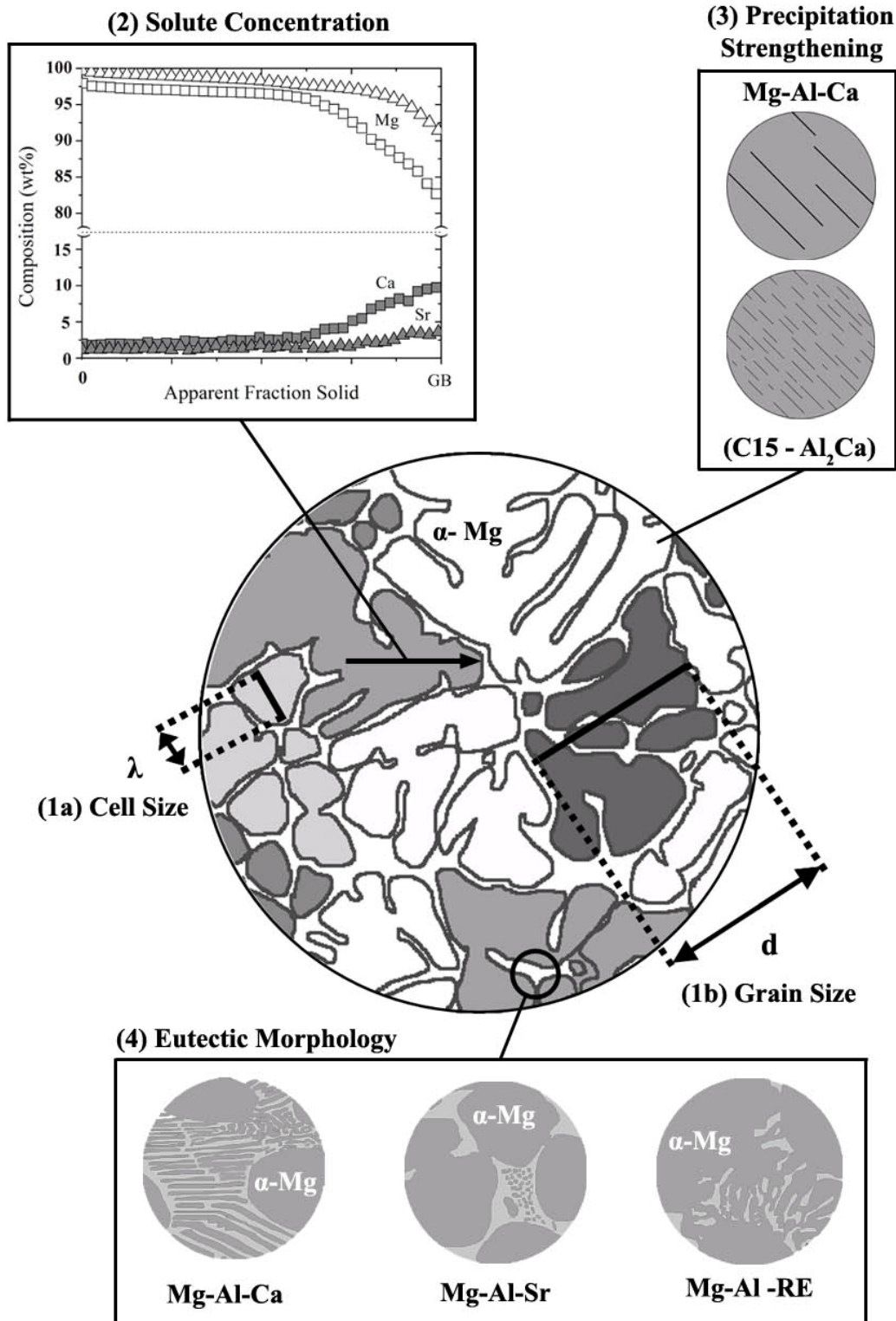
Figure 5.10 Schematic of microstructure for permanent mold cast condition illustrating features characterized for creep strengthening contributions (1) (λ) cell and (d) grain size (2) solute concentration (3) precipitation strengthening and (4) eutectic morphology.

5.2.1 Effects of Grain Size

The grain size of these alloys was determined to be an important microstructural feature affecting the creep behavior. The average grain sizes of permanent mold cast alloys (Table 4.6) was 127, 158, and 257 μm for AJ44, AXJ530 and AX44, respectively. The grain size for the die-cast AXJ530 was 19 μm. There was approximately an order of magnitude lower creep rate in the fine grained die-cast AXJ530 compared to the coarse grained permanent mold cast AXJ530. There were two orders of magnitude difference in minimum creep rate between fine grained AXJ530 and the coarse grained AJ44 and AX44, though some of this difference is attributed to other microstructural features (i.e. solute and precipitates) discussed in subsequent sections.

Considering diffusion and GBS creep models, Table 5.3, grain size has a significant influence on creep rate. Investigations (in other alloy systems) [78-80] observe that decreases in grain size increase the minimum creep rate, contrary to the behavior observed here. Stress exponents measured in this study and reported in the literature for Mg alloys (between 3 and 20, Table 2.6) between indicate that power-law creep is operative. Grain size variation in the range examined in this study are not typically accounted for in power-law creep models [64], since grain size does not usually strongly influence creep.

Table 5.3 Diffusion and GBS creep models

Model		Reference	Variables	Equation
$\dot{\varepsilon} = \dfrac{D_{sd}\sigma b^3}{kTd^2}$	Nabarro-Herring	[75, 76]	D_{sd} - diffusion coefficient σ – stress b – Burgers vector k – Boltzmann's constant T – temperature d – grain size	Equation 5.1
$\dot{\varepsilon} = \dfrac{\alpha_3 D_{gb}\sigma b^4}{kTd^3}$	Coble	[77]	α – material constant D_{gb} - diffusion coefficient σ – stress b – Burgers vector k – Boltzmann's constant T – temperature d – grain size	Equation 5.2
$\dot{\varepsilon} = 42\dfrac{\tau_a\Omega}{kT}\dfrac{1}{d^2}D_{eff}$	Raj-Ashby	[78]	τ_a – applied shear stress Ω – atomic volume k – Boltzmann's constant T – temperature d – grain size D_{eff} – iffusion coefficient	Equation 5.3

Considering the microstructure of the die-cast and permanent mold cast AXJ530, where each had the same microstructure (i.e. area fraction primary phase, eutectic morphology, precipitate distribution) but different grain sizes and different minimum creep rates. Figure 5.11 shows the dependence of the minimum creep rate on grain size. Permanent mold cast AX44 and AJ44 have been included for completeness though the contribution of other creep strengthening effects (e.g. solute element and concentration) are not decoupled from the grain size.

The relationship between grain size and minimum creep rate has an exponent of ~1.7 where the diffusional creep theory predicts an exponent of -2 or -3. No power-law creep models mechanistically describe such improvements in creep strength from grain size. In Chapter 6, it will be shown that grain size influences plastic strain distributions during creep.
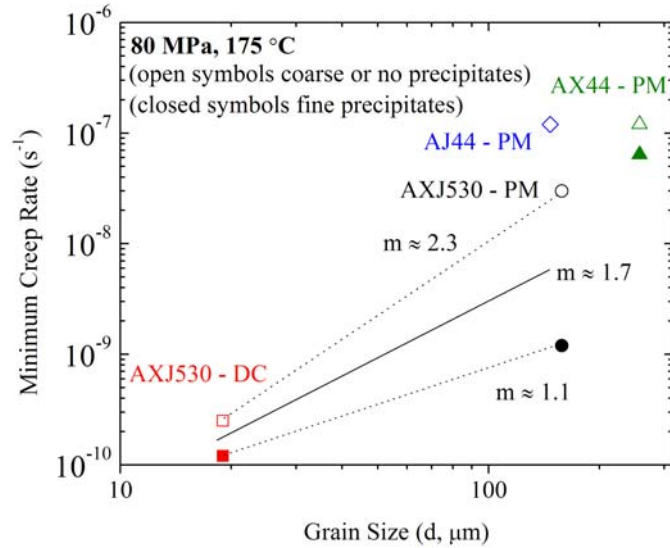
Figure 5.11 Dependence of grain size on minimum creep rate at 80 MPa and 175 °C for die-cast and permanent mold cast AXJ530. Permanent mold cast AX44 and AJ44 are included for completeness.

5.2.2   Influence of solute on creep

Permanent mold cast AXJ530, AX44, and AJ44, have modest variability in grain size (between 127 and 257 μm) which allows comparison of solute concentration (both Al and ternary additions) and the role this may have on creep behavior. AXJ530 has the highest solute concentration (both Al and Ca) and had one order of magnitude lower minimum creep rate than AX44. The AX44 and AJ44 have similar microstructures (i.e. grain size, area fraction phases, no (or few) precipitates) and essentially the same contribution of solute have similar creep properties. The rare earth containing alloys had comparable Al and limited Ce or La in solution and this could account for the 3-4 orders of magnitude lower creep resistance compared to the Ca/Se containing alloys.

Dargusch et al. [86, 162] suggested that solute aluminum (in the α-Mg grains of AM50/AS21) may improve creep resistance however, they did not quantify solute concentrations in the alloys. Powell et al. [10, 11] carefully measured the concentration of RE in solution (AE42 alloy) and concluded, due to the low levels of RE, that there was not a likelihood of solid solution strengthening. However, others [91, 208] have argued that rare earth elements contribute to solid solution strengthening of the α-Mg matrix, although, again, no experimental verification was made. Suzuki et al. [139] investigated

133

the addition of Sr to Mg-Al-Ca and quantified solid solution strengthening at room temperature using room temperature nano-indention.

Despite the high stress exponents, dislocation substructures during creep consist of isolated dislocations that appear to be viscously moving though the grain structure, as described in section 4.4.2. Thus it is of interest to evaluate the influence of solute concentration on creep using models for viscous-glide controlled creep. A model on viscous-glide developed by Mohamed and Langdon [209], Equation 5.4, accounts for solute concentration through the variable A.

$$\dot{\varepsilon} \approx \frac{\pi(1-v)\sigma^3}{6AG^2}$$ Equation 5.4

$$A \approx \frac{e^2 c b^5 G^2}{kT\widetilde{D}}$$ Equation 5.5

In Equation 5.4, v is the Poisson's ratio, σ the applied load, A is a constant dependent on the mechanism of solute-dislocation interaction, and G is the shear modulus. Cottrell and Jaswon [210] proposed an approximation for A, Equation 5.5, accounting for the solute-dislocation interaction where e is the solute-solvent size difference, c is the concentration of solute atoms, b is the Burgers vector, G the shear modulus and D the diffusion coefficient of the solute atom. The variables e, c and D, Equation 5.5, are the features that vary among the alloys investigated, and thus can be evaluated to compare the influence solute has on creep. Table 5.4 contains the values of e calculated from atomic radii of each element relative to that of magnesium.

Table 5.4 Element addition, atomic radii [26] and solute-solvent size difference (e) with respect to Mg.

Element	Atomic Radii (Å)	e
Mg	1.60	-
Al	1.43	0.17
Ca	1.97	0.37
Ce	1.83	0.23
La	1.87	0.27
Sr	2.15	0.55

Representative concentrations (of solute) were determined from the Scheil analysis, and described in Section 4.5. The values were determined for two representative conditions. The first was the average of the solute within the primary α-Mg (e.g. the average of Al composition from 0 to 80% apparent f_s for AX44). The second was the solute concentration in the matrix determined by the average of 30 points at the near grain boundary region (30 points accounted for ~ 5% area fraction from the grain boundary back into the primary grain). These values (average and maximum concentration) for each alloy system are shown in Table 5.5. Although these concentrations do not directly account for variations in creep (which also requires values for e and D), several interesting trends are observed. First the Mg-Al-Ca alloys have the greatest concentrations of Al and ternary addition compared to the other alloys. Secondly, ordering the alloys in decreasing concentration for both Al and ternary additions follows the order of decreasing creep resistance.

There is one significant consideration in comparing the concentrations values. The Mg-Al-Ca alloys, compositional measurements were completed on as-cast samples containing similar size and spatial distribution of $C15-Al_2Ca$ precipitates in the primary α-Mg matrix. Since the precipitates were much smaller than the beam size (in measuring composition with an EPMA), their contribution to the compositional profile could not be de-coupled from solute in the matrix. Therefore, the compositions reported for AX44 and AXJ530 include Al and Ca contributions that include precipitates in the matrix and which would not contribute to solid solution strengthening (though they will contribute to precipitation strengthening, Section 5.2.3).

Table 5.5 Compositions measured from EPMA in the Scheil analysis, section 4.5, with the α-Mg phase.

Alloy	Al		Ternary Addition		Mg	
	Average wt%	Max. wt%	Average wt%	Max. wt%	Average wt%	Bal. wt%
AX44	1.8	4.6	0.8	4.5	97.5	90.9
ACe44	1.6	2.4	0.2	0.6	98.1	96.9
ALa44	1.4	1.5	0.1	0.1	98.2	97.7
AJ44	1.8	3.2	0.3	1.7	97.1	94.4
AXJ530	4.1	11.1	1.4	6.8	93.5	82.1
	Average at%	Max. at%	Average at%	Max. at%	Average at%	Bal. at%
AX44	1.6	4.2	0.5	2.8	97.9	93.0
ACe44	1.4	2.2	0.0	0.1	98.5	97.7
ALa44	1.3	1.4	0.0	0.0	98.7	98.6
AJ44	1.6	2.9	0.1	0.5	98.3	96.6
AXJ530	3.8	10.4	0.9	4.3	95.4	85.3

Values for diffusivity from the literature are shown in Table 5.6. Limited data was found for diffusion coefficients of the alloying elements in Mg [203, 211, 212], especially for the creep temperatures of interest. It was assumed that differences in the diffusivity of Al in Mg are negligible between alloys due to the low concentrations (in comparison to Al) of the ternary additions in solution. Therefore the diffusion coefficient was not considered as a variable when calculating differences in the viscous drag effect from Al solute.

This was not the case for the ternary additions. It is reasonable to assume (based on the differences in atomic radii between ternary additions) that the diffusion coefficients will be different for Ca, Sr and the rare earths in Mg. Comparable values of e^2c can be calculated between AX44 and AXJ530 (the diffusion coefficient for Ca in Mg would be approximately the same for these alloys) and between ACe44 and ALa44 (the diffusion coefficients are similar) but meaningful comparisons between each ternary system cannot be made without incorporating the diffusion coefficient. Regardless, it is reasonable to assume that Al will have the major contribution to viscous drag because of its higher concentration.

Table 5.6 Diffusion coefficients of ternary elements in Mg at various temperatures.

Temperature (°C)	Element	$D \left(\dfrac{cm^2}{s} \right)$	Reference
420	Al	8.0×10^{-11}	[203]
175	Al	6.6×10^{-17}	[203]
550	Ce	2.9×10^{-9}	[211]
540	La	5.9×10^{-9}	[211]

Calculated values of e^2c for the Al and ternary elements, are shown, Table 5.7. The most notable result of these calculations is that the values for Al concentrations, considering $e^2c_{maximum}$, would predict the following decreasing creep resistance: AXJ530, AX44, AJ44, ACe44 and ALa44. Experimentally this is similar to the order of decreasing creep resistance: AXJ530, AX44, AJ44, ALa44, and ACe44. Considering the average solute concentration for Al, the creep resistance follows the same order and also predicts similar creep strength for AX44 and AJ44. These alloys have similar creep resistance when AX44 contains coarse C15 precipitates, whereas AX44 is about an order of magnitude more creep resistant with a fine precipitate distribution, indicating the improvement in creep strength from precipitates. For the ternary addition, direct comparisons can be made between AX44 and AXJ530 and between ACe44 and ALa44, as the diffusivities of Al and the ternary addition should be very similar in these systems. Considering the influence of solute (both Al and Ca) in the Mg-Al-Ca alloys, it is clear that AXJ530 should be more creep resistant than AX44, which is indeed the case. Likewise there should be little difference between ACe44 and ALa44 and this, too, is the observed behavior. It is therefore reasonable to conclude that both the Al and the ternary additions in solid solution are important components to creep strengthening in these alloys. The influence of the diffusivity of the solute elements will be considered in the following discussion.

Table 5.7 The e^2c term of A for viscous drag creep models.

Alloy	Al		Ternary Addition	
	$e^2c_{maximum}$	$e^2c_{average}$	$e^2c_{maximum}$	$e^2c_{average}$
AX44	0.12	0.05	0.38	0.07
ACe44	0.06	0.04	0.01	0.00
ALa44	0.04	0.04	0.00	0.00
AJ44	0.09	0.05	0.15	0.03
AXJ530	0.30	0.11	0.59	0.12

Though the diffusion coefficients are unknown, reasonable assumptions of their values can be made to allow approximate predictions between the Ca and Sr containing alloys. The calculated values of $(e^2c)/D$ are listed in Table 5.8 assume that the diffusion coefficient of Al in Mg [203] is 6.6 x 10^{-17} cm^2 s^{-1} and is the same in each alloy, and that the diffusion coefficient for Ca and Sr (in Mg) is one and two order of magnitude lower respectively (6.6 x 10^{-18} cm^2 s^{-1} and 6.6 x 10^{-18} cm^2 s^{-1}) than that for Al. Calcium and Sr have larger atomic radii than Mg, with Sr being the larger of the two. The diffusivities of the rare earths were not considered due to their near zero solute concentrations and lack of diffusivity data. From these calculations, assuming Sr has a lower diffusion coefficient than Ca, Sr would have more influence on the creep rate than Ca. AJ44 and AX44 are similar in creep resistance (with coarse precipitates in AX44), and the aluminum solute concentrations are comparable between these two alloys. Shifts in alloy composition to increase the amount of Al and the ternary additions in solution will provide additional creep strength in these alloys.

Considering the calculated values of Table 5.8 for these alloys from a viscous-glide creep model [209, 210], differences of up to three orders of magnitude in creep rate could be accounted for, considering only the influence of solute. Experimentally, the variation in creep rate is five orders of magnitude. Thus, it is expected given that other factors also influence the creep behavior. As discussed in Section 5.2.1, grain size contributes approximately one order of magnitude. In the following section the contribution of precipitates is evaluated.

Table 5.8 The e^2c/D term of A for viscous drag creep models.

Alloy	Al		Ternary Addition	
	$\dfrac{e^2c_{maximum}}{D_{Al\to Mg}}$	$\dfrac{e^2c_{average}}{D_{Al\to Mg}}$	$\dfrac{e^2c_{maximum}}{D_{x\to Mg}}$	$\dfrac{e^2c_{average}}{D_{x\to Mg}}$
AX44	1.8×10^{15}	7.6×10^{15}	5.8×10^{16}	1.1×10^{16}
ACe44	9.1×10^{14}	6.1×10^{14}	-	-
ALa44	6.1×10^{14}	6.1×10^{14}	-	-
AJ44	1.4×10^{15}	7.6×10^{15}	2.3×10^{17}	4.5×10^{16}
AXJ530	4.5×10^{15}	1.7×10^{15}	8.9×10^{16}	1.8×10^{16}

The differences in solute concentrations in the alloys studied can be attributed to the different solidification paths. Figure 5.12 shows the superimposed liquidus projection (constructed from [51, 143] after [139]) of Mg-Al-Ca and Mg-Al-Sr. Also included is the measured Al composition profile for AXJ530, AX44, and AJ44 from Scheil analysis. Plotted on the projection is the estimated solidification path (from alloy composition, the liquidus projection and thermal analysis data) for AXJ530 (black), AX44 (red) and AJ44 (blue). The partitioning of Al for each alloy is indicated from the tie line (at A, B and C) and is in good agreement with the measured compositions from the Scheil analysis.
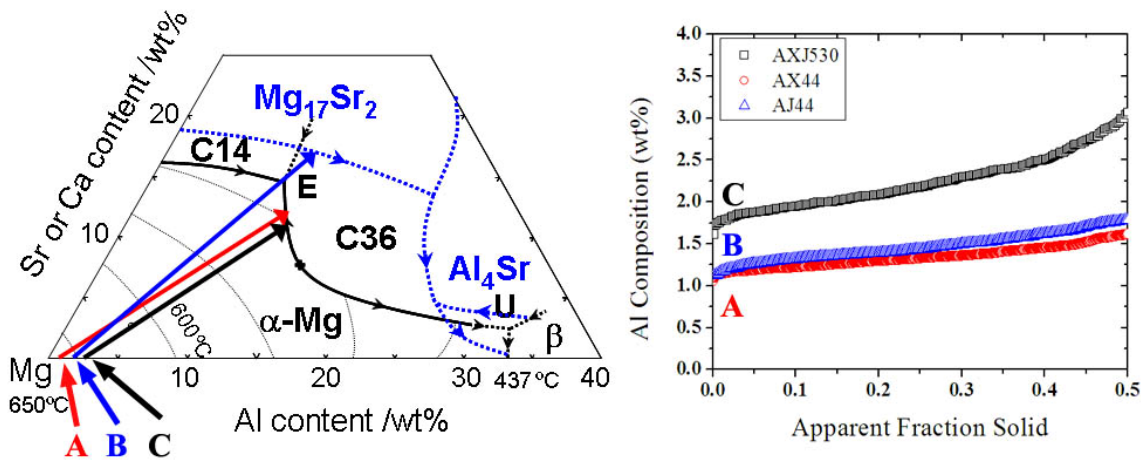
Figure 5.12 Liquidus project of Mg-Al-Ca and Mg-Al-Sr after [139] and composition profile of Al for AXJ530, AX44, and AJ44.

Considering these results, additional solute strengthening may be possible through two methods. First, the alloy composition can be shifted such that higher aluminum (and

ternary) concentrations are gained. Care must be taken with this approach. For example, in the Mg-Al-Ca system additions above ~8 Al wt% (at 3 wt% Ca) will move the solidification path past the saddle point and could lead to the formation of a less creep resistant microstructure that contains $\beta - Mg_{17}Al_{12}$. Second, a more favorable approach would be to add quaternary additions to either Mg-Al-Ca or Mg-Al-Sr affect partitioning of Al and the ternary constituent to the α-Mg phase. The additions would ideally widen the primary phase field, moving the eutectic valley further down the Mg-X (ternary addition) axis and shift the liquidus surface such that the tie-line would dictate a greater concentration of Al and ternary addition in α-Mg. From, Figure 5.12 this would rotate the tie-line counter clockwise from those already superimposed.

5.2.3   Effect of Precipitate Strengthening

The influence of the C15 – Al_2Ca precipitates (Figure 4.17 and Figure 4.18) on the creep strength of the permanent mold cast Mg-Al-Ca alloys has been measured, Figure 5.5 and Figure 5.7. Fine precipitates within the α-Mg matrix decreased the minimum creep rate by approximately an order of magnitude compared to coarse precipitates. A previous study [57] demonstrated modest (~5 times lower minimum creep rates) improvements in creep of die-cast AXJ530 through aging treatments at low temperatures (200-300 °C). Figure 5.13 compares the creep behavior of permanent mold and die-cast AXJ530 for two precipitate conditions: (1) coarse (as-permanent-mold-cast $T_{mold} \approx 383$ °C) or no precipitates (as-die-cast) and (2) fine precipitates (aged DC and as-permanent-mold-cast $T_{mold} \approx 246$ °C).

AXJ530 - Permanent Mold vs Die-Cast
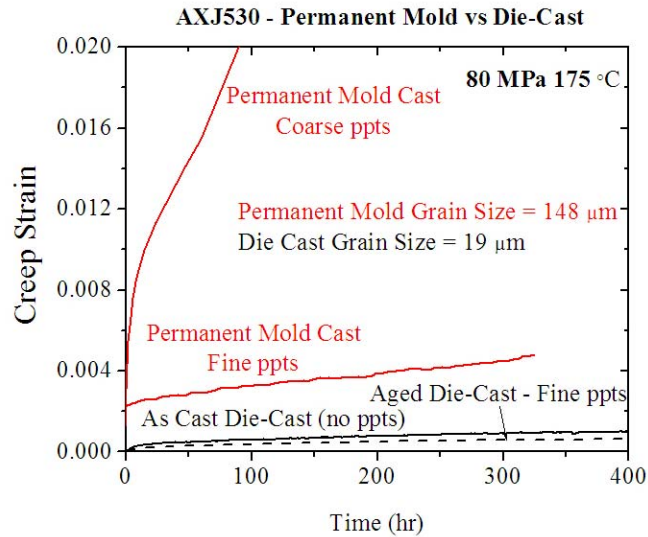
Figure 5.13 Comparison of the creep behavior for permanent mold (PM) and die-cast (DC) AXJ530.

The creep strengthening effect of the precipitates is significantly different in the permanent-mold-cast, compared to the die-cast, condition. The permanent mold cast specimens exhibited a decrease in minimum creep rate of approximately one order of magnitude from a coarse to fine distribution of the $C15$-Al_2Ca precipitates. In the die-cast condition the reduction in minimum creep rate with precipitates was somewhat less (about a factor of five). The reason for the modest increase in creep strength for die-cast, while a substantial increase for permanent mold cast is not well understood. Though not investigated in this study, precipitate distribution and dislocation interaction with the precipitates and/or grain boundaries could be explanations for the difference in creep strength influence of precipitates, and warrants further investigation.

To quantify the strengthening contribution of the precipitates the Orowan equation (5.6) was used, where G is the shear modulus, b is the Burgers vector, and L is the (average) distance between obstacles on the slip plane. Classically, the Orowan equation quantifies material strengthening through assuming that the most significant barrier to dislocation motion within the matrix is from precipitates that dislocation must cut, climb around and/or, bow and loop. This discussion assumes that the precipitates act as significant barriers to dislocations, though a diffusion accommodated bypass mechanism is operative. The shear modulus and Burgers vector at room temperature are 17.3 GPa and 0.32 nm (for basal slip), respectively [3, 213]. Proper application of the

141

Orowan equation to creep strength requires calculating the shear modulus at test temperature and making representative measurements of precipitates with respect to the slip plane.

$$\tau = \frac{Gb}{L} \qquad\qquad \text{Equation 5.6}$$

The shear modulus, μ, for the temperature of interest (448 K), is calculated using Equation 5.7 [60] where μ_o is the shear modulus (17.3 GPa) at room temperature (300 K), T is the temperature (448 K) of interest, T_m is the melt temperature (924 K), and (T_m/μ_o) (d_μ/dT) is a constant (-0.49 for magnesium [60]). This yields a temperature corrected shear modulus of 15.9 GPa (for magnesium at 175 °C (448 K)).

$$\mu = \mu_o \left(1 + \left(\frac{T-300}{T_m} \right) \left(\frac{T_m}{\mu_o} \frac{d_\mu}{dT} \right) \right) \qquad\qquad \text{Equation 5.7}$$

The precipitates observed in these alloys are plate-like in morphology and oriented along the basal plane. Slip has been reported to occur predominantly on the basal plane [36, 38-45], thus the precipitates would pose marginal obstacles to dislocations gliding on the basal plane. Conversely, to accommodate deformation in a randomly oriented polycrystalline material, slip must occur on multiple systems where precipitates become more effective barriers. It is clear that slip occurs on basal and non-basal systems, as shown in Figure 4.21, Figure 4.23, and discussed in [16, 135, 178]. Thus the strengthening effect of the precipitates should be considered on slip systems other than basal where the precipitates have a larger effective cross section than to dislocations gliding on the basal slip.

A schematic representation of the precipitates is shown in Figure 5.14. The important points to consider are: (a) the precipitates do not occupy every basal plane (b) there are large distances (with respect to basal plane separation) between precipitates and (c) viewing the precipitates from the edge-on orientation obscures precipitate density on the basal plane, making it impossible to accurately determine an average spacing (L) with respect to dislocations gliding (on the basal plane).
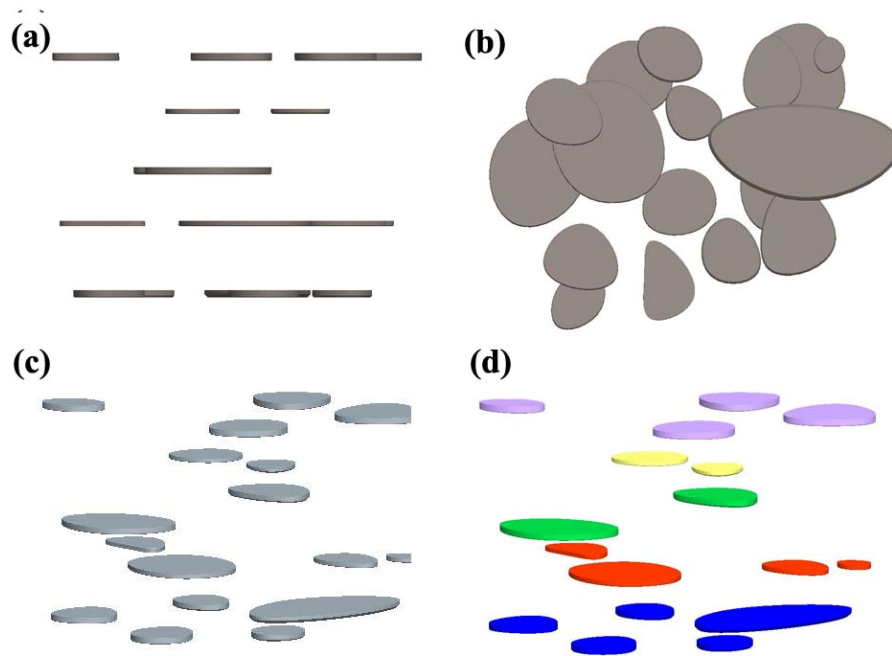
Figure 5.14 Schematic representation of C15 - Al$_2$Ca precipitates in α-Mg matrix (a) edge view, after orientation of Figure 4.17 (b) Top view where precipitate density per plane is indistinguishable (c) 3D view of precipitates and (d) 3D view where precipitates on the same plane are grouped by color. Note precipitates are several atomic planes thick indicating that there are many basal planes in α-Mg that contain few or no precipitates.

In formulating an initial representation of the strengthening effect of the precipitates the average spacing (L) will be quantified through a linear intercept method by measuring the perpendicular distance between precipitates oriented along the basal plane. This distance would be representative of the strengthening effect of non-basal dislocations. A more complete analysis would involve considering the influence of basal gliding dislocations and the non-basal dislocations that would interact more directly with the precipitates. This warrants further investigations quantifying the contribution of basal and non-basal dislocations to the creep strain.

Table 5.9, contains the results from the Orowan analysis, accounting for the strengthening influence from the precipitates. The finest observed precipitates, with an average basal plane spacing of 41 nm, had a significant influence on the resistance to dislocation motion contributing up to 124 MPa. The larger distances for the coarse precipitate are responsible for more modest increases in shear strengthening of the

materials of 25.5 MPa and 14.1 MPa. Converting these values from a shear to applied tensile stress, taking a Taylor factor for a polycrystalline aggregate ($\bar{M} \sim 3.0$ [61, 214]), values of 372, 76.5 and 42.3 MPa result. These are unreasonably high stress values in comparison to the applied load (80 MPa) and UTS (~100 to 135 MPa).

Table 5.9 Calculated Strengthening from precipitates using Orowan equation.

Mold Temperature (°C)	Spacing (nm)	G (GPa)	b - basal plane (nm)	Shear Strength (MPa)
212	41	15.9	0.32	124.1
326	360	15.9	0.32	14.1
350	208	15.9	0.32	24.5

A fine precipitate distribution has a strong influence on the creep strength of the permanent mold cast Mg-Al-Ca alloys. It can also be concluded that (L) must be misrepresented in the average perpendicular distance between precipitates. Dislocations predominantly glide on the basal plane thus the strengthening effect of the precipitates is lessened. When dislocations are active on other slip systems (i.e. prismatic or pyramidal) the strengthening effect of the precipitates is stronger. Therefore an order of magnitude decrease (in creep rate) has been shown with a fine precipitate distribution.

Future investigations that further quantify precipitate strengthening will require an understanding of the slip systems that are most active following basal (and their Burgers vector) and a representative distribution of precipitates spacing (L) (with respect to that slip system). Additional investigations of both optimal precipitation distribution in Mg-Al-Ca alloys and precipitation strengthening through alternative elemental additions are recommended. Both precipitation strengthening and solute strengthening are occurring in the Mg-Al-Ca alloys and an optimal balance of those two creep strengthening features should be investigated. Though the Mg-Al-RE have little RE in solution, beneficial effects of precipitation strengthening have been reported for non-aluminum containing rare earth additions [175, 176], especially in the heavy rare earths systems [166, 215, 216]. Elements, especially ternary additions that are readily soluble in Mg at higher temperatures and have a decreased solubility at aging temperatures are most attractive.

5.2.4   Interdendritic Morphology

The grain size, solute concentration, and precipitate density have been investigated in each alloy. These microstructural features have been associated with an increase in creep strength (die-cast over permanent mold cast AXJ530, permanent mold cast AXJ530 over AX44, and fine precipitate distribution over no precipitates) of about an order of magnitude for each microstructural feature. Estimating diffusion coefficients solute concentrations can be attributed to three orders of magnitude difference in creep rate (and following the same order of creep resistance that was experimentally observed). There is five orders of magnitude difference in creep rate across the alloys investigated. This indicates that either the diffusion coefficients estimated are conservative or other microstructural features are contributing to the difference in creep strength.   This difference may be an effect of eutectic morphology though for permanent mold cast alloys it is not a major effect. The rare earth alloys had less solute and no observed precipitates in the matrix, and five orders of magnitude higher minimum creep rates than die-cast AXJ530. They also had lower volume fractions primary magnesium and a different eutectic morphology.

The difference in eutectic morphology between alloys is distinct and has been schematically represented in Figure 5.10. The Mg-Al-Ca alloys have the C36 phase that has a semi-continuous aspect (Figure 4.8) of two distinct morphologies: interconnected plates (not lamella) and script. The plates are connected by webs that traverse the near center of the plates. The AJ44 also has a semi-continuous eutectic structure with pockets of Mg dispersed throughout. However the eutectic morphology of the two rare earth alloys is less continuous. Others [157] have reported from TEM analysis (in a die cast Mg-Al-RE alloy (AE42)) a complex body-centered orthorhombic $Al_{11}RE_3$ phase and described it as: 'quite complicated with parallel laths connect to crosswise branches. The laths are less than 0.1 μm thick and with a typical length and width of 2 μm and 0.5 μm respectively. The overall extent of a particle is usually 5-10 μm.' The study concludes that a component of the improved creep strength of the rare earth containing alloys (compared to Mg-Al-Si (AS21) alloys) is in the ability for this complex shaped phase to 'grip several neighbouring matrix grains' [157], though experimental verification of this hypotheses was not completed.

Since direct experimental evidence is lacking, additional investigations (dislocation substructure development with creep via TEM or strain mapping) are required (and recommended) to quantify the role of the eutectic structure in creep strengthening. Inferences can be made by only considering the eutectic morphology and creep resistance between alloys. The more creep resistant microstructures, AXJ530, AX44 and AJ44, have a semi-continuous morphology, where the less creep resistant alloys have a lath or block like morphology that is not continuous on the length scale of the grains. Within the literature, this strengthening technique has been attributed to pinning the grains (cells) to prevent grain boundary sliding [13, 84, 162], though no experimental evidence has been provided. As will be shown in Chapter 6, extremely limited evidence of GBS was observed in the post crept samples.

5.3   Summary

The tensile creep behavior of the permanent mold cast alloys can be ordered, for increasing minimum creep rate: AXJ530, AX44, AJ44, ALa44 and ACe44 (over the stresses and temperatures investigated). Die-cast AXJ530, with a similar microstructure, except a smaller grain size than permanent mold AXJ530, was the most creep resistant. All alloys exhibited a power-law creep behavior with the permanent mold cast AJ44, AX44, and AXJ530 having a stress exponent (for $\sigma = 40 - 100$ MPa at 175 °C) between 14.2 and 17.5. Only two stresses were investigated for the die-cast AXJ530, but the stress exponent appears lower n ≈ 6.8 and close to that reported for die-cast AX53 (n=8.5) [84].

The microstructural characteristics were quantified considering the creep behavior of each alloy. The grain size was found to have a significant effect on the creep strength, where an order of magnitude decrease in grain size (158 μm to 19 μm) lead to an order of magnitude lower minimum creep rate. This is at odds with all diffusion/GBS creep models where decreases in grain size are attributed to faster creep rates and grain size is not accounted for in power-law creep models. The solute concentration (both the Al and ternary addition) was also found to have a significant influence on creep strength. AXJ530, with the highest concentrations of Al and Ca in solution was an order of magnitude more creep resistant than AX44 with the same microstructure. Through

estimations of diffusion coefficients and considering solute concentrations, solute-induced differences in minimum creep rates of up to three orders of magnitude were predicted while measured creep rates varied by five orders of magnitude. A fine distribution of precipitates (C15-Al$_2$Ca) in the matrix of permanent mold cast Mg-Al-Ca alloys contributed to an order of magnitude improvement in creep rate. Thus the microstructural features evaluated: grain size, solute in the α-Mg, and precipitates account for the majority of the creep resistance in these alloys. The same distribution in die-cast AXJ530 was less beneficial, with a factor of five lower minimum creep rate. Precipitates were not observed in the permanent mold cast AJ44, ACe44 and ALa44. The eutectic structures are distinct between the alloys but their effect on creep resistance could not be isolated and future investigations to quantify the role of this structure in creep are recommended.

In Chapter 6, the role of microstructure on creep strain distribution is investigated. Strain mapping experiments on the permanent mold and die-cast Mg-Al-Ca alloys are presented. The strain was found to be distributed heterogeneously on the scale of the grains and was indicative of strain hardening during primary creep. Near the minimum creep rate the strain localized along grain boundaries. Where the resolved shear stress was sufficiently different between adjacent grains, localized damage as cavities/voids and cracks were nucleated. As additional creep strain accumulated, the creep rate accelerated, and additional damage was nucleated throughout the sample. Grain size influenced the plastic strain distribution during creep, where the die-cast AXJ530 had a finer strain distribution than coarse grained AXJ530. These results indicate that additional creep strengthening of these alloys should focus on strengthening the primary α-Mg grains. Extremely limited evidence of grain boundary sliding was observed.

Chapter 6

Creep Strain Distribution and Localized Damage Accumulation

This chapter reports the results of a set of studies on creep strain distribution, at the grain scale, using a surface displacement technique. The first section discusses the role of local microstructure and strain heterogeneities in creep of permanent mold cast Mg-Al-Ca alloys (AX44 and AXJ530). Next, evidence of localized creep damage accumulation, on the length scale of the grain size is presented. Following this are results of the creep strain distribution and localized damage accumulation on a die-cast AXJ530 specimen with comparison to the as-permanent-mold-cast behavior. The chapter ends with a summary and conclusion in section 6.6, including discussion of the relationships between grain size, creep behavior, and measured strain heterogeneities.

The strain mapping technique described in Chapter 3 was successfully applied to tensile creep testing for temperatures up to 175 °C and times greater than 1000 hours. Creep strain accumulation was found to be heterogeneous at the scale of the grain size, not the cell size, in the permanent mold cast alloys. Strain accumulated primarily within α-Mg grains and was up to ten times greater in magnitude within individual grains than the bulk strain. There was excellent agreement between the average tensile strain measured by strain mapping and the bulk strain measured by conventional extensometry.

Localized creep damage developed in these alloys at or near the minimum creep rate (near 1% creep strain for AXJ530). The damage observed in near-grain-boundary regions consisted of cavities and cracks. The damage primarily accumulated between grains with different resolved shear stresses and was macroscopically (on average) transverse to the applied stress (though microscopically the damage was oriented perpendicular up to 45° with respect to the applied load). Plasticity was observed as slip offsets contained within the grains predominately at the near grain boundary regions. Slip bands were observed to span several neighboring α-Mg cells and interdendritic regions.

6.1.1   Localized and Bulk Creep Strain Comparison

The tensile creep strains (ε_{yy}) from the strain mapping, when averaged over several regions, agree with the bulk strain (ε_y) measurements. Other studies [22, 23, 184] utilizing this technique for room temperature tensile testing, also report good agreement between the calculated tensile strain (ε_{yy}) and bulk strain (ε_y) measurements from extensometry. Secondly, localized damage observed on the surface is observed at the location of ultimate specimen failure. This is an indication that damage observed on the surface occurs simultaneously with damage throughout the bulk.

The measured bulk strain from extensometry and the average tensile strain (ε_{yy}) calculated from strain mapping are in good agreement when averaged over several regions, as shown in Table 6.1. The measurements reported are for permanent mold cast AXJ530 ($T_{mold} \approx 371$ °C), Figure 6.5. The reported strains of Table 6.1, were the bulk strains from extensometry ($\varepsilon_{y\text{ - extensometry}}$) and the total average of the averaged tensile strain ($\varepsilon_{yy\text{ - averaged}}$) for each of the four regions investigated (taken at each step of the creep curve). The total area of these four regions was approximately 0.825 mm^2.

Table 6.1 AXJ530 $T_{mold} \approx 371$ °C, Figure 6.5, bulk measured creep strains (from extensometry) against averaged (4 regions) 'ε_{yy}' strains from strain mapping. Each line denotes a step, or between two steps, within the creep test.

Creep Step	% Creep Strain ($\varepsilon_{y\text{ - extensometry}}$)	Strain Mapping ($\varepsilon_{yy\text{ - Averaged}}$)
AB	0.32	0.37
AC	0.70	0.79
AD	1.00	1.24
AE	1.15	Not Calculated
BC	0.38	0.56
CD	0.15	0.26

As the sample accumulates strain, damage, in the form of cavities and voids, is formed. These cavities are continually formed, with limited growth (further discussed in Section 6.3.1). Damage formation and coalesce both on the surface and through the interior of the sample, leads to eventual failure. If the strain and damage accumulated on the surface was diminished compared to that within the bulk, then the location of creep

149

rupture would be independent of observed damage on the surface. Conversely if the surface was accumulating both strain and damage at levels greater than that of the bulk, failure would occur at the surface region of highest damage, due to the decreased cross section and lessened load carrying capacity. If both the surface and bulk are accumulating damage concurrently, failure would occur at a region where surface damage is high, but not necessarily at the location of greatest observed density, since damage below the surface cannot be directly investigated and accounted.

Figure 6.1, shows a section of the gage of the permanent mold cast AXJ530 (T_{mold} ≈ 390 °C) with (a) an overview of the gage surface, prior to failure (end of step 2, Figure 6.8) at the location where failure occurs. Figure 6.1b has this same region with the path of failure outlined on the surface. Figure 6.1c depicts a separate region of the gage (also at the end of step 2), where the damage on the surface was observed to be the most severe prior to failure. In this region damage is observed nearly continuous across the entire surface of the gage generally transverse to the applied load. Note that this region of damage is several millimeters away from the final region of failure. The failed sample, Figure 6.2, occurred at a location where the degree of surface damage was elevated but not at the location where the surface damage was most severe (as in the region depicted in Figure 6.1c). Since failure did not occur at the location of highest observed surface damage, or at a location with relatively limited observed surface damage, the creep strain and damage accumulation must occur within the bulk and surface concurrently.
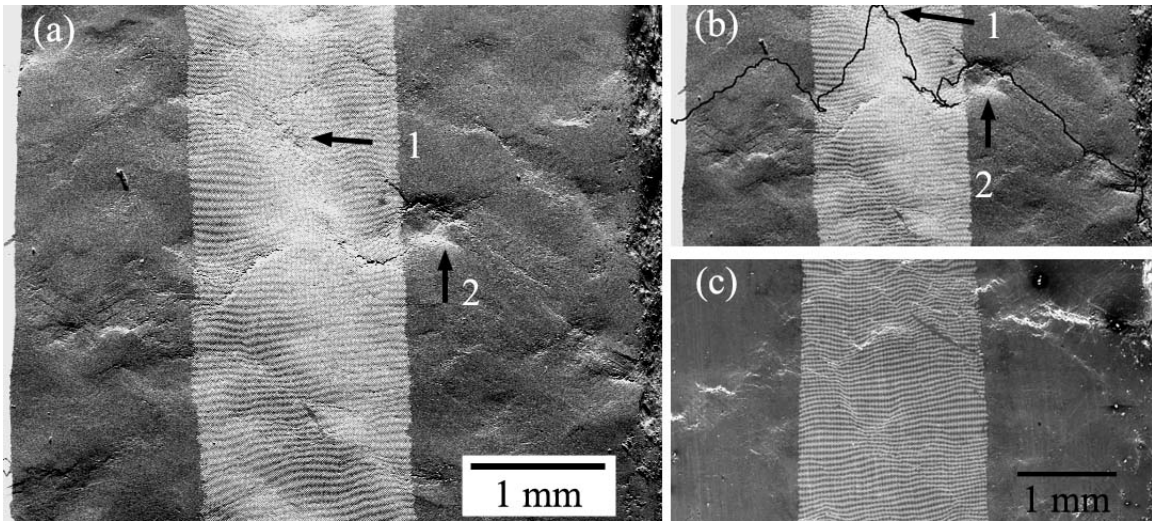
Figure 6.1 Crept AXJ530 (T$_{mold}$ ≈ 390 °C) for (a) Gage surface at step 2 prior to failure. (b) Denotes the approximate location of crack path from region (a) on the surface after failure. (c) A separate region of the sample at step 3 (failure), where the greatest degree of localized surface damage was observed across the gage. This region is several millimeters away from the failure region outlined in (b). The tensile loading direction is in the vertical.
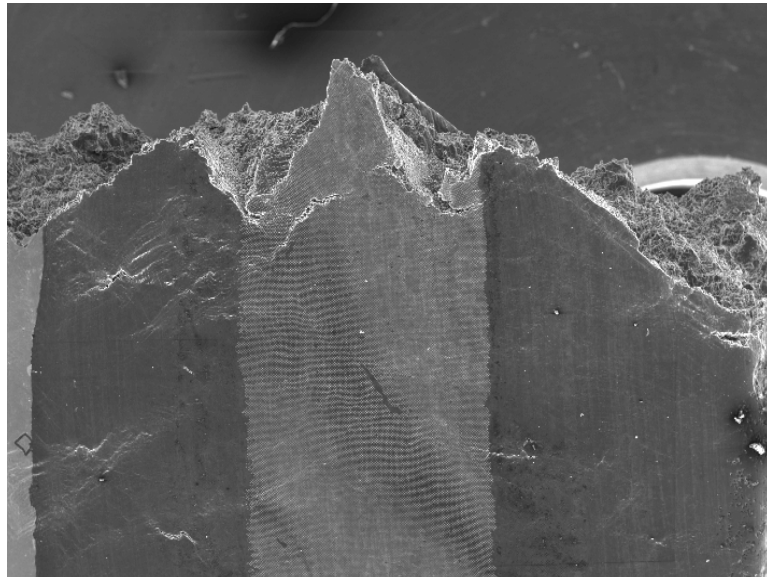
Figure 6.2 Failure region of AXJ530 sample 29 from Figure 6.1b.

6.2   Role of Local Microstructure in Creep

Figure 6.3 shows a portion of the gage region for a creep sample of permanent mold cast AXJ530, where the underlying microstructure and deposited grid are observed prior to creep. Note that the scale of the grid is sufficiently fine to measure marker displacement in neighboring cells (and grains) and displacements across cells and grain

boundaries. Figure 6.4 shows a portion of the gage after creep, at 10% strain to failure, where it is observed that the interdendritic region does not disrupt the strain distribution. A few of these locations have been indicated with black arrows. Further evidence and explanation of the role of the grain structure on strain distribution is discussed in Section 6.2. Also observed in this image are several regions of localized damage, where cavities have formed.
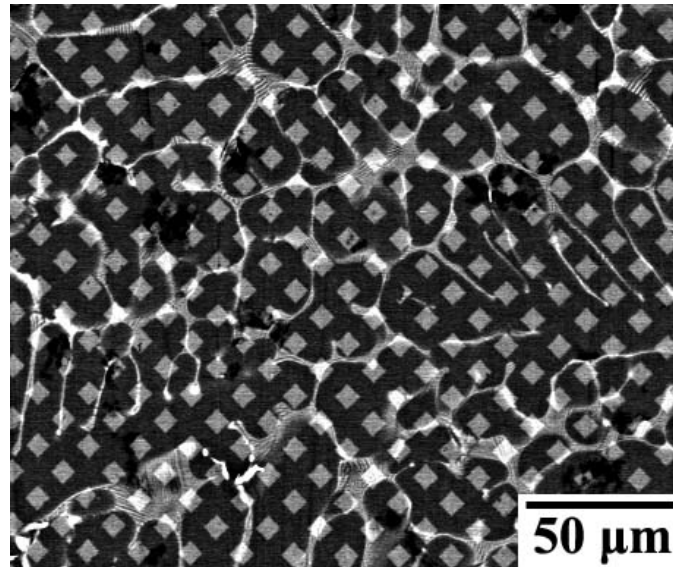
Figure 6.3 Strain mapping grid deposited on surface of a permanent mold cast AXJ530 creep sample prior to testing.
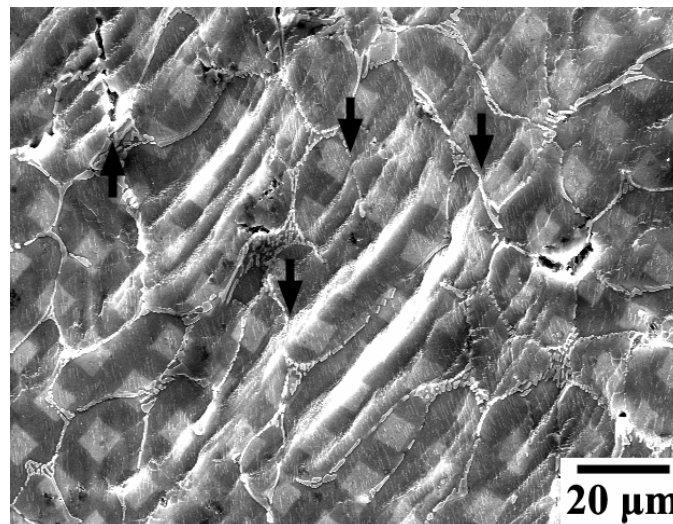
Figure 6.4 Permanent mold cast AX44 crept to 10% strain (failure) with slip offsets (indicated with arrows) spanning several cells.

Strain distributions that developed during creep were characterized in as-permanent-mold-cast AXJ530 and AX44. As described in previous chapters, the Mg-Al-Ca alloys AX44 and AXJ530 have nearly the same microstructure but with different solute concentrations. AXJ530 had an order of magnitude lower creep rate attributed to an increased solute concentration (Section 5.2.2) than AX44.

Creep tests were periodically interrupted to observe the microstructure and measure grid displacements at low strains (< 1.6%) on AXJ530 – $T_{mold} \approx 371$ °C, intermediate strains (1-3%) on AXJ530 – $T_{mold} \approx 390$ °C, and high strains (3-10% (failure)) on AX44 – $T_{mold} \approx 346$ °C. The results of these tests are presented in the three following sub-sections.

There are several notable characteristics of the strain contour plots presented here. The tensile direction (y) in all plots is vertical. All strains maps presented show the calculated Von Mises strain. Comparisons are made between the tensile strain (ε_{yy}) from strain mapping and the bulk tensile strain (ε_y) from extensometry and are indicated in each section. The strain maps, except where stated, are displayed with the pre-crept microstructure visible beneath the strain contour map.

The color contours of the strain map are representative of different degrees of strain. In all cases the regions of highest strain are represented by red and lowest strain are dark purple to black. The scale bar on the left of each strain map is scaled to the maximum and minimum strain observed in that individual plot. It is not normalized to all other strain plots presented. Therefore, when making comparisons between strain contour plots, care must be taken to compare the relative measured strain (and the corresponding color) with respect to each image (e.g. red in one plot may represent 5% strain where in another plot red may represent 20% strain and blue could represent 5% strain).

6.2.1   Permanent Mold Cast AXJ530 – Low Creep Strains (< 1%)

The creep behavior at 80 MPa (78 MPa) and 175 °C of the as-permanent-mold-cast AXJ530 ($T_{mold} \approx 371$ °C) is shown in Figure 6.5. The test has been periodically interrupted (cooled and unloaded) to measure grid displacement and inspect microstructure. Each loading and unloading strain step has been labeled on Figure 6.5.

At the beginning of each reload there is a stage of primary creep attributed to recovery during sample heating prior to reapplying the load. Strain contours were calculated at each step and where pertinent between steps (e.g. step 2 to 4). Four distinct regions of the gage were tracked at each step. Two of these regions, where strains contours were calculated for each step, are shown in Figure 6.6 and Figure 6.7.
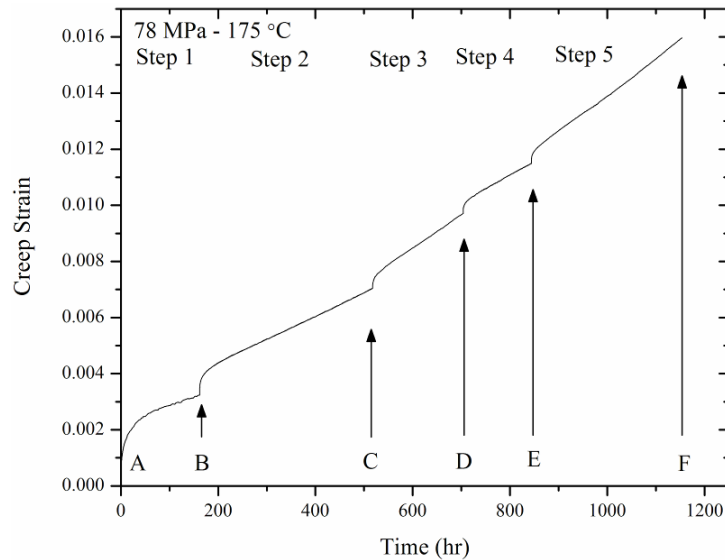
Figure 6.5 Creep curve for AXJ530 – $T_{mold} \approx 371$ °C with (5) steps used to periodically investigate the strain heterogeneity.

Figure 6.6(a,b) and Figure 6.7(a-f), show that the creep strain accumulation is heterogeneous on the scale of the grain size, with some grains accumulating significantly above-average strains while adjacent regions, also on the length scale of the grain size, accumulated very minimal creep strain. The regions of high creep strain accumulation, for example on the right side of Figure 6.6a,b, accumulate insignificant additional strain during subsequent creep strain steps, Figure 6.6c-e. This indicates that a grain strain hardens and once hardened the load is shifted to other grains. This same behavior was observed in other regions of the gage, Figure 6.6.

Quantifying the magnitude of the strain localization within a field of view with respect to the average tensile strain (ε_{yy}) from strain mapping and bulk strain, provides a measure of severity of the strain concentration. In Figure 6.6a the grain on the right side of the figure, has accumulated ~2-2.5 % creep strain (ε_{yy}), approximately ten times greater than the bulk creep strain (ε_y) of (0.3%), and double the average strain (ε_{yy}) in the

154

field of view (0.9%). These degrees of strain localization are similar across the different microstructural regions observed. From Figure 6.7a, the average strain for the grain at the right and the grain at the middle- top is approximately 1.5 %. This is five times the bulk creep strain measured at this step (0.3%) and two to three times the average strain (ε_{yy}) of 0.67% in the field of view.

One check to ensure consistency in the strain mapping results was to calculate the strain contours for each step (i.e. step 1, step 2, etc) and then compare the sum of the measured strain (from each contour) to the strain determined calculating directly from the first step to the last step (i.e. step 1 to 5). Figure 6.6 show the same regions on the gage for each step (i.e. Figure 6.6a is for step 1, Figure 6.6b is for step 2, etc.). The same is true for Figure 6.7 at different region on the gage. Figure 6.6f and Figure 6.7f show the calculated strain contour maps calculating step 1 directly to step 5 (from point A to F on Figure 6.5). Examining the strain calculated from Figure 6.6a and b, steps 1 and 2, for the grain on the right, an average Von Mises strain of approximately 2 and 1.5 %, respectively, is reported. Insignificant additional strain is observed in this grain for additional creep strain, steps 3-5, Figure 6.6c-e, respectively. Considering step 1 directly to step 5, Figure 6.6f, this grain accumulated an average (Von Mises) strain of ~3.5 %, which is in agreement with the linear combination of each step, specifically 1 and 2 where 2% and 1.5% creep strain was calculated in this grain, respectively.
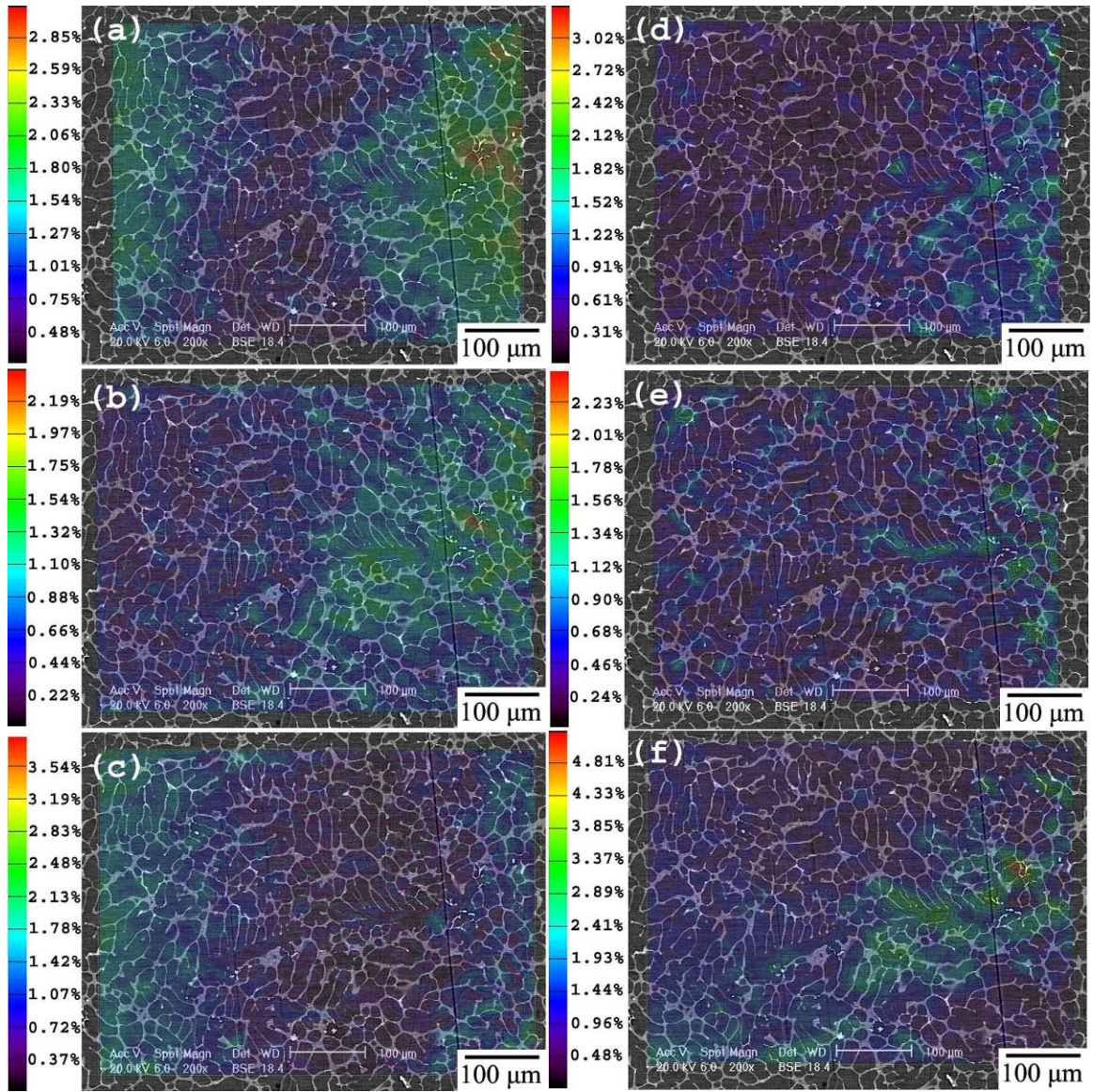
Figure 6.6 AXJ530 ($T_{mold} \approx 371$ °C, grain size ≈ 157 μm) creep strain (Von Mises) accumulation for one locations at steps and strains of (a) A to B, $\varepsilon_{y-total} \approx 0.32\%$ (b) B to C, $\varepsilon_{y-total} \approx 0.70\%$ (c) C to D, $\varepsilon_{y-total} \approx 1.00\%$ (d) D to E, $\varepsilon_{y-total} \approx 1.15\%$ (e) E to F, $\varepsilon_{y-total} \approx 1.6\%$ and (f) accumulation of step 1 to 5, A to F.
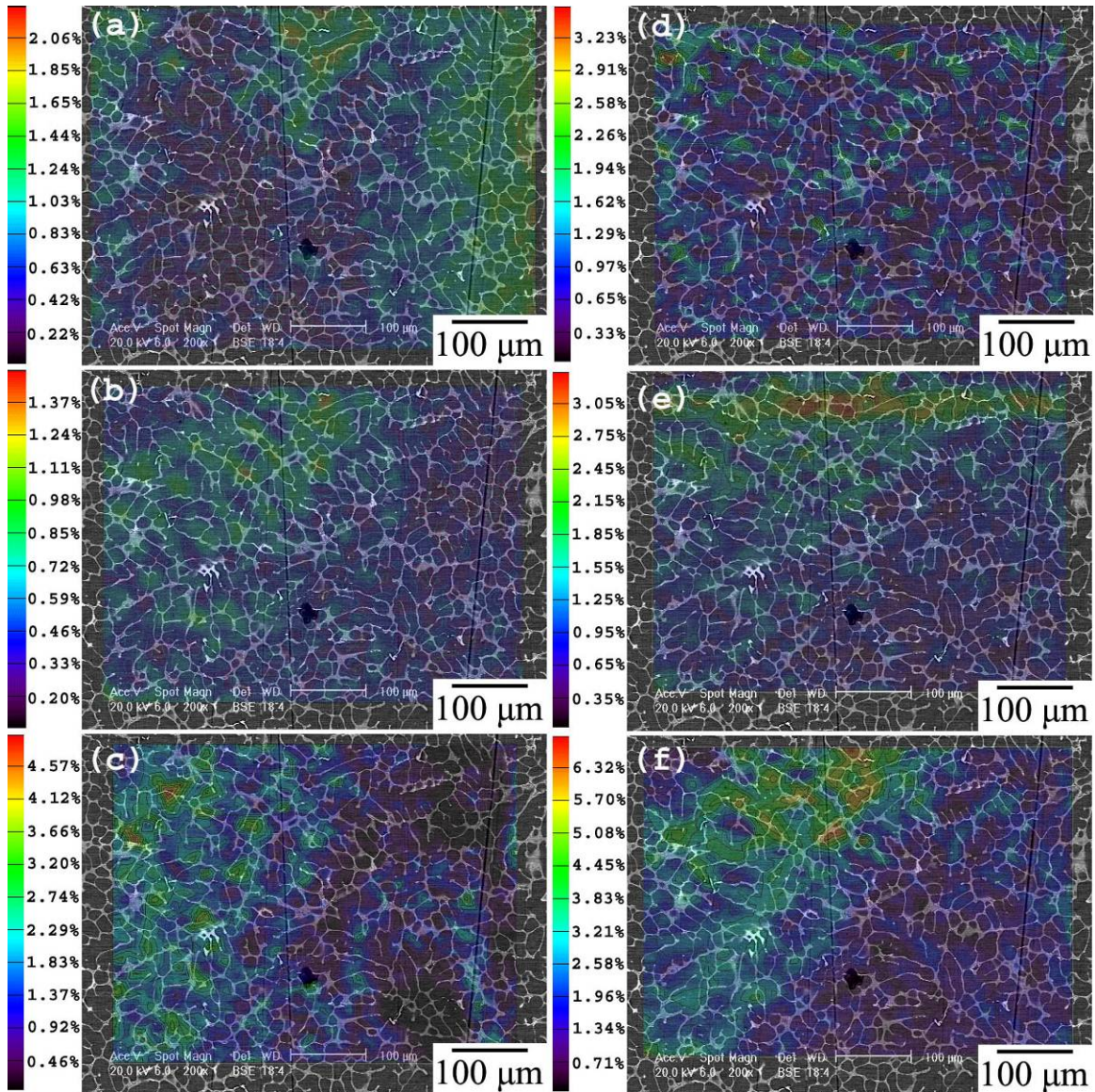
Figure 6.7 AXJ530 ($T_{mold} \approx 371$ °C, grain size ≈ 157 μm) creep strain accumulation for second location at steps and strains of (a) A to B, $\varepsilon_{y \text{ - total}} \approx 0.32\%$ (b) B to C, $\varepsilon_{y \text{ - total}} \approx 0.70\%$ (c) C to D, $\varepsilon_{y \text{ - total}} \approx 1.00\%$ (d) D to E, $\varepsilon_{y \text{ - total}} \approx 1.15\%$ (e) E to F, $\varepsilon_{y \text{ - total}} \approx 1.6\%$ and (f) accumulation of step 1 to 5, A to F.

6.2.2   Permanent Mold Cast AXJ530 – Intermediate Creep Strains (1 – 3 %)

The creep curve at 80 MPa and 175 °C of the as-permanent-mold-cast AXJ530 ($T_{mold} \approx 390$ °C) is shown in Figure 6.8. This test differs from the previous test AXJ530 ($T_{mold} \approx 371$ °C) in that it was crept to higher levels of creep strain prior to investigating the creep strain distribution. The first interruption was at 1.2% creep strain, followed by additional strains steps of 1.1% (step 2) and 0.7% (step 3 to failure).

157
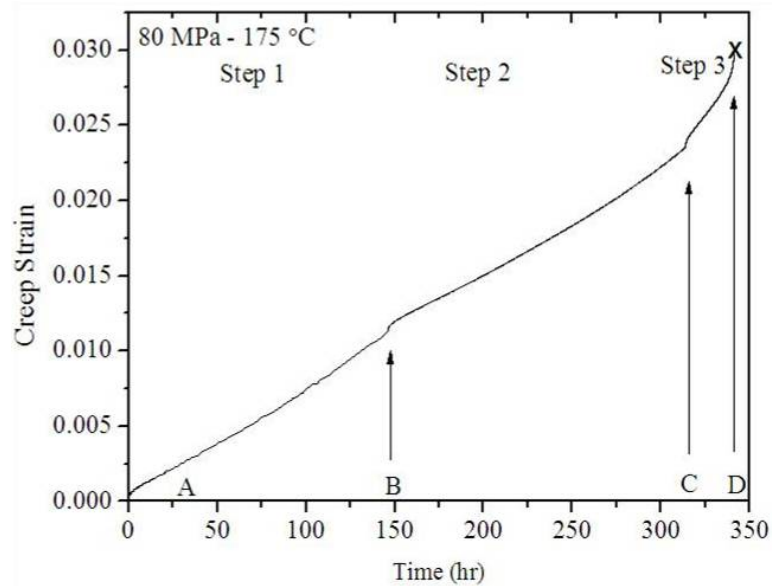
Figure 6.8 Creep curve for AXJ530 – T$_{mold}$ ≈ 390 °C with 3 steps used to periodically investigate the strain heterogeneity at intermediate levels of strain.

The creep strain (Von Mises) distribution plots for this test are shown in Figure 6.9. The strain contour plots are presented in the same manner as in the previous section. As the bulk creep strain increases, the strain remains heterogeneous up to failure, as expected, on the grain size length scale. The strain concentrations are similar to that at the lower strains. At the end of step 1 the bulk creep strain is about 1.2 %. Considering the region of highest strain (10.3%), it is ten times greater than the bulk strain (1.2%). The average strain measured for the field of view (4.5%) is four times greater than the bulk creep strain.

As bulk creep strain increases, for times beyond that to reach the minimum creep rate (~ 1%), strain concentrates within bands. For example in Figure 6.9, this occurs at the region of high strain (yellow and red) oriented at about 45 ° to the loading direction (across the middle of the field of view). This domain measures ~250 μm long and 30-50 μm wide. The average measured grain size in this material is 147 μm with the interdendritic grain boundary region 1-10 μm wide. Though it is not evident from the figure, these bands extend across grain boundaries. Direct evidence of this is shown later, in Section 6.3.2, where the grain boundaries are clearly indicated (e.g. shown in Figure 6.24 as the pileup of slip offset adjacent to the grain boundary).

As the specimen is subjected to additional creep strain this region continues to accumulate strain, as observed in Figure 6.9a-c, and the load is not shifted as seen in the early stages of creep straining, prior to reaching the minimum creep rate. At the end of step 2, the two regions of greatest strain (~10%), are at each end of this localized band of strain. These two regions of elevated strain nucleate damage, as shown in Figure 6.10. At the stage immediately prior to failure, the majority of the creep strain in this field of view is localized within the domain. Further support that the strain is concentrating along grain boundary at greater creep strains will be provided in the subsequent sections. The important points are that strain accumulates heterogeneously and that the regions of highest strain are where damage first appears.
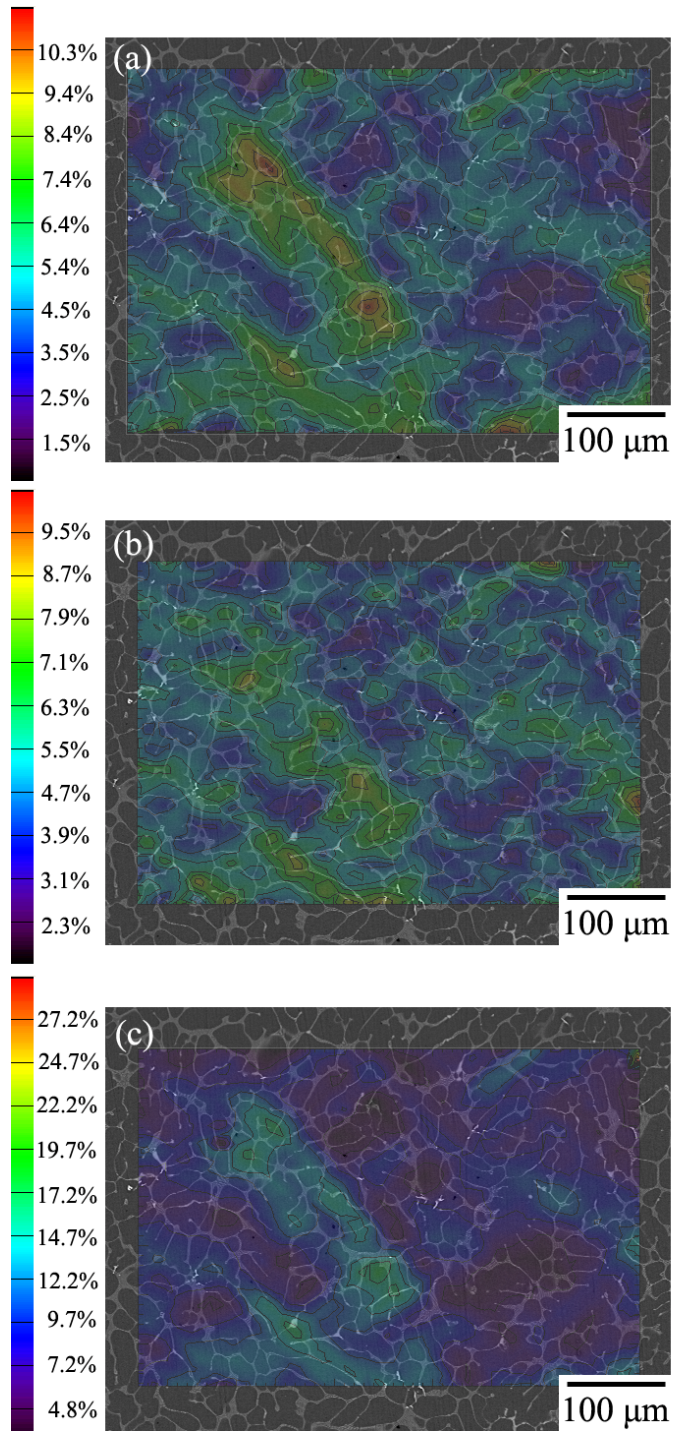
Figure 6.9 AXJ530 ($T_{mold} \approx 390$ °C, grain size ≈ 157 μm) creep strain accumulation. Strain contours at steps and strains of (a) A to B, $\varepsilon_{total} \approx 1.2\%$ (b) B to C, $\varepsilon_{total} \approx 2.3\%$ (c) C to D, $\varepsilon_{total} \approx 3.0\%$ (Failure).
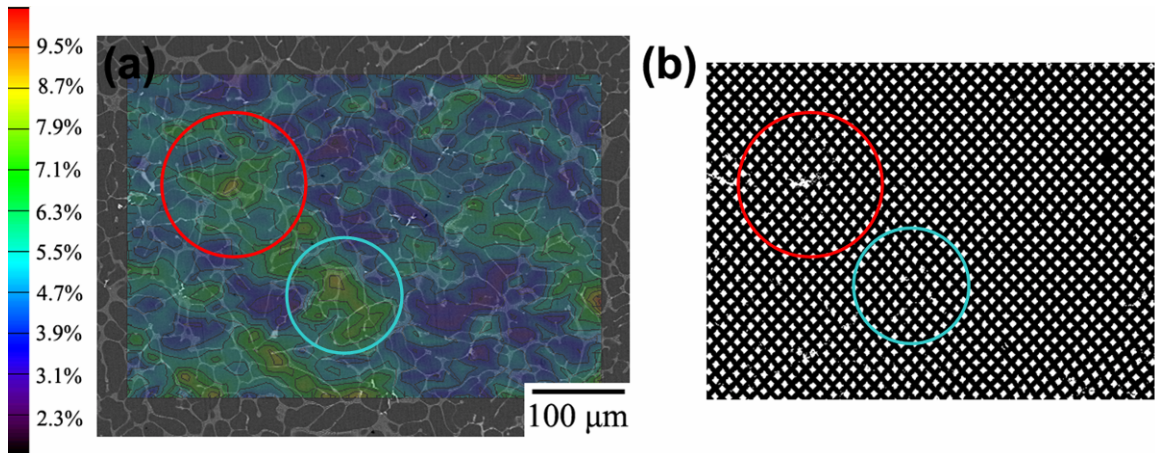
Figure 6.10 AXJ530 ($T_{mold} \approx 390$ °C) for (a) Strain distribution plot step 2 ($\varepsilon_{total} \approx 2.3\%$) and (b) strain markers of same region step 3 ($\varepsilon_{total} \approx 3.0\%$ (Failure)). Note that the regions of high localized strain (circled in red and blue), develop localized damage.

6.2.3 Permanent Mold Cast AX44 – Elevated Creep Strains (>3%)

The creep behavior at 80 MPa and 175 °C of the as-permanent-mold-cast AX44 ($T_{mold} \approx 346$ °C) is shown in Figure 6.11. This alloy has a higher creep rate (about an order of magnitude) than AXJ530 (of the two previous sections), though the microstructures (except for solute concentration), are similar. AXJ530 has a higher concentration of Al and Ca in the α-primary grains, most significantly at the near grain boundaries, leading to creep strengthening from solute (section 5.2.2). This work thus agrees that near-grain-boundary strengthening is a mechanism for the improved creep strength, as suggested by Moreno et al. [159], higher localized strains at the near grain boundary region are observed in AX44 compared to AXJ530 (due to the decreased concentrations of the solute). Dislocations would be more mobile in AX44, than in the solid strengthened near grain boundary regions of AXJ530, leading to greater ductility and lower creep strength.

The bulk creep strain accumulated in AX44 was significantly higher prior to the tests being interrupted compared to the previous two sections on AXJ530 ($\varepsilon_y \sim 7\%$ compared to $\varepsilon_y \sim 1.3\%$). The AX44 alloys had significantly greater creep ductility than the AXJ530 (section 5.1). The creep curve for AX44 ($T_{mold} \approx 346$ °C) is shown in Figure 6.11.
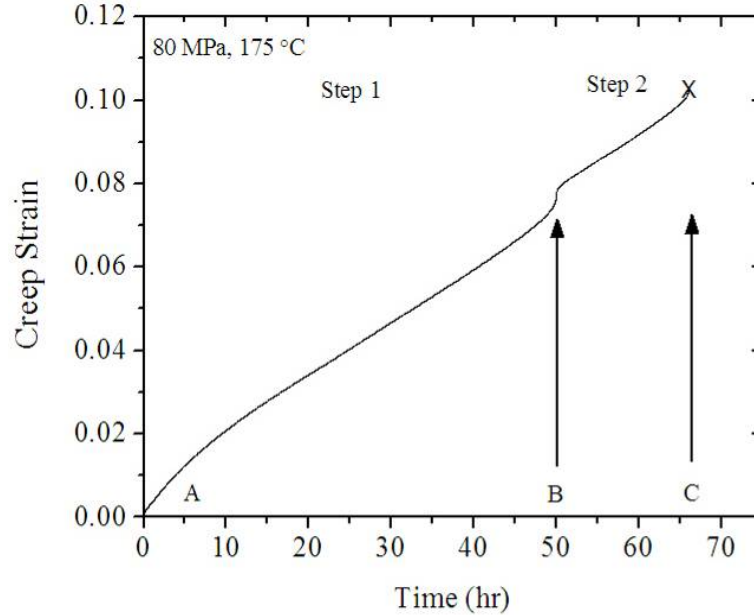
Figure 6.11 Creep curve for AX44 ($T_{mold} \approx 346$ °C) with two steps used for periodic investigations of the microstructural strain heterogeneity.

The creep strain (Von Mises) distribution for this test is shown in Figure 6.12. The strain contour plots are presented in the same manner as in the previous sections. Again, as for AXJ530 strain accumulated heterogeneously on the length scale of the grains within the microstructure. The localized strain ε_{yy} measured (22 - 26%) was approximately four times greater than both the bulk strain (ε_y) measured from extensometry (7.8%) and the average strain (ε_{yy}) in the field of view (6.1%). An observable difference for this alloy is that the highest localized strain (Von Mises) was measured at 40%, and strains of this magnitude (30 to 40%) were observed in other regions on this sample. The regions surrounding the high strain concentrations accumulated ~ 5-6% creep strain. For the AX44, the high strain regions (30 to 40%) did not have observable localized damage in all cases, indicating a greater degree of ductility than in the AXJ530 alloys. The increase in ductility is also evident in comparison of the elongation to failure, the AXJ530 accumulated 3% creep strain, where the AX44 accumulated 10% creep strain (to failure). These results are consistent with the Scheil analyses (section 4.5) and solute creep strengthening (section 5.2.2) where AXJ530 has increased solute concentrations compared to the AX44 and best creep resistance.

.

162
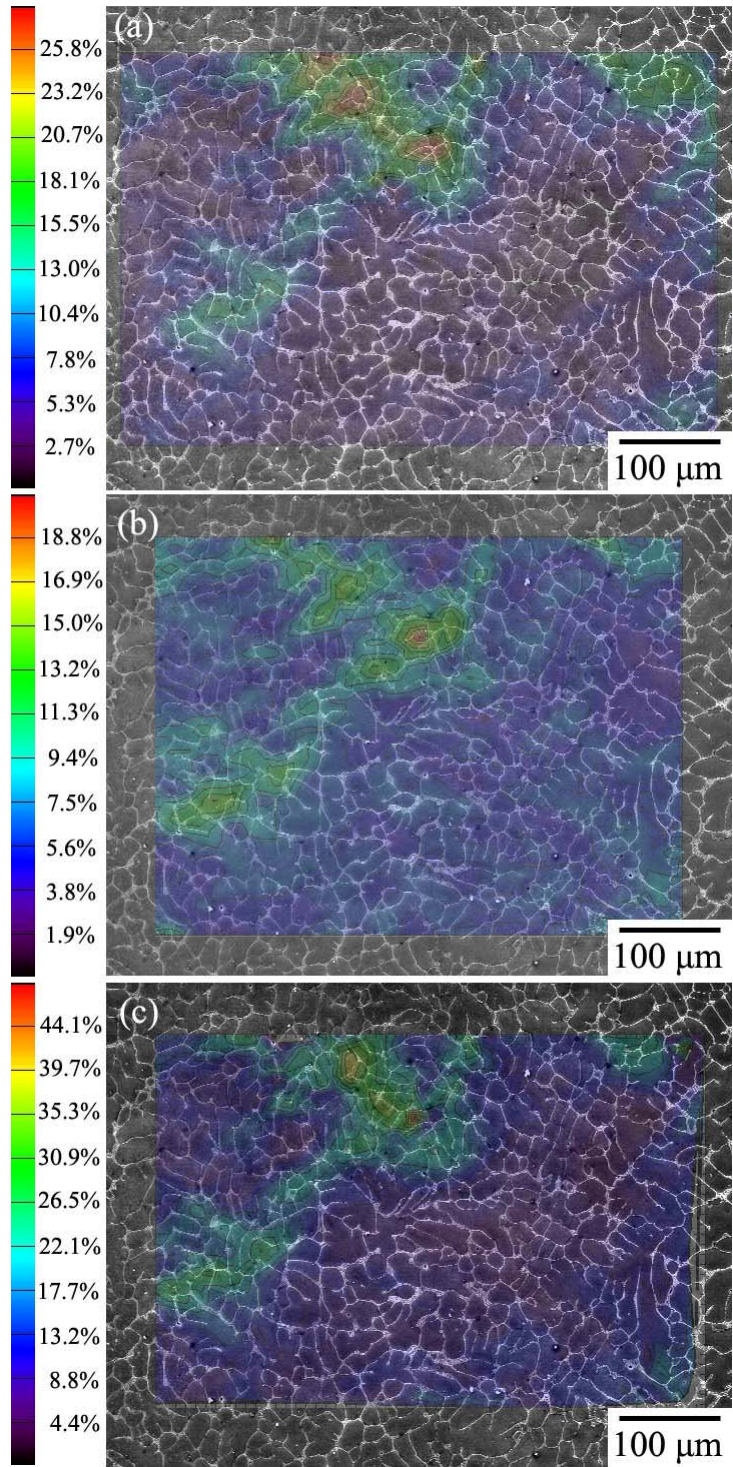
Figure 6.12 AX44 strain distribution for (a) step 1, 7.8% strain (b) step 2, 2.2% strain and (c) the combination of step 1 and 2, 10% strain to failure.

6.3   Localized Damage Accumulation

This section discusses the development, morphology, heterogeneity and microstructural influence of the localized damage accumulation and deformation observed in the as-permanent-mold-cast Mg-Al-Ca alloys. Damage was observed as cavities/voids and cracks, and plasticity was observed as slip offsets. The first section focuses on the morphology and development of creep damage. Next an examination of the heterogeneity of damage is presented. The final discussion is on the influence of microstructure to creep damage accumulation and deformation.   Each sample investigated for damage exhibited similar creep behavior (i.e. development of strain heterogeneities). It is concluded that there is no difference in creep mechanisms between alloys tested at the stress and temperature of 80 MPa, 175 °C. All localized damage results are presented independent of the alloy and sample, with that information included in the captions for completeness and reference.

6.3.1   Development and Morphology of Localized Damage

Localized damage, shown in Figure 6.13, is first observed at or near the minimum creep rate (~1% strain). The creep strain behavior of these samples has been reported above in Figure 6.5 for the sample shown in Figure 6.13a and in Figure 6.8 for the sample shown in Figure 6.13b/c. Figure 6.13 shows three montages of the gage each at a different creep strain, where Figure 6.13a is at 1 % creep strain (AXJ530, $T_{mold} \approx 371$ °C) Figure 6.13b is at 2.3% creep strain (AXJ530, $T_{mold} \approx 390$ °C) and Figure 6.13c is at 3.0% creep strain (AXJ530, $T_{mold} \approx 390$ °C). The surface of the gage is overall free of large out of plane offsets and has only a few locations exhibiting damage (indicated by black arrows). The gage of the sample prior to 1% creep strain (not shown, but investigated at 0.7% creep strain (ε_y)) had no evidence of this localized damage observed at later creep strains. Subjecting the sample to additional creep strains (beyond 1%) caused additional damage to be formed. This damage is on average transverse to the applied load and can clearly be seen in Figure 6.13b and c for creep strains of 2.3% and 3.0% (failure), respectively. Direct comparisons may be made between Figure 6.13b and c; they are the same sample gage at two successive creep strains. Note limited growth in the majority of the localized damage, indicating that damage is nucleating more rapidly

than it grows and links up with damage coalesce occuring late in the creep life of the sample. Also, the localized damage is very heterogeneous with many regions of the gage having little and no observable damage.
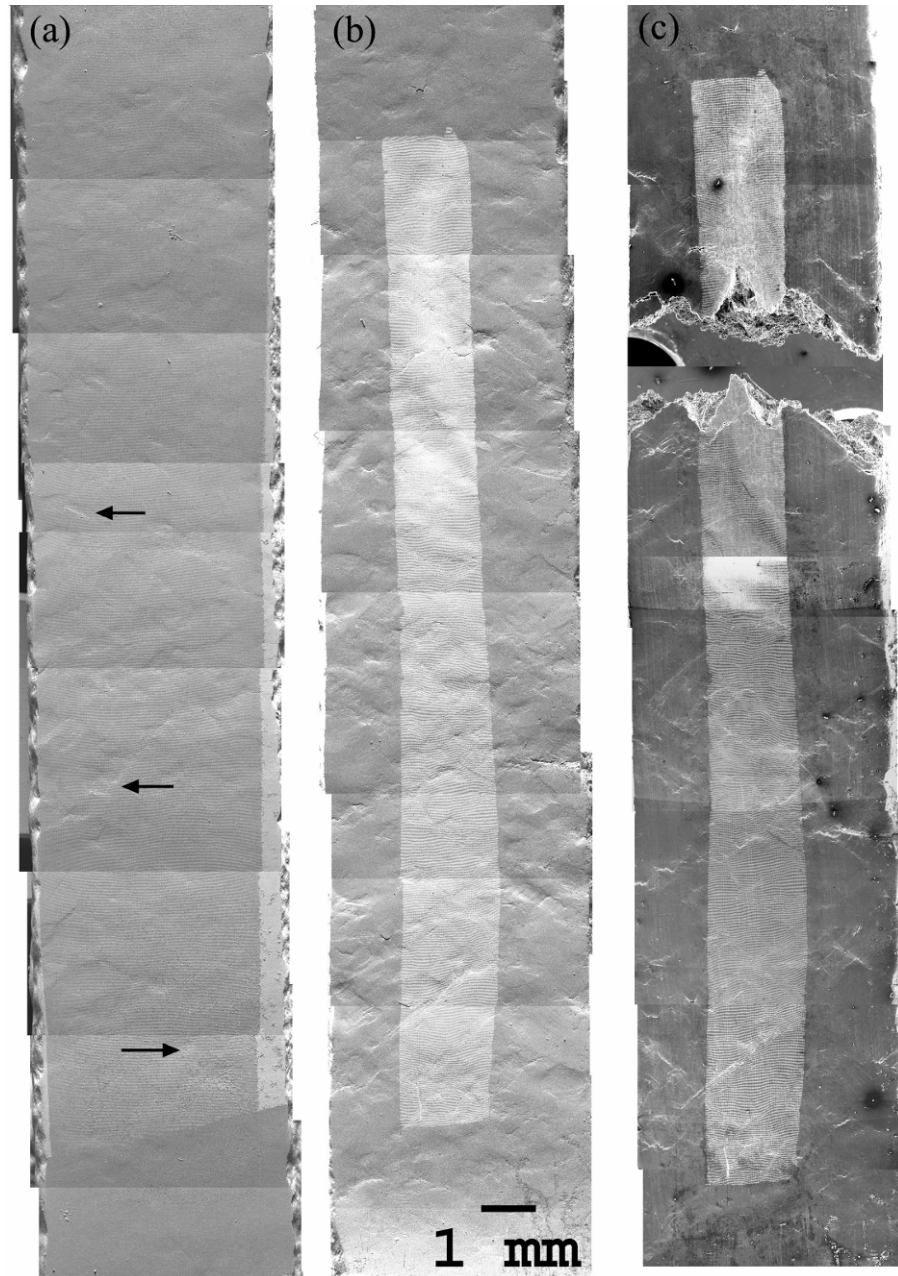
Figure 6.13 Gage section of crept AXJ530 for (a) $T_{mold} \approx 371$ °C at step 3 ($\varepsilon_{total} \approx 1.0\%$) and (b) $T_{mold} \approx 390$ °C at step 2 ($\varepsilon_{total} \approx 2.3\%$) and (c) $T_{mold} \approx 390$ °C at step 3 ($\varepsilon_{total} \approx 3.0\%$) failure. Arrows (a) indicate a few regions of localized damage. Large rectangular areas of bright contrast observed in (b) and (c) are the area where markers were deposited for strain mapping investigations.

The morphology and growth (with additional creep strain) of the damage is presented in Figure 6.14 through Figure 6.18. It is shown that the damage is on the length scale of the grain size and although macroscopically transverse to the load direction is often locally oriented between 0 and 45 ° (to the loading direction). Limited growth is observed after the initial formation.

Figure 6.14 shows a detailed view of localized damage at the same location for three creep strains of a – 1.0%, b – 1.2%, and c – 1.6%. The tensile direction is vertical. The corresponding creep curve for these steps has been shown in Figure 6.5. This localized deformation, that surrounds some small (< 5 μm) cavities, formed between the bulk creep strains of 0.7% and 1.0%. Little addition growth of this region was observed with increasing creep strain.
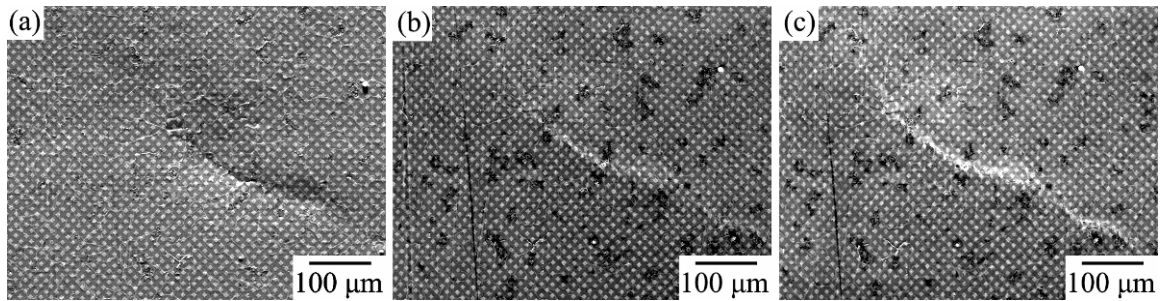
Figure 6.14 AXJ530 ($T_{mold} \approx 371$ °C) creep damage accumulation for steps, strains of (a) 3, $\varepsilon_{total} \approx 1\%$ (b) 4, $\varepsilon_{total} \approx 1.2\%$ and (c) 5, $\varepsilon_{total} \approx 1.6\%$.

Figure 6.15 shows the formation of a cavity/void with respect to increasing creep strains of: a – 1.2 %, b – 2.3%, and c – 3.0%. The creep curve of this sample has been shown in Figure 6.8. The cavity was not observed prior to creep testing the specimen. The interior surface (into the specimen) of the cavity does not exhibit tearing (as is shown in other regions of localized damage, Figure 6.18) and appears relatively smooth, shown in Figure 6.15b, indicating (due to the lack of roughness from tearing) that subsurface shrinkage porosity, formed during solidification, may have been the initiator of this cavity. Though it does widen some (~ 13 μm) for an addition of 1.1% bulk creep strain, (Figure 6.15a to b, relating to an overall sample extension of 437 μm), the additional opening of this cavity would be responsible for less than 3% of the overall creep strain accumulation (this assumes that the material across the gage at this region also deformed with the cavity). This indicates that the growth of this cavity is very small regarding the overall creep extension. In the next step of the creep curve (accumulating an addition

0.7% bulk strain up to failure), little to no additional opening of the cavity is observed. Note that the cavity is on the length scale of the grains as well as the measured strain heterogeneities previously reported.
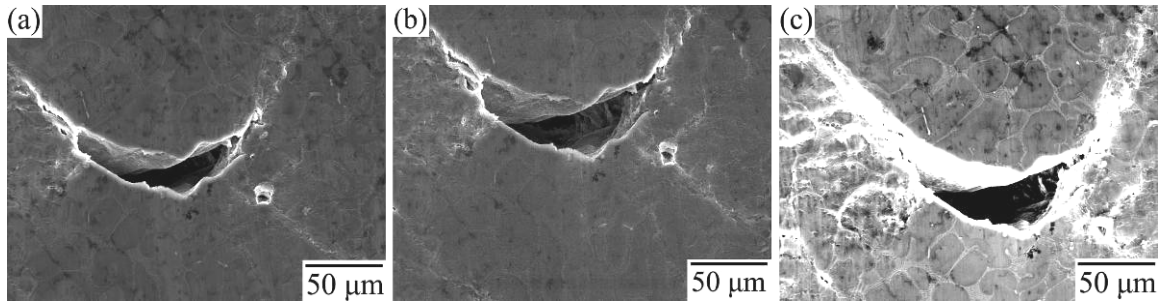
Figure 6.15 Localized creep damage for AXJ530 $T_{mold} \approx 390$ °C at steps and accumulated strain, from Figure 6.8 of (a) step 1 - 1.2% (b) step 2 – 2.3% (c) step 3 – 3.0% failure.

Figure 6.16 depicts another region (AXJ530 ($T_{mold} \approx 390$ °C)) of localized damage accumulation observed at creep strains of: a – 1.2%, b – 2.3 %, and c – 3.0% (failure). The creep behavior of this sample has been shown in Figure 6.8. The development of damage has been observed with incremental increases in bulk creep strain. Note that there is limited additional damage accumulation (for the region in Figure 6.16) with increasing creep strain. The distortions of the individual markers used for strain mapping calculation are used to gage severity of localized damage. Some of the markers, presumably in the near-grain boundary regions, have experienced shear up to 61% and an elongation (in the tensile direction) of 46%, Figure 6.16c. Also note the cavity/void formation as a result of the high shear. Shear such as this could indicate GBS, though (a) the contribution to creep strain is small and (b) few regions exhibiting such local shearing were observed (e.g. Figure 6.14, Figure 6.15, Figure 6.17, Figure 6.18, and Figure 6.21 through Figure 6.24). This is an indication that, though GBS may be occurring on a minor scale but it is not a dominant creep deformation mechanism observed in these alloys at the creep testing condition investigated.
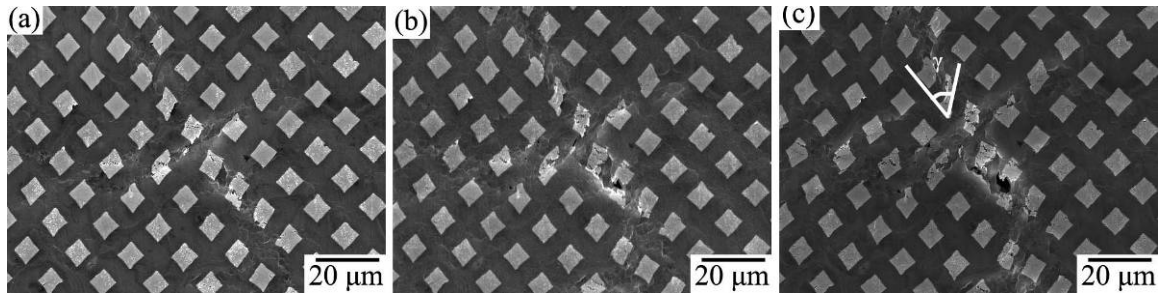
Figure 6.16 Localized creep damage for AXJ530 $T_{mold} \approx 390$ °C at steps and accumulated strain, from Figure 6.8 of (a) step 1 - 1.2% (b) step 2 – 2.3% (c) step 3 – 3.0% failure.
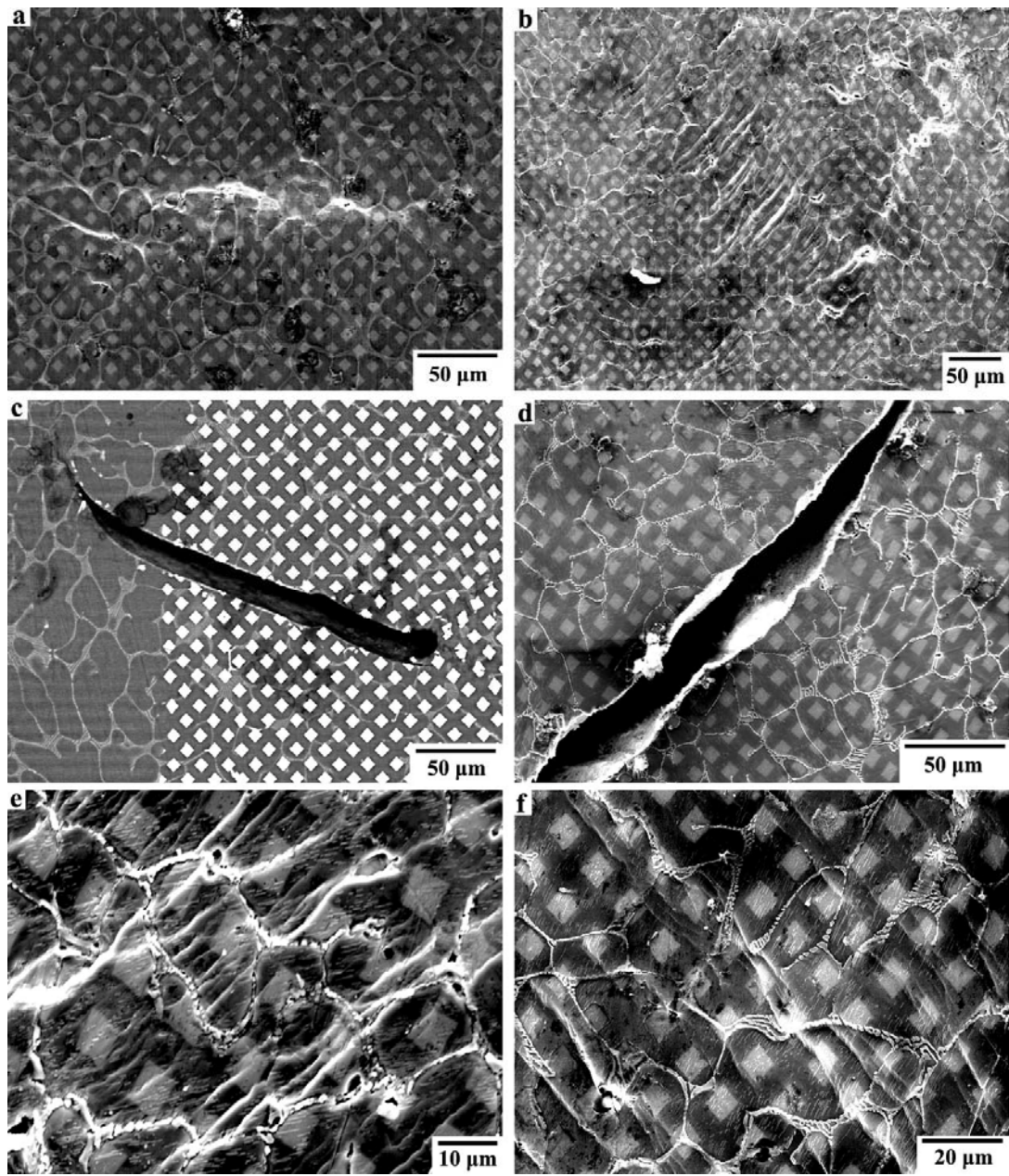
Figure 6.17 Regions of localized creep damage and plasticity for Mg-Al-Ca.

168

Figure 6.18 shows a location of severe damage accumulation, a crack running perpendicular to the loading direction. Arrows have been used in the figure to mark the same features in each image to aid in comparison. The feature, unlike the void of Figure 6.15 has a very rough crack interior indicating tearing of material during crack growth and displacement. The crack seen in Figure 6.18a is ~5-10 μm wide and 173 μm long. Seen in Figure 6.18b, the crack measures ~30-40 μm wide and has more than doubled in length to 365 μm.

At this second step, additional voids and cracks have formed in the vicinity of the primary crack. The crack appears to be following along a grain boundary within the material. As more damage, aside from the primary crack, continues to accumulate in this region it occurs on the scale of the grain structure, not the cell structure. In the following sections it will be shown that this damage is localized to near grain boundary regions. In the regions adjacent to the crack there appear to be shear offsets on domains of grain size. This is most observable to the right of arrow (2) in Figure 6.18b. As the crack is growing and widening, with additional creep strain, the surrounding grains accommodate this damage through plastic slip. As the surrounding neighborhood of grains strain harden, localized damage (i.e. cracks, cavities/voids) results.
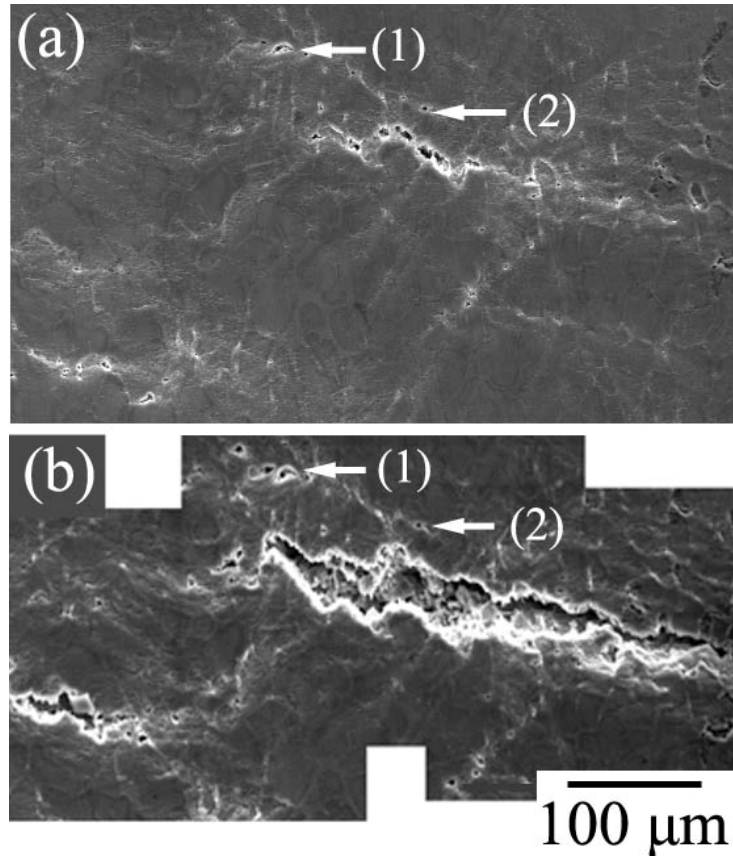
Figure 6.18 Localized creep damage for AXJ530 $T_{mold} \approx 390$ °C at strains (a) 1.2% and (b) 2.3%. Arrows (1) and (2) denoting same features in figure (a) and (b).

6.3.2   Heterogeneity of Damage

As apparent from the previous sections discussion, damage accumulation is heterogeneous, as would be expected.   Heterogeneous plasticity is expected in polycrystalline HCP systems.   There are 3 (or 4) active systems (basal, prismatic, pyramidal I, and pyramidal II - Table 2.2) for the creep temperatures tested. Each system has a different critical resolved shear stress [41] and each grain orientation will thus favor a specific slip system [43], therefore deformation between grains will be anisotropic. This anisotropy and grain to grain differences in plastic strain will create stress concentrations along grain boundaries. Five independent slip systems are required to produce a generally homogeneous strain in a polycrystalline material [214], and the heterogeneity of creep strain observed suggests that this is difficult during creep of these Mg alloys.

Figure 6.19 shows the accumulation of deformation and damage across a 1.128 mm^2 section of the gage. The deformation observed is semi-continuous, and measures ~1190 μm from tip to tip. It is also oriented between 0 and 45 ° to the loading direction. A few small cavities/voids may be observed along the location of greatest deformation, seen at the top right and bottom left of the figure. One key observation from the image is that the regions above (and to the left) and below (and to the right) of the deformation and damage show no sign of localized plasticity or damage accumulation. Secondly, the localized deformation and damage appears to follow the microstructural feature of grain boundaries. A few branches of the crack are observed to curve over and around features on the length scale of the grains.
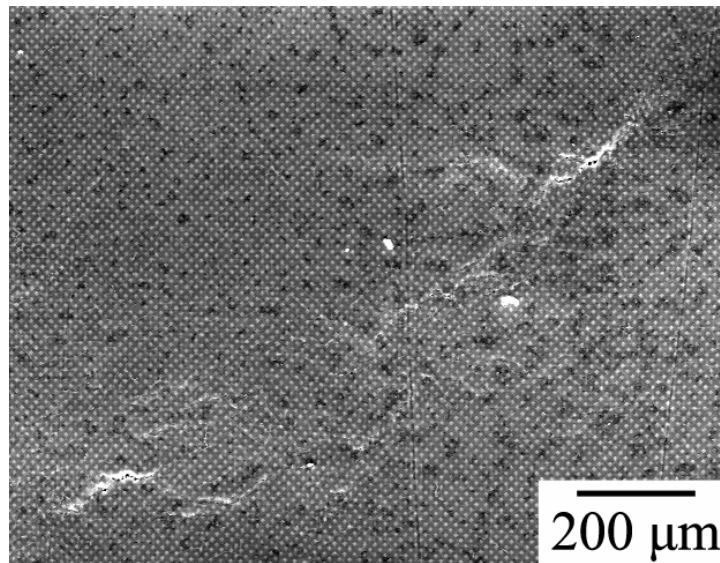
Figure 6.19 AXJ530 T$_{mold}$ ≈ 371 °C step 5 (ε ≈ 1.6%).

Figure 6.20 shows a region of the gage including markers used for strain mapping. There is no observable localized plasticity or damage (concluded through SEM analysis of strain mapping markers and microstructure). The region covers ~ 1.084 mm^2 and the sample has been subjected to 2.3% creep strain. The representative creep curve has been shown in Figure 6.9. This further supports that the accumulation of creep damage is highly heterogeneous, with large regions accumulating little damage and others accumulating severe damage.
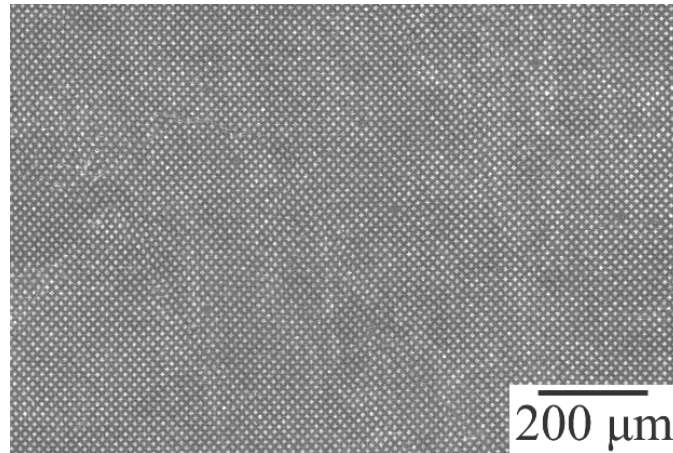
Figure 6.20 AXJ530 T$_{mold}$ ≈ 390 °C step 2 (ε = 2.3%). Note limited to no damage accumulated on the surface in this field of view.

Figure 6.21 summarizes several key features: that localized creep plasticity and damage accumulation is highly heterogeneous and that damage forms as cracks and cavities/voids. The majority of the damage has limited growth after forming indicating that damage nucleation occurs at a higher rate than growth of cavities into major cracks. This indicates that the load is shed from a highly deformed region to a region with less accumulated strain supporting localized work hardening. The damage is on the length scale of the grains and accumulates at grain boundaries. Slip offsets can be clearly seen in the center of Figure 6.21a. Neighboring grains show little to no plasticity or the formation of slip offsets. This mismatch in the straining behavior of individual grains results in stress concentrations that nucleate cracks and cavities/voids.
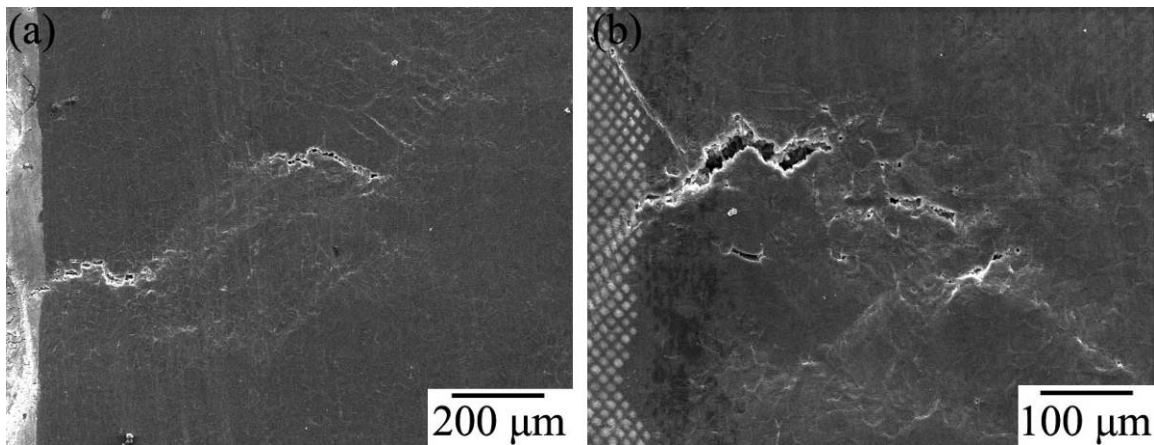
Figure 6.21 AXJ530 T$_{mold}$ ≈ 390 °C step 2 (ε = 2.3%) at (a) near sample edge and (b) near gage center. Note large regions on surface of non-deformed material and regions of high localized damage adjacent to cavities.

172

6.3.3   Microstructural Influence on Strain and Damage Accumulation

This section provides evidence of the interaction between microstructure, creep plasticity and damage localization. In the AX44 alloy coarse precipitates were large enough to be visible in the SEM. Basal traces could thus be distinguished from the orientation of the precipitates providing crystallographic reference for each grain. The boundaries where the precipitates changed orientation could be identified as grain boundaries, without the need for OIM data. This also allowed for approximation of τ_{rss} of individual grains, discussed in a later section.

An example of the microstructural influence on strain accumulation and damage heterogeneity is shown in Figure 6.22. Two triple points are shown (ABC and ACD), with the grains outlined in red (A), green (B), blue (C) and teal (D). Grain A contains localized damage at the near grain boundary region (center of the image). The crack follows the grain boundary and has several cavities/voids along its 80 μm length. It is of the same morphology as the previously presented localized damage in AXJ530. The surrounding grains have undergone limited plastic deformation (as slip bands, seen in grain B and primarily in C).   The slip offsets in grains B and C are parallel to the basal trace of those grains indicating that deformation (in those grains) is occurring primarily by basal slip. An analysis of the resolved shear stresses for the grains follows.

The relationship for resolved shear stress of an applied stress is below in Equation 6.1 (the Schmid factor is the product of the cosine terms). Assume that φ is the angle between the load and slip plane normal and λ is the angle between the load and slip direction. From the precipitate orientation (indicating the basal trace), Schmid factors can be estimated, within a range, for the grains in Figure 6.21. It is recognized that the basal plane could rotate about the basal trace since only information concerning the intersection of the basal plane with the viewing plane is known.

$$\tau = \sigma \cos\varphi \cos\lambda \qquad\qquad\qquad \text{Equation 6.1}$$

The resolved shear stress calculations for each grain are in Table 6.2. Considering grain A, the basal plane normal is nearly orthogonal (85 °) to the loading direction. Basal slip occurs in the $<11\overline{2}0>$ directions and there are three equivalent

directions oriented 120° apart in an HCP lattice. A rotation of the HCP lattice around the normal would bring a favored slip direction between (nearly) 0° and 60° (the point at where an (equivalent) adjacent slip direction would be favored. Taking the slip direction as 5° (assuming slip oriented in most favorable condition) to 60°, the resolved shear stress for grain A would be between 3.5 to 6.9 MPa, respectively. Considering grain B, a rotation of the lattice around the basal trace normal (with respect to the load) changes the angle between slip direction and load very little (~88° to 90°). The resolved shear stress for grain B would be ~2.8 MPa. Grain C, oriented most favorably would have a resolved shear stress in the range of 16.8 to 31.7 MPa. Grain D, has an approximate resolved shear stress between 2.6 and 25.9 MPa.

It can be concluded that this damage is localized at a triple point of high angle grain boundaries. Grains oriented for basal slip deform extensively, while neighboring grains experience limited plasticity. Grain C, most favorably oriented for basal deformation exhibits the highest plastic strains, as expected. The other grains (A, B, and D) are oriented less favorably for basal deformation (low resolved shear stresses on basal planes), and must have other (prism, pyramidal) slip systems active to accommodate deformation and maintain continuity at the grain boundary. Since activating other slip systems in Mg requires greater resolved shear stresses, a discontinuity in strain forms at the grain boundary leading to localized plasticity and the eventual nucleation of cavities.
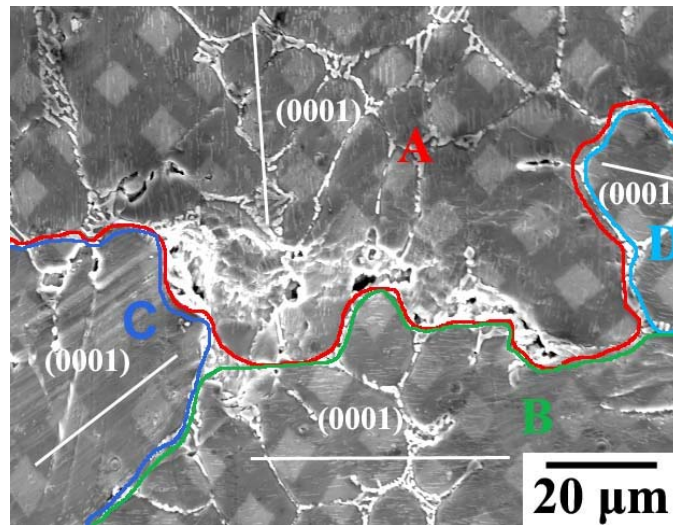
Figure 6.22 AX44 $T_{mold} \approx 346$ °C step 1 ($\varepsilon = 7.8\%$). Basal plane has been traced and grain boundaries highlighted in color. Tensile direction is vertical.

Table 6.2 Resolved shear stress (MPa) referenced to Figure 6.22.

Grain	Basal Normal to Load	Maximum Slip Direction to Load Angle	Minimum Slip Direction to Load Angle	Maximum τ_{rss} $\sigma \cos(\varphi) \cos(\lambda)$	Minimum τ_{rss} $\sigma \cos(\varphi) \cos(\lambda)$
A	85°	60°	5°	6.9	3.5
B	2°	88°		2.8	
C	31°	70°	50°	31.7	16.8
D	19°	88°	70°	25.9	2.6

Figure 6.23 shows additional evidence of the influence of grain orientation on damage accumulation. Figure 6.23a shows a grain boundary where the two grains (with a difference in orientation of ~44 °) have been outlined in red and green and the basal traces of each grain have been labeled. Near the center of this image there is a crack located at the boundary. Figure 6.23b shows the crack at a higher magnification. Shear offsets contained within the grain (outlined in green) are clearly impinging the boundary parallel to the basal trace. This basal plane lies ~47° to the tensile axis. The localized damage and difference in resolved shear stresses between these grains indicate again that there is a non-deforming grain adjacent to a strongly deforming grain.
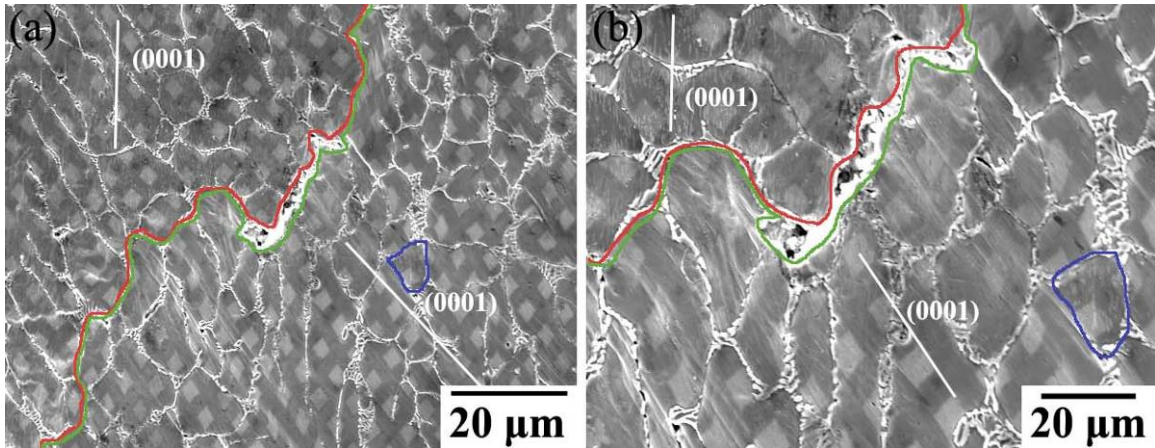
Figure 6.23 AX44 $T_{mold} \approx 346$ °C step 1 showing damage accumulation and onset of cavity formation between grains (a) overview of region and (b) detail of cavity.

Figure 6.24 shows another interesting feature that has been previously discussed in Figure 4.21 through Figure 4.23 concerning dislocations within the α-Mg grains. Slip offsets, as seen in this figure near the grain boundary (highlighted in green), have been discussed in previous figures. These offsets are commonly observed in the grains that have experienced plasticity. The slip offsets observed in this region are not parallel to the

basal trace, as in other regions. This indicates that slip systems other than basal are active in accommodating creep strain. Secondly these slip offsets exhibit little additional growth with increased creep strains, as seen in comparing Figure 6.24a and b. The non-basal slip offsets tend to accumulate near the grain boundary regions where the basal oriented slip offsets are observed both at the grain boundaries and across the grains. Therefore the majority of deformation occurs at the near grain boundaries with limited deformation occurring in the grain interiors. Secondly the slip offsets are observed to cross several cells and do not terminate at the interdendritic regions between the cells. The cellular and intercellular structures of the α-Mg grains have little influence on the morphology of the offsets. This further supports that the grain size of the material is the important microstructural feature for deformation, not the cells.
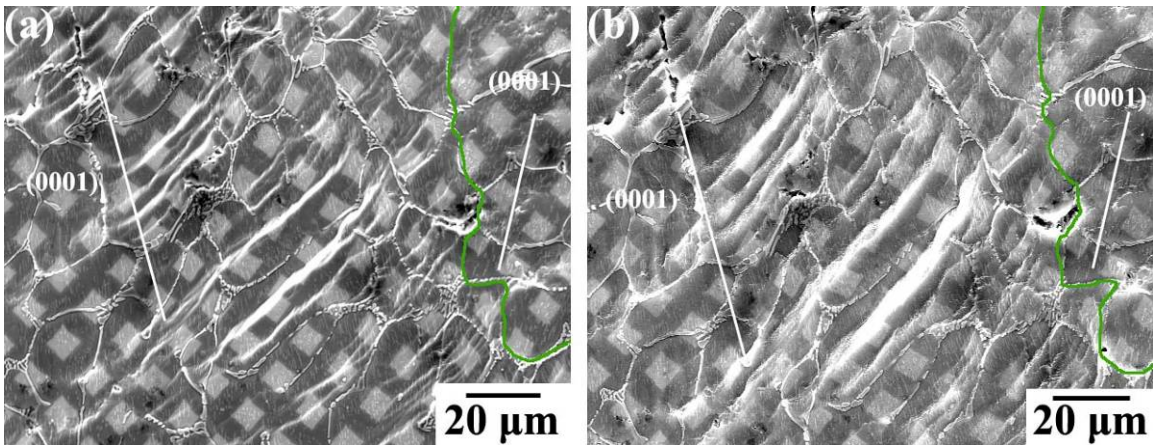
Figure 6.24 AX44 $T_{mold} \approx 346$ °C with creep damage accumulation near grain boundary of two adjacent grains at (a) step 1, $\varepsilon \approx 7.8$ % and (b) step 2, $\varepsilon \approx 10\%$ (at failure).

6.4   Die-cast AXJ530

The creep strain development and damage localization has been studied for as-permanent-mold-cast Mg-Al-Ca alloys. These alloys (AX44 and AXJ530) have the same microstructure (i.e. grain size, intermetallic phases, and area fraction phases) except that AXJ530 has an increased solute (Al and Ca) concentration in the α-Mg grains. These investigations have provided detail of microstructural influence on the creep behavior of the alloys. The majority of magnesium alloys for automotive powertrain applications will be used in the as-die-cast form, so a detailed understanding of these finer grain materials is important. Thus the remaining question is, do die-cast and permanent mold

cast alloys, exhibiting similar creep behavior and microstructures (for the Mg-Al-Ca alloys), have the same form of strain accumulation and localized damage? The following section addresses this question by applying the strain mapping technique to a die-cast AXJ530 sample.

6.4.1 Strain Distribution and Accumulation

Figure 6.25 shows the creep behavior of the die-cast AXJ530. The sample was first strained to 0.1%, the strain mapping markers imaged, and then incremented to a total creep strain of 0.6%. Strain contour plots were calculated at each step and for the combined steps. Several locations across the gage were tracked.
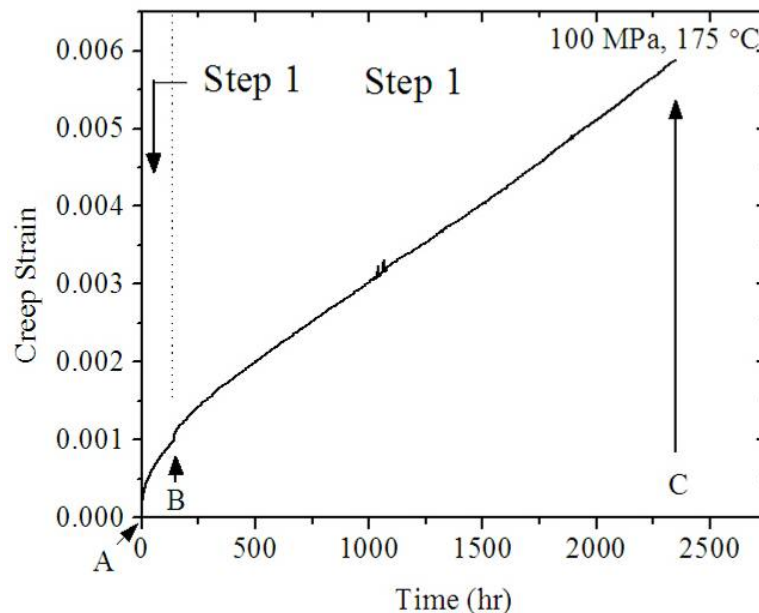
Figure 6.25 Creep strain mapping 'strain stepped' test for AXJ530 – die cast.

A strain distribution plot for the die-cast AXJ530 is shown in Figure 6.26. The strain is heterogeneous and on the length scale of the die-cast magnesium grains, as in the as-permanent mold cast alloy. The average grain size measured for the die-cast AXJ530 was 19 μm. The highest local strain measured was 3.4% at step 1, more than 30x greater than the measured bulk strain of 0.1%. The average strain measured in the field of view was 1.0%, 10x greater than the bulk strain. The difference between the calculated and bulk measured strains in the die-cast AXJ530 is significantly greater than that measured in the permanent mold AXJ530 at low ($\varepsilon \sim 0.1\%$) strains.

For the second step of the creep test, a maximum localized strain of 2.6% was recorded, just more than 5x the bulk strain of 0.5%. The average strain (ε_{yy}) in the field of view was 0.8% which was about the same as the bulk strain (ε_y). If the entire creep test is considered (from point A to C of Figure 6.25), then the greatest concentration is 4.3%, just over 6x the bulk strain. When this is compared to the average strain in the field of view (1.3%) it is only 2x that of the bulk strain.

The creep strain accumulation behavior (at ~0.65% bulk creep strain) for the as-die-cast and as-permanent-mold-cast AXJ530 is compared in Figure 6.27. The strain is localized (concentrated) on the scale of the grain structure for both die-cast and permanent mold cast condition. Secondly, the severity of the strain concentration is comparable between cast conditions for similar bulk creep strain. The normalized strain value (greatest strain concentration to bulk creep strain), Table 6.3, for die-cast and permanent mold cast are 6.4 and 7.2, respectively. Normalizing the average strain (in the field of view) to the bulk creep strain for the die cast and permanent mold cast conditions yield values of 2.0 and 2.1, respectively. Thus the finer grain size is beneficial because it suppresses severe strain concentrations.

Table 6.3 Strain concentrations (($\varepsilon_{concentration}$ or $\varepsilon_{average}$) / ε_y) during creep for as-permanent-mold-cast and as-die-cast AXJ530 for approximately the same bulk strain.

Strain Condition	As-permanent-mold-cast	Normalized Strain	As-die-cast	Normalized Strain
Localized (ε_{yy}) Creep Strain	4.50%*	6.43	4.30%**	7.17
Bulk (ε_y) Creep Strain	0.70%		0.60%	
Average (ε_{yy}) Creep Strain	1.37%*	1.96	1.27%**	2.12
Bulk (ε_y) Creep Strain	0.70%		0.60%	

  * Values from Figure 6.7
 ** Values from Figure 6.27
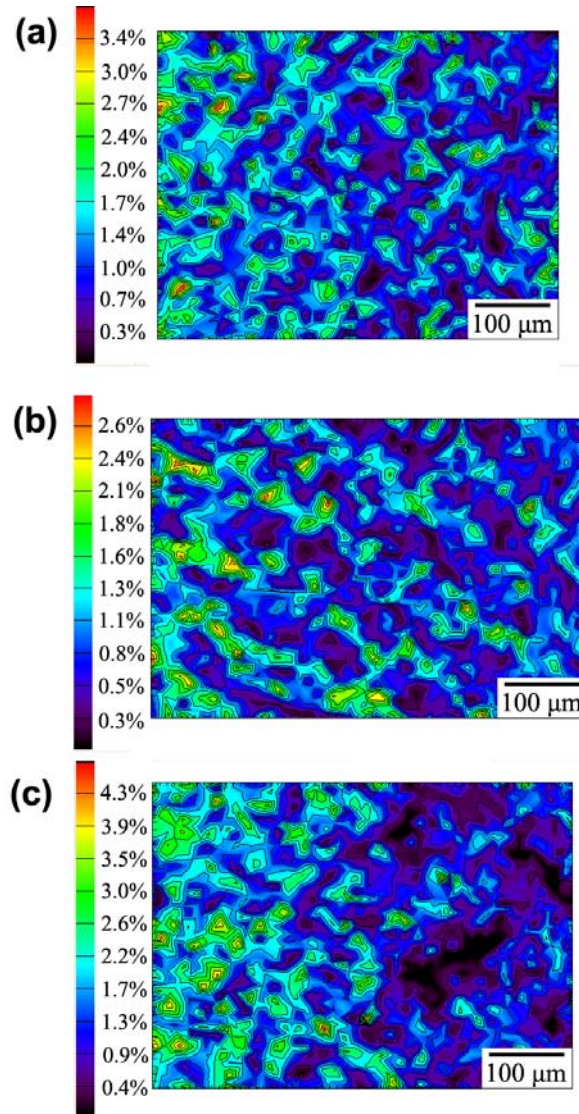
Figure 6.26 Von Mises strain distributions for as-die-cast AXJ530 (a) step 1 – ε ≈ 0.1% (b) step 2 - ε ≈ 0.5 % and (c) combined step 1 and 2 - ε ≈ 0.6% strain.
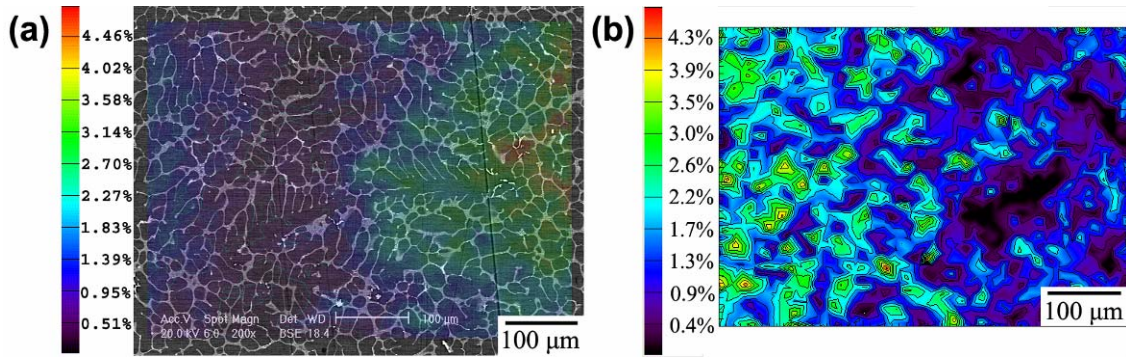
Figure 6.27 Comparison of strain distribution at 0.6% creep strain for (a) permanent mold cast AXJ530 $T_{mold} \approx 371$ °C, reference creep curve Figure 6.5, steps 1 through 3 and (b) as-die-cast, reference Figure 6.25.

The strain distributions for the die-cast alloy have several complications. The markers used to calculate creep strain, as shown in Figure 3.15, are 5 μm square, with a center to center distance of ~13 μm. Since the average grain size is 19 μm, at best only a few markers may be deposited within a single grain. Since a minimum of three markers are required to calculate a strain locally, accurate strain measurements within individual α-Mg grains was beyond the resolution of this technique, though individual marker distortion can be used to quantify local deformation. As shown, strain distributions were successfully calculated and an understanding of the strain heterogeneity with creep strain was developed.

A second complication with strain mapping the die-cast alloy was that the underlying microstructure was not successfully imaged prior to conducting strain mapping. Therefore the microstructure is not under laid in the strain distribution contours. Several regions had orientation imaging completed prior to preparing the sample for strain mapping, yet these OIM regions, had inconsistent markers (or the markers in those regions spalled during testing) after marker deposition and testing. Note that without microstructure to aid in aligning the calculated strain contours, each image may be a slightly shifted field of view (up to 1 row of markers (13 μm)).

6.4.2   Die-Cast AXJ530 Localized Damage

Creep damage, for the die-cast AXJ530, was examined at each step of the creep test. After step 1, 0.1% creep strain, there was no observable damage on the gage of the die-cast AXJ530. Localized damage, shown in Figure 6.28, was observed at the end of

step 2, 0.6% total creep strain. Localized damage was not observed in the as-permanent mold cast samples until after 0.7% creep strain (the minimum creep rate was observed at ~1% creep strain). Test times were significantly shorter in the as permanent mold cast case compared to the die-cast (i.e. 500 h vs. 2500 h, respectively). This suggests that damage is more strain- than time-dependent for AXJ530 at the temperatures and stresses investigated.

The localized damage observed in the die-cast AXJ530 was of two distinct varieties. Shown in Figure 6.28a, is an overview of the first type of damage. This damage was observed in separate clusters throughout the gage with each cluster a few hundred micrometers in diameter. These clusters were not uniformly distributed across the gage. In each cluster, there was on average 10-20 μm between each damage location. Higher magnification images of the damage are shown in Figure 6.28b and c. This damage accumulated within the primary magnesium phase, along interdendritic regions. Cavities were generally less than 2 μm in length and 1 μm wide.

The second type of damage, in Figure 6.28d, e and f, is larger (5-50 μm) and is more widely spaced (compared to the damage described above) between each site of damage (50-100 μm) than the previously discussed damage. It was observed more often across the gage, though was not uniform in distribution. The damage included several neighboring magnesium cells and was generally concentrated on the interdendritic boundary. It is proposed that this damage nucleated from larger α-Mg grains, not porosity. The porosity observed in the gage of this alloy (< 5%) occurs less frequently than the observed localized damage. Secondly, the larger magnesium grains, shown distributed in the EBSD image of Figure 4.27, are spaced on approximately the same length scale (50-100 μm) as the localized damage. This indicates that the occasional larger α-Mg grains within the die-cast alloy are probably significantly contributing to the overall creep strain. These grains having a larger volume than the smaller neighboring grains, would be able to accommodate greater strains before work hardening to the same degree as the smaller grains. The length scale of the localized strain accumulation, Figure 6.26, matches that of this form of localized damage though no evidence of plasticity or damage was observed at the locations were localized strain was measured. It

is important to note that no sliding in the interdendritic region or shearing of the markers was observed indicating that GBS was not contributing to the creep deformation.
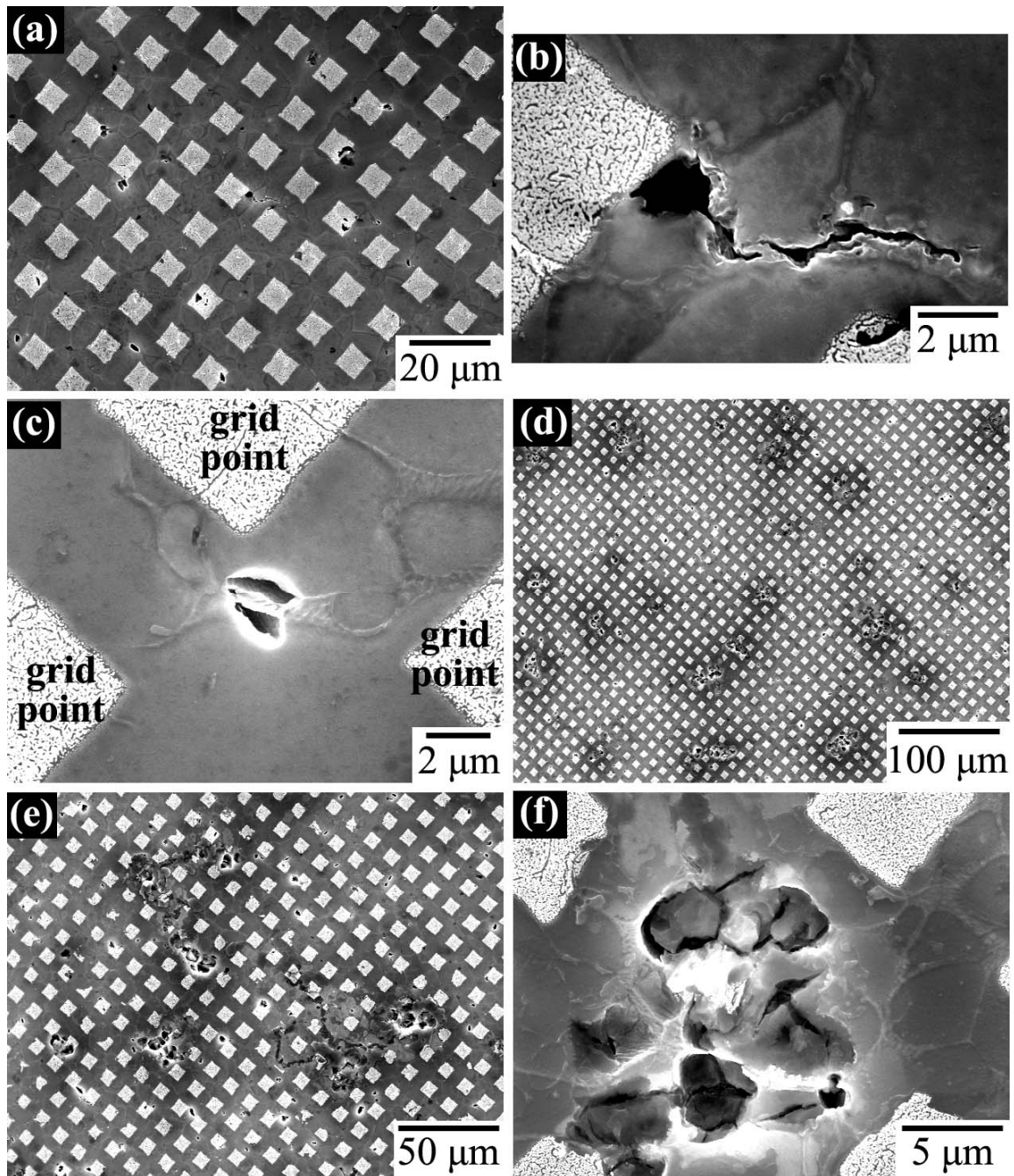
Figure 6.28 Damage accumulation in die-cast AXJ530 after 0.6% creep strain. (a) Large field of view with dark voids/cavities. (b) and (c) show morphology of cavities in (a). (d) Large field of view with larger voids/cavities. (e) and (f) show morphology of larger cavities.

6.5   The Role of Grain Boundary Sliding

As discussed in detail in Chapter 2, grain boundary sliding has been a proposed dominant creep mechanism for magnesium alloys, especially at low stresses. The growing acceptance in the community that GBS sliding has a prominent role in the creep deformation of these alloys stems from several key reports in the literature. The most convincing investigation quantified the offset (at the grain boundaries) of marker lines in a post crept single phase solid solution strengthened Mg-0.78 Al (wt%) alloy (tested at ~17.2 MPa at 200 °C to ~500+ hrs and 2.49% creep strain) [181]. Dargusch et al. [86] observed a region of localized damage (with < 5 μm line offset), at an unspecified microstructural location in a multiphase die-cast AZ91 sample (crept between 20-40 MPa (not specified) at 150 °C to 20% strain). The damage was concluded to be a result of grain boundary sliding and no further attempts were made to quantify the degree of GBS. Later, a review of creep resistant Mg alloys [9] presented the supporting literature on GBS and stated that several alloy systems (e.g. Mg-Al-Ca) were developed by creating second phase particles at the grain boundaries that inhibit sliding. These investigations and publications led future investigators to attribute low (n < 2) stress exponent to creep deformation controlled through GBS. Thus many of the reports [180, 182, 183] in the literature infer GBS mechanisms from constitutive creep behavior, not microstructural evidence.

The strain mapping and localized damage observations show that GBS, for the range of stress and temperature investigated, is not a dominant creep deformation mechanism in these alloys. Localized damage is predominately formed through the following process. Strain accumulates preferentially within grains with high resolved shear stresses. This heterogeneous plasticity leads to strain concentrations, and eventual localized damage accumulation at triple points and high angle grain boundaries. The localized damage is in the form of cavities/voids and cracks. Experimental evidence of the creep strain distribution, local plasticity and nucleated damage have been well established above (Figure 6.17, Figure 6.18, Figure 6.22, Figure 6.24, and Figure 6.28) with only one observed region that contained localized shearing that could be attributable to GBS (Figure 6.16).

Strain mapping experiments have shown that strain accumulates in the α-Mg grains and is not strongly affected by cell boundaries. At or near the minimum creep rate (near 1% creep strain for the permanent mold cast alloys), the favorably oriented grains have strain hardened and localized damage is observed along high angle grain boundaries. Further creep strengthening of the Mg-Al-Ca alloys should thus focus on decreasing dislocation mobility in the primary α-Mg grains. This is further supported by the creep strengthening effect and dislocation interactions of the grain interior C15 precipitates and the creep strengthening of increased solute (Al and Ca) in AXJ50 versus AX44. Grain boundary offsets were occasionally observed along favorably oriented boundaries, but this does not account for the majority of the creep deformation that is observed in these alloys for the stresses and temperatures investigated. Grain boundary sliding is also classically associated with lower stresses and cannot be ruled out as a deformation mechanism in these alloys at low stresses (< 40 MPa).

Another indication that grain boundary sliding is not a dominant creep mechanism in AXJ530, for the stresses and temperature investigated, is the dependence of creep rate on grain size. As discussed in Chapter 5, as grain size decreased the creep resistance of AXJ530 increased. The Raj-Ashby equation [78] models creep due to grain boundary sliding, in simplified terms, that equates an improvement in creep resistance with the inverse square of the grain size (i.e. $\dot{\varepsilon} \propto \dfrac{1}{d^2}$). The proposition considers that the plasticity is a result of GBS through diffusion accommodation where plastic strain is localized entirely to the near grain boundary region with no deformation in the grain interiors. Since plastic strain was observed both throughout the grain and at times to the near grain boundary region and since creep resistance did not decrease with decreased grain size it was concluded that grain boundary sliding is not the dominant creep deformation process in these alloys.

6.6   Discussion and Conclusion

An investigation of the strain distribution and localized damage in the as-permanent-mold cast Mg-Al-Ca alloys and die-cast AXJ530 was completed. The strain mapping technique, previously utilized for room temperature tensile testing, was

successfully applied to creep testing up to 175 °C and for times of 2500 hours. The results of the strain mapping experiments showed that creep strain was heterogeneous in the Mg-Al-Ca alloys. The heterogeneity was on the length scale of the grain size of these alloys and was not dependent on the cellular structure or intercellular region. Localized damage, on the length scale of the microstructure, was observed in the as-permanent-mold-cast samples at or near the minimum creep rate (~1% creep strain). The localized damage was also sensitive to microstructure and formed as cracks and cavities/voids. Damage was observed in the die-cast sample at ~0.6% creep strain. The growth rate of the damage was slow after initial formation. The creep rate accelerated after the formation of the initial damage and continued damage nucleated was observed leading to eventual failure.

The creep strain distribution was calculated at periodic intervals, between bulk creep strains of 0.3 and 10% in the as-permanent-mold-cast Mg-Al-Ca alloys. The creep strain distribution was also calculated in die-cast AXJ530 for bulk creep strains between 0.1 and 0.6%. It was found that the creep strain localized to domains on the length scale of the grains at low creep strains (< 1%). These domains were generally uniform in strain distribution and accumulated strain 2 to 10x that measured in the bulk. In the permanent mold cast condition, additional creep strain accumulated along grain boundaries measuring 20-40% strain in these regions, 5 to 10x greater than the bulk creep strain. For the majority of these highly strained regions, localized damage was observed.

Grain boundary sliding (GBS) has previously been proposed as a dominant creep mechanism in these alloys. The results and conclusions of this study indicate that GBS is not a dominant creep mechanism at the stresses and temperatures investigated. Plasticity is occurring first as slip in the primary α-Mg grains. As the grains oriented for slip strain harden, stress concentrations arise. The stress concentrations are localized damage that is observed in near grain boundary regions as cracks and cavities/voids. The onset of this damage occurs near the minimum creep rate. As creep damage accumulates, mostly in the form of newly nucleated damage sites, the creep rate increases leading to failure. Further evidence that GBS is not occurring is that as the grain size is decreased, the creep resistance improves. This is inverse to predictions of grain boundary sliding creep models [78].

The strain mapping and localized damage investigations have indicated the microstructural characteristics that should be focused on for future alloy strengthening. In comparing microstructure and creep results of the permanent mold cast AXJ530 to the AX44 there was no difference in creep stress dependence or microstructure (except solute concentration) yet an order of magnitude decrease in minimum creep rate (for AX44). This difference in creep strength has been attributed to the decrease of solute within the α-Mg in AX44 compared to AXJ530. AXJ530 and AX44 behave the same in terms of strain distribution but AX44 accumulated greater strains, in the α-Mg grains (adjacent to the boundaries), prior to damage nucleation. This indicates that the near grain boundary regions in AXJ530 are less damage resistant than the AX44 and this is attributed to the increased solute (Al and Ca) concentration. Therefore creep strengthening of these alloys should focus on the near grain boundary region. Secondly, the majority of the damage was on the same length scale and distribution as the α-Mg grains indicating that the grain size has a significant contribution to creep strain accumulation. This is in strong agreement with the results of Chapter 5, where it was shown that creep rate was dependent on grain size. Future creep strengthening in these alloys should further address grain refinement.

Chapter 7

Conclusions and Recommendations

7.1   Conclusions

The objective of this research was to investigate the role of composition on solidification behavior, permanent mold castability, microstructural development and mechanisms of creep in a series of ternary magnesium alloys. From these investigations the following conclusions and recommendations can be made.

7.1.1   Solidification and Casting

The freezing range of these alloys decreased in the following order: AX44, AXJ530, AJ44, ALa44 and ACe44. This freezing range strongly influenced the castability of the alloys for the permanent mold process. The rare earth containing alloys were particularly difficult to cast due to the narrow freezing range (~25 °C) that led to premature freeze-offs. A higher superheat (750 °C compared to 685 °C) permitted complete mold filling and solidification with minimal porosity. Permanent mold temperatures varied for each cycle during a casting campaign. Through changes in mold temperature, a change in cooling rate of the casting resulted. The different cooling rates led to different precipitate sizes and spacing in the primary α-Mg grains for the Ca-containing alloys. These precipitates had an influence on creep strength and are discussed below.

Scheil analyses were completed on as-cast samples. There was a difference in the concentrations levels of solute (Al and ternary addition) in the α-Mg. These differences between alloys, further discussed below, strongly correlated to the differences in creep strength. This indicates that the elemental segregation is important to creep strength and can be influenced with alloying constituents. Future alloy design should focus on elemental additions that (1) provide the best freezing range for castability and (2)

influence the segregation behavior by increasing solute in magnesium both for solid solution strengthening and precipitation strengthening.

7.1.2 Creep Behavior

The tensile creep behavior was investigated between 40 and 100 MPa at 175 °C. The creep resistance of the alloys in descending order was: Die-cast AXJ530 followed by the permanent mold cast alloys AXJ530, AX44, AJ44, ALa44 and ACe44. Except for the rare earth containing alloys, there was approximately one order of magnitude difference in the minimum creep rate between each alloy following the descending order of creep resistance. The ACe44 and ALa44 were approximately five and two orders of magnitude less creep resistant than die-cast AXJ530 and permanent mold cast AJ44, respectively. Power-law creep was observed with stress exponents between 14.2 and 17.5, for the permanent mold cast AX44, AJ44 and AXJ530 alloys. The stress exponent was lower (~6.8) for the die-cast AXJ530. This indicated that for the stress and temperatures investigated there was no change in creep mechanism over the range of creep conditions investigated.

7.1.3 Microstructure and Creep Resistance of Mg Alloys

The as-cast microstructures consisted of a primary α-Mg globular dendritic phase, surrounded by a network of intermetallic(s). The Ca and Sr alloys had an area fraction α-Mg between 79-81% and the Ce and La alloys were between 59-61%. The eutectic region comprised the balance.

Solute in solution in the primary α-Mg and its relationship to solidification segregation was quantified. The AXJ530 had the greatest concentration of solute followed by AX44 and AJ44. The rare earth containing alloys had lower levels of Al and the lowest (≤ 0.1 at.%) concentration of ternary addition. This followed the order of creep resistance for the alloys. Considering viscous drag creep models, these differences in solute concentration can account for up to three orders of magnitude difference in creep rate (between the alloys) whereas five orders of magnitude difference was experimentally observed. The remaining contributions to creep arise from grain size differences and precipitation strengthening.

In both die-cast and permanent mold cast conditions the grain structure of each alloy was found to be comprised of many neighboring cells. The grain size of the permanent mold cast alloys was several hundred microns whereas the die-cast was 19 μm. The cell size was similar for permanent mold and die-cast conditions (i.e. 22 μm to 10 μm, respectively). While many past studies have associated the cells as grains and identified grain boundary sliding as a dominant creep mechanism, care must be taken in future studies to determine the grain size, location of grain boundaries, and how they influence the operative creep deformation. The die-cast and permanent mold cast AXJ530 had the same microstructure (i.e. solute concentration, eutectic morphology, area fraction α-Mg) but different grain size that are attributed to the faster creep rate of the later (approximately an order of magnitude).

The creep strength in the Mg-Al-Ca alloys was improved by about an order of magnitude in the as-permanent-mold-cast condition through precipitation in the matrix of C15 – Al_2Ca precipitates. The improvement in creep resistance in the die-cast condition was more modest, between ~3 to 5x. In the permanent mold cast alloys, precipitate size and spacing was controlled through changes to the cooling rate of a casting via different permanent mold temperatures. The samples with the finest precipitate spacing (~41 nm) had an order of magnitude lower creep rate than those solidified with a coarse (or no) precipitate structure. Precipitate size or density was not observed to change with distance from the interdendritic interface but the difference in Al and Ca concentration between AXJ530 and AX44 did vary and can be attributed to differences in solidification paths. Precipitates were not observed in the Sr, Ce or La containing alloys.

The major intermetallic phases were C36 (Mg,Al_2Ca) for the AX44 and AXJ530 alloys, hP38 ($Mg_{17}Sr_2$) for the AJ44, and $Al_{11}RE_3$/Al_2RE for the rare earths. The morphology of the interdendritic region was semi-continuous for the Ca and Sr containing alloys. The Ce and La containing alloys had a lath structure that was not continuous between grains. Direct evidence of the intermetallic phase and/or morphology contributing to the strengthening of these alloys was not observed.

Future alloy development of creep resistant Mg alloys should focus processing (die-casting or grain refinement) such that small grain size results. Secondly, selecting alloy composition to maximize solubility of the constituent elements in the matrix would

further improve creep resistance. Investigating optimal precipitate size and distribution and utilizing processing condition that result in as-cast matrix precipitates will further contribute to creep strength.

7.1.4   Strain Distribution and Localized Damage Accumulation

Creep strain distribution on the microstructural length scale was investigated for die-cast and permanent mold cast AXJ530 using a strain mapping technique. The technique was successfully applied to quantify creep strain heterogeneities for temperatures up to 175 °C and times greater than 2500 h.

In the permanent mold cast AXJ530, at the early stages of creep the strain was heterogeneous and accumulated uniformly on the length scale of the grains. With additional creep strain, these regions ceased strain accumulation, indicative of strain hardening. As the bulk creep strain further increased, concentrated strain was observed along grain boundaries. These regions reached creep strains between 20 and 40% (in AX44 whereas in AXJ530 they were lower at ~10%). These locations of high strain were often the sites of damage nucleation. The variation in localized plasticity in these regions was attributed to the difference in solute (both Al and Ca) in the near grain boundary regions between AX44 and AXJ530. It can be concluded that improvements in the creep resistance of these alloys should focus on the α-Mg grains and then the near grain boundary regions.

Also in the permanent mold cast AXJ530, the onset of damage corresponded to ~ 1% creep strain (near the minimum creep rate) and can also be associated with an increasing creep rate. The damage was heterogeneous and in the form of cavities/voids and cracks located primarily at the grain boundaries. Limited growth of the damage was observed after initial formation but rather additional creep strain lead to the nucleation of more damage. This further supports strain hardening within the grains. The damage was most often observed between grains of different resolved shear stress. Plastic strain concentrations observed as slip bands in the Mg grains was associated with the onset of damage. The offsets were primarily observed throughout a grain oriented for basal slip and at the grain boundaries of those not. The observed damage was located between a grain exhibiting plasticity and one with limited plasticity.

For the die-cast AXJ530 the strain distribution was heterogeneous, as in the permanent mold cast condition. No slip offsets were observed in the die-cast alloy, though cavities/voids and crack similar in morphology as those reported in the permanent mold cast condition were observed. The die-cast sample was crept to a maximum creep strain of 0.6% (in 2500 h) where plasticity was first observed in the permanent mold condition at 0.6% creep strain after 350 hours. This indicates that damage is more strain dependent than time dependent for the creep conditions investigated. No evidence of shearing along grain boundaries (shear of individual markers or localized damage) indicates that GBS was not an operative creep mechanism in the die-cast alloy.

The conclusions from the stain distribution investigations are that additional creep strengthening in these alloys will be gained through strengthening of the primary grains and the near grain boundary regions. Grain boundary sliding was not observed in either cast condition as a dominant creep mechanism for the temperature and stresses investigated. A detailed investigation on the influence of the active slip systems for creep is another recommendation for future studies.

7.2   Recommendations for Future Research

Based on the findings of this study, the following recommendations are made for future investigations in this area.

(1)   A detailed investigation of the liquidus surface, phase stabilities and precipitation strengthening of the Mg - 4 Al - 4 RE alloys. Though these alloys were successfully permanent mold cast, they were the least creep resistant and most challenging to cast. They have improved creep resistance when die-cast [157]. The investigation should focus on a detailed diffraction analysis of the intermetallics formed in the rare earth containing alloys. This investigation should include thermal stability studies. Reports [10, 11] indicate a decrease in creep resistance at temperatures greater than 150 °C. These reports have suggested this decrease was caused due to phase transformations, though morphological changes in intermetallic were not observed after creep testing at 175 °C in this investigations (though test times were < 100 h). Investigations of the magnesium rich corner of the ternary phase diagrams for both alloys Mg-Al-Ce and Mg-

Al-La would be beneficial since alloy composition has shifted in recent years from AE42 to AE44 [14] and can aid in selecting alloy composition for maximum solubility of elemental additions. Though these alloy systems have commercial interest and application, they are posed at an unfortunate economic position. Their respective creep resistance is the same or inferior to other automotive creep resistant alloy systems (i.e. AJ62, MRI230D, AXJ530) yet they retain the associated high costs of the mischmetal additions. This cost would be further increased for individual rare earth additions. The alloys creep resistance is not great enough to warrant wide spread utilization in the aerospace industry currently dominated by precipitation strengthened heat treatable sand cast Mg alloys.

(2)   An investigation on a wider spectrum of grain sizes and distributions is needed. In this investigation, grain size was found to influence the creep behavior of the Mg-Al-Ca alloys. A detailed understanding of the grain size distribution would provide insight on the frequency of the various sized grains and the influence these grains had on the creep behavior. Results from the strain distribution and localized damage accumulation of the die-cast AXJ530 indicate that the larger grains may be significant contributors to the creep deformation. The same could also be true in the permanent mold case.

(3)   The influence and method of processing the alloys to net shape. In the aerospace industry the alloys are sand cast creating low porosity, heat treatable components. Automotive alloys have been designed to be die-cast, which leads to high (> 5 % by volume) levels of porosity. The porosity within the components led to blistering (surface spallation due to the expansion of entrapped gas) during heat treatments.   Through tailoring new processing techniques (i.e. vacuum assist die-casting), adjusting die mold temperatures such that precipitates could be formed through the solidification process (as in the permanent mold casting), and/or investigating low temperature-short time heat treatments to avoid blistering, improvements in the creep behavior of these alloys may be gained.

(4)   Investigate additional or alternative alloying constituents to develop precipitation strengthening alloys and processing routes. The (costly) heavy rare earth containing alloys have been shown to form precipitates within the α-Mg. Heat treatments to develop precipitates within the magnesium matrix may be readily developed for the rare earth

(mischmetal) containing alloys, though (Ce and La) solubility is low indicating a low volume fraction of precipitates.

Investigations on higher order alloy systems (e.g. quaternary and quinternary) with the alloying elements selected from creep resistant ternaries have yet to show improvements in creep resistance. An example is the Mg-Al-Ca-Sr quaternary system [139, 182, 217]. Due to the limited solubility of most alloying elements in α-Mg, the constituents segregate to the eutectic region. As the alloy further solidifies, several intermetallics form in the interdendritic region. It has been shown that strengthening of the α-Mg matrix (i.e. grain size, solutes, precipitates) is responsible for improvements in creep strength and the plasticity of the α-Mg matrix is responsible for the majority of the creep deformation. Thus the interdendritic intermetallics contribute less to the creep strength of the alloys studied. The alloying additions that contribute to the formation of intermetallics do not constitute an improvement in creep strength. Improvements in the creep behavior will be gained from higher order alloy systems by several routes. First changing the solidification path and behavior such that elemental additions with limited solubility will now segregate (or at least increase the solubility) to the α-Mg matrix. These elements in solution could provide solute strengthening of the α-Mg matrix and/or be precipitated through heat treatments. The second approach to creep strengthening with higher order alloy systems is to suppress the formation of phases detrimental to the creep behavior. This approach is currently used with current creep resistant alloys by adding ternary additions that suppress the formation of the thermally unstable (at service temperatures) β phase ($Mg_{17}Al_{12}$). The third advantage that would be gained by higher order alloying additions would be to decrease the grain size of the alloy through grain refinement. Research [94, 197-200] has investigated several feasible options for grain refinement in Mg alloys.

(5) An investigation of the role of the interdendritic eutectic morphology on creep resistance. Though in the permanent mold cast alloys, the role of the eutectic region on creep deformation was minimal in comparison to the other microstructural features (i.e. grain size, solute concentration, and precipitation strengthening) this may not be the case across all microstructures and grain sizes. Strain mapping experiments should be

completed on die-cast, permanent mold cast, and sand cast alloys with different eutectic morphologies to quantify the influence of eutectic morphology on creep behavior.

(6)   Detailed investigations of the active slip systems during creep deformation. As presented for the as-permanent-mold-cast alloys, plasticity in the α-Mg matrix is the primary contributor to creep deformation at the stresses and temperatures investigated. Though much of the literature discusses basal slip in magnesium it is clear that slip occurred on multiple systems, as necessary to accommodate plastic deformation in polycrystalline materials. Ideally these investigations would build on the work of Kelly and Hosford [43, 44], Burke and Hiddard [41], and Agnew et al. [47] beginning with deforming at single crystals, at elevated temperature, oriented such that τ_{crss} could be measured for different slip systems. Micro-samples could also be cut on several crept samples of an alloy that had been subjected to various strains. A focused ion beam (FIB) could be used to remove a section of material within a single grain for TEM dislocation analysis.   Dislocation investigations would quantify the active slip systems for temperature and orientation.   Solute (Al, Li) could be added to single crystals and experiments repeated to determine the influence of solute content on τ_{crss}.   A better understanding of the active slip systems at creep testing temperature and the influence of solute on resolved shear stress of a slip system will aid in developing more creep resistant alloys.

Appendix A

Part Drawings
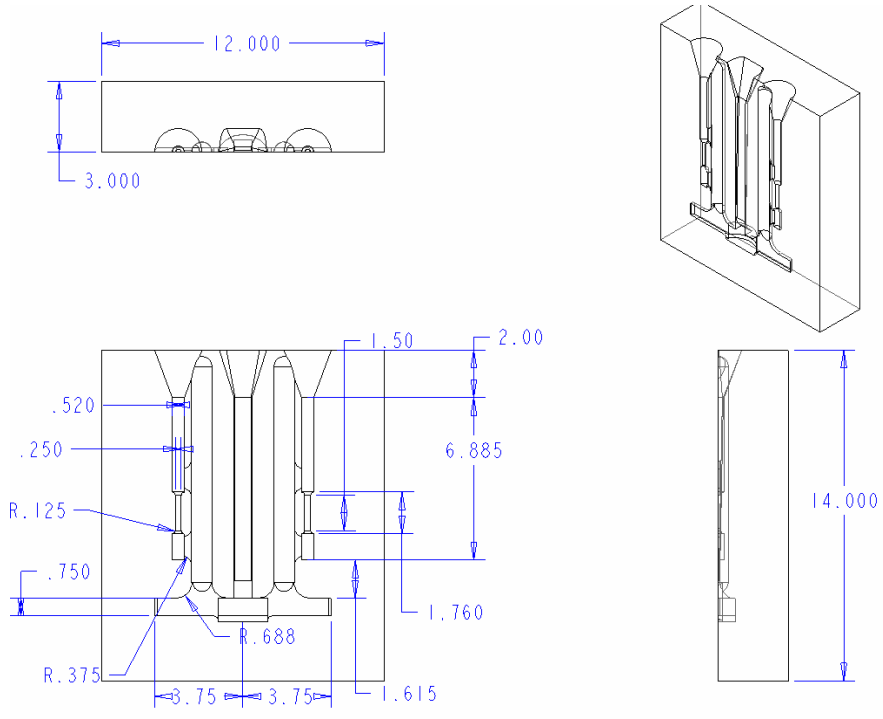
Appendix A.1 Permanent mold half part drawing.

.
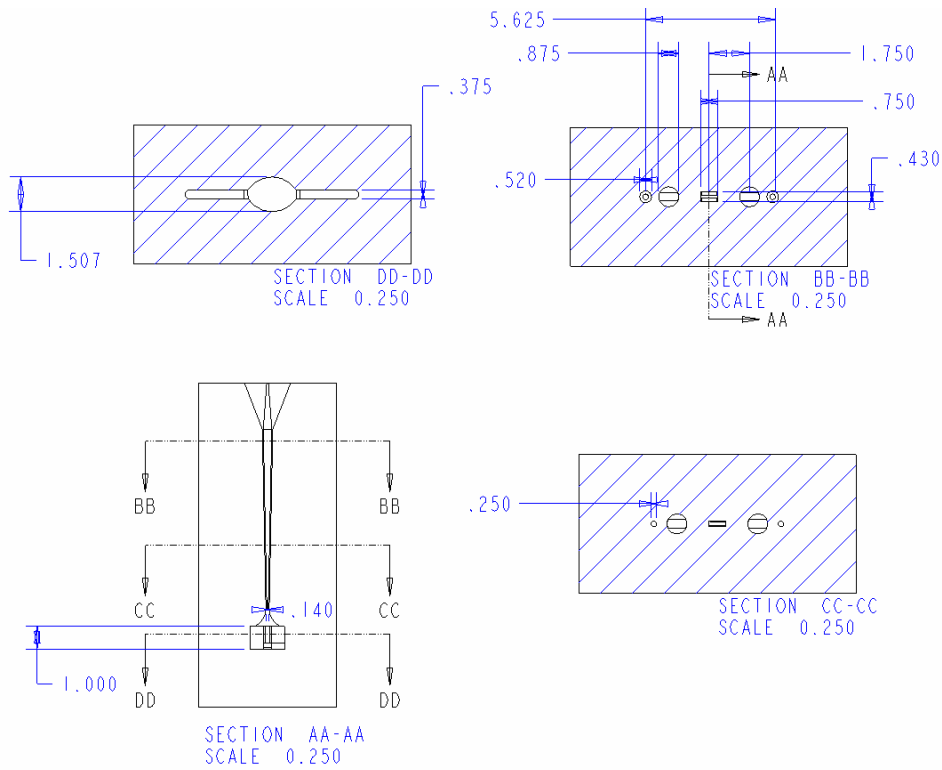
Appendix A.2 Permanent mold combined halves machine part drawing.

NOTES:

1) The central section of the part is shaded with cross hatched lines and represents a non-machined surface. It should be left in the as-cast condition, except for the milled flats.

2) Machining should be done in such a way so that the thinner central section is not put under much load. Since this is a meaterial testing sample, it is important to keep the center section in its original condition.

3) Center holes at the ends of the specimen are acceptable.

DEFAULT TOLERANCE UNLESS SPECIFIED		UNIVERSITY OF MICHIGAN				
DECIMAL	TOLERANCE	MATERIALS SCIENCE AND ENGINEERING				
.0	+/- 0.1					
.00	+/- 0.01	TITLE:				
.000	+/- 0.005	Creep Testing Specimen				
.0000	+/- 0.001	Threaded Ends (#05)				
ALL ANGLES +/- 0.5 DEGREE UNLESS SPECIFIED						
MATERIAL: Cast Magnesium		SIZE A	DWG. NO. 110036	FILENAME: CR_T_05_110036		REV
		SCALE 1.5 X	DRAWN BY: CTorbet		DATE: 27May05	

Appendix A.3 Strain mapping creep specimen machine drawing.

References

1. Luo, A.A., *Recent magnesium alloy development for elevated temperature applications*. International Materials Reviews, 2004. **49**(1): p. 13-30.

2. Luo, A.A. and M.O. Pekguleryuz, *Review of Cast Magnesium Alloys for Elevated Temperature Applications*. Journal of Materials Science, 1994. **29**: p. 5259-5271.

3. Friedrich, H.E. and B.L. Mordike, eds. *Magnesium Technology - Metallurgy, Design Data, Applications*. 2006, Springer: Berlin. 665.

4. Raynor, G.V., *The Physical Metallurgy of Magnesium and its Alloys*. Metal Physics and Physical Metallurgy, ed. G.V. Raynor. 1959, New York: Pergaman Press. 531.

5. Nave, M.D., A.K. Dahle, and D.H. StJohn, "*Eutetic Growth Morphologies in Magnesium-Aluminum Alloys," Magnesium Technology 2000,* ed. H.I. Kaplan, J. Hryn, and B. Clow, (TMS, Warrendale, PA, 2000), 233-242.

6. Dahle, A.K., Y.C. Lee, M.D. Nave, P.L. Schaffer, and D.H. StJohn, *Development of the as-cast microstructure in magnesium-aluminum alloys*. Journal of Light Metals, 2001(1): p. 61-72.

7. Waltrip, J.S., "*Fresh Look at Some Old Magnesium Die Casting Alloys for Elevated Temperature Applications," Past to Future: 47th Annual World of Magnesium Conference,* ed. (International Magnesium Association, Mclean, Virginia, 1990), 124-139.

8. Sohn, K.Y., J.W. Jones, and J.E. Allison, "*The Effect of Calcium on Creep and Bolt Load Retention Behavior of Die-Cast AM50 Alloy," Magnesium Technology 2000,* ed. H.I. Kaplan, J. Hryn, and B. Clow, (TMS, Warrendale, PA, 2000), 271-278.

9. Luo, A.A., *Recent Magnesium Alloy Development for Automotive Powertrain Applications*. Materials Science Forum, 2003. **419-422**: p. 57-66.

10. Powell, B.R., V. Rezhets, M.P. Balogh, and R.A. Waldo, "*The Relationship Between Microstructure and Creep Behavior in AE42 Magnesium Die Casting Alloy," Magnesium Technology 2001,* ed. J. Hryn, (TMS, Warrendale, PA, 2001), 175-181.

11. Powell, B.R., V. Rezhets, M.P. Balogh, and R.A. Waldo, *Microstructure and Creep Behavior in AE42 Magnesium Die-Casting Alloy*. JOM, 2002. **54**(8): p. 34-38.

12. Bakke, P., A. Fischersworring-Bunk, I.d. Lima, H. Lilholt, I. Bertilsson, F. Abdulwahab, and P. Labelle, "The European Union Mg-Engine Project - Generation of Material Property Data for Four Die Cast Mg-Alloys," *SAE* No.2006-01-0070, (Warrendale, Pa: SAE, 2006).

13. Koike, S., K. Washizu, S. Tanaka, T. Baba, and K. Kikawa, "Development of Lightweight Oil Pans Made of a Heat-Resistant Magnesium Alloy for Hybrid Engines," *SAE* No.2000-01-1117, (Warrendale, PA: SAE, 2000).

14. Aragones, J., K. Goundan, S. Kolp, R. Osborne, L. Ouimet, and W. Pinch, "Development of the 2006 Corvette Z06 Structural Cast Magnesium Crossmember," *SAE* No.2005-01-0340, (Warrendale, PA: SAE, 2005).

15. Baril, E., P. Labelle, and A. Fischerworring-Bunk, "AJ (Mg-Al-Sr) Alloy System Used for New Engine Block," *SAE Technical Paper* No.2004-01-0659, (Warrendale, Pa: SAE, 2004).

16. Beals, R.S., Z.-K. Liu, J.W. Jones, P.K. Mallick, D. Emadi, D. Schwam, and B.R. Powell, *USAMP Magnesium Powertrain Cast Components: Fundamental Research Summary.* JOM, 2007. **59**(8): p. 43-48.

17. Hines, J.A., R.C. McCune, J.E. Allison, B.R. Powell, L. Ouimet, W.L. Miller, R. Beals, L. Kopka, and P.P. Ried, "The USAMP Magnesium Powertrain Cast Components Project," *SAE Technical Paper* No.2006-01-0522, (Warrendale, Pa: SAE, 2006).

18. Nastac, L., L.S. Chou, and Y. Pang, *Assessment of Solidification-Kinetics Parameters for Titanium-Based Alloys*, in *Liquid Metal Processing*. 1999, AVS: Santa Fe, NM. p. 207-223.

19. Huang, S.C., L. Peluso, and D. Backman, *Measurements of Solute Segregation Coefficients in Quaternary Ni-based Superalloys*, in *Solidification*. 1999, TMS: Warrendale, Pa. p. 163-172.

20. Gungor, M.N., *A Statistically Significant Experimental Technique for Investigating Microsegregation in Cast Alloys*. Metallurgical and Materials Transaction A, 1989. **20A**: p. 2529-2533.

21. Caceres, C.H. and D.M. Rovera, *Solid Solution Strengthening in Concentrated Mg-Al alloys*. Journal of Light Metals, 2001. **1**(1): p. 151-156.

22. Biery, N., M.D. Graf, and T.M. Pollock, *A Method for Measuring Microstructural-Scale Strains Using a Scanning Electron Microscope: Applications to gamma-Titanium Aluminides*. Metallurgical and Materials Transaction A, 2003. **34A**(10): p. 2301-2313.

23. Biery, N.E., M.D. Graef, and T.M. Pollock, *Influence of microstructure and strain distribution on failure in intermetallic TiAl based alloys.* Materials Science and Engineering A, 2001. **319-321**: p. 613-617.

24. Weast, R.C., ed. *Handbook of Chemistry and Physics*. 57th ed. 1976, CRC Press: Cleveland.

25. Reed-Hill, R.E. and R. Abbaschian, *Physical Metallurgy Principles*. Third ed. 1994, Boston: PWS Publishing Company. 926.

26. Sutton, L.E., ed. *Table of interatomic distances and configuration in molecules and ions*. Vol. 18. 1965, Chemical Society: London.

27. Nowotny, H., E. Wormnes, and A. Mohrnheim, *Investigation on the Al-Ca, Mg-Ca, and Mg-Zr Systems.* Zeitschrift fuer Metallkund, 1940. **32**: p. 39-42.

28. Busk, R.S., *Lattice Parameters of Magnesium Alloys.* Transactions of AIME, 1950. **188**: p. 1460-1464.

29. Nayeb-Hashemi, A.A. and J.B. Clark, *Mg-Sr (Magnesium-Strontium)*, in *Phase Diagrams of Binary Magnesium Alloys*, A.A. Nayeb-Hashemi and J.B. Clark, Editors. 1988, ASM International. p. 305-312.

30. Nayeb-Hashemi, A.A. and J.B. Clark, *Ce-Mg (Cerium-Magnesium)*, in *Phase Diagrams of Binary Magnesium Alloys*, A.A. Nayeb-Hashemi and J.B. Clark, Editors. 1988, ASM International. p. 78-88.

31. Nayeb-Hashemi, A.A. and J.B. Clark, *La-Mg (Lanthanum-Magnesium)*, in *Phase Diagrams of Binary Magnesium Alloys*, A.A. Nayeb-Hashemi and J.B. Clark, Editors. 1988, ASM International. p. 178-183.

32. Murray, J.L., *Al-Mg (Aluminum-Magnesium)*, in *Phase Diagrams of Binary Magnesium Alloys*, A.A. Nayeb-Hashemi and J.B. Clark, Editors. 1988, ASM International. p. 17-34.

33. Reed-Hill, R.E. and W.D. Robertson, *Deformation of Magnesium Single Crystals by Non-basal Slip.* Transactions of AIME, 1957. **209**: p. 496.

34. Couret, A. and D. Caillard, *An In Situ study of prismatic glide in magnesium - I. The rate controlling mechanism.* Acta Metallurgica, 1985. **33**(8): p. 1447-1454.

35. Couret, A. and D. Caillard, *An in situ study of prismatic glide in magnesium - II. Microscopic Activation Parameters.* Acta Metallurgica, 1985. **33**(8): p. 1455-1461.

36. Vagarali, S.S. and T.G. Langdon, *Deformation mechanisms in H.C.P. metals at elevated temperature - II. Creep Behavior of Mg-0.8% Al Solid Solution Alloy.* Acta Metallurgica, 1981. **30**: p. 1157-1170.

37. Akhtar, A. and E. Teghtsoonian, *Solid solution strengthening of magnesium single crystals - II. The effect of solute on the ease of prismatic slip.* Acta Metallurgica, 1969. **17**: p. 1351-1356.

38. Vagarali, S.S. and T.G. Langdon, *Deformation mechanisms in H.C.P. Metals at Elevated Temperatures - I. Creep Behavior of Magnesium.* Acta Metallurgica, 1981. **29**: p. 1968-1982.

39. Hsu, S.S. and B.D. Cullity, *On the Torsional Deformation and Recovery of Single Crystals.* Transactions of AIME, 1954. **200**: p. 305.

40. Bakarian, P.W. and C.H. Mathewson, *Slip and Twinning of Magnesium Single Crystals at Elevated Temperatures.* Transactions of AIME, 1943. **152**: p. 226.

41. Burke, E.C. and W.R.H. Jr., *Plastic Deformation of Magnesium Single Crystals.* Transactions of AIME, 1952. **195**: p. 295-303.

42. Conrad, H. and W.D. Robertson, *Effect of Temperature on the Flow Stress and Strain-Hardening Coefficient of Magnesium Single Crystals.* Transactions of AIME, 1957. **209**: p. 503.

43. Kelley, E.W. and W.F.H. Jr., *Plane-Strain Compression of Magnesium and Magnesium Alloy Crystals.* Transactions of AIME, 1968. **242**: p. 5-13.

44. Kelley, E.W. and W.F.H. Jr., *The Deformation Characteristics of Textured Magnesium.* Transactions of AIME, 1968. **242**: p. 654-661.

45. Akhtar, A. and E. Teghtsoonian, *Solid solution strengthening of magnesium single crystals - I. Alloying behavior in basal slip.* Acta Metallurgica, 1969. **17**: p. 1339-1349.

46. Agnew, S.R., M.H. Yoo, and C.N. Tomé, *Application of texture simulation to understanding mechanical behavior of Mg and solid solution alloys containing Li or Y.* Acta Materialia, 2001. **49**: p. 4277-4289.

47. Agnew, S.R., J.A. Horton, and M.H. Yoo, *Transmission Electron Microscopy Investigation of <c+a> Dislocations in Mg and alpha-Solid Solution Mg-Li Alloys.* Metallurgical and Materials Transaction A, 2002. **33A**: p. 851-858.

48. Obara, T., H. Yoshinga, and S. Morozumi, *{1122}<1123> Slip System in Magnesium.* Acta Metallurgica, 1972. **21**: p. 845-853.

49. Stohr, J.F. and J.P. Poirier, *Etude en Microscopie Electronique du Glissement Pyramidal {1122}<1123> dans le Magnesium.* Philosophical Magazine, 1971. **25**: p. 1313-1329.

50. Suzuki, A., N.D. Saddock, J.W. Jones, and T.M. Pollock, *Structure and transition of eutectic (Mg,Al)2Ca Laves phase in a die-cast Mg–Al–Ca base alloy.* Scripta Materialia, 2004. **51**(10): p. 1005-1010.

51. Suzuki, A., N.D. Saddock, J.W. Jones, and T.M. Pollock, *Solidification paths and eutectic intermetallics phases in Mg-Al-Ca ternary Alloys.* Acta Materialia, 2005. **53**: p. 2823-2834.

52. Zindel, J. and L. Godlewski, *Computed tomography of a die-cast aluminum A/C housing.* 2005: Ann Arbor, MI.

53. *Magnesium*, in *Metals Handbook*. 1979, American Society For Metals: Metals Park. p. 525-609.

54. Zhu, S.M., B.L. Mordike, and J.F. Nie, *Creep properties of a Mg-Al-Ca alloy produced by different casting technologies.* Materials Science and Engineering A, 2007. **In Press**.

55. Bettles, C.J., C.T. Forwood, D.H. StJohn, M.T. Frost, D.S. Jones, M. Qian, G.-L. Song, J.R. Griffiths, and J.F. Nie, "*AMC-SC1: An Elevated Temperature Magnesium Alloy Suitable for Precision Sand Casting of Powertrain Components," Magnesium Technology 2003,* ed. H.I. Kaplan, (TMS, Warrendale, PA, 2003), 223-226.

56. Niu, X.P., B.H. Hu, I. Pinwill, and H. Li, *Vacuum assisted high pressure die casting of aluminum alloys.* Journal of Materials Processing Technology, 2000. **105**: p. 119-127.

57. Suzuki, A., N.D. Saddock, J.R. TerBush, B.R. Powell, J.W. Jones, and T.M. Pollock, "*Precipitation Strengthening of a Mg-Al-Ca Based Die-Cast Alloy with Al$_2$Ca Phase," Magnesium Technology 2007,* ed. R. Beals, (TMS, Warrendale, PA, 2007),

58. Hall, E.O., *The Deformation and Ageing of Mild Steel: III Discussion of Results.* Proceedings of the Physical Society. Section B, 1951. **64**(9): p. 747-753.

59. Petch, N.J., Iron and Steel Institute, 1953: p. 25-28.

60. Frost, H.J. and M.F. Ashby, *Deformation-Mechanism Maps - The Plasticity and Creep of Metals and Ceramics*. 1982: Pergamon Press. 166.

61.   Courtney, T.H., *Creep Mechanisms*, in *Mechanical Behavior of Materials*. 2000, McGraw Hill: Boston. p. 297-314.

62.   Dieter, G.E., *Creep and Stress Rupture*, in *Mechanical Metallurgy*. 1961, McGraw-Hill: New York. p. 432-470.

63.   Sherby, O.D. and P.M. Burke, *Mechanical Behavior of Crystalline Solids at Elevated Temperature*. Progress in Materials Science, 1967. **13**: p. 325-390.

64.   Kassner, M.E. and M.T. Perez-Prado, *Fundamentals of creep in metals and alloys*. 2004, New York: Elsevier. 272.

65.   Gittus, J., *Creep, viscoelasticity and creep fracture in solids*. 1975, London: Applied Science Publishers. 725.

66.   Evans, R.W. and B. Wilshire, *Creep of Metals and Alloys*. 1985, London: The Institute of Metals. 314.

67.   Kassner, M.E., P. Kumar, and W. Blum, *Harper-Dorn creep*. International Journal of Plasticity, 2007. **23**: p. 980-1000.

68.   Nabarro, F.R.N., *Do we have an acceptable model of power-law creep?* Materials Science and Engineering A, 2004. **387-389**: p. 659-664.

69.   Langdon, T.G., *Grain boundary sliding revisited: Developments in sliding over four decades*. Journal of Materials Science, 2006. **41**(3): p. 597-609.

70.   Ashby, M.F., *A first report on deformation-mechanism maps*. Acta Metallurgica, 1972. **20**(7): p. 887-897.

71.   Ruano, O.A., O.D. Sherby, J. Wadsworth, and J. Wolfenstine, *Rebuttal to "In defense of diffusional creep"*. Materials Science and Engineering A, 1996. **A211**: p. 66-71.

72.   Burton, B. and G.L. Reynolds, *In defense of diffusional creep*. Materials Science and Engineering A, 1995. **A191**: p. 135-141.

73.   Greenwood, G.W., *Denuded zones and diffusional creep*. Scripta Metallurgica et Materialia, 1994. **30**(12): p. 1527-1530.

74.   Mohamed, F.A., *Harper-Down creep: Controversy, requirements, and origin*. Materials Science and Engineering A, 2007. **A463**: p. 177-184.

75.   Nabarro, F.R.N., "*Deformation of crystals by motion of a single ions,*" *Conference on the Strength of Solids,* ed. N.F. Mott, (Physical Society, London, Bristol, 1947), 75-90.

76. Herring, C., *Diffusional Viscosity of a Polycrystalline Solid.* Journal of Applied Physics, 1950. **21**(5): p. 437-445.

77. Coble, R.L., *A Model for Boundary Diffusion Controlled Creep in Polycrystalline Materials.* Journal of Applied Physics, 1963. **34**(6): p. 1679-1682.

78. Raj, R. and M.F. Ashby, *On Grain Boundary Sliding and Diffusional Creep.* Metallurgical Transactions, 1971. **2**: p. 1113-1127.

79. Akira, M., G. Shoji, T. Michihiro, and A. Setsuo, *Effect of Grain Size on Creep-Deformation Behavior of Cu-30mass% Zn Alloy.* Journal of the Materials Science Society of Japan, 1998. **35**(5): p. 251-257.

80. Johnson, W.R., R. Barrett, and W.D. Nix, *The effect of environment and grain size on the creep behavior of a ni-6 pct w solid solution.* Metallurgical and Materials Transaction B, 1971. **3**(3): p. 695-698.

81. Weertman, J., *Steady-State Creep through Dislocation Climb.* Journal of Applied Physics, 1957. **28**(3): p. 362-364.

82. Yavari, P., F. Mohamed, and T.G. Langdon, *Creep and substructure formation in an Al-5% Mg solid solution alloy.* Acta Metallurgica, 1981. **29**: p. 1495-1507.

83. Jones, J.W., *Theory of Creep Deformation*, in *Metals Handbook-Mechanical Testing*. 1985, American Society of Materials: Metals Park, OH. p. 308-310.

84. Luo, A.A., M.P. Balogh, and B.R. Powell, *Creep and Microstructure of Magnesium-Aluminum-Calcium Based Alloys.* Metallurgical and Materials Transaction A, 2002. **33A**: p. 567-574.

85. Dargusch, M.S., G.L. Dunlop, and K. Pettersen, *Transactions of the 19th International Die Casting Congress,* ed. (North American Die Casting Association, Rosemont, IL, 1997),

86. Dargusch, M., *The Role of Microstructure in the Creep of Die Cast Magnesium Alloys*, in *Mining, Minerals and Materials Engineering*. 1998, University of Queensland: Brisbane, Austrialia. p. 164.

87. Shi, L. and D.O. Northwood, *Strain-hardening and recovery during the creep of pure polycrystalline magnesium.* Acta Metallurgica et Materialia, 1994. **42**(3): p. 871-977.

88. Milicka, K., *Primary and steady-state creep of magnesium.* Zwitschruft fuer Metallkunde, 1970. **61**(2): p. 145-151.

89.   Milicka, K., J. Cadek, and P. Rys, *High Temperature Creep Mechanisms in Magnesium.* Acta Metallurgica, 1970. **18**: p. 1071-1082.

90.   Foerster, G.S., *Designing Alloys for Die Casting.* Metals Engineering Quarterly, 1973. **13**(1): p. 19-22.

91.   Foerster, G.S., *Designing Die Casting Alloys.* Light Metals Age, 1972: p. 11-13.

92.   Riddle, Y. and M. Makhlouf, *Characterizing Solidification By Non-Equilibrium Thermal Analysis.* 2003.

93.   Riddle, Y.W., L. Barber, and M.M. Makhlouf, "*Characterization of Mg Alloy Solidification and As-Cast Microstructures," Magnesium Technology 2004,* ed. A.A. Lou, (TMS, Warrendale, PA, 2004), 203-208.

94.   StJohn, D.H., A.K. Dahle, T. Abbott, M.D. Nave, and M. Qian, "*Solidification of Cast Magnesium Alloys," Magnesium Technology 2003,* ed. H.I. Kaplan, (TMS, Warrendale, PA, 2003), 95-100.

95.   Agnew, S.R., K.C. Liu, E.A. Kenik, and S. Viswanathan, "*Tensile and compressive creep behavior of die cast magnesium alloy AM60B," Magnesium Technology 2000,* ed. H. Kaplan, J.N. Hryn, and B.B. Clow, (TMS, Warrendale, Pa, 2000), 285-290.

96.   Bowles, A.L., J.R. Griffiths, and C.J. Davidson, "*Ductility and the Skin Effect in High Pressure Die Cast Mg-Al Alloys," Magnesium Technology 2001,* ed. J. Hryn, (TMS, Warrendale, PA, 2001), 161-168.

97.   Chadha, G., J.E. Allison, and J.W. Jones, "*The Role of Microstructure and Porosity in Ductility of Die Cast AM50 and AM60 Magnesium Alloys," Magnesium Technology 2004,* ed. A.A. Luo, (TMS, Warrendale, PA, 2004), 181-186.

98.   Chadha, G., J.E. Allison, and J.W. Jones, *The Role of Microstructure on Ductility of Die-Cast AM50 and AM60 Magnesium Alloys.* Metallurgical and Materials Transaction A, 2007. **38A**: p. 286-296.

99.   Dargusch, M.S., G.L. Dunlop, and K. Pettersen, "*Elevated Temperature Creep and Microstructure of Die Cast Mg-Al Alloys," Magnesium Alloys and their Applications,* ed. B.L. Mordike and K.U. Kainer,Wolfsburg, Germany, 1998), 277-282.

100.   Ishimatsu, N., Y. Terada, T. Sato, and K. Ohori, *Creep Characteristics of a Diecast AM50 Magnesium Alloy.* Metallurgical and Materials Transaction A, 2006. **37A**(1): p. 243-248.

101.   Sakkinen, D.J., "Physical Metallurgy of Magnesium Die Cast Alloys," *SAE Technical Paper* No.940779, (Warrendale, Pa: SAE, 1994).

102.   Blum, W., P. Zhang, B. Watzinger, B.v. Grossmann, and H.G. Haldenwanger, *Comparative study of creep of the die-cast Mg-alloys AZ91, AS21, AS41, AM60 and AE42.* Materials Science and Engineering A, 2001. **A319-321**: p. 735-740.

103.   Suman, C., "Creep of Diecast Magnesium Alloys AZ91D and AM60B," *SAE* No.910416, (Warrendale, Pa: SAE, 1991).

104.   Dargusch, M.S., K. Pettersen, K. Nogita, M. Nave, and G. Dunlop, *The Effect of Aluminum Content on the Mechanical Properties and Microstructure of Die Cast Binary Magnesium-Aluminium Alloys.* Materials Transactions, 2006. **47**(4): p. 977-982.

105.   Sato, H., K. Sawada, K. Maruyama, and H. Oikawa, *Improvement of creep rupture life by high temperature pre-creep in magnesium-aluminum binary solid solutions.* Materials Science and Engineering A, 2001. **A319-321**: p. 746-750.

106.   Roberts, C.S., *Interaction of Precipitation and Creep In Mg-Al Alloys.* Journal of Metals, 1956: p. 146-8.

107.   Fukuchi, M. and F. Watanabe, Journal of Japan Institute of Light Metals, 1980. **30**(5): p. 253.

108.   Lukác, P., *Solid Solution Hardening in Mg-Cd Single Crystals.* Physica Status Solidi, 1992. **131**: p. 377-390.

109.   Boas, W. and E. Schmid, *Über die Dehnung von Cadium-Krystallen.* Zeitschrift fuer Physik, 1929. **54**: p. 16.

110.   Jillison, D.C., *Quantitative Stress-Strain Studies on Zinc Single Crystals in Tension.* Transactions of AIME, 1950. **188**: p. 1129.

111.   Regev, M., E. Aghion, and A. Rosen, *Creep studies of AZ91D pressure die casting.* Materials Science and Engineering A, 1997. **234-236**: p. 123-126.

112.   Regev, M., E. Aghion, A. Rosen, and M. Bamberger, *Creep studies of coarse-grained AZ91D magnesium castings.* Materials Science and Engineering A, 1998. **252**: p. 6-16.

113.   Saddock, N.D., A. Suzuki, J.R. TerBush, J. Zindel, J.E. Allison, J.W. Jones, and T.M. Pollock, "Permanent Mold Casting and Creep Behavior of Mg - 4 Al - 4 X: (Ca, Ce, La, and Sr) Alloys," *SAE Technical Paper* (Warrendale, Pa: SAE, 2007).

114. Celotto, S., *TEM Study of Continuous Precipitation in Mg-9 Wt%Al - 1 Wt%Zn Alloy.* Acta Materialia, 2000. **48**: p. 1775-1787.

115. Bettles, C.J., *The effect of gold additions on the ageing behavior and creep properties of the magnesium alloy AZ91E.* Materials Science and Engineering A, 2003. **348**(1): p. 280-288.

116. Fuchs, H.J., Magnesium Alloys Having a High Resistance to Permanent Creep Deformation at Elevated Temperatures, 847992, Britian (1960).

117. Luo, A. and T. Shinoda, "A New Magnesium Alloy for Automotive Powertrain Applications," *SAE Technical Paper* No.980086, (Warrendale, Pa: SAE, 1998).

118. Luo, A.A., M.P. Balogh, and B.R. Powell, "Tensile Creep and Microstructure of Magnesium-Aluminum-Calcium Based Alloys for Powertrain Applications - Part 2 of 2," *SAE Technical Paper* No.2001-01-0423, (Warrendale, Pa: SAE, 2001).

119. Powell, B.R., V. Rexhets, A.A. Luo, and B.L. Tiwari, Creep-Resistant Magnesium Die Castings, 6264763, USA (2001).

120. Powell, B.R., A.A. Luo, V. Rezhets, J. Bommarito, and B.L. Tiwari, "Development of Creep-Resistant Magnesium Alloys for Powertrain Applications: Part 1 of 2," *SAE Technical Paper* No.2001-01-0422, (Warrendale, Pa: SAE, 2001).

121. Horie, T., H. Iwahori, Y. Seno, and Y. Awano, "*Development of High Creep-Resistant Magnesium Alloy Strengthened by Ca Addition," Magnesium Technology 2000,* ed. H.I. Kaplan, J. Hryn, and B. Clow, (TMS, Warrendale, PA, 2000), 261-269.

122. Pekguleryuz, M. and J. Renaud, "*Creep Resistance in Mg-Al-Ca Casting Alloys," Magnesium Technology 2000,* ed. H. Kaplan, J. Hryn, and B. Clow,Warrendale, PA, 2000), 279-284.

123. Cao, G. and S. Kou, "*Hot Cracking of Mg-Al-Ca Alloy Castings," Magnesium Technology 2007,* ed. R.S. Beals, N.R. Neelameggham, and M.O. Pekguleryuz, (TMS, Warrendale, Pa, 2007), 133-138.

124. Sohn, K.Y., J.W. Jones, J. Berkmortel, H. Hu, and J.E. Allison, "Creep and Bolt Load Retention Behavior of Die Cast Magnesium Alloys for High Temperature Applications: Part 2 of 2," *SAE* No.2000-01-1120, (Warrendale, PA: SAE, 2000).

125. Sohn, K.Y., J.A. Yurko, F.C. Chen, J.W. Jones, and J.E. Allison, "*Creep and Bolt-Load Retention Behavior of Die-Cast Magnesium Alloys,"* ed. 1998),

126. Terada, Y., N. Ishimatsu, R. Sota, T. Sato, and K. Ohori, *Creep Characteristics of Ca-added Die-Cast AM50 Magnesium Alloys.* Materials Science Forum, 2003. **419-422**: p. 459-464.

127. Suzuki, A., N.D. Saddock, J.W. Jones, and T.M. Pollock, *Phase Equilibria in the Mg-Al-Ca Ternary System at 773 and 673 K.* Metallurgical and Materials Transaction A, 2006. **37A**: p. 975-983.

128. Saddock, N.D., A. Suzuki, J.R. TerBush, T.M. Pollock, and J.W. Jones, "*Creep Behavior of Permanent Mold Cast Mg-Al-Ca Based Alloys," Magnesium Technology 2007,* ed. R. Beals, (TMS, Warrendale, PA, 2007), 407-412.

129. Pekguleryuz, M.O. and J. Renaud, "*Creep Resistance in Mg-Al-Ca Casting Alloys," Magnesium Technology 2000,* ed. H.I. Kaplan, J. Hryn, and B. Clow, (TMS, Warrendale, Pa, 2000), 279-284.

130. Ozturk, K., Y. Zhong, A.A. Lou, and Z.-K. Liu, *Creep Resistant Mg-Al-Ca Alloys: Computational Thermodynamics and Experimental Investigation.* JOM, 2003. **55**(11): p. 40-44.

131. Aghion, E., B. Bronfin, F.V. Buch, S. Schumann, and H. Friedrich, "*Dead Sea Magnesium Alloys Newly Developed for High Temperature Applications," Magnesium Technology 2003,* ed. H.I. Kaplan, (TMS, Warrendale, PA, 2003), 177-182.

132. Mendis, C., L. Bourgeois, B. Muddle, and J.-F. Nie, "*Effects of Ca Additions on Microstructures, Age Hardening Response and Creep Behaviour of Mg-8Zn-4Al Casting Alloy," Magnesium Technology 2003,* ed. H.I. Kaplan, (TMS, Warrendale, PA, 2003), 183-188.

133. Terada, Y., N. Ishimatsu, Y. Mori, and T. Sato, *Eutectic Phase Investigation in a Ca-added AM50 Magnesium Alloy Produced by Die Casting.* Materials Transactions, 2005. **46**(2): p. 145-147.

134. Ninomiya, R., T. Ojiro, and K. Kubota, *Improved Heat Resistance of Mg-Al Alloys by The Ca Addition.* Acta Materialia, 1994. **43**(2): p. 669-674.

135. Suzuki, A., N.D. Saddock, J.R. TerBush, J.W. Jones, T.M. Pollock, and B.R. Powell, "The Mg-Al-Ca Alloy System for Structural Applications at Elevated Temperaures," *SAE* (Warrendale, Pa: SAE, 2007).

136. Mori, Y., Y. Terada, and T. Sato, *Microstructure Stability and Creep Strength in Die-cast AX52 Magnesium Alloy.* Materials Transactions, 2005. **46**(8): p. 1749-1752.

137. Buch, F.v., S. Schumann, H. Friedrich, E. Aghion, B. Bronfin, B.L. Mordike, M. Bamberger, and D. Eliezer, "*New Die-Casting Alloy MRI153 For Power-Train Applications," Magnesium Technology 2002,* ed. H.I. Kaplan, (TMS, Warrendale, PA, 2002), 61-67.

138. Suzuki, A., N.D. Saddock, J.W. Jones, and T.M. Pollock, "*Phase Transformation and Creep of Mg-Al-Ca Based Die-Cast Alloys," Magnesium Technology 2005,* ed. N.R. Neelameggham, H.I. Kaplan, and B.R. Powell, (TMS, Warrendale, PA, 2005), 111-116.

139. Suzuki, A., N.D. Saddock, L. Riester, E. Lara-Curzio, J.W. Jones, and T.M. Pollock, *Effect of Sr Additions on the Microstructure and Strength of a Mg-Al-Ca Ternary Alloy.* Metallurgical and Materials Transaction A, 2007. **38**(2): p. 420-427.

140. Aliravci, C.A., J.E. Gruzleski, and F.C. Dimayuga, *Effect of Strontium on Shrinkage Microporosity in Magnesium Sand Castings.* AFS Transactions, 1992. **115**: p. 353-362.

141. Parvez, M.A., M. Medraj, E. Essadiqi, A. Muntasar, and G. Denes, *Experimental Study of the Ternary Magnesium-Aluminum-Strontium System.* Journal of Alloys and Compounds, 2005.

142. Chartrand, P. and A.D. Pelton, *Critical Evaluation and Optimization of the Thermodynamic Properties and Phase Diagrams of the Al-Mg, Al-Sr, Mg-Sr, and Al-Mg-Sr Systems.* Journal of Phase Equilibria, 1994. **15**(6): p. 591-605.

143. Cao, H., J. Zhu, C. Zhang, K. Wu, N.D. Saddock, J.W. Jones, T.M. Pollock, R. Schmid-Fetzer, and Y.A. Chang, *Experimental investigation and thermodynamic modelling of the Mg - Al -rich region of the Mg - Al - Sr System.* International Journal of Materials Research, 2006. **97**(4): p. 422-428.

144. Pekguleryuz, M., P. Labelle, and D. Argo, "Magnesium Die Casting Alloy AJ62x with Superior Creep Resistance, Ductility and Die Castability," *SAE* No.2003-01-0190, (Warrendale, PA: SAE, 2003).

145. Argo, D., M. Pekguleryuz, M. Dierks, T. Sparks, and T. Waltemate, "*Diecastability and properties of Mg-Al-Sr Based Alloys," Magnesium Technology 2001,* ed. J. Hyrn, (TMS, Warrendale, Pa, 2001), 131-136.

146. Labelle, P., M. Pekgularyuz, M. Lefebvre, and R. Bouchard, "New Aspects of Temperature Behavior of AJ52x, Creep Resistant Magnesium Alloy," *SAE* No.2002-01-0079, (Warrendale, PA: SAE, 2002).

147. Baril, E., P. Labelle, and M.O. Pekguleryuz, *Elevated Temperature Mg-Al-Sr: Creep Resistance, Mechanical Properties, and Microstructure.* JOM, 2003: p. 34-39.

148. Leontis, T.E., *The Properties of Sand Cast Magnesium-Rare Earth Alloys.* Metals Transactions, 1949. **185**: p. 968-983.

149. Mellor, G.A. and R.W. Ridley, *The creep strength at 200 °C. of some magnesium alloys containing cerium.* Journal of the Institute of Metals, 1948. **75**: p. 679-692.

150. Murphy, A.J. and J.M. Payne, *Magnesium-Cerium-Zirconium alloys: Properties at elevated temperatures.* Journal of the Institute of Metals, 1947. **73**: p. 105-27.

151. Bakke, P., H. Westengen, S. Sannes, and D. Albright, "Powertrain Components - Opportunities for the Die Cast AE Family of Alloys," *SAE Technical Paper* No.2004-01-0655, (Warrendale, Pa: SAE, 2004).

152. Mellor, G.A. and R.W. Ridley, *Creep at 250 °C and 300 °C. of some magnesium alloys containing cerium.* Journal of the Institute of Metals, 1953. **81**: p. 245.

153. Wei, L.Y., *Age hardening and precipitation in a cast magnesium-rare-earth alloy.* Journal of Materials Science, 1996. **31**: p. 387-397.

154. Wu, K. and A. Chang, *Private Communication.* 2004: Ann Arbor, MI.

155. Wei, L.Y. and G.L. Dunlop, *Precipitation Hardening in a cast Magnesium-Rare Earth Alloy.* Magnesium alloys and their applications, 1992: p. 335-342.

156. Moreno, I.P., T.K. Nandy, J.W. Jones, J.E. Allison, and T.M. Pollock, *Microstructural characterization of die-cast magnesium rare-earth alloy.* Scripta Materialia, 2001. **45**: p. 1423-1429.

157. Pettersen, G., H. Westengen, R. Hoier, and O. Lohne, *Microstructure of a pressure die cast magnesium-4wt% aluminum alloy modified with rare earth additions.* Materials Science and Engineering A, 1996. **207**: p. 115-120.

158. Sieracki, E.G., J.J. Velazquez, and K. Kabiri, "Compressive Stress Retention Characteristics of High Pressure Die Cast Magnesium Alloys," *SAE* No.960421, (Warrendale, PA: SAE, 1996).

159. Moreno, I.P., T.K. Nandy, J.W. Jones, J.E. Allison, and T.M. Pollock, *Microstructural stability and creep of rare-earth containing magnesium alloys.* Scripta Materialia, 2003. **48**: p. 1029-1034.

160. Beer, S., G. Frommeyer, and E. Schmid, "*Development of Mg-Mg₂Si light weight alloys," Magnesium Alloys and Their Applications,* ed. B.L. Mordike and F. Hehmann,1992), 317-325.

161. Bronfin, B., M. Katsir, and E. Aghion, "*Preparation and Solidification Features of AS Series Magnesium Alloys," Magnesium Technology 2000,* ed. H.I. Kaplan, J. Hryn, and B. Clow, (TMS, Warrendale, PA, 2000), 253-259.

162. Dargusch, M.S., A.L. Bowles, K. Pettersen, P. Bakke, and G.L. Dunlop, *The Effect of Silicon Content on the Microstructure and Creep Behavior in Die-Cast Magnesium AS Alloys.* Metallurgical and Materials Transaction A, 2004. **35A**: p. 1905-1909.

163. McDonald, J.C., Magnesium base alloy, 2,371,531, USA (1945).

164. Leontis, T.E., *Properties of Magnesium-Thorium And Magnesium-Thorium-Cerium Alloys.* Transactions of AIME, 1952. **194**: p. 287-294.

165. Leontis, T.E., *Effect of Rare-Earth Metals On the Properties of Extruded Magnesium.* Transactions of AIME, 1951: p. 987-993.

166. Nie, J.F. and B.C. Muddle, *Characterisation of Strengthening Precipitate Phases in a Mg-Y-Nd Alloy.* Acta Materialia, 2000. **48**: p. 1691-1703.

167. Polmear, I.L., "*Physical Metallurgy of Magnesium Alloys," Magnesium Alloys and Their Applications,* ed. B.L. Mordike and F. Hehmann,Germany, 1992), 201-212.

168. Kiehn, J., B. Smola, P. Vostry, I. Stulikova, and K.U. Kainer, *Microstructure Changes in Isochronally Annealed Alumina Fibre Reinforced Mg-Ag-Nd-Zr Alloy.* Physica Status Solidi, 1997. **164**: p. 709-723.

169. Pahutova, M., V. Sklenicka, K. Kucharova, M. Svoboda, and K.U. Kainer, "*Creep Reinforced and Unreinforced QE22 Magnesium Alloy," Magnesium Alloys and Their Applications,* ed. K.U. Kainer, (Wiley-VCH, Germany, 2003), 360-365.

170. Trojanova, Z., P. Lukac, W. Riehemann, and B.L. Mordike, "*Internal Friction of QE22 - Ca Alloys," Magnesium Alloys and Their Applications,* ed. B.L. Mordike and K.U. Kainer, (Werkstoff-Informationsgesellschaft, Germany, 1998), 357-362.

171. Lambri, O.A. and W. Riehemann, *Damping due to incoherent precipitates in commerical QE22 magnesium alloy.* Scripta Materialia, 2005. **52**: p. 93-97.

172. Mordike, B.L. and F.v. Buch, "*Development of High Temperature Creep Resistant Alloys," Magnesium alloys and applications,* ed. K.U. Kainer, (Wiley-VGM, Germany, 2000), 35-40.

173. Grobner, J. and R. Schmid-Fetzer, *Selection of promising quaternary candidates from Mg-Mn-(Sc, Gd, Y, Zr) for development of creep resistant magnesium alloys.* Journal of Alloys and Compounds, 2001. **320**: p. 296-301.

174. Stulikova, I., B. Smola, J. Pelcova, and B.L. Mordike, "*Ageing Characteristics and Creep Resistance of Mg-Y-Nd-Sc-Mn Alloy," Magnesium Alloys and Their Applications,* ed. K.U. Kainer, (Wiley-VCH, Germany, 2003), 116-121.

175. Bettles, C.J. and C.T. Forwood, Creep resistant magnesium alloy, 7,048,812 B2, USA (2006).

176. Bettles, C.J., C.T. Forwood, D.S. Jones, J.R. Griffiths, M.T. Frost, D.H.S. John, M. Qian, G.-L. Song, and J.F. Nie, "AMC-SC1: A New Magnesium Alloy Suitable for Powertrain Applications," *SAE* No.2003-01-1365, (Warrendale, PA: SAE, 2003).

177. Dunlop, G., C.J. Bettles, J.R. Griffiths, K. Venkatesan, L. Zheng, and M. Qian, "*The Effect of Grain Size on the Mechanical Properties of AM-SC1," Magnesium Alloys and Their Applications,* ed. K.U. Kainer, (Wiley-VCH, Germany, 2003), 100-105.

178. Suzuki, A., N.D. Saddock, J.R. TerBush, B.R. Powell, J.W. Jones, and T.M. Pollock, *Precipitation Strengthening of a Mg-Al-Ca Based AXJ530 Die-Cast Alloy.* Metallurgical and Materials Transaction A, 2007. **Accepted for Publication**.

179. Miller, W.K., *Creep of Die Cast AZ91 Magnesium at Room Temperature and Low Stress.* Metallurgical and Materials Transaction A, 1991. **22A**: p. 873-877.

180. Mabuchi, M., K. Kubota, and K. Higashi, *Elevated temperature mechanical properties of magnesium alloys containing Mg_2Si.* Materials Science and Technology, 1996. **12**: p. 35-39.

181. Bell, R.L. and T.G. Langdon, *An Investigation of Grain-Boundary Sliding during Creep.* Journal of Materials Science, 1967. **2**: p. 313-323.

182. Jing, B., S. Yangshan, X. Shan, X. Feng, and Z. Tianbai, *Microstructure and tensile creep behavior of Mg-4Al based magnesium alloys with alkaline-earth elements Sr and Ca additions.* Materials Science and Engineering A, 2006. **419**: p. 181-8.

183. Anyanwu, I.A., Y. Gokan, A. Suzuki, S. Kamado, Y. Kojima, S. Takeda, and T. Ishida, *Effect of subsitituting cerium-rich mischmetal with lanthanum on high temperature properties of die-cast Mg-Zn-Al-Ca-RE alloys.* Materials Science and Engineering A, 2004. **380**: p. 93-99.

184. Wu, A., M.D. Graef, and T.M. Pollock, *Grain-scale strain mapping for analysis of slip activity in polycrystalline B2 RuAl.* Philosophical Magazine, 2006. **86**(25-26): p. 3995-4008.

185. Zeisler-Mashl, K.L. and B.J. Pletka, "*Segregation During Solidification in Mar-M247 System," Superalloys,* ed. (TMS, Warrendale, PA, 1992), 175-184.

186. Scheil, E., Metallforschung, 1947. **2**: p. 69.

187. Brody, H.D. and M.C. Flemings, *Solute Redistributon in Dendritic Solidification.* Transactions of AIME, 1966. **236**: p. 615-624.

188. Tryon, B., *MULTI-LAYERED RUTHENIUM-CONTAINING BOND COATS FOR THERMAL BARRIER COATINGS*, in *Department of Materials Science and Engineering*. 2005, University of Michigan: Ann Arbor. p. 154.

189. Suzuki, A., N.D. Saddock, J.W. Jones, and T.M. Pollock, "*Phase Equilibria of Mg-Al-Ca Ternary System at 773 and 673 K," Magnesium Technology 2006,* ed. A.A. Luo, N.R. Neelameggham, and R.S. Beals, (TMS, Warrendale, PA, 2006), 63-68.

190. Guangyin, Y., L. Manping, D. Wenjiang, and A. Inoue, *Development of Cheep Creep Resistant Mg-Al-Zn-Si-base Alloy.* Materials Science Forum, 2003. **419-422**: p. 425-432.

191. Pekguleryuz, M.O. and E. Baril, *Creep Resistant Magnesium Diecasting Alloys Based on Alkaline Earth Elements.* Materials Transactions, 2001. **42**(7): p. 1258-1267.

192. Regev, M., O. Botstein, M. Bamberger, and A. Rosen, *Continuous versus interrupted creep in AZ91D mangesium alloy.* Materials Science and Engineering A, 2001. **302**: p. 51-55.

193. Morgan, J.E. and B.L. Mordike, "*Development of Creep Resistant Magnesium Rare Earth Alloys," Strength of metals and alloys,* ed. R.C. Gifkins, (Oxford, New York, 1983), 643-648.

194. Deming, H., C. Yungui, T. Yongbai, L. Hongmei, and N. Gao, *Indentation creep behavior of AE42 and Ca-containing AE41 alloys.* Materials Letters, 2007. **61**: p. 1015-1019.

195. Gutman, E.M., Y. Unigovski, M. Levkovich, Z. Koren, E. Aghion, and M. Dangur, *Influence of technological parameters of permanent mold casting and die casting on creep and strength of Mg alloy AZ91D.* Materials Science and Engineering A, 1997(A234-236): p. 880-883.

196. Regev, M., M. Bamberger, A. Rosen, and E. Aghion, "*Creep Studies of AZ91D Castings," Magnesium Alloys and their Applications,* ed. B.L. Mordike and K.U. Kainer, (Werkstoff-Informationsgesellschaft, Frankfurt, Germany, 1998), 283-288.

197. Cao, P., M. Qian, and D.H. StJohn, *Native grain refinement of magnesium alloys.* Scripta Materialia, 2005. **53**: p. 841-844.

198. StJohn, D.H., M. Qian, M.A. Easton, P. Cao, and Z. Hildebrand, *Grain refinement of Magnesium Alloys.* Metallurgical and Materials Transaction A, 2005. **36A**(7): p. 1669-1679.

199. Cao, P., M. Qian, and D.H. StJohn, *Mechanism for grain refinement of magnesium alloys by superheating.* Scripta Materialia, 2007. **56**: p. 633-636.

200. Cao, P., M. Qian, and D.H. StJohn, *Effect of manganese on grain refinement of Mg-Al based alloys.* Scripta Materialia, 2006. **54**: p. 1853-1858.

201. Fox, F.A., Journal of the Institute of Metals, 1945. **71**: p. 415-439.

202. Swiostek, J., J. Göken, D. Letzig, and K.U. Kainer, *Hydrostatic extrusion of commercial magnesium alloys at 100 °C and its mechanical influence on grain refinement and mechanical properties.* Materials Science and Engineering A, 2006. **424**: p. 223-229.

203. Moreau, G., J.A. Cornet, and D. Calais, *Acceleration de la Diffusion Chimique sous Irradiation dans le Systeme Aluminium-Magnesium.* Journal of Nuclear Materials, 1971. **38**: p. 171-202.

204. Nayeb-Hashemi, A.A. and J.B. Clark, *Ca-Mg (Calcium-Magnesium)*, in *Phase Diagrams of Binary Magnesium Alloys*, A.A. Nayeb-Hashemi and J.B. Clark, Editors. 1988, ASM International. p. 62-69.

205. Pekguleryuz, M.O. and E. Baril, "*Development of Creep Resistant Mg-Al-Sr Alloys," Magnesium Technology 2001,* ed. J. Hryn, (TMS, Warrendale, PA, 2001), 119-125.

206. Terada, Y., Y. Mori, and T. Sato, *Role of Eutectic Intermetallic Phase on Creep Strength in a Die-Cast Mg-Al-Ca Alloy: Evaluation by Internal Stress Measurement.* Materials Transactions, 2007. **48**(2): p. 97-100.

207. Wei, L.Y., G.L. Dunlop, and H. Westengen, *Precipitation Hardening of Mg-Zn and Mg-Zn-RE Alloys.* Metallurgical and Materials Transaction A, 1995. **26A**: p. 1705-1716.

208. Roberts, C.S., *Creep Behavior of Magnesium-Cerium Alloys.* Journal of Metals, 1954: p. 634-640.

209. Mohamed, F.A. and T.G. Langdon, *The transition from dislocation climb to viscous glide in creep of solid solution alloys.* Acta Metallurgica, 1974. **22**(6): p. 779-788.

210. Cottrell, A.H. and M.A. Jaswon, "*Distribution of solute atoms round a slow dislocation," Proceedings from the Royal Society of London,* ed. London, 1949), 104-114.

211. Xu, Y., L.S. Chumbley, G.A. Weigelt, and F.C. Laabs, *Analysis of interdiffusion of Dy, Nd, and Pr in Mg.* Journal of Materials Research, 2001. **16**(11): p. 3287-3292.

212. Brubaker, C. and Z.-K. Liu, "*Diffusion Couple Study of the Mg-Al System," Magnesium Technology 2004,* ed. A.A. Luo, (TMS, Warrendale, Pa, 2004), 229-234.

213. Hertzburg, R.W., *Deformation and Fracture Mechanics of Engineering Material.* 1976, New York: John Wiley.

214. Meyers, M.A. and K.K. Chawla, *Geometry of Deformation and Work-Hardening*, in *Mechanical Behavior of Materials*. 1999, Prentice Hall: Upper Saddle River. p. 680.

215. Bronfin, B., E. Aghion, N. Fantetti, F.V. Buch, S. Schumann, and H. Friedrich, "High-temperature Mg alloys for sand and permanent mold applications," *SAE Technical Paper* No.2004-01-0656, (Warrendale, Pa: SAE, 2004).

216. Mordike, B.L. and W. Henning, "*Creep and high temperature properties of magnesium based alloys," Magnesium Technology,* ed. (Institute of Metals, London, 1987), 54-59.

217. Suzuki, A., N.D. Saddock, L. Riester, E. Lara-Curzio, J.W. Jones, and T.M. Pollock, "*Effect of Sr on the Microstructure and Mechanical Properties of Mg-Al-Ca Alloys," Magnesium Technology 2006,* ed. A.A. Luo, N.R. Neelameggham, and R.S. Beals, (TMS, Warrendale, PA, 2006), 523-528.